NNT : 2025AIXM0084

THÈSE DE DOCTORAT

Soutenue à Aix-Marseille Université
le 23 Avril 2025 par

Gaelle NASSAR

Graphene superlattice induced by zwitterionic supramolecular networks: an STM/nc-AFM study

Discipline
Sciences chimiques

École doctorale
ED 250 SCIENCES CHIMIQUES DE MARSEILLE

Laboratoire/Partenaires de recherche
CINaM – UMR - 7325
Centre Interdisciplinaire de Nanosciences de Marseille

Composition du jury

Jérôme LAGOUTE DR Université Paris Cité CNRS	Rapporteur
Stéphane LENFANT DR Université de Lille CNRS	Rapporteur
Muriel SICOT CR Université de Lorraine CNRS	Examinatrice
Fabienne MICHELINI PR Aix Marseille Université	Présidente du jury
Gabriel CANARD PR Aix Marseille Université	Directeur de thèse
Thomas LEONI MCF Aix Marseille Université	Co-encadrant de thèse

Affidavit

I, undersigned, Gaelle Nassar, hereby declare that the work presented in this manuscript is my own work, carried out under the scientific direction of Pr. Gabriel Canard and Dr. Thomas Leoni, in accordance with the principles of honesty, integrity and responsibility inherent to the research mission. The research work and the writing of this manuscript have been carried out in compliance with both the French national charter for Research Integrity and the Aix-Marseille University charter on the fight against plagiarism.

This work has not been submitted previously either in this country or in another country in the same or in a similar version to any other examination body.

Completed in Marseille, on 4 February 2025



Cette œuvre est mise à disposition selon les termes de la Licence Creative Commons Attribution - Pas d'Utilisation Commerciale - Pas de Modification 4.0 International.

List of Publications and Participation in Conferences

List of Publications[1] in the Context of the Thesis project:

1. Nassar, G., Cortés-Arriagada, D., Sanhueza-Vega, L., Landois, P., Paillet, M., Hrich, H., Contreras, S., Siri, O., Pascal, S., Masson, L., Becker, C., Ranguis, A., Parret, R., Canard, G. & Leoni, T." High-order commensurate zwitterionic quinonoid phase induces a nanoscale dipole lattice on Graphene". J. Phys. Chem. C, 128, 23, 9712–9721, (2024). https://doi.org/10.1021/acs.jpcc.4c01695

Participation in Conferences[2] and Summer schools during the PhD:

Oral communications :

1. "High Order Commensurate zwitterionic supramolecular network on HOPG". **24th edition of the Scanning Probe Microscopy meeting**, 3-7 April 2023, Obernai, France.

   Nassar G.,* Canard G., Masson L., Becker C., and Leoni T.

   http://www.sondeslocales.fr/node/624

2. "High Order Commensurate zwitterionic supramolecular network on HOPG".

   Online seminars of GdR NS-CPU, 30 May 2023.

   Nassar G.,* Canard G., Nony L., Loppacher C., Clair S., Masson L., Becker C., and Leoni T.

   https://www.nanosciences-spm-uhv.com/gdr/seminaires

3. "Can we induce a Moiré effect with a supramolecular layer of zwitterions?"

   25th edition of the Scanning Probe Microscopy meeting, 22-26 April 2024, Lyon, France. **Oral communication prize.**

   Nassar G.,* Canard G., Nony L., Loppacher C., Clair S., Masson L., Becker C., and Leoni T.

   http://www.sondeslocales.fr/programme2024

[1] This list comprises published articles, articles submitted for publication, and articles in preparation, as well as books, book chapters, and/or all forms of dissemination of results relevant to the discipline of the thesis project.

[2] The term 'conference' is generic. It refers to 'conference', 'congress', 'workshop', 'symposium', 'national and/or international meetings', etc.

Poster communications :

4. "Can we induce a Moiré effect with a supramolecular layer of zwitterions?"

   8th EuChems Conference on Nitrogen Ligands. 3-7 june 2024, Cassis, France. **Poster Prize**

   Nassar G.,* Canard G., Nony L., Loppacher C., Clair S., Masson L., Becker C., and Leoni T.

   https://www.cinam.univ-mrs.fr/site/NLigands2024/index.php?page=program

5. "Can we induce a Moiré effect with a supramolecular layer of zwitterions?"

   ED 250 doctoral school day. 24 june 2024. Marseille, France. **Poster Prize.**

   Nassar G.,* Canard G., Nony L., Loppacher C., Clair S., Masson L., Becker C., and Leoni T.

6. "High Order Commensurate zwitterionic supramolecular network on HOPG"

   3rd edition of Nanosciences with near-field microscopy under ultra-high vacuum GdR NS-CPU. 21-23 November 2023, Nancy, France.

   Nassar G., Canard G., Cortés-Arriagada D., Sanhueza Vega L., and Leoni T.

   https://www.nanosciences-spm-uhv.com/en/gdr/journees-du-gdr-2/journees-du-gdr-2023

7. "Graphene superlattice induced by zwitterionic supramolecular networks".

   2nd edition of Nanosciences with near-field microscopy under ultra-high vacuum GdR NS-CPU. 22-24 November 2022, Paris, France.

   Nassar G., Canard G., Nony L., Loppacher C., Clair S., Masson L., Becker C., and Leoni T.

   https://www.nanosciences-spm-uhv.com/en/gdr/journees-du-gdr-2/journees-du-gdr-2022

Participation in a Summer School

1. **Nanosum**. International summer school on nanosciences and nanotechnologies. 13-17 june 2022, Carry le Rouet, France. https://nanosum.org

Résumé

Imposer un super-réseau sur des matériaux bidimensionnels (2D) est considéré comme une stratégie efficace pour modifier leur structure de bande, induisant des phénomènes quantiques non-conventionnels tel que la supraconductivité et la ferroélectricité.[1,2] Dans les hétérostructures de van der Waals, ce super-réseau résulte d'une commensuration à grande échelle des réseaux cristallins entre des couches 2D empilées. Aux nœuds de ce super-réseau, le potentiel électrostatique de surface va être modifié périodiquement et va générer une nouvelle structure de bande électronique. Pour élargir ce concept, nous proposons l'utilisation d'une hétérostructure hybride organique-inorganique composée d'une couche supramoléculaire 2D de molécules zwittérioniques déposées sur une surface de graphene. Deux familles de molécules ont été étudiées dans ce travail de Thèse: des dérivés des zwittérions benzoquinonemonoimine di-substitué (QZ) et du quinoxalino[2,3-b]phénazine di-substitué. Grâce à leur fort caractère dipolaire intrinsèque et leurs groupements fonctionnels périphériques, ces molécules ont été synthétisées pour permettre une modulation spatiale du potentiel électrostatique de surface tout en offrant un contrôle des paramètres de périodicité de ce potentiel via l'assemblage supramoléculaire. Parmi un ensemble de molécules synthétisées deux systèmes ont été étudiés plus en détail en raison de leur capacité à former des réseaux supramoléculaire étendus: la molécule QZ di-substituée par des groupes phényle (DPQZ) et le zwittérion quinoxalino[2,3-b]phénazine di-substitué par des groupes phényle (ZTAP). Ces molécules ont été thermo-évaporées sous ultravide sur des substrats de graphite pyrolytique orienté (HOPG) et de graphene épitaxié sur SiC. La phase supramoléculaire de la monocouche a été caractérisée par microscopie à effet tunnel (STM). DPQZ s'auto-assemble sur le graphene en phases supramoléculaires arrangées en tête-bêche, stabilisées par des liaisons hydrogène NH…O assistées par charge (CAHB) et qui présentent un Moiré structural, suggérant une phase commensurée à grande échelle (HOC) avec le graphene. Le dipôle des DPQZ s'aligne parallèlement au substrat. ZTAP s'assemble en rubans et ces molécules adoptent une orientation inclinée par rapport à la surface. L'étude de l'épitaxie entre ZTAP et la surface a démontré qu'ils sont HOC. Une analyse structurale par STM et la cartographie du potentiel électrostatique de surface réalisée par microscopie à sonde de Kelvin révèlent des variations périodiques de la différence de potentiel de contact, directement corrélées aux dipôles moléculaires. Ces mesures démontrent, pour la première fois, la capacité de moduler périodiquement le potentiel électrostatique de surface du graphène avec des couches moléculaires organiques. Cette approche met en évidence le potentiel des réseau supramoléculaires organiques pour ajuster les propriétés électroniques des matériaux 2D, ouvrant de nouvelles perspectives pour les dispositifs électroniques de nouvelle génération.

Mots clés : Super-réseau, Moiré, zwittérions, matériaux bidimensionnels, graphene, microscopie à effet tunnel.

Abstract

Imposing a Moiré superlattice on two-dimensional (2D) materials is considered to be an effective strategy to modify their band structure and induce quantum phenomena, such as unconventional superconductivity and ferroelectricity.[1,2]

In van der Waals heterostructures, this superlattice is typically achieved through lattice misorientation between stacked 2D sheets. Expanding this concept, we propose the use of supramolecular 2D layers made of zwitterionic organic molecules as an alternative to inorganic layers. The molecules studied are derivatives of the di-substituted benzoquinonemonoimine zwitterion (QZ) and the di-substituted quinoxalino[2,3-b]phenazine zwitterion (ZTAP). These molecules, with their strong dipolar character, enable spatial modulation of the electrostatic surface potential and allow precise structural control via chemical synthesis.

In this doctoral Thesis, 2 systems are investigated in detail: the di-phenyl functionalized QZ (DPQZ) and the di-phenyl functionalized ZTAP. When deposited on substrates such as Highly Oriented Pyrolytic Graphite (HOPG) and epitaxial graphene on silicon carbide Gr/SiC(0001) under ultrahigh vacuum (UHV), these molecules form the same supramolecular phases on both, as observed by Low-Temperature Scanning Tunneling Microscopy (LT-STM). DPQZ on Gr/SiC forms self-assembled supramolecular phases in a head-to-tail arrangement stabilized by strong NH…O charge-assisted hydrogen bonds (CAHBs). The dipole moment of DPQZ is aligned in the plane of the substrate, along one of its crystallographic directions. This molecular assembly shows a structural Moiré pattern, suggesting a high-order commensurate phase arising from specific interactions with the graphene/HOPG lattice nodes. ZTAP on Gr/SiC self-assembles in ribbons parallel to a crystallographic direction of graphene. The molecules adopt a titled orientation, forming an angle with the surface. The study of the epitaxy of these molecules with the surface, through cross correlation of the 2 lattices, demonstrated that the 2 networks are high order commensurate. Structural analysis using STM and electrostatic surface potential mapping using Kelvin Probe Force Microscopy (KPFM) reveals periodic shifts in the Local Contact Potential Difference (LCPD), directly correlated with the molecular dipole positions. These findings demonstrate, for the first time, the ability to induce a Moiré effect and modulate the surface potential of graphene using organic molecular layers. This approach highlights the potential of organic superlattices in tuning the electronic properties of 2D materials, paving the way for the development of strongly correlated systems and next-generation electronic devices.

Keywords: Superlattice, Moiré, zwitterions 2D materials, graphene, scanning tunneling microscopy.

Résumé Etendu de la Thèse

Ce travail de thèse vise à développer et caractériser des hétérostructures hybrides organique/inorganique de van der Waals basées sur un réseau supramoléculaire de molécules zwittérioniques déposées sur une surface de graphene par microscopie à sonde locale. L'intérêt de synthétiser une telle hétérostructure réside dans sa potentielle capacité à simuler des effets de Moiré sur graphene via l'introduction de la chimie organique.

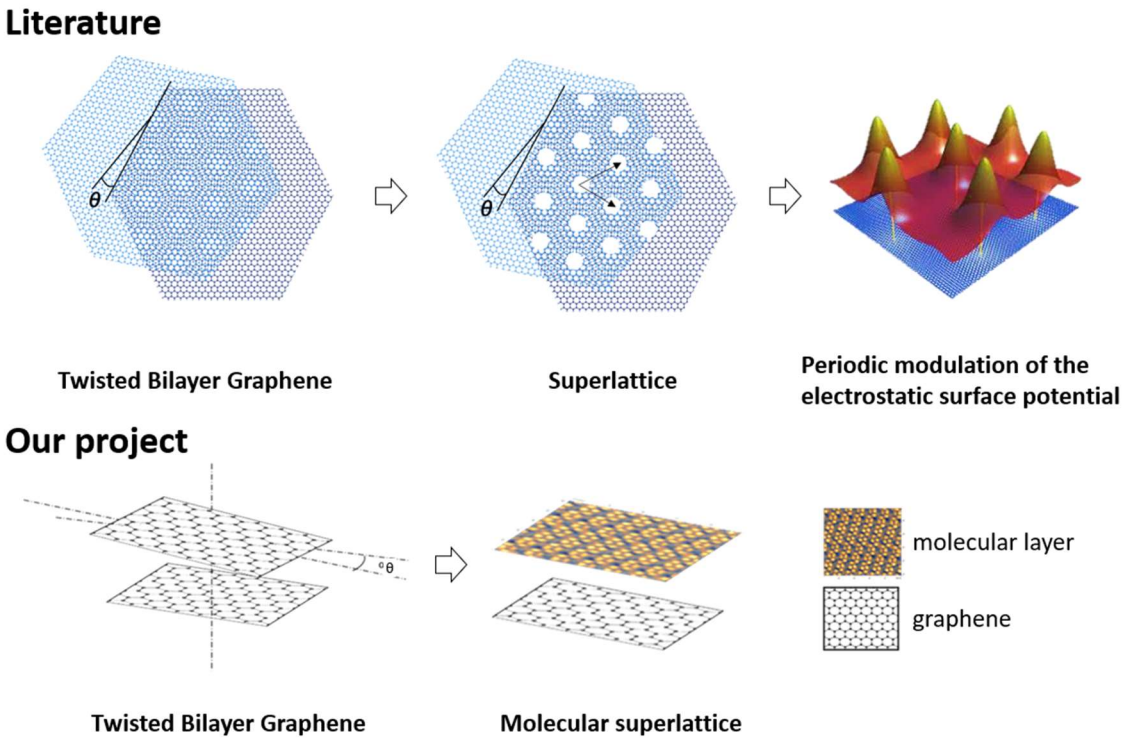


Figure 1 : Illustration du concept de super-réseau dans le graphene bicouche torsadé (twisted bilayer graphene). Le décalage entre les couches de graphene crée un super-réseau qui induit une modulation périodique du potentiel de surface sur les nœuds du super-réseau. En dessous, un schéma illustrant notre projet, la création d'un super-réseau par le remplacement de la deuxième couche de graphene tournée par une couche supramoléculaire de molécules organiques.

En effet, imposer un effet de Moiré au graphene via l'empilement de couches de graphene tournées les unes par rapport aux autres est considéré comme une stratégie prometteuse dans le domaine de l'optoélectronique avec l'apparition de phases électroniques non-conventionnelles. Ce domaine de recherche, consistant à former des hétérostructures de van der Waals dans le but de forcer l'apparition de systèmes électroniques fortement corrélés, porte aujourd'hui le nom de Twistronique. L'effet de Moiré dans le graphene bicouche torsadé (twisted bilayer graphene) engendre des

modifications dans sa structure de bande électronique. Lorsque deux couches de graphene sont superposées avec un faible angle de torsion, un effet de Moiré apparait, donnant naissance à un super-réseau aux nœuds du Moiré. Ce super-réseau crée des interférences périodiques qui modifient les propriétés électroniques du matériau. Ces ajustements induisent l'apparition de bandes plates au niveau de Fermi, favorisant une densité d'états élevée à des énergies spécifiques. Ces bandes plates ont ainsi permis de faire émerger dans ces empilements de matériaux 2D des phénomènes dits non-conventionnels comme la supraconductivité non-conventionnelle et la ferroélectricité non-conventionnelle.[1,2]

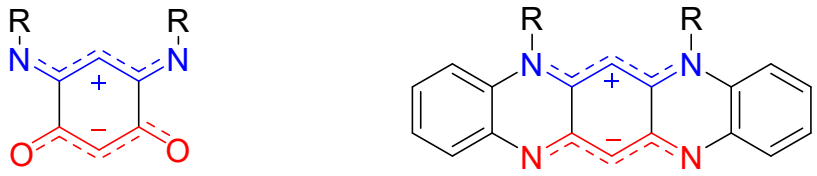
L'une des principales questions de ce travail de thèse est de savoir si l'on peut simuler un super-réseau sur le graphene à l'aide d'une couche supramoléculaire sur le graphene et non plus uniquement à l'aide d'un empilement de couches de graphene. L'intérêt d'introduire une couche supramoléculaire réside dans la versatilité de la chimie organique qui permet de modifier presque à volonté les groupements fonctionnels des molécules et leur topologie chimique afin de contrôler, de moduler *in fine* les propriétés du super-réseau et donc de l'hétérostructure.

Pour simuler ce super-réseau, il nous faudra une couche de molécules organisées de manière cristalline à la surface du graphene et qui module périodiquement le potentiel électrostatique de surface. En effet l'influence principale du super-réseau en Twistronique sur l'hétérostructure est de modifier périodiquement le potentiel électrostatique de surface aux nœuds de ce super-réseau. Nous devrons donc remplir *a minima* deux objectifs avec notre couche moléculaire pour espérer simuler un super – réseau :

i) Obtenir une organisation supramoléculaire pour induire la périodicité.
ii) Moduler le potentiel électrostatique de surface au-dessus de chaque molécule.

La combinaison de i) et ii) fera émerger une modulation périodique du potentiel de surface du graphene, et donc *a priori* les effets d'un super-réseau.

En choisissant judicieusement des espèces moléculaires fonctionnalisées, il est possible de favoriser leur autoassemblage en une monocouche organique cristalline, tout en contrôlant la géométrie et les dimensions du paramètre de maille du réseau moléculaire. C'est le fruit des travaux publiés depuis une trentaine d'années sur les réseaux supramoléculaires. De plus, si l'on introduit un fort dipôle permanent dans l'espèce moléculaire (molécule zwittérionique), on pourra générer un champ électrique local sur la molécule qui modifiera le potentiel électrostatique de la surface sur laquelle la molécule est adsorbée. Cela permettrait de concevoir un réseau de potentiels ajustables localement dans ces matériaux 2D par le dépôt de molécules spécifiques. Pour ce projet, nous avons choisi de tester deux familles de molécules zwittérioniques : les QZ (les molécules *p*-benzoquinonemonoimine zwittérioniques) et les ZTAP (molécules de la famille des quinoxalino[2,3-b]phenazine disubstitués). Ces deux familles de molécules sont schématisées dans la Figure 2.



QZ **ZTAP**

Figure 2 : Représentation des deux familles de molécules étudiées dans ce travail, mettant en évidence leurs structures distinctes. Les molécules peuvent comprendre plusieurs groupements fonctionnels périphériques R. ***QZ1****: R= CH_2-CH_2-OH;* ***QZ2****: R= CH_3;* ***QZ3****: R= $CH(CH_3)CH_2CH_3$;* ***QZ4****: R= $(CH_2)_3CH_3$;* ***QZ5****: R= $CH_2CH_2N(CH_3)_2$;* ***QZ6****: R = C_6H_4-OCH_3;* ***QZ7****: R= Ph (désigné sous le nom de DPQZ dans le manuscrit).* ***ZTAP1****: R= C_6H_5 (désigné sous le nom de ZTAP dans le manuscrit);* ***ZTAP2****: R=C_6H_4-OCH_3;* ***ZTAP3****: R=C_8H_{17}.*

Pour ces deux familles de molécules zwittérioniques, il est possible par la synthèse organique, de modifier pour chaque molécule les différents groupes fonctionnels périphériques 'R' tout en gardant son caractère zwittérionique intacte avec un fort moment dipolaire (d'environ 10 Debye) pour la molécule isolée. Ces groupes fonctionnels périphériques nous permettront de contrôler la taille du paramètre de maille ainsi que la géométrie d'assemblage du super-réseau crée.

Le déroulement du travail de cette thèse, sera de tout d'abord de créer une librairie de ces molécules zwittérioniques par synthèse organique. Par la suite, tester le dépôt de ces molécules sur graphene pour sélectionner une espèce chimique et optimiser la croissance d'une phase cristalline autoassemblée sous ultravide. Cette surface sera caractérisée de l'échelle micrométrique à l'échelle moléculaire par microscopie à effet tunnel (STM) à basse température (78 K ou 9 K). Enfin, les effets locaux du dipôle de ces couche supramoléculaires seront mesurés par microscopie à sonde de Kelvin (KPFM) en mode AFM non-contact (nc-AFM) afin de vérifier si le potentiel électrostatique de surface est effectivement modifié périodiquement. A cet effet, des cartographies 4D (X Y, Z, V_{CPD}) de spectroscopies KPFM et 3D STS (X ,Y, dI/dV) seront réalisées à l'échelle intramoléculaire.

Le manuscrit de thèse se structure comme suit :

Le **chapitre 1** est un chapitre de bibliographie composé de trois parties qui donne un aperçu de l'état de l'art concernant les mécanismes élémentaires de la croissance supramoléculaire sous ultravide. Les interactions intermoléculaires jouent un rôle important dans l'organisation et la stabilité des assemblages supramoléculaires. Ces interactions intermoléculaires présentées dans la première partie du chapitre, incluent les forces non-covalentes telles que les liaisons hydrogènes, les interactions π-π, les forces de van der Waals et les interactions électrostatiques. Ces forces influencent la géométrie des réseaux supramoléculaires, ce qui est démontré dans la deuxième partie de ce chapitre. Ce dernier met en évidence des exemples d'assemblages sur le graphene épitaxié sur la face (0001) du carbure de silicium SiC(0001) guidés par diverses interactions non-covalentes présentées dans la première partie de ce chapitre. Ces mécanismes illustrent les différentes interactions mises en jeu lors de la formation des motifs moléculaires sur la surface de graphene. La troisième partie présente la bibliographie sur l'assemblage et

les propriétés de couches de zwittérions appartenant à la famille des QZ sur différentes surfaces. Elle explore les mécanismes d'adsorption, les interactions spécifiques avec le substrat, ainsi que l'impact des différents groupes fonctionnels périphériques des dérivés de la molécule QZ sur les propriétés électroniques et structurales des surfaces étudiées.

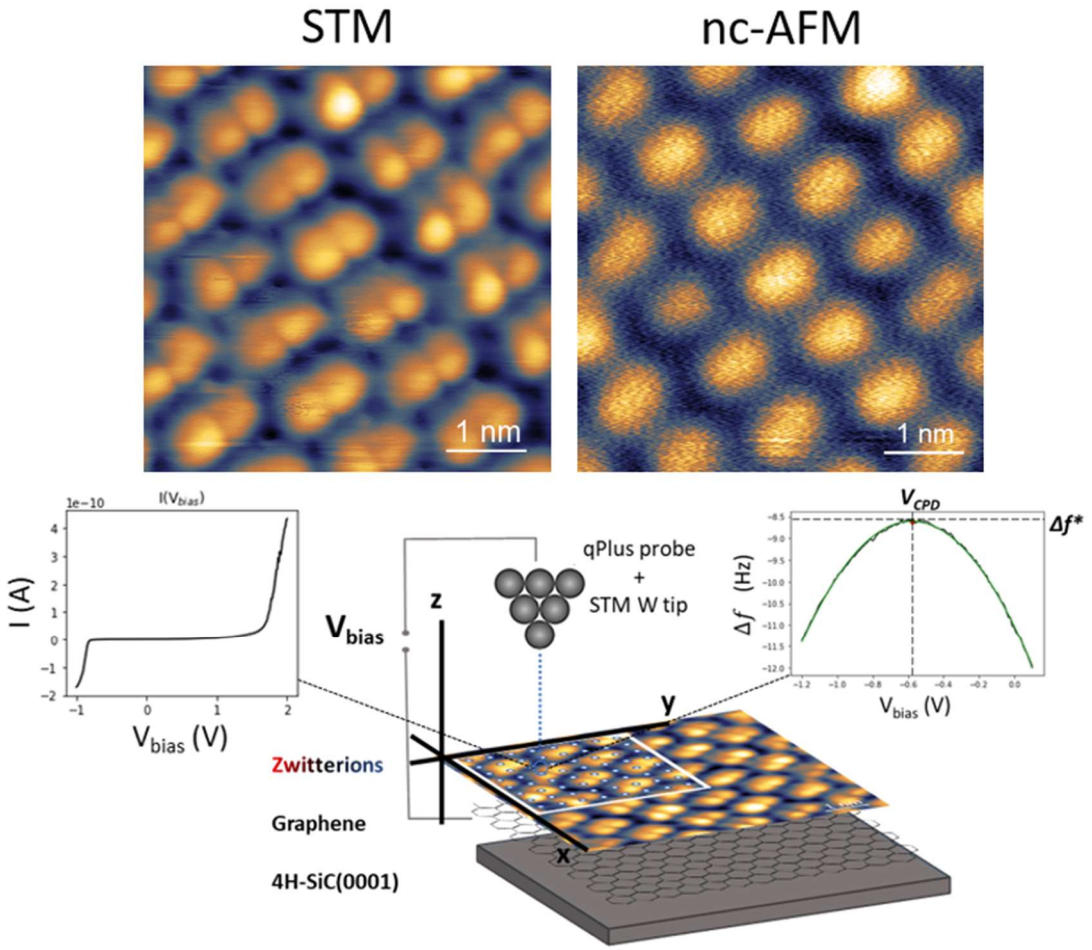


Figure 3 : Schéma illustrant les techniques de microscopie à effet tunnel (STM) et de microcopie à force atomique non-contact (nc-AFM). Schéma d'une sonde qPlus avec une pointe STM en tungstène (W) au bout qui sonde un auto assemblage de molécules zwittérioniques sur une surface de Gr/SiC. Les spectroscopies typiques qu'on peut avoir avec ce genre d'instrument sont : la spectroscopie tunnel STS pour le STM et la mesure de la différence de potentiel de surface V_{CPD} pour le KPFM. En haut du schéma, une image STM révèle la topographie de la surface en régulant sur le courant tunnel. La même zone de surface est enregistré en nc-AFM révélant le contraste topographique en régulant sur le signal Δf.

Le **chapitre 2** introduit les techniques STM, nc-AFM et KPFM en expliquant leurs principes fondamentaux et leurs modes de fonctionnement. Une section dédiée à la microscopie à effet tunnel (STM) aborde l'effet tunnel et sa théorie. La spectroscopie tunnel (STS) est également discutée pour illustrer comment les informations électroniques locales peuvent être obtenues. Une schématisation du microscope STM/nc-AFM, accompagnée d'un exemple d'image STM, une autre en nc-AFM et de spectroscopie STS et KPFM est présentée dans la Figure 3.

Le KPFM est brièvement expliqué en mettant en avant ses principes, la différence de potentiel de contact (V_{CPD}) et l'interprétation de son signe en termes d'orientation des

dipôles moléculaires ou des variations de charges partiels localisées sur la surface. En complément, ce chapitre détaille les caractéristiques des instruments utilisés pour obtenir les images et données présentées dans cette thèse. Une attention particulière est portée aux paramètres expérimentaux spécifiques et aux configurations des microscopes LT- STM/nc-AFM utilisés pour ces expériences.

Le **chapitre 3** détaille les modalités de préparation sous ultravide (UHV) des substrats étudiés, à savoir le HOPG (acheté) et le Gr/SiC(0001) (synthétisé au laboratoire L2C à Montpellier), avant dépôt. La caractérisation par STM de ses surfaces nues, avant dépôt, est présenté. Les images STM du graphene sur SiC montrent des variations de contraste le long de directions cristallographiques préférentielles. Après analyse, ces variations ont été attribuées à la présence de la couche tampon (BuL) qui croît de manière hétérogène sous la monocouche de graphene (MLG) (la Figure 4(a)). L'étude de cette couche tampon par STM a révélé qu'elle est structurellement désordonnée et composée principalement d'agrégats en forme de trimère ou de tétramère, qui sont responsables de la variation de contraste observée sous le graphene (voir Figure 4(b, c)).

L'étude du graphene par spectroscopie tunnel montre un point de Dirac vers l'énergie de- 420 meV ce qui correspond à la signature du graphene dopé n (voir Figure 4(d)) ainsi que la présence attendue d'un pseudogap électronique de largeur ~100 meV au niveau de Fermi (voir *Figure 4*(e)) (de taille variable suivant l'état de la pointe). Cette étude nous a aussi permis d'examiner l'impact de plusieurs paramètres expérimentaux, tels que la distance pointe-surface, l'amplitude de modulation de la tension de bias et la morphologie de la pointe, sur les spectres obtenus. Ces analyses ont démontré comment ces facteurs influencent la résolution et l'interprétation des états électroniques du graphene. Par ailleurs, ce chapitre introduit le concept de cartographie STS spatialement résolue, mettant en lumière son rôle crucial pour révéler les variations locales de la structure électronique du graphene dû à la couche tampon.

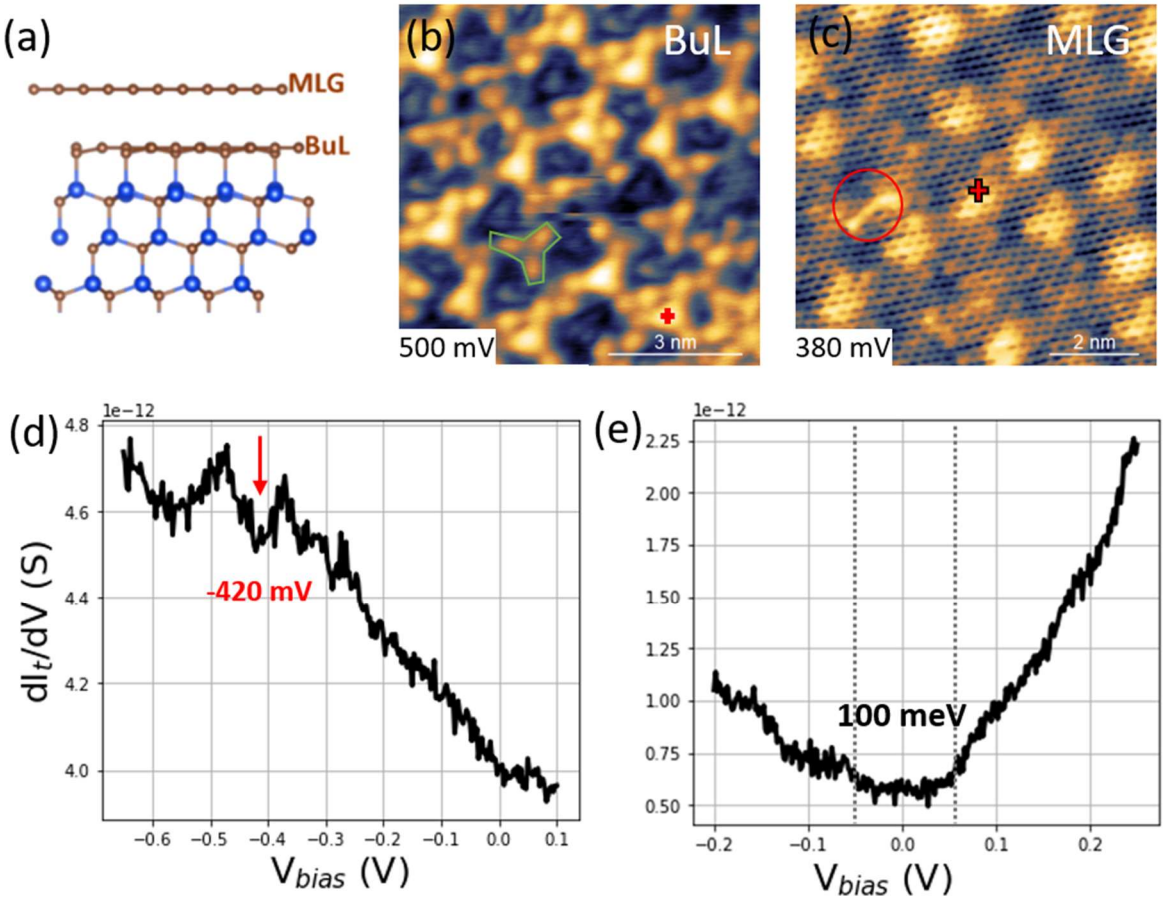


Figure 4 : ***(a)*** *Synthèse du graphene épitaxié monocouche (MLG) d'un substrat de carbure de silicium SiC par chauffage sous atmosphère contrôlé. Les atomes de silicium (en bleu) se subliment préférentiellement du SiC créant ainsi une couche riche en carbone (atomes de C en marron). La couche tampon (BuL) hétérogène se reconstruit d'abord et s'enrichit en atomes de carbone jusqu'à se transformer en une monocouche de graphene (MLG). Schéma adapté de travaux précédents. (b) Image STM qui montre la couche tampon sous le graphene. Les caractéristiques structures brillantes de la BuL sont visibles et sont marquées par une croix rouge. Conditions tunnel : V_{bias}= 500 mV, I_t= 25 pA. (c) Image STM de réseau en nid d'abeilles du graphene, montrant une modulation du contraste influencée par les caractéristiques de la BuL. Conditions tunnel : V_{bias}= 380 mV, I_t= 25 pA. (d) Spectre dI_t/dV d'un point sur le graphene, dans une plage de tension de bias de [- 100 mV, - 650 mV] obtenu par la technique de lock-in. Paramètres du lock-in : V_{mod}= 20 mV, F_{mod}= 408 Hz. Conditions tunnel : V_{bias}= - 760 mV, I_t= 15 pA. Paramètres de stabilisation : V_{bias}= - 100 mV, I_t= 15 pA. (e) Spectre dI_t/dV (V_{bias}) d'un point sur le graphene dans une plage de tensions de bias de [- 200 mV, - 250 mV] obtenu par la technique de lock-in. Paramètres du lock-in : V_{mod}= 2 mV, F_{mod}= 434 Hz. Conditions tunnel : V_{bias}= 110 mV, I_t= 30 pA.*

En prenant en compte toutes les contraintes expérimentales, il a été démontré que la sur-structure du graphene induite par le substrat n'affecte pas les propriétés électroniques intrinsèques du matériau. Ce chapitre permet de mieux comprendre, la morphologie de la surface de Gr/SiC avec la présence de monocouche de graphene, de bicouche de graphene, d'une couche tampon et de leurs effets sur le contraste en topographie STM. Mais également les propriétés électroniques mesurables en STS du graphene et l'influence de la couche tampon.

Le **chapitre 4** est consacré à la synthèse chimique des molécules utilisées dans cette thèse. Une introduction aux colorants polyméthines et une présentation de leur historique

est donnée, notamment l'introduction à la transamination et aux zwittérions π. Les cyanines zwittérioniques constituent une sous-classe unique de colorants cyanines, caractérisée par la présence simultanée de charges positives et négatives au sein de la même molécule. Ces polyméthines couplées zwittérioniques comprennent deux systèmes indépendants où les électrons π sont totalement délocalisés sur la chaîne polyméthine. Ces molécules présentent un dipôle permanent, avec les charges positive et négative respectivement délocalisées sur la chaine polyméthine et les hétérocycles terminaux associés. Bien qu'elles soient globalement neutres, leur moment dipolaire interne est important.[3–5]

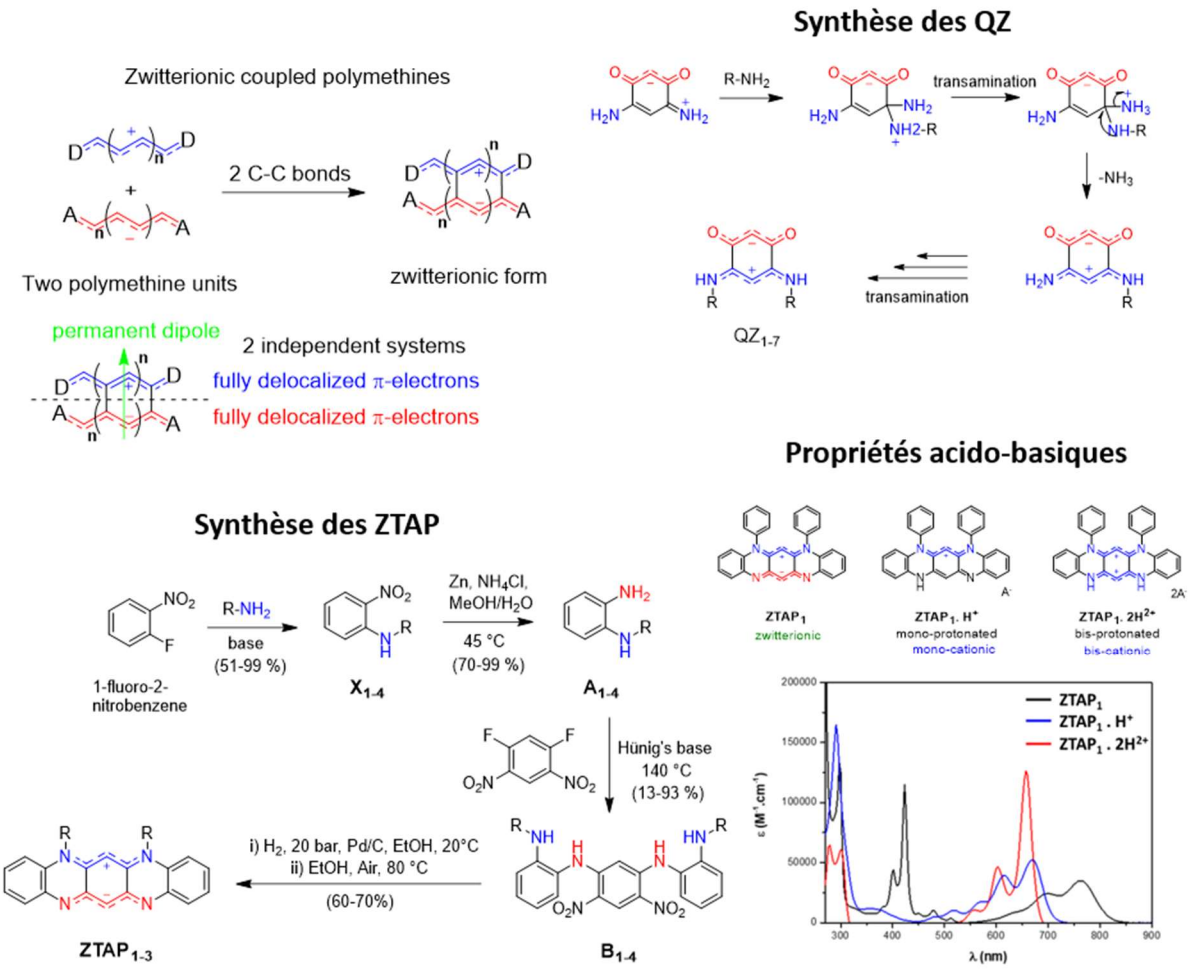


Figure 5 : Les polyméthines zwittérioniques couplées. Les méthodes générales de synthèse des dérivés QZ et ZTAP. Les propriétés acido-basiques de ZTAP$_1$.

L'avancée dans la synthèse des QZ ainsi que les propriétés structurales des QZ et des ZTAP sont décrites, un schéma récapitulatif (Figure 5) montre les principaux travaux de synthèse effectués. Les synthèses réalisées sont décrites en détail, incluant la transamination des QZ, la synthèse de ZTAP et sa fonctionnalisation avec des groupes donneurs ou accepteurs. L'effet de cette fonctionnalisation a été étudié sur les étapes de la synthèse. Enfin, on étudie la réactivité des molécules synthétisées, en explorant leurs propriétés acido-basiques pour mieux comprendre leur stabilité et leur potentiel dans

différents environnements. Les réactions d'alkylation et d'oxydation de ces composés sont également étudiées afin de mettre en lumière leurs transformations possibles. Ces analyses sont complétées par une caractérisation optique, permettant d'évaluer leurs propriétés électroniques et photophysiques.

La synthèse du dérivé QZ a suivi une voie simple et bien établie, démontrant un processus prévisible et efficace. A l'inverse, la synthèse de ZTAP a posé des défis importants en raison d'une voie de synthèse longue et moins familière. Malgré ces difficultés, la synthèse et la caractérisation de dérivés de ZTAP ont été menées à bien, ouvrant la voie à une exploration plus approfondie de sa réactivité. Lors de cette étude, une oxydation inattendue de ZTAP en sa forme dimère (d-ZTAP$_1$) a été observée, sa déshalogénation et la synthèse d'un nouveau composé mono-alkylé de R-ZTAP$_2$. Ces résultats mettent en évidence la diversité fonctionnelle de ZTAP et élargissent son potentiel pour diverses applications.

Le dépôt de ces molécules sur des surfaces de HOPG et de graphene a ensuite été étudié pour évaluer leur capacités d'autoassemblage. Cependant, toutes les molécules testées n'ont pas abouti à la formation de réseaux cristallins organisés à grande échelle (les molécules n'ayant pas abouti à une croissance supramoléculaire sont présentées en annexe E). Les prochains chapitres se concentreront sur deux systèmes où un réseau supramoléculaire a été observé, en détaillant les résultats obtenus et leur interprétation.

Le **chapitre 5** présente une étude du premier système, le zwittérion QZ fonctionnalisé avec deux groupes phényl (DPQZ) qui a été déposé sur des surfaces de HOPG et de graphene. Cette étude, réalisée à l'aide du STM à basse température et soutenue par des simulations numériques (réalisées par Dr. Cortes-Arriagada D. and Dr. Sanhueza-Vega L.), révèle que les molécules adoptent sur les deux substrats une configuration structurale identique.

Les molécules DPQZ s'assemblent avec un alignement antiparallèle de leurs dipôles, dans une organisation dimère tête bêche à plat sur la surface. Les mesures topographiques ont mis en évidence une croissance anisotrope de cette couche avec des domaines très étendus dans une direction (plusieurs centaines de nanomètres) et réduite dans l'autre direction du plan (une dizaine de nanomètres). Cette organisation est accompagnée d'un Moiré structural (voir Figure 6(a)), dont l'origine réside dans la commensurabilité à grande échelle (HOC) entre le réseau moléculaire et celui du graphene ou du HOPG. Ce résultat a été confirmé par une étude de l'épitaxie par corrélation croisée des deux réseaux.

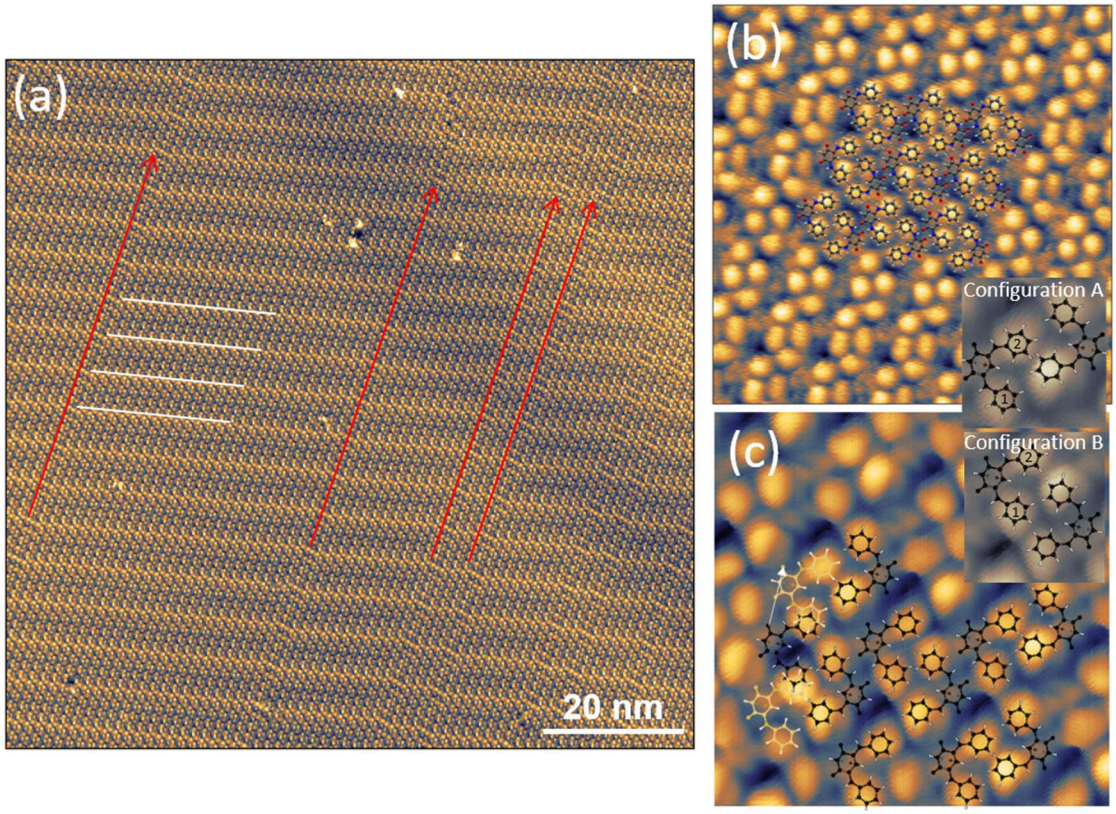


Figure 6 : ***(a)*** *Image STM des DPQZ auto-assemblés sur une surface de HOPG un Moiré structural peut être observé en lignes de contraste plus clair surlignées par une ligne blanche. Les parois de domaine sont marquées par des flèches rouges. Conditions tunnel :* I_t *= 2 pA,* V_{bias}*= 1.0 V.* ***(b)*** *Image STM des molécules DPQZ auto-assemblées en une monocouche sur une surface d'HOPG, le modèle d'assemblage proposé est superposé sur l'image. Conditions tunnel :* I_t*=2 pA,* V_{bias}*= 1.0 V.* ***(c)*** *Image STM qui montre la présence de bords de domaines caractérisés par un décalage de la position d'une molécule d'un dimer par rapport à l'autre. Ce décalage est expliqué dans l'encart où les phényls sont numérotés pour plus de clarté. Conditions tunnel :* I_t *=2 pA,* V_{bias}*= 1.70 V.*

Des calculs DFT ont permis de comprendre quel type d'interactions stabilisent cette structure auto-assemblée. Ces calculs montrent que les dimères de DPQZ sont maintenus par des liaisons hydrogène assistées par charge (CAHBs) et par des forces de van der Waals entre les cycles phényls de molécules voisines. Les différences significatives entre ces interactions, notamment en ce qui concerne leur orientation, leur énergie de liaison et leur mode d'association, expliquent bien la croissance anisotrope dans la couche moléculaire. L'organisation en dimer tête-bêche réduit le dipôle global de ce dernier. L'adsorption de ces dimères sur le graphene induit une redistribution locale de la densité électronique du graphene. Cette redistribution casse la symétrie du dipôle résultant et génère finalement un plus petit dipôle localisé à l'interface estimé par le calcul à environ 3.4 Debye par dimer. Le fait que le dipôle soit dans le plan du graphene et qu'il soit fortement réduit par un assemblage des molécules en dimère tête-bêche nous a poussé à nous concentrer sur une autre espèce chimique, plus à même de moduler fortement le potentiel électrostatique de surface.

Le **chapitre 6** présente l'étude du deuxième système : le dépôt d'une molécule ZTAP sur graphene. L'étude structurale par STM de la monocouche de ZTAP montre que ces molécules adoptent une orientation inclinée, formant un angle distinct avec la surface (voir Figure 7(b, c)). L'étude de l'épitaxie de ces molécules avec la surface par corrélation croisée des deux réseaux a démontré que ces deux réseaux sont commensurés à grande échelle.

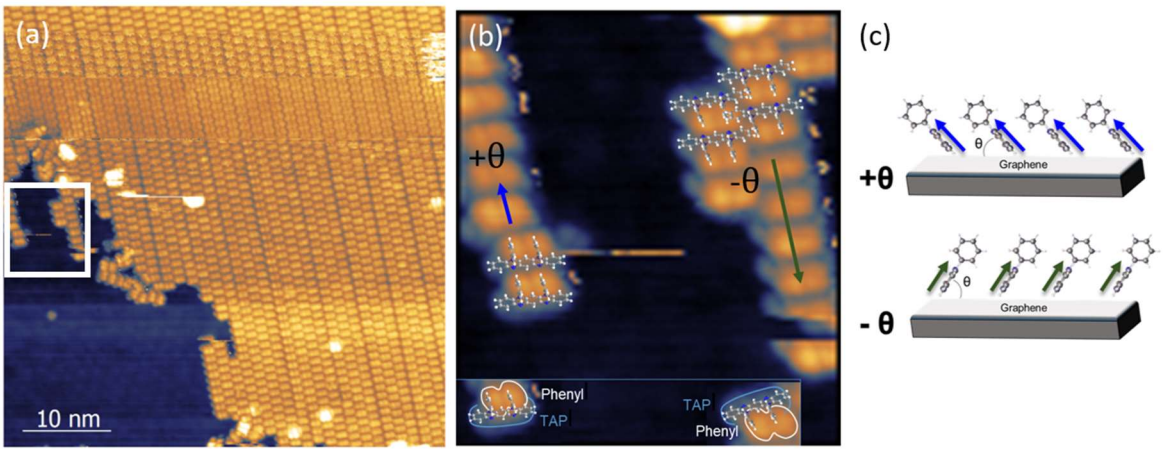


Figure 7 : ***(a)*** *Image STM à l'interface entre le réseau de ZTAP et le graphene.* ***(b)*** *Vue agrandie d'une zone sur l'image dans (a) où le contraste des molécules individuelles est perceptible. Les flèches bleues et vertes montrent deux configurations d'adsorption identiques de ZTAP inclinées de part et d'autre de la normale qui sont schématisées dans* ***(c)****, θ représente l'angle que fait ZTAP avec la surface.*

Une étude combinant l'AFM à température ambiante et l'imagerie KPFM à confirmé l'adsorption sur la tranche et l'orientation du dipôle de la première couche.

Une seconde étude en nc-AFM à basse température a permis de réaliser des spectroscopies Kelvin en 4 dimensions (4D (X, Y, Z, V_{CPD})) pour analyser le potentiel de surface du système à l'échelle intramoléculaire. Les résultats de la cartographie de différence de potentiel de contact (V_{CPD}) sur cette assemblée de molécules (Figure 8(b)) montrent une forte modulation du potentiel de surface entre le centre de la molécule où est localisé le dipôle et les bords de la molécule. Cette variation se reproduit de manière parfaitement similaire d'une molécule à l'autre entrainant la modulation périodique du potentiel de surface tant recherché. Ces valeurs de variation de V_{CPD} montrent que pour la monocouche, les dipôles des molécules ZTAP pointent vers l'extérieur de la surface.

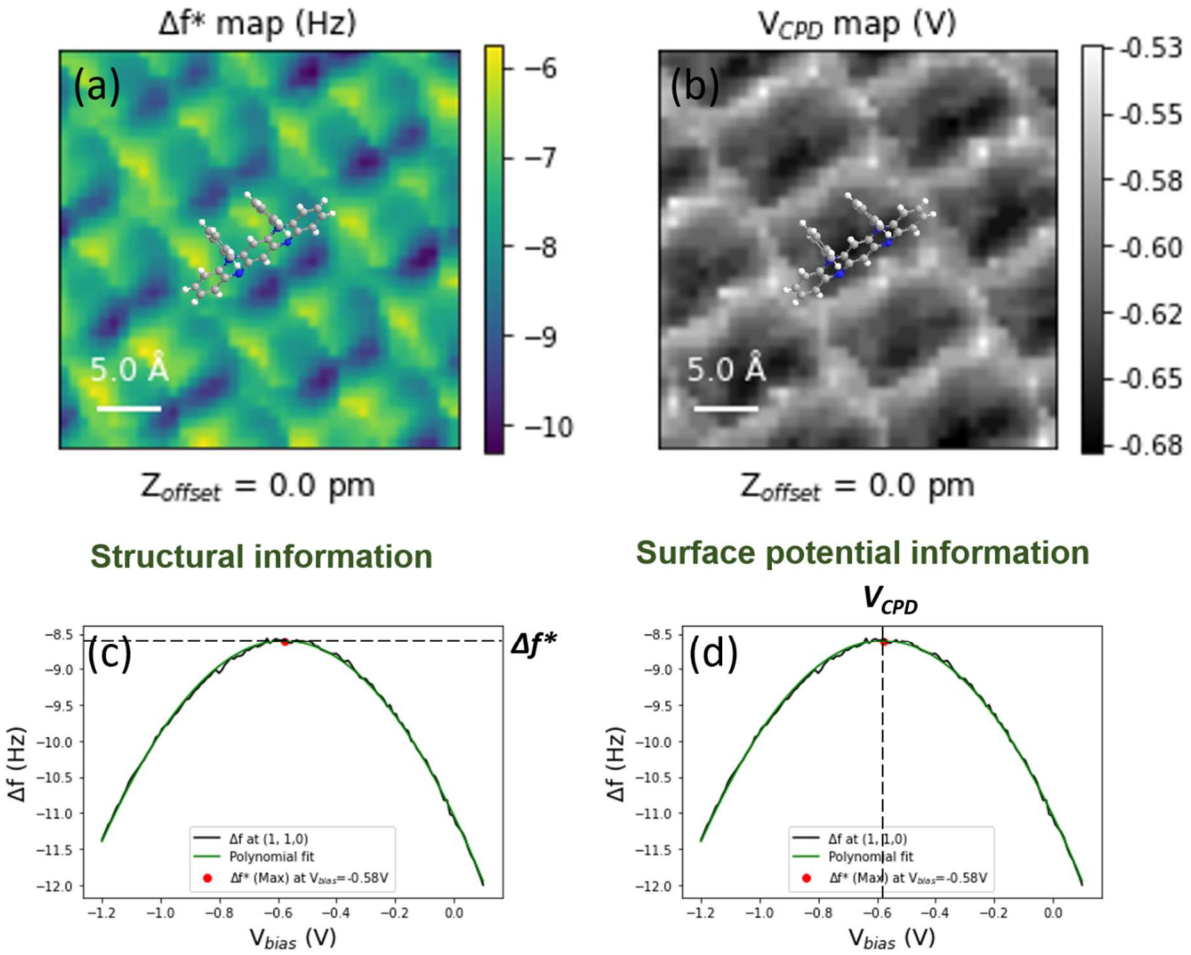


Figure 8 : ***(a)*** *Cartographie du maximum de la variation de fréquence Δf^* de l'assemblage de ZTAP sur graphene.* ***(b)*** *Cartographie de différence de potentiel de contact (CPD) correspondant aux valeurs de Δf^* dans (a).* ***(c)*** *Spectroscopie Kelvin au point (X= 1, Y= 1, Z= 0) de la surface, le maximum de Δf définit la valeur de Δf^*.* ***(d)*** *Spectroscopie Kelvin en un point (1, 1, 0) de la surface, la tension de bias pour laquelle la parabole de Δf atteint un maximum, correspond au V_{CPD}.*

Une analyse supplémentaire de cet assemblage a été menée par spectroscopie à effet tunnel (STS) à basse température (9 K), permettant de révéler des informations essentielles sur les propriétés électroniques de l'assemblage moléculaire. Des spectroscopies de conductance différentielle (dI/dV) obtenues à différentes distances de la surface ont mis en évidence les principaux états résonants moléculaires, tels que les HOMO, LUMO et LUMO+1 qui sont modifiés par les états électroniques du graphene.

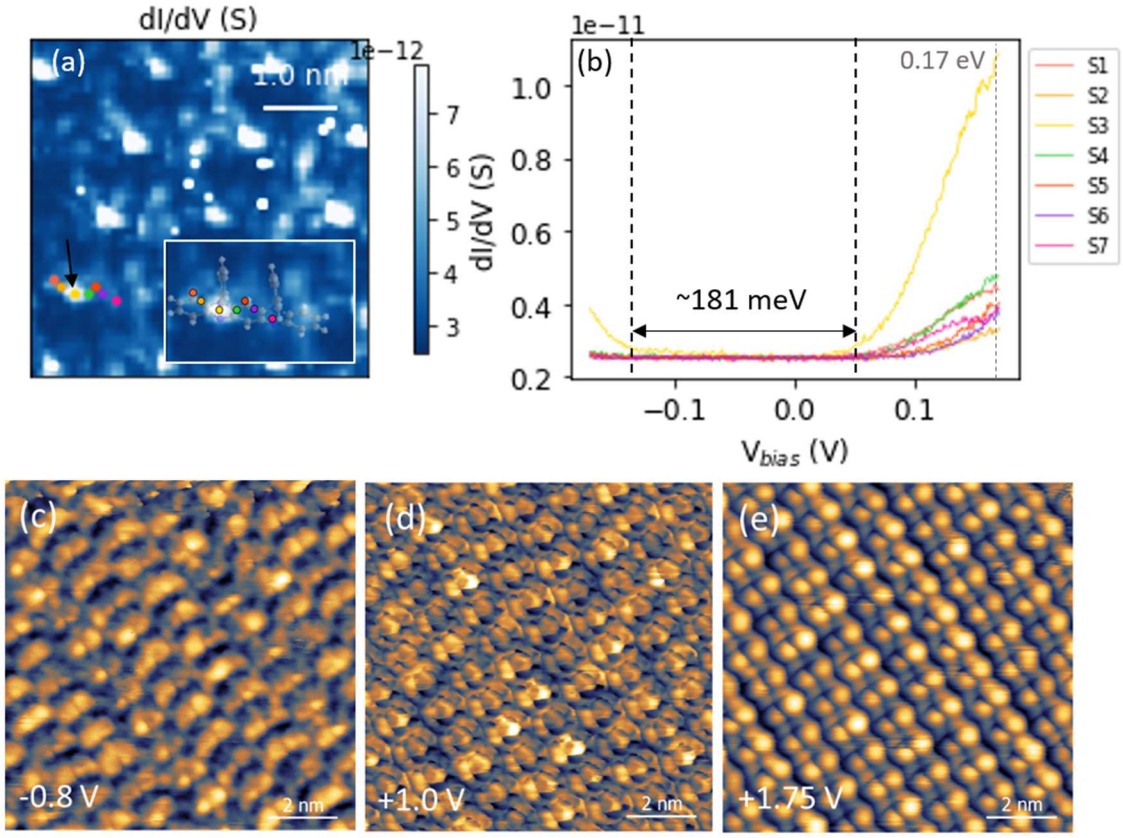


Figure 9 : ***(a)*** *Cartographie dI/dV montrant la distribution spatiale de la conductance différentielle sous des régions spécifiques de la molécule ZTAP. La cartographie comprend des points colorés, étiquetés de S1 à S7, représentant des points de la grille de spectroscopie sélectionnés correspondant à des zones différentes au-dessus de la molécule. Echelle= 1.0 nm.* ***(b)*** *Spectroscopies dI/dV mesurées aux points de données identifiés dans (a). Les courbes mettent en évidence des variations dans la largeur du gap électronique, avec une attention particulière portée au point S3 en jaune qui correspond à la région représentée dans l'encadré de la molécule. Les images STM de l'assemblage des ZTAP à différentes valeurs de V_{bias} sont montrées respectivement dans* ***(c)*** *- 0.80 V,* ***(d)*** *1.0 V et* ***(e)*** *1.75 V. Conditions tunnel : I_t= 3.7 pA. Echelle= 2.0 nm*

En comparant les calculs[6] de la distribution spatiale de ces états d'énergie moléculaire pour une molécule isolée (HOMO, LUMO, LUMO+1) et les images STM enregistrées à ces énergies, nous avons pu établir une correspondance entre les pics des spectroscopies et ces états.(Figure 9(c, d, e)). Une étude spatiale des états électroniques proches du niveau de Fermi a été réalisée à travers des cartographies dI/dV dans des fenêtres d'énergie étroites, avec la pointe positionnée aussi proche que possible de la surface. Ces cartographies montrent des motifs brillants périodiques correspondant à la périodicité du réseau moléculaire, illustrant une modulation périodique de la structure électronique de graphene au niveau des nœuds de l'assemblage moléculaire. Ces nœuds sont situés à la base d'un phényl de la molécule et non au niveau du cœur zwittérionique comme on pourrait s'y attendre. Cette analyse met en évidence l'interaction complexe entre l'assemblage des ZTAP et le graphene.

Résultats Principaux

La question de savoir si on peut induire une modulation périodique du potentiel de surface sur le graphene par le dépôt d'une couche organique, en l'occurrence une couche de molécules zwittérioniques, trouve une réponse positive à travers les résultats expérimentaux obtenus. Les réalisations de ce travail de thèse peuvent se décliner ainsi :

- Synthèse d'un des composés de la famille des QZ, le di-phényl QZ (DPQZ).
- Synthèse de composés dérivés de la famille des ZTAP. Le ZTAP fonctionnalisé avec des groupes phényle, 4-méthoxy-phényle et octyle. Lors de cette étude, une oxydation inattendue de ZTAP en sa forme dimère (d-ZTAP$_1$) a été observée ainsi que la synthèse d'un nouveau composé mono-alkylé R-ZTAP$_2$. Ces résultats mettent en évidence la diversité fonctionnelle de ZTAP et élargissent son potentiel pour diverses applications.
- Croissance et caractérisation structurale d'un réseau supramoléculaire de DPQZ sur HOPG et graphene par STM. Mise en évidence d'une croissance anisotrope du réseau supramoléculaire induite par une anisotropie des interactions intermoléculaire dans les 2 directions du réseau (interaction hydrogène dans une direction et van der Waals dans une autre direction). Mise en évidence d'un assemblage de molécules en dimère tête-bêche positionnées à plat sur la surface favorisant une diminution du dipôle global du dimère. Mise en évidence d'une phase commensurée à grande échelle avec le graphene.
- Croissance et caractérisation structurale par STM, caractérisation par KPFM et STS d'un réseau supramoléculaire de ZTAP sur graphene. Mise en évidence d'une adsorption sur la tranche de la molécule faisant un angle $+\theta$ avec le graphene. Mise en évidence d'une symétrie de l'adsorption à un angle $-\theta$. Mise en évidence, par 4D-KPFS à l'échelle intramoléculaire, d'une modulation périodique de potentiel de surface dont le pas de réseau est celui du pas du réseau moléculaire. Mise en évidence des états électroniques moléculaires par STS. Mise en évidence de la modification et de la localisation spatiale des états électroniques de la surface par les molécules via l'enregistrement de cartographie spatiale de STS.

L'autoassemblage des molécules DPQZ sur HOPG et graphene aboutit à une organisation où le dipôle est parallèle au plan du substrat, tandis que les molécules ZTAP s'assemblent sur la tranche faisant un angle avec entre la surface et l'axe latéral de la molécule. Dans ce deuxième système (ZTAP sur graphene), le dipôle est presque perpendiculaire au plan, ce qui lui donne une influence plus significative sur le potentiel de surface. Cette configuration a motivé la mesure du potentiel de surface par des cartographies 4D KPFM à basse température, qui montrent une modulation de 150 meV pic-pic dont le maximum est localisé sur chaque dipôle moléculaire. Nous en concluons que les ZTAP peuvent jouer le rôle de super-réseau sur graphene car le caractère zwittérionique de chaque molécule a été préservé lors de l'assemblage et modifie localement le potentiel électrostatique de surface.

Conclusions et Perspectives

Cette thèse a permis de caractériser en détail les interactions entre les réseaux de QZ et ZTAP et le graphene. Les QZ s'assemblent avec leur dipôle parallèle à la surface avec un dipôle résultant calculé dans le plan du graphene tandis que les ZTAP s'assemblent sur la tranche avec le dipôle qui pointe vers l'extérieur de la surface.

Les principales avancées incluent la démonstration de l'alternance du dipôle en fonction du nombre de couches, la cartographie des états électroniques près du niveau de Fermi montre une modulation périodique spatiale de ces états.

Les travaux futurs sur ce projet seraient d'étudier l'effet d'autres types de molécules zwittérioniques sur le graphene afin de mieux comprendre l'influence des différents groupes fonctionnels périphériques sur l'assemblage. Des simulations théoriques du potentiel de surface ainsi que de la valeur du dipôle résultant dans cet assemblage sont nécessaires pour appuyer les résultats expérimentaux et approfondir la compréhension des interactions intermoléculaires ou interactions molécule-surface mises en jeu pour la formation de ces réseaux supramoléculaires. Maintenant que nous avons mis en évidence la présence de cette modulation il serait intéressant d'en mesurer les conséquences sur les propriétés mésoscopiques du graphene tel que le transport et la structure bande.

Acknowledgments

I would like to express my heartfelt gratitude to everyone who supported me throughout this joyful and challenging journey of my life. This work would not have been possible wihout the guidance, encouragement, and collaboration of many.

I am profoundly thankful and grateful to my PhD supervisors Pr. Gabriel Canard and Dr. Thomas Leoni, your shared expertise, guidance and unwavering support have been invaluable and helped shape this work into a very enriching experience. Thank you for your kindness and understanding through difficult times. I have learned so much from both of you and genuinely appreciated our work together. Your mentorship has not only guided my academic journey but has also inspired me personally. I will carry the lessons and values you've imparted with me into the next stages of my life and hope I can have the chance to work with you again in the future.

I am very grateful for the jury members, Dr. Jérome Lagoute and Dr. Stéphane Lenfant for the time dedicated to evaluating this work and for your valuable feedback which greatly contributed to its improvement. I also extend my sincere thank you to the examiners Pr. Fabienne Michelini and Dr. Muriel Sicot for your interest in this work and for the insightful discussions during the defense that provided valuable perspectives on this work.

I extend my appreciation and thank you to the 2D ASAP and CHROMA team leaders Pr. Laurence Masson and Dr. Olivier Siri for the very warm welcome into your respective teams for all these years. Thank you to my team members Pr. Conrad Becker, Dr. Romain Parret, Dr. Simon Pascal, Dr. Elena Zaborova and Dr. Anthony Kermagoret whose contributions have greatly enriched this research and PhD experience by sharing their expertise, innovative ideas and suggestions. The seamless interdisciplinary collaboration between the two teams has been truly motivating. I extend my thanks to Dr. Frederic Brunel for your help setting up the NMR machine and experiments and for your constant attention to safety in the lab.

A special thank you for the Nanostructuration team members of the IM2NP lab for the collaborative work on the project. Thank you Dr. Laurent Nony for the very appreciated constructive discussions on the nc-AFM technique as well as for the long work hours for setting up the experiments. I have learned a lot from you. Thank you Dr. Sylvain Clair and Dr. Christian Loppacher for the help in setting up experiments, the constructive discussions and the collaborative spirit which defined our work together. Thank you Dr. Elie Geagea for the VT-AFM measurements as well as your creative input in this work regarding on-surface molecule arrangements.

I would like to thank all the collaborators in this PhD project: Dr. Diego Cortes-Arriagada and Dr. Luis Sanhueza-Vega for the DFT calculations on the DPQZ/graphene

molecular system and Dr. Périne Landois, Dr. Mathieu Paillet and their team for providing us with the graphene samples for our experiments.

A very sincere thank you Mr. Alain Ranguis for your assistance with the LT-STM in CINaM, your technical advice, tireless work in making sure everything ran smoothly. Thank you for your precious help with the countless sample preparations and transfers during my PhD, always carried out with your characteristic good mood.

Thank you to my office mates for the support and company and to the lab's very talented PhDs and postdoc researchers in physics and in chemistry for all the shared knowledge, support and good vibes throughout the years.

I would like to thank my precious family and close friends back home, to my brother Anthony, my sister Elsa and my friends Lara, Mira, Rim, Mélissa and Sueyeong for always being by my side throughout the ups and downs. I couldn't have done it without your constant unwavering support.

I dedicate this work to my mother and father. Your unconditional love and encouragement have been, and always will be, my everyday strength. To my mother Fadia, you always know how to give me strength and cheer me up and always push me to be the best version of myself, you are the greatest treasure in my life, I am so grateful for you. To my father Ghazi, whose loving memory continues to guide me everyday through life and give me strength, you remain present in every step of this journey.

Table of Contents

Affidavit **1**
List of Publications and Participation in Conferences **2**
Résumé **4**
Abstract **5**
Résumé Etendu de la Thèse **6**
Résultats Principaux 18
Conclusions et Perspectives 19
Acknowledgments **20**
Table of Contents **22**
List of acronyms **25**
Motivation of this work **27**
I. Supramolecular self-assembly on surfaces in UHV environment **29**
I.1. Basic principles of supramolecular self-assembly 29
I.2. Intermolecular interactions 33
I.2.1. The Coulomb interactions 33
I.2.2. The Hydrogen bonds 34
I.2.3. Van der Waals interactions 35
I.3. State-of-the-Art: molecular self-assembly on Gr/SiC 36
I.3.1. Van der Waals interactions 37
I.3.2. Hydrogen bonds 38
I.4. State of the art: zwitterionic molecules on surfaces 40
I.5. Conclusion 43
II. Theoretical Concepts and equipment overview **44**
II.1. Scanning Tunneling Microscopy 44
II.1.1. The tunneling effect 44
II.1.2. Electron tunneling theory 45
II.1.3. Fundamentals and Operational Modes of Scanning Tunneling Microscopy 49
II.1.4. Scanning tunneling spectroscopy (STS) 50
II.2. Non-contact AFM 54
II.2.1. Principle of nc-AFM 54

II.2.2. Fundamentals of non-contact AFM 55
II.3. Kelvin Probe Force Microscopy (KPFM) 57
II.3.1. Principle of KPFM 57
II.3.2. CPD sign and dipole orientation 59
II.4. Experimental setup 60
II.4.1. LT-STM (CINaM laboratory) 60
II.4.2. LT-STM/nc-AFM (IM2NP laboratory) 62
III. Structural and electrical properties of the substrates 64
III.1. Substrates preparation 64
III.2. Highly Oriented Pyrolytic Graphite 65
III.3. Graphene 66
III.3.1. Overview on graphene's structural and electronic properties 66
III.3.2. Growth of EG on 4H-SiC(0001) 68
III.3.3. Literature overview: STS on Gr/SiC 74
III.3.4. Single-point STS measurements on graphene 77
III.3.5. Influence of the tip-sample distance and of the modulation amplitude on the STS spectra. 79
III.3.6. Spatial mapping of spectroscopic data 81
III.4. Conclusion 87
IV. Synthesis of zwitterionic molecules 88
IV.1. Introduction on polymethines 88
IV.2. Historical milestones in synthesis 90
IV.2.1. Introduction to transamination and π-zwitterions 90
IV.2.2. Advancements in the synthesis of QZ 92
IV.2.3. Structural properties of BQMIs and ZTAP 94
IV.3. Synthesis conducted in this Thesis 96
IV.3.1. Transamination of benzoquinonemonoimine zwitterions 96
IV.3.2. Synthesis of ZTAP 97
IV.3.3. Functionalization of ZTAP 98
IV.3.4. Reactivity 104
IV.3.5. Acid-base properties of ZTAP 104
IV.3.6. Alkylation of ZTAP 106
IV.3.7. Oxidation of ZTAP 107
IV.3.8. Optical characterization of ZTAP 108
IV.4. Conclusions 113

V. DPQZ growth on HOPG and graphene 115
V.1. STM study of DPQZ on HOPG and graphene surfaces 116
V.1.1. DPQZ assembly on HOPG 116
V.1.2. DPQZ assembly on graphene 125
V.2. Computational results 126
V.3. Conclusions 129
VI. ZTAP on graphene 130
VI.1. Probing molecular self-assembly by STM 130
VI.1.1. Experimental Methods 130
VI.1.2. ZTAP assembly on graphene: STM studies 131
VI.2. ZTAP assembly on graphene: KPFM studies 140
VI.2.1. Multi-layer on VT-AFM 141
VI.2.2. 4D KPFS map: on closed-cycle LT-STM 143
VI.3. ZTAP assembly on graphene: Scanning Tunneling Spectroscopy 156
VI.3.1. Scanning tunneling spectroscopy on molecular assembly. 156
VI.3.2. STS maps 159
VI.3.3. Energy study of dI/dV spectra 159
VI.3.4. Spatial study of STS maps 164
VI.4. Conclusion 168
General Conclusion 169
Bibliography 170
Appendix 184
A. Electronic properties of graphene 184
B. Particle tunneling in a unidimensional potential barrier 188
C. Experimental methods 192
D. Python code 209
E. Challenges and unsuccessful attempts 215

List of acronyms

Acronym	Description
1D	Unidimensional
2D	Two dimensional
AFM	Atomic force microscopy
BuL	Buffer layer
BLA	Bond length alternation
BLG	Graphene bilayer
BQZ	Butyl-functionalized zwitterionic *p*-benzoquinonemonoimine
CAHB	Charge assisted hydrogen bond
CPD	Contact potential difference
DFT	Density functional theory
DMPQZ	Di-methoxyphenyl *p*-benzoquinonemonoimine zwitterion
DOS	Density of states
DPDQZ	Bis (di-methylaminophenyl) *p*-benzoquinonemonoimine zwitterion
DPQZ	di-phenyl functionalized QZ
EG	Epitaxial Graphene
EQZ	Ethyl functionalized zwitterionic *p*-benzoquinonemonoimine
FFT	Fast fourier transform
Gr	Graphene
Gr/SiC	Graphene on silicon carbide
HOC	High order commensurate
HOMO	Highest occupied molecular orbital
HOPG	Highly oriented pyrolytic graphite
HRMS	High resolution mass spectrometry
KPFM	Kelvin probe force microscopy

KPFS	Kelvin probe force spectroscopy
LDOS	Local density of states
LHe	Liquid Helium
LN2	Liquid Nitrogen
LT	Low temperature
LT-STM	Low-temperature scanning tunneling microscopy
LUMO	Lowest unoccupied molecular orbital
nc-AFM	nc-AFM
MLG	Graphene monolayer
MS	Mass spectrometry
NMR	Nuclear magnetic resonance
POL-E	Point on line epitaxy
PTCDA	perylene-3,4,9,10-tetracarboxylic dianhydride
PTCDI	perylenetetracarboxylic diimide
QZ	di-substituted *p*-benzoquinonemonoimine zwitterion
RT	Room temperature
STM	Scanning tunneling microscopy
STS	Scanning tunneling spectroscopy
SiC	Silicon carbide
TAP	Tetraazapentacene
TCNQ	Tetracyanoquinodimethane
UHV	Ultra-High Vacuum
vdW	van der Waals
vdW-H	Van der Waals Heterostructures
VT-AFM	Variable temperature atomic force microscope
XRD	X-ray diffraction
ZTAP	quinoxalino[2,3-b]phenazine zwitterion / di-phenyl functionalized ZTAP

Motivation of this work

This PhD work is part of a project that focuses on the development of hybrid organic/inorganic van der Waals heterostructures based on supramolecular networks of zwitterionic molecules deposited on graphene. The hybrid structures are formed by a monolayer of organic molecules self-assembled on graphene. The lattice mismatch between the organic layer and graphene forms a superlattice or a structural Moiré effect if these 2 networks are commensurate. A superlattice has shown to locally modify the electrostatic surface potential of graphene.[7,8] Its geometry can be controlled at the molecular level by varying the molecular unit or introducing peripheral functional groups which can drive the assembly, act as spacers and determine the periodicity of the network.[9] In addition, if the molecular unit comprises a strong permanent dipole, it can generate local electric fields, further modifying the electrostatic potential in their vicinity.[7] This approach allows for the design of a network of locally tunable potentials in 2D materials through the strategic deposition of specific molecules.[10]

In this project, the molecules we chose to work with belong to 2 families of zwitterionic molecules: QZ (*p*-benzoquinonemonoimine zwitterions referred to as BQMIs in the literature)[3] and ZTAP (quinoxalino[2,3-b]phenazine derivatives)[11]. It is possible to modify the peripheral functional groups of these zwitterionic molecules via organic synthesis. These molecules feature a stable ground state zwitterionic structure, a high intrinsic dipole moment (of approximately 10 Debye)[12–14] and have shown to conserve their dipolar nature after self-assembly.[15]

The research question driving this work is the following: **Can we induce a Moiré effect or a superlattice on graphene by depositing an organic monolayer of zwitterionic molecules and how might such a superlattice modify the electronic properties of these 2D materials?**

The creation of a superlattice or Moiré effect has emerged as a promising strategy for altering the band structure of 2D materials and controlling the resulting quantum phenomena, thereby enabling the emergence of unconventional properties in these materials such as unconventional superconductivity and ferroelectricity.[1,2]

The research work will be done in several steps as follows:

1. Synthesizing a library of the QZ and ZTAP zwitterionic molecules.
2. Optimizing the growth of a self-assembled crystalline phase of these molecules under ultra-high vacuum (UHV) on graphene.
3. Characterizing the resulting molecular layer and its epitaxy with the substrate by using low-temperature scanning tunneling microscopy (STM) at 78 K or 9 K.

4. Measuring the effects of the local dipole of these molecules on graphene by contact potential difference maps. This is done by using Kelvin Probe Force Microscopy (KPFM) in non-contact AFM mode (nc-AFM) at low temperature for the sub-monolayer regime.

I. Supramolecular self-assembly on surfaces in UHV environment

This PhD research principally focuses on investigating supramolecular self-assemblies at the atomic scale, specifically on graphene grown on silicon carbide (Gr/SiC(0001)) and Highly Oriented Pyrolytic Graphite (HOPG) surfaces under ultrahigh vacuum (UHV) conditions.

The first part of this bibliographic chapter provides a comprehensive overview on the state-of-the-art of the elementary mechanisms driving supramolecular growth (restrained to UHV environment; self-assembly process in liquid is not presented). The second part presents recent results of supramolecular assembly on Gr/SiC(0001) and the last part is dedicated to zwitterionic molecules self-assembly on various surfaces.

I.1. Basic principles of supramolecular self-assembly

Supramolecular networks are stable structures formed by the self-assembly of individual molecules through non-covalent interactions, such as hydrogen bonds, van der Waals forces, π-π and electrostatic interactions. These interactions are usually classified as weak interactions.[16]

'Self-assembly', frequently used interchangeably with 'molecular self-assembly', is recognized as the primary strategy for the non-covalent synthesis of complex systems that integrate multiple components with molecular-recognition capacities. This process is distinct from self-organization, which occurs when the system is trapped in kinetically limited states, not reaching equilibrium.[17]

In the self-assembly regime, close to the most thermodynamically stable phase and because of the weak nature of the interactions, self-assembled networks can exist in intermediate metastable phases that are temporary and relatively stable. In these metastable phases, the system remains in a local energy minimum but can transit to a more stable equilibrium phase if a sufficient perturbation is given.[18] This dynamic nature allows for both bond formation and bond breaking in the system, governed by the interplay between intermolecular and molecule-substrate interactions. It is also influenced by factors like the substrate temperature which affects molecular diffusivity (D) and molecular flux (F) which have an effect on the deposition rate and nucleation density.

On one hand, the balance between molecular flux and surface diffusivity plays a key role, with a high flux and a low diffusivity leading to a diffusion-limited phase. On the other hand, a low flux and a high diffusivity lead to a thermodynamically favored structure as illustrated in Figure 10.

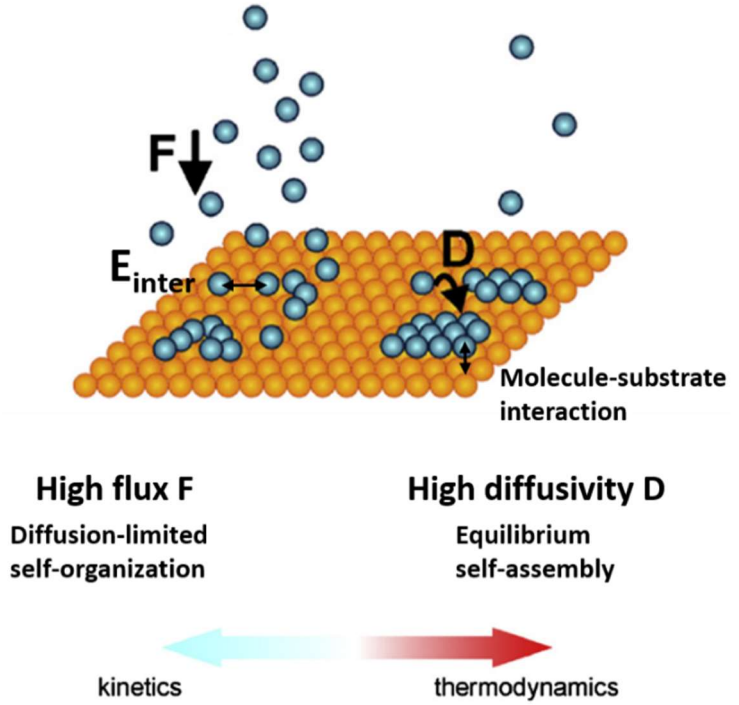


Figure 10: ***Schematic illustrating the difference between self-organization and self-assembly****. Depending on the flux (F) of incoming molecules and the diffusivity (D) of the molecules on the surface, either diffusion-limited self-organized structures or self-assembled structures are formed. Self-organized structures form when the flux is high and the diffusivity is low. These structures are governed by the kinetics of the system and can be far from equilibrium (left-side blue arrow). On the other hand, when the flux is low and diffusivity is high, self-assembled structures at the thermodynamic equilibrium are formed (right-side red arrow). Schematic adapted from earlier reference.*[17]

The schematic of Figure 10 shows the influence of the flux and of the diffusion parameters on the favored structure and is described more precisely in terms of energy balance. Self-assembly can only occur if the molecules (i) have the opportunity to meet on the surface and (ii) can explore several intermolecular configurations reaching the most stable one.

The Figure 11 illustrates all these different energy processes in detail but the main idea always follows this 2-step process, which includes a 2-level energy equilibrium:

1. A first equilibrium between the kinetic energy (E_{kin}) of the molecule, the adsorption energy between molecule and surface (E_{ad}) and the energy of the thermal diffusion barrier (E_m) of the substrate. E_{kin} should be high enough to overcome E_m of the surface but should not exceed E_{ad} otherwise the molecules would desorb from the surface.

2. Once this is achieved, molecules can meet and the second energy equilibrium occurs: the intermolecular energy E_{inter} (that can be decomposed in several energy components) should be weak enough to allow for molecular movement, rotation essentially (E_{rot}), in order to search for the different possible intermolecular configurations) and strong enough to be able to form stable structures (through physisorption or chemisorption mechanisms).

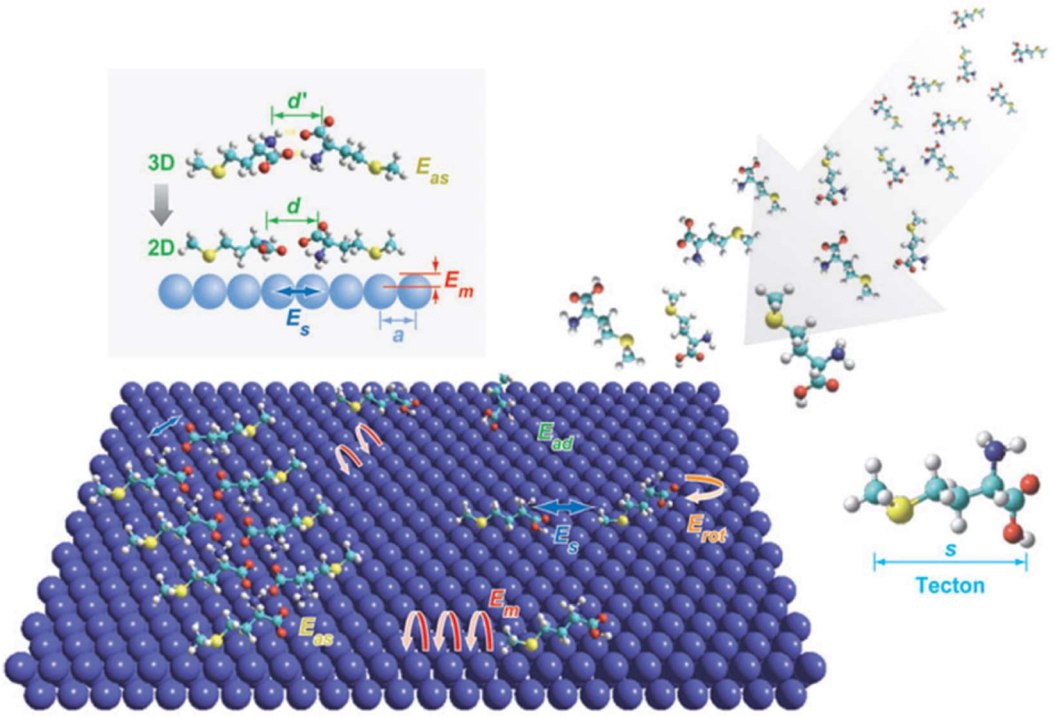


Figure 11: ***Supramolecular engineering in two dimensions:*** *the substrate atomic lattice is exposed to a beam of molecular building blocks. Decisive for the assembly of nanoscale architectures are adsorption (energy* $\boldsymbol{E_{ad}}$*), thermal migration (barrier* $\boldsymbol{E_m}$*), rotational motions (barrier* $\boldsymbol{E_{rot}}$ *), substrate-mediated and direct lateral interactions (energy* $\boldsymbol{E_s}$ *and* $\boldsymbol{E_{inter}}$*). An exemplary tecton with 2 functional groups (S atom in yellow; N and O in the amino group in red and blue, respectively) and length* $\boldsymbol{s}$ *is shown. It self-assembles into the twin chain depicted at the left, which is stable at thermodynamic equilibrium. The inset in a side view illustrates how surface atoms (*$\boldsymbol{a}$ *is the lattice periodicity) can influence the supramolecular synthon characteristics and the non-covalent-bond length* $\boldsymbol{d}$*. Adapted from earlier work.*[19]

Finally, the term used in the literature to summarize all these equilibria is "the balance between molecule-substrate and molecule-molecule interaction".

The Figure 11 illustrates the principles of two-dimensional (2D) supramolecular engineering: A molecular beam is directed onto a well-prepared surface, where tectons, such as an amino acid, adsorb on the surface, gaining adsorption energy (E_{ad}).

These molecules typically adsorb in specific configurations and sites, influenced by the atomic lattice of the substrate, which determines the supramolecular synthon characteristics, such as the bond strength and length (d) (inset of Figure 11). Thermally activated processes, including surface migration and 2D rotation associated with energy barriers (E_m) and (E_{rot}), facilitate the molecular recognition and direct non-covalent

bond formation between functional groups (energy gain (E_{as})). This leads to the self-assembly of distinct molecular nanostructures near thermodynamic equilibrium, with self-correction mechanisms eliminating transient effects. Additionally, indirect substrate-mediated interactions (maximum strength (E_s)) can influence molecular mobility and self-assembly.

For a comprehensive understanding and effective control of molecule-surface interactions in non-covalent synthesis, the Table 1 summarizes and compares the energies of various non-covalent intermolecular interactions as well as the strength and nature of the bonds formed.

Table 1: Classification of basic interactions and processes, with associated energy (barrier) and typical distances relevant when functional molecular species are employed to engineer molecular architectures on metal substrates.[19]

	Energy range	**Distance**	**Character**
Adsorption	$E_{ad} \approx$ 0.5- 10 eV	≈ 1.5-3 Å	Directional, site selective
Surface migration	$E_{ad} \approx$ 0.5- 10 eV	≈ 2.5-4 Å	1D/2D
Rotational motion	$E_{ad} \approx$ 0.5- 10 eV	s	2D
Indirect substrate mediated	$E_{ad} \approx$ 0.5- 10 eV	Å to nm range	Oscillatory
Reconstruction mediated	$E_{ad} \approx$ 0.5- 10 eV	Short range	Covalent
Van der Waals	$E_{as} \approx$ 0.02- 0.1 eV	$<$ 1 nm	Nonselective
Hydrogen bonding	$E_{ad} \approx$ 0.05- 0.7 eV	≈ 1.5-3 Å	Selective, directional
Electrostatic ionic	$E_{as} \approx$ 0.05- 2.5 eV	Long range	nonselective
Metal-ligand interactions	$E_{as} \approx$ 0.5- 2 eV	≈ 1.5- 2 Å	Selective, directional

In the following section the physical nature of the intermolecular interactions is detailed.

I.2. Intermolecular interactions

Intermolecular interactions are interactions between 2 molecules that are not covalently bound. On one hand, covalent bonds involve the sharing of electrons between atoms within a single molecule and are characterized by strong and directional bonds. Intermolecular forces on the other hand, are weaker forces of attraction (at least one order of magnitude smaller) or repulsion between molecules. There are several types of intermolecular forces:

I.2.1. The Coulomb interactions

Ionic bonding involves the complete transfer of valence electrons between atoms, resulting from the formation of 2 oppositely charged ions. When there's a significant difference in electronegativity between the 2 elements involved, electrons tend to migrate from the less electronegative element (often metals) to the more electronegative one (typically a non-metal). This electron transfer enables the atoms to reach a stable configuration. In strict terms, an ionic bond refers to the electrostatic attraction experienced between the electric charges of a cation $q_1$and an anion q_2, in contrast with a purely covalent bond.[20]

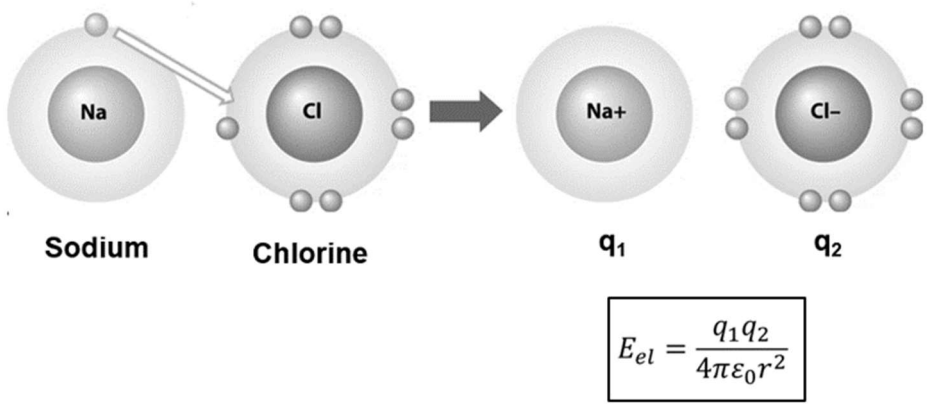


Figure 12: Schematic representation of NaCl ionic bond formation from sodium and chlorine atoms. The valence electrons of the outer shell are represented each by a small circle. The Coulomb electrostatic force E_{el} is expressed as a function of the electric charges of the cation and the anion, q_1 and q_2, respectively and is inversely proportional to the square of the distance r between the ions.

The latter will undergo a Coulomb electrostatic force E_{el}, whose expression is shown in Figure 12, with ε_0 being the dielectric constant of the medium and r the distance between the ions. This interaction is spherically symmetric and acts at long distances ($1/r^2$). It is responsible for bonding energies ranging from 0.5 to 5 eV and consequently, short interatomic distances (a few Å). This interaction ensures, for example, the cohesion of ionic crystals.

Sodium chloride (NaCl) is a typical example of a crystal whose cohesion is governed by ionic bonding. In this example, sodium acts as the cation and chlorine as the anion. The intensity of the Coulomb interaction decreases with increasing distance between the charges. Similarly, we experimentally observe this distance-intensity dependence because the larger the lattice parameter of an ionic crystal, the weaker the bond.

I.2.2. The Hydrogen bonds

The importance of hydrogen bonding cannot be overemphasized. It may best be summarized using a definition for hydrogen bonding given in the Penguin dictionary as "a weak electrostatic chemical bond which forms between covalently bonded hydrogen atoms and a strongly electronegative atom with a lone pair of electrons… life would be impossible without this type of bond.[21]

Despite almost a century of study, the IUPAC definition of the hydrogen bond (H-bond) was changed as recently as 2011, as describing its complexity with its electrostatic, dispersion, covalent and exchange contributions is challenging. It is thus defined to be an electrostatic attraction between a hydrogen atom covalently bonded to a more electronegative "donor" atom or group 'X' and another electronegative atom bearing a lone pair of electrons-the hydrogen bond acceptor 'A'. This interaction is represented as $X\delta^- — H\delta^+ \ldots A\delta^-$, with the solid line representing a polar covalent bond and the dotted line indicating the hydrogen bond.[22] The scheme of Figure 13(a) shows the neutral H-bond between 2 water molecules.

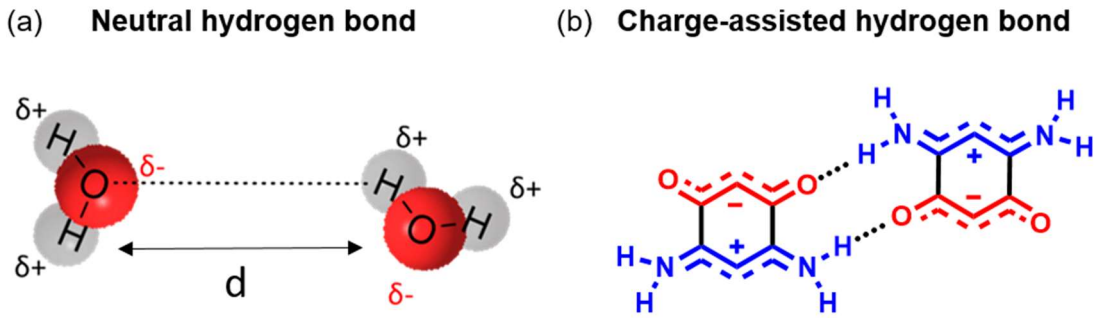


Figure 13: ***(a)*** *Prototype of a hydrogen bond between 2 molecules of water, d is the distance between O…H atoms.* ***(b)*** *Structure model of a charge-assisted hydrogen bond (CAHB) between 2 zwitterionic p-benzoquinonemonoimine molecules.*

The H-bond can be intermolecular or intramolecular. Directionality is a defining characteristic for the H-bond, its length 'd' can range from 3.0 to 3.2 Å and the X-H…A angle is usually linear (180°) and the closer the angle is to 180°, the stronger is the hydrogen bond and the shorter is the H…Y distance.

The study of H-bonding is extensive, reflecting its crucial role across various scientific domains like biochemistry,[23] organic synthesis,[24] and crystal engineering.[25] Particularly relevant to this thesis is its significance in crystal engineering and self-assembly at

surfaces. Recent research has intensely explored the utilization of hydrogen bonding along with other non-covalent interactions and covalent bonds to engineer supramolecular lattices on surfaces.[19,26]

A specific type of H-bond that was found to be stronger than the neutral H-bond is the charge-assisted hydrogen bond (CAHB).[22] In that type, the interaction is strengthened by the presence of an additional electrostatic interaction involving charged species that are involved in the hydrogen bond.

I.2.3. Van der Waals interactions

The van der Waals interactions are attractive or repulsive forces between molecular entities (or between groups within the same molecular entity) other than those due to bond formation or to the electrostatic interaction of ions or of ionic groups with one another or with neutral molecules.[20] The term includes dipole–dipole (Keesom forces), dipole-induced dipole (Debye forces) and instantaneous dipole-induced dipole forces (London), the schemes in Figure 14 illustrate these interactions.

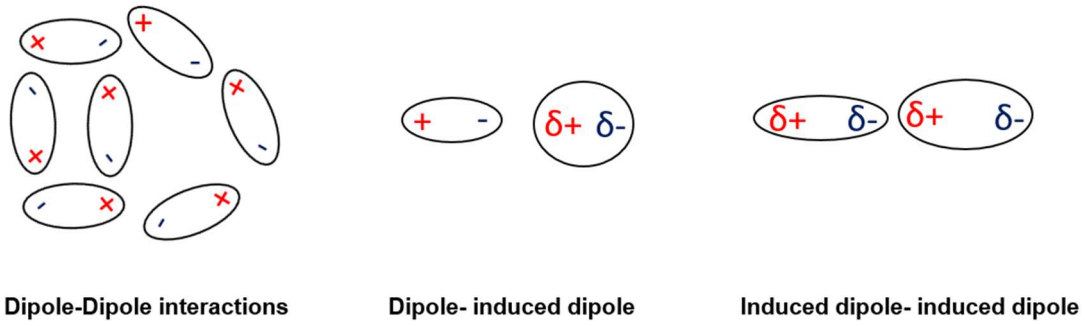


Figure 14: Schematic representation of various dipole-dipole interactions. The atom with the highest electronegativity is symbolized by δ^- and the atom with the lowest electronegativity is symbolized by δ^+.

I.2.3.1. Keesom force (permanent dipole-permanent dipole)

The Keesom force is a temperature dependent interaction that takes place between 2 rotating permanent dipoles in polar molecules. This force only occurs between 2 polar molecules due to differences in electronegativity between atoms within the molecule. These forces are stronger than the London and the Debye forces, but are weaker than hydrogen bonding. The more polar the molecules, the stronger the attractive force is between them.

I.2.3.2. Debye force (permanent dipole-induced dipole)

The Debye forces arise from interactions between the permanent dipoles in one molecule and the induced dipoles in another molecule. These forces are weaker than Keesom forces, but stronger than London dispersion forces. They occur when a polar molecule induces a dipole in a neighboring non-polar molecule.

I.2.3.3. London force (induced dipole-induced dipole)

London dispersion forces arise from temporary fluctuations in electron density within atoms or molecules, leading to the formation of temporary or induced dipoles. These forces are the weakest type of van der Waals forces. They occur between all atoms and molecules, regardless of their polarity.

I.3. State-of-the-Art: molecular self-assembly on Gr/SiC

Since the discovery of graphene and its isolation in the form of freestanding monolayer films in 2004 by Geim and Novoselov,[27] this material has gained a significant amount of attention from both a fundamental as well as an applied point of view. It has emerged as a promising substrate due to its electronic, mechanical and chemical properties that outperform most of the existing materials.[28,29] This section delves into research on the latest advancements in molecular self-assembly on graphene, followed by a closer look of zwitterionic molecules self-assembly on various surfaces. We will examine the types of intermolecular interactions driving these assemblies and discuss their potential applications and challenges.

The following subsections will categorize and analyze the self-assembly processes based on the predominant types of intermolecular interactions involved only on epitaxial graphene (EG) surfaces grown on 4H- and 6H-SiC(0001) substrates, in accordance with the one used in the experiments conducted in this thesis work. The literature concerning molecules on graphene being exhaustive, we chose to keep only Gr/SiC surfaces and exclusively the resulting supramolecular networks, omitting the covalent assemblies.

1. We focus on the molecular deposit on Gr/SiC and we do not present the studies of systems on graphene grown on metallic surfaces because, as outlined in the introduction, the physical nature of graphene is significantly altered when supported by a metal (Gr/metal). Overall, what stands out from these supramolecular systems on Gr/metal is that the molecule-substrate interactions dominate the intermolecular interactions. This leads to very different assembly mechanisms between weakly perturbed graphene (exfoliated graphene or Gr/SiC) and graphene/metal.[30]

2. We furthermore limit our study to supramolecular assemblies, thus to non-covalent assemblies, even though there are many examples of large-scale self-assembled molecular systems via coordination frameworks on Gr/SiC.[31] These systems are interesting to force specific metal-molecule catalyzed reactions that however, do not contribute to clarifying the work of this thesis during which we did not work on on-surface synthesis nor on molecule/metal co-evaporations. Reason for which they will not be presented in this manuscript.

Finally, we would like to acknowledge several reviews on molecular self-assembly on graphene from which only the examples about supramolecular networks on Gr/SiC were selected. [10,32–36]

I.3.1. Van der Waals interactions

We have chosen to explore the self-assembly of fullerene (C_{60}), 4,4,5,5-tetrakis-(dodecylthio)-2,2-bi(1,3-dithiolylidene) tetrathiafulvalene molecules (TTC_{12}-TTF) and copper hexadecafluoro-phthalocyanine (F_{16}CuPc) molecules on Gr/SiC. These molecules were selected due to their unique properties and the insights they can provide into van der Waals interactions on graphene-based systems. C_{60}, with its closed-cage structure, serves as a model for understanding electron acceptor behavior in organic photovoltaics and has shown reduced interaction with graphene compared to metallic substrates. It shows to form (see Figure 15(a)) well-ordered, compact domains on Gr/ 6H-SiC(0001) with a self-assembly behavior of van der Waals interactions.[37]

Another example of weak interactions is the TTC_{12}-TTF molecule known for its electron-donor properties. It complements the electron-accepting nature of C_{60}, allowing for the investigation of donor-acceptor interactions on graphene. TTC_{12}-TTF assembles in 1D rows of 2D layers on EG on 6H-SiC(0001). The extended alkylthiol chains compel the molecules to take on an edge-on orientation due to their van der Waals interactions. This orientation minimizes the distance between the TTF core to less than 3.8 Å, facilitating complete π-π overlap.[38]

F_{16}CuPc, a phtalocyanine derivative, introduces another dimension of study with its strong intermolecular interactions and its ability to form close-packed molecular islands with the exact geometry determined by the shape of the molecule. The F_{16}CuPc molecules tend to accumulate at lower step edges of steps of the EG on 6H-SiC(0001) surface.[39] When the self-assembly of these molecules is studied on Gr/SiC it can help elucidate how van der Waals interactions, as opposed to stronger chemical bonds, can guide this assembly.

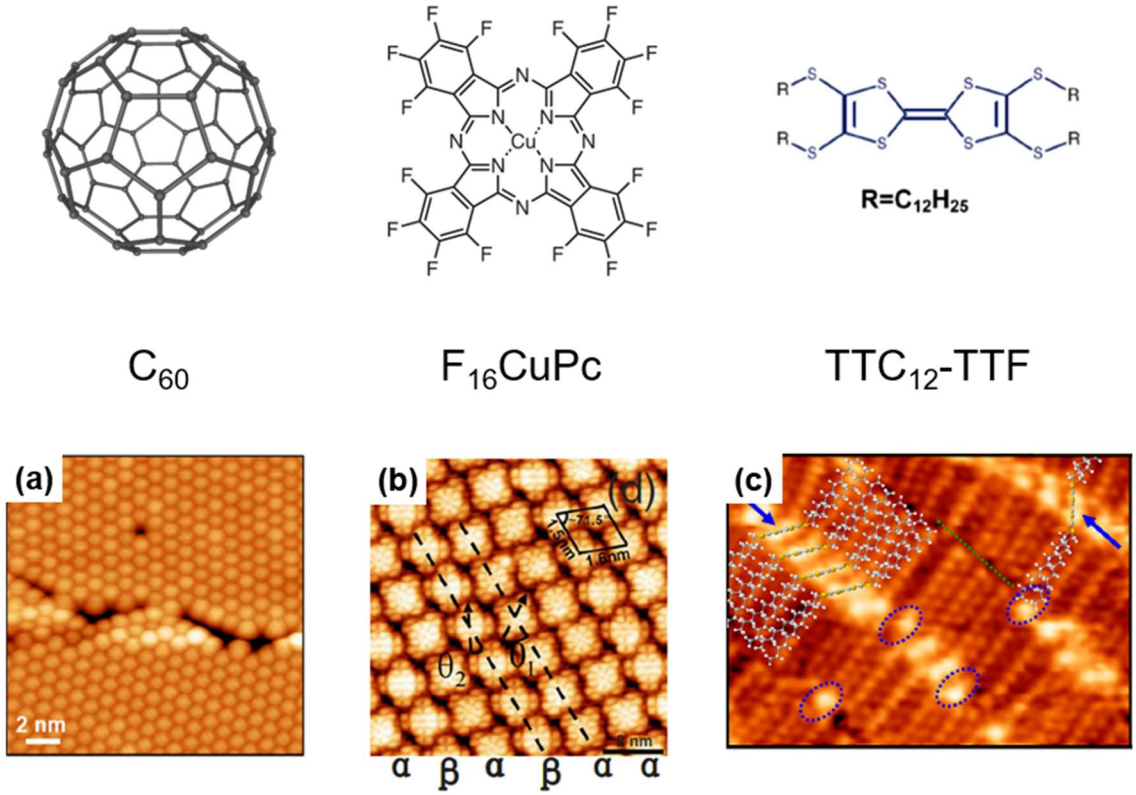


Figure 15: (a) STM topographic image of an initial stage of growth of C_{60} molecule adsorbed on a submonolayer of epitaxial graphene grown on SiC. This image displays a single vacancy of the molecule and the domain boundary between molecular islands. Tunneling conditions: V_{bias}= - 2 V, I_t= 20 pA. Reproduced from earlier work.[37] (b) High-resolution STM image of a F_{16}CuPc on epitaxial graphene, where the dashed lines indicate orientations of molecular rows and arrows indicate molecular axes. Tunneling conditions: V_{bias}= 1.5 V, I_t= 0.1 nA. Reproduced from earlier work.[39] (c) STM image of the TTC_{12}-TTF monolayer on graphene drawn to scale in edge-on conformation. The sulfur atoms are displayed in yellow and the carbon in gray. It seems that the molecules prefer to adsorb and to form a molecular layer in chair-like conformation with the dodecylthio chains slightly interdigitated. 2 different chair-like conformations are indicated by the blue arrows: the two TTF cores are symmetric with respect to the green dotted line. Defects in the molecular row due to the intercalation of molecules between the rows are highlighted by dotted ellipses. Dimensions: 7.0 nm × 5.1 nm. Tunneling conditions: V_{bias}= 1.6 V. Reproduced from earlier work.[38]

Following our exploration of C_{60}, TTC_{12}-TTF and F_{16}CuPc on Gr/SiC, we now turn our attention to perylene-3,4,9,10-tetracarboxylic dianhydride (PTCDA) and perylenetetracarboxylic diimide (PTCDI). Unlike the previously studied molecules, PTCDA and PTCDI are characterized by their planar, extended π-conjugated structures and their ability to form hydrogen bonds. These differences in shape and properties lead to distinct self-assembly behaviors on graphene surfaces.

I.3.2. Hydrogen bonds

Room temperature (RT) investigations of the self-assembly of PTCDA and PTCDI on Gr/SiC(0001) showcases an assembly in a herringbone pattern, with the molecules lying flat on the surface to maximize intermolecular hydrogen bonds (C-H…O and N-H…O respectively). [40,41] These hydrogen bonds do not only dictate the molecular orientation but also stabilize the assembled structures, allowing the growth of uninterrupted

networks over step edges and defects in the underlying graphene. Stronger step-edge behavior is seen for PTCDI because of the stronger H-bonding than PTCDA (see Figure 16(c-f)).

The observed stabilization of the well-ordered PTCDI island edge structure at RT may therefore be the result of the comparatively strong N-H…O intermolecular hydrogen bonds that form between neighboring PTCDI molecules.

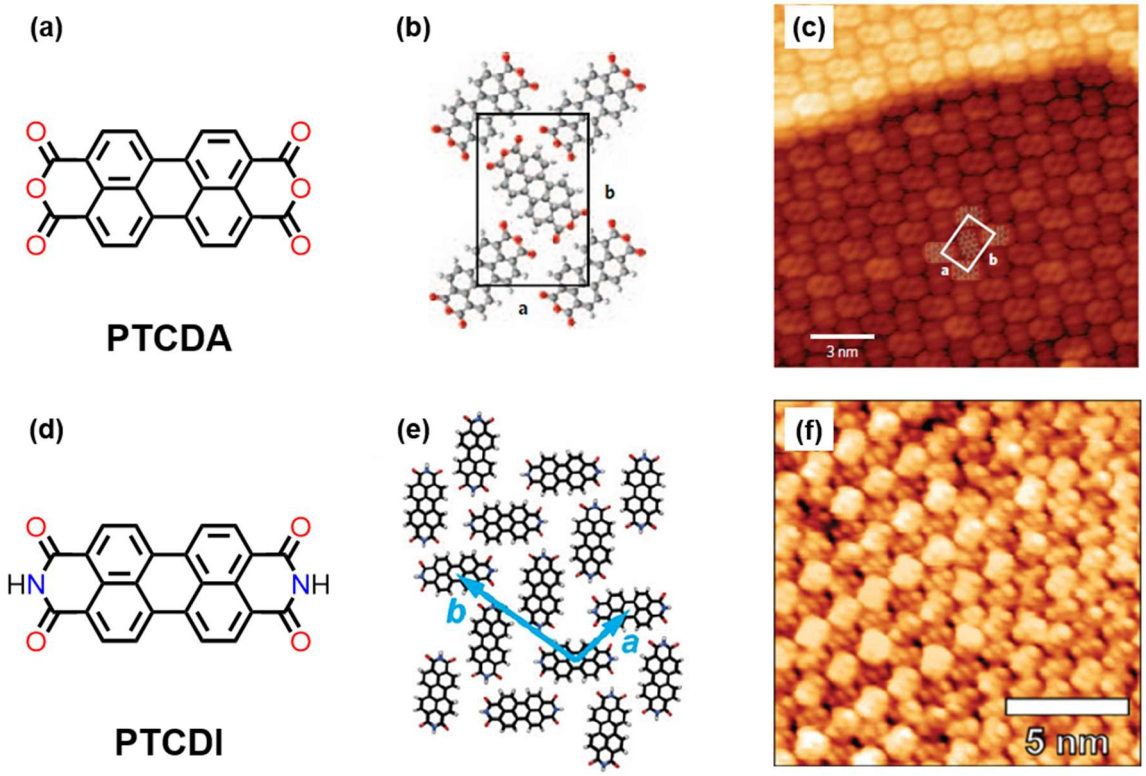


Figure 16: ***(a)*** *Structure of PTCDA.* ***(b)*** *PTCDA herringbone unit cell, with the lattice vectors a and b shown.* ***(c)*** *Molecular-resolution STM image of the PTCDA monolayer. The PTCDA molecular structure and unit cell outline are overlaid. The monolayer continuously follows the graphene sheet over the SiC step edge. Tunneling conditions:* V_{bias} *= -2 V,* I_t *= 50 pA.* ***(d)*** *Structure of PTCDI.* ***(e)*** *Schematic of the PTCDI herringbone motif, with lattice vectors a and b.* ***(f)*** *Molecular-resolution STM image of the PTCDI monolayer. Tunneling conditions:* V_{bias} *= - 1.0 V,* I_t *= 40 pA. Reproduced from prior research.*[40,41]

These studies observed growth of multiple domains, which were not aligned to the high-symmetry directions of graphene. The high degree of order in these assemblies offers insights into the balance of intermolecular and molecule-substrate interactions. It particularly highlights the unique contribution of H-bonding to the assembly process.

I.4. State of the art: zwitterionic molecules on surfaces

This subsection introduces previous work on substrate functionalization with zwitterionic molecules that present a large intrinsic dipole. These studies give insight on the interplay between molecule-molecule interactions and molecule-substrate interactions. The zwitterionic molecules we focus on are the zwitterionic *p*-benzoquinonemonoimine and its derivatives that were first synthesized by Siri and Braunstein in 2002.[3] These quinonoid molecules, carry positive and negative charges delocalized on different parts of the molecule and are electrically neutral as a whole. The delocalization of the 12π-electron system therefore appears to be confined within 2 independent subunits of the molecule. This generates a significant electric dipole across the planar 6-membered ring of the benzoquinonemonoimine core.

The large intrinsic dipole moment of these compounds makes them ideal candidates for the study of adsorbate dipole interactions at conducting and non-conducting substrate interfaces.[15,42–53]

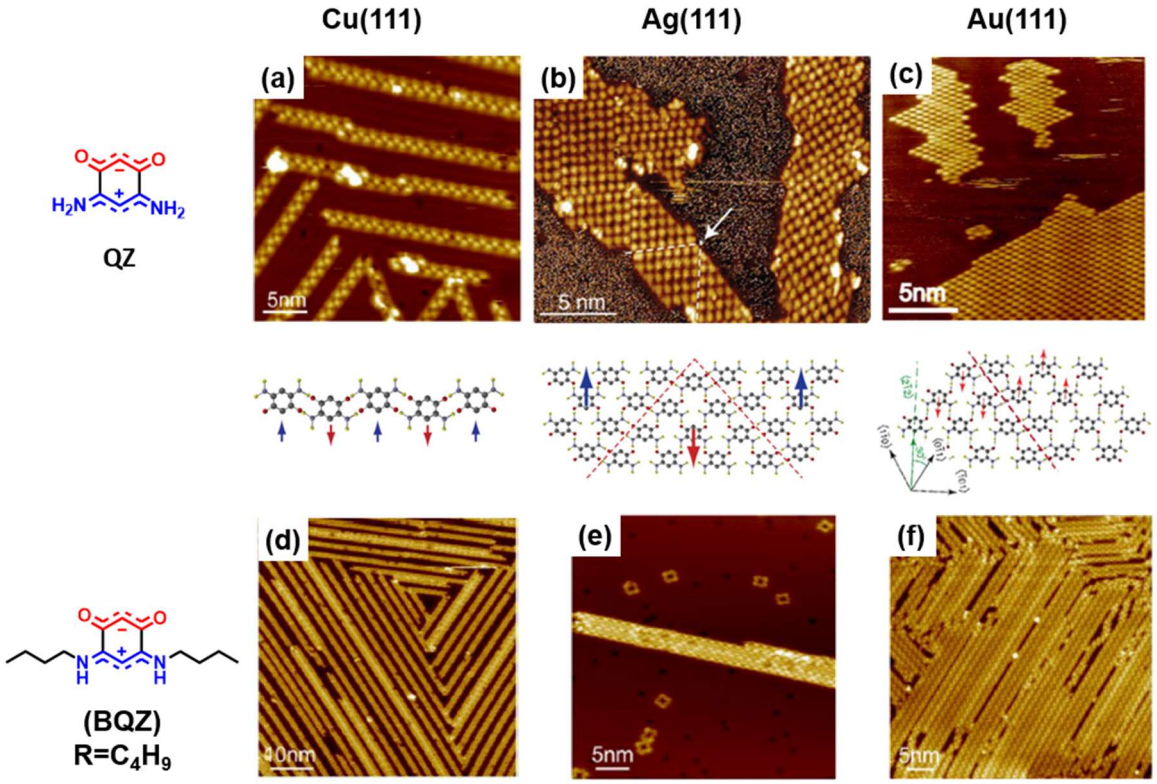


Figure 17: ***(a)*** *STM image of QZ on Cu(111). Tunneling parameters: V_{bias} = - 0.5 V, I_t = 300 pA. The proposed structural model of the 1D chains and the orientation of the intrinsic dipoles. (Color code: oxygen (red), carbon (grey), nitrogen (blue), hydrogen (yellow)).* ***(b)*** *STM image of QZ on Ag(111). White dashed lines mark the boundaries between selected structural domains.* ***(c)*** *A zoom in of self-assembled networks of QZ on Au(111), STM topography imaged at V_{bias} = 0.30 V, I_t = 300 pA with the proposed bonding model showing 2 domains of aligned molecules separated a dashed line.* ***(d)*** *Representative STM images of BQZ on Cu(111) for sub-monolayer coverage.* ***(e)*** *Representative STM images of BQZ on Ag(111) for sub-monolayer coverage.* ***(f)*** *Representative STM images of BQZ on Au(111) for sub-monolayer coverage.*

From these studies, only the experiments performed by sublimation of the zwitterionic molecules under UHV will be reviewed with focus on the derivatives of the zwitterionic *p*-benzoquinonemonoimine compounds and their derivatives (referred to as QZ in the following). The 2D arrangement of these molecules with strong electric dipoles can exhibit significant intermolecular interactions, influenced by the substrate on which the molecules are adsorbed.

Under UHV and on the (111) faces of metals like Ag, Au and Cu, molecule-substrate interactions play a significant role in determining the self-assembled structures of quinonoid zwitterions. The dipole moment of a molecule adsorbed onto a metal substrate often deviates drastically from the dipole moment of a free molecule. For instance, the dipole moment of a QZ molecule adsorbed on Ag or Cu clusters is approximately one sixth of the free molecule value, resulting from a substrate-mediated charge exchange between the HOMO and the LUMO of the molecules.

The QZ molecules typically form 2D islands on Ag(111) and Au(111) surfaces.[44,54] Each QZ molecule binds to 2 neighboring molecules via N-H…O bonds creating a near square shaped unit cell (see Figure 17(b-c)). These molecules show a parallel alignment, resulting in islands with a non-zero electric polarization. Small clusters, such as heptamers, are occasionally seen, especially on Ag(111) (see Figure 17(e)).[15] Larger rings are more frequent for QZ compared to the ethyl functionalized QZ (EQZ) and the butyl-functionalized QZ (BQZ) due to smaller geometry constrains from the added functional groups.

The QZ self-assembles in one-dimensional (1D) chains on the Cu(111) surface (see Figure 17(a))[53]: each molecule forms 2 CAHBs with its neighbor from the chain with an alternating molecular orientation that cancels the in-plane dipole moment. At low coverage, repulsive interactions between the chains keeps them separated. At higher coverage, the chains come closer together, reducing repulsion. STM images reveal a decreased electron density under the anionic oxygen functions and an increase of the electron density under the cationic nitrogen functions, indicating interactions with the Cu substrate.

BQZ forms linear chains on all the previously mentioned substrates (see Figure 17(d, e, f)) influenced by the larger butyl groups. EQZ typically forms linear chains but can also form 2D islands.[42] Both EQZ and BQZ chains follow the herringbone reconstruction of Au(111), aligning without lifting the reconstruction. At high coverage, chains straighten by overcoming the substrate template effect. Repulsive interactions are common at low coverage, leading to equidistant separation of chains. This repulsion diminishes at higher coverage. EZQ and BZQ exhibit a lock-and-key arrangement on Cu(111). The stacking and interaction patterns of EZQ chains varies depending on the substrate, showing different binding configurations depending on the surface.

In regards to works on the topic of adsorption on graphene, studies have explored the self-assembly of Tetracyanoquinodimethane (TCNQ)-functionalized BQZ on graphene/Cu and gold.[55] The TCNQ-BQZ exhibits various molecular orientations and packing

arrangements depending on the substrate and deposition method (solution vs gas phase). It discusses how functionalization (here with donor TCNQ group) could enrich their properties leading to stronger intermolecular interactions, distinct from non-functionalized BQZ and improve charge separation finding potential applications in organic solar cells.

To summarize, quinonoid zwitterions with different functional groups and a strong intrinsic dipole moment have been previously used to evaluate the driving forces leading to assembly on coinage metals. The authors concluded that the size and nature of the functional groups significantly influences the assembly patterns, with larger groups leading to constrained and specific bonding geometries. In addition, molecular interactions change with coverage levels, showing repulsive interactions at low coverage that lessen as coverage increases. The repulsive interaction between molecular chains, substrate-mediated, is the result of charge redistribution (pillow effect) in the proximity of the contact area between adsorbates and the substrate.[15]

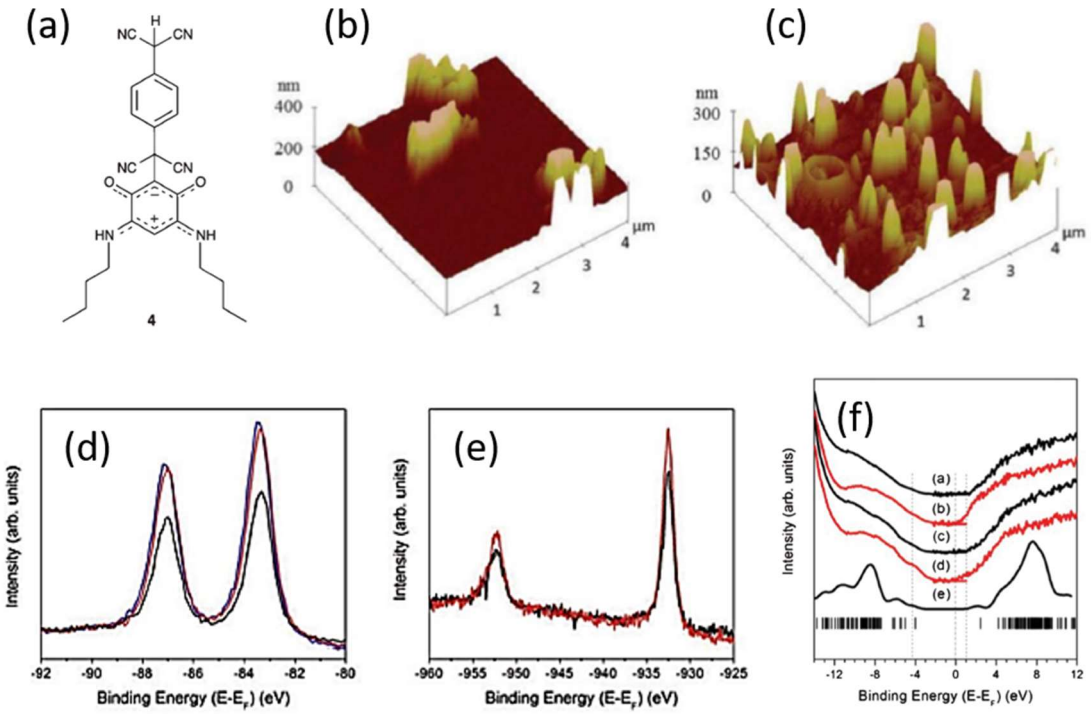


Figure 18: ***(a)*** *TCNQ-derived p-benzoquinonemonoimine zwitterion 4. Atomic force microscopy (AFM) images of the thicker molecular films of 4* ***(b)*** *on Au and* ***(c)*** *on graphene. The molecular thin film roughness are about 200 nm and 150 nm, respectively, while the roughness of the substrates are below 20 nm. The attenuation of the X-ray photoemission substrate signal from the* ***(d)*** *Au (Au 4f core levels) and* ***(e)*** *graphene on Cu (the Cu 3p core levels) substrates. The core level spectra are shown for clean Au (blue) and the substrates following adsorption of 1 to 2 molecular monolayers of zwitterion 4 on Au (a) and graphene on Cu (b) (in red). Much thicker molecular films create islands of zwitterion 4 molecules but do not suppress more than 15-30 % of the substrate X-ray photoemission signal (black).* ***(f)*** *Comparison of the combined photoemission and inverse photoemission spectra of molecular films of zwitterion 4 on graphene on Cu f(a,b) and on Au f(c,d), along with the calculated density of states by PM3 f(e) : f(a) thick molecular film on graphene; f(b) thin molecular film on graphene; f(c) thick molecular film deposited on Au; (d) thin molecular film on gold. Reproduced from earlier work.*[48]

In contrast to these results, the deposition of zwitterionic molecules on graphene has shown dominant intermolecular interactions, independent of the substrate.

The principal results of the work of Kong et al. show that the zwitterion tendency to form islands can be argued to be caused by strong intermolecular interactions rather than substrate specific effects.[48] The AFM images of the deposition on Au and graphene in Figure 18(b, c), shows the tendency of these molecules to form island growth rather than molecular films on both substrates. This could give insight about dominating intermolecular interactions over molecule-substrate interactions.

Furthermore, the X-ray photoemission spectra for Au (Figure 18(d)), shows a decrease in 4f binding energies, meaning charge donation to the Au surface. However, for graphene (Figure 18(e)), no charge transfer occurs, which is an additional argument for minimizing the zwitterions' interaction with the substrate.

Additionally, at low molecular coverage, the HOMO-LUMO gap of the zwitterion are similar on both Au and graphene, (Figure 18(f)) further backing up the conclusion that the observed behavior is attributable to the nature of the zwitterionic molecules rather than the differences between graphene and gold substrates. This publication is the only example of an attempt of zwitterionic supramolecular networks on graphene. The experimental conditions (chemical vapor deposition from liquid, graphene on a metallic substrate) are very far from what we are seeking (physical vapor deposition under UHV, graphene on a SiC substrate). This thesis experiments therefore appear to be highly complementary in light of this bibliography.

I.5. Conclusion

A key finding of these studies is that depending on the adsorption geometry, the arrangement of the supramolecular network and interaction with the substrate, the interface dipole can be changed through several effects such as charge transfer, mirror dipoles and surface enhanced dipole moments.[56] Moreover, the resulting pattern of the dipole network cannot be easily deduced from the addition of these 2 pieces of information: the dipole orientation of a single molecule and the supramolecular arrangement. The interplay between multiple interactions (Coulomb force, details of the local electrostatic potential and intermolecular interactions) make this resulting pattern *a priori* inaccessible without measurement or simulation. Moreover, it is for this reason that in this Thesis work we tried to measure the resulting dipole at the molecular scale meanwhile having a collaboration with theoretical and computational chemists to evaluate it through theoretical modeling.

II.Theoretical Concepts and equipment overview

II.1. Scanning Tunneling Microscopy

II.1.1. The tunneling effect

The idea of the Scanning Tunneling Microscope (STM) was conceived by Gerd Binning and Heinrich Rohrer at the IBM research laboratory in Zürich in 1982.[57] They obtained unprecedented topographic images of surfaces at an atomic scale resolution by using vacuum tunneling and their work was rewarded with the Nobel Prize in Physics in 1986.[58] The STM was a groundbreaking tool in the field of nanotechnology, it revolutionized our ability to visualize and manipulate matter at the atomic and molecular levels. This tool relies on the combination of a coarse approach and piezoelectric transducers. A sharp, metallic tip is brought into close proximity (a few Å) to the sample, which means that the electron wave functions of tip and sample start to overlap. A bias voltage applied between the tip and the sample causes electrons to pass through the vacuum barrier between the tip and the sample (see Figure 19(a)), creating a small current, called the tunneling current.

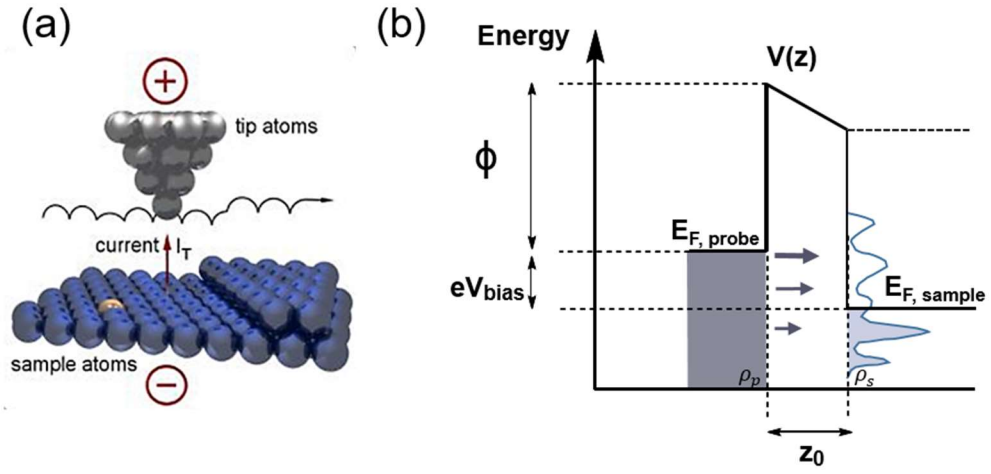


Figure 19: Principle of an STM. ***(a)*** *A bias voltage yields electron tunneling between the sample and the tip. By keeping the tunneling current constant while scanning the tip over the surface, the tip height follows a contour of constant LDOS. Adapted from reference.*[59] ***(b)*** *Energy levels diagram of a unidimensional potential barrier between a metallic probe of density of states ρ_p and a sample with a density of states ρ_s.*

Quantum tunneling, a phenomenon central to the operation of the STM, challenges classical notions of impenetrable potential barriers. Electrons, existing as both particles and waves, navigate through potential energy barriers, defying classical limitations of physics. This behavior of electrons enables the STM to achieve unprecedented resolution at the atomic level. The phenomenon is harnessed by exploiting the probability of electrons passing through a barrier between a sharp metallic tip and the sample surface.

II.1.2. Electron tunneling theory

With the advent of quantum theory and the description of particles by wavefunctions, the description of the tunneling process has emerged. The possibility for an electron with energy E to overcome a potential/energy barrier U > E becomes feasible if it is sufficiently narrow in the electron propagation direction. That is to say, if the barrier is smaller than the decreasing spatial extension of the electronic wavefunction, we can speak of a tunneling effect where a single electron in vacuum, can find itself on the other side of a forbidden 1D potential barrier. In this simplest case of a 1D potential barrier, the transmission coefficient of the barrier T, which gives the probability of an electron to tunnel through a potential barrier can be described using (II.1):

$$T \approx e^{(-2\kappa z_0)} \tag{II.1}$$

κ is the decay constant related to the potential barrier and z_0 is the width of the barrier. The decay constant κ can be expressed as:

$$\kappa = \frac{\sqrt{2m(U-E)}}{\hbar}$$

Where m is the mass of the electron, U the height of the potential barrier, E the energy of the electron and $\hbar$ the reduced Plank constant.

Because the particle wavefunction is non-zero in the barrier and is decreasing exponentially, the particle has a non-zero probability to tunnel through the barrier. (See appendix A. 21). In 1961, John Bardeen first advanced experimentally in the understanding of tunneling processes in metal-insulator-metal planar junctions.[60] Bardeen introduced the concepts of electronic density of states (DOS) on either side of the barrier and how these states are filled according to the Fermi-Dirac distribution. In this approach, the 2 electrodes composing the tunnel junction are considered as independent systems.

The tunneling current calculation as a function of the sample and tip density of states has been first developed for planar junctions.

In this approximation, the particles transfer through the barrier is described by the Hamiltonian in (II.2):

$$H = H_L + H_R + H_T \tag{II.2}$$

H_L and H_R are the Hamiltonians corresponding to the left and right electrodes. $H_T$is the transfer Hamiltonian which is responsible for the transfer of electrons across the junction. Energies and eigenstates of H_L and H_R are respectively E_μ, ψ_μ and E_ν, ψ_ν and the tunneling current I_t can be expressed as (II.3):

$$I_t = \frac{2\pi e}{\hbar}\sum_{\mu,\nu} f(E_\mu)[1 - f(E_\nu + eV)]\left|M_{\mu\nu}\right|^2 \delta(E_\mu - E_\nu) \tag{II.3}$$

with f(E) the Fermi-Dirac distribution function and V the voltage drop across the junction (this term will be referred to V_{bias} in subsequent sections of this manuscript).

$M_{\mu\nu}$ is the matrix element of H_T which couples the eigenstates ψ_μ of the tip and the eigenstates ψ_ν of the surface. Bardeen expressed this $M_{\mu\nu}$ matrix element as follows:

$$M_{\mu\nu} = -\frac{\hbar^2}{2m}\int_{S_0} \overrightarrow{dS}\left[\psi_\mu^* \vec{\nabla}\psi_\nu - \psi_\nu \vec{\nabla}\psi_\mu^*\right] \tag{II.4}$$

with S_0 being the surface of the 2 electrodes.

In order to understand tunneling in STM, the previous equation has to be reevaluated in terms of real space wave functions.

Bardeen's theory was applied to the STM in 1983 by Tersoff and Hamann.[61] They performed one of the first calculation of the tunneling matrix element for the STM junctions, no longer assuming planar electrodes, but simplifying the geometry of the electrodes as follows: electrons of the tip in vacuum are described by an evanescent wave coming from the tip apex supposed to be a sphere of radius R and center r_0:

$$\psi_\mu(r) = A_\mu \frac{e^{-\kappa|r - r_0|}}{|r - r_0|} \tag{II.5}$$

with

$$\kappa = \sqrt{\frac{2m(\phi - E)}{\hbar^2}}$$

The inverse range of the evanescent wave of an electron has an energy E in vacuum, ϕ represents the work function, A_μ a renormalization constant and κ the decay constant related to the potential barrier.

To describe the electronic states at the vicinity of the surface, Tersoff and Hamann considered a periodic crystal. The wave function ψ_ν of the sample in a given point r of the tunnel barrier is thus a Bloch wave in the (x, y) plane. This Bloch wave is weighted by an exponentially decreasing component along z :

$$\psi_\nu(r) = \psi_{k_{II},E} = \sum_G C_{k_{II},G} e^{i(k_{II}+G)x}\, e^{-\alpha_{\nu,G}\, z} \qquad \text{(II. 6)}$$

With $\alpha_{\nu,G} = \sqrt{|k_{II} + G|^2 + K_\nu^2}$ and $K_\nu = \sqrt{2m(\phi - E)/\hbar^2}$.

Here, k_{II} is the wave vector component parallel to the surface, G is a wave vector of the reciprocal 2D lattice and $C_{k_{II},G}$ are the coefficients of the Fourier series development. Moreover, by supposing that tunneling voltages are small with respect to the work function and that states are close to the Fermi surface, we get:

$$K_\mu = K_\nu = \frac{\sqrt{2m\phi}}{\hbar} \qquad \text{(III. 7)}$$

For simplicity, this expression assumes that the work function is the same for the tip and the sample $\phi_\mu = \phi_\nu$.

By replacing (II.5) and (II. 6) in (II.4) we get (II. 8).

$$M_{\mu\nu} = -\frac{2\pi\hbar^2}{m} A_\mu \psi_\nu(r_0) \qquad \text{(II. 8)}$$

Thus, the tunneling current can be written as:

$$I_t = \frac{(2\pi\hbar)^3}{m}\sum_{\mu,\nu} A_\mu^2 |\psi_\nu(r_0)|^2 \left(f(E_\nu) - f(E_\mu)\delta(E_\nu - E_\mu + eV)\right) \quad \text{(II. 9)}$$

A_μ is assumed constant; by expressing the density of states in terms of wave functions, the expression of I_t becomes:

$$I_t \propto \int dE\, \rho_s(r_0, E)\, \rho_p(E - eV)\big(f(E - eV) - f(E)\big) \quad \text{(II. 10)}$$

where $\rho_s(r_0, E) = \sum_\nu |\psi_\nu(r_0)|^2\ \delta(E - E_\nu)$ is the local density of states (LDOS) of the sample at the position of the tip apex, calculated from (II. 6). $\rho_p(E - eV)$ represents the density if states (DOS) of the probe (tip) at the energy $E - eV$. The difference $f(E - eV) - f(E)$ represents the difference in occupation probabilities between the probe and the sample. The tunneling current expression can be generalized to the expression (II. 11).

$$I_t = \frac{e}{\hbar}\int_{-\infty}^{+\infty} dE\, \rho_s(r_0, E)\, \rho_p(E - eV) T(E, V, z)\big(f(E - eV) - f(E)\big) \quad \text{(II. 11)}$$

$T(E, V, z)$ represents the transmission factor of the tunnel barrier. This term contains the exponential dependence. As this term is a function of z, it shows the deformation of the barrier for high voltages applied to the junction $V \sim \phi/e$. When working on metallic surfaces, the voltage is always weak (from few mV to few V) compared to the tunneling barrier ϕ and the Fermi energy E_F. In that case, the following approximation for the transmission factor can be applied $T(E, V, z) \approx T(E_F, z)$ and the tunneling current expression can be simplified to (II. 12).

$$I_t = \frac{eT(E_F, z)}{\hbar}\int_{-\infty}^{+\infty} dE\, \rho_s(r_0, E)\, \rho_p(E - eV)\big(f(E - eV) - f(E)\big) \quad \text{(II. 12)}$$

Given the context of tunneling in STM, more approximations can be applied to furthermore simplify the expression of the tunneling current. First, the DOS of the tip can be considered constant (because we consider a metallic tip and a small variation of V_{bias}), which simplifies to $\rho_p(E - eV) \approx \rho_p(E_F)$ and the DOS can be taken out of the integral as in (II. 13).

$$I_t = \frac{eT(E_F, z)\,\rho_p(E_F)}{\hbar} \int_{-\infty}^{+\infty} dE\,\rho_s(r_0, E)\big(f(E - eV) - f(E)\big) \qquad (II.13)$$

The system is also considered to be at absolute zero temperature (0 K), temperature at which the Fermi-Dirac distribution function f(E) can be expressed as a step function:

$$f(E) = \begin{cases} 1 & \text{if } E < E_F \\ 0 & \text{if } E > E_F \end{cases}$$

The integral is simplified depending on the sign of V which is the bias voltage applied V_{bias}. Depending on the sign of the bias voltage, the tunneling current probes empty states ($V > 0$) or filled states ($V < 0$).

Thus, for $V = V_{bias} > 0$:

$$I_t \approx \frac{eT(E_F, z)\,\rho_p(E_F)}{\hbar} \int_{E_F}^{E_F + eV_{bias}} \rho_s(E)dE \qquad (II.14)$$

The Figure 19(b) schematically displays a configuration in which a positive bias voltage V_{bias} is applied to the surface in the case of a 1D potential barrier of height V and width z_0. According to quantum mechanics, a particle with an energy $E_{F,probe}$ can penetrate a such a barrier $\phi > E_{F,probe}$ with a non-zero probability.

II.1.3. Fundamentals and Operational Modes of Scanning Tunneling Microscopy

The STM operates by using a tip usually made of tungsten (W) connected to a piezo drive. When a voltage is applied, the piezoelectric transducer undergoes expansion or contraction. The *XY* piezo enables the tip to scan across the surface, while the Z piezo is responsible for bringing the tip and sample close to up to a few Å of each other. This proximity causes the wavefunctions of the tip and sample to overlap and electrons to tunnel from the sample to the tip, or vice versa.

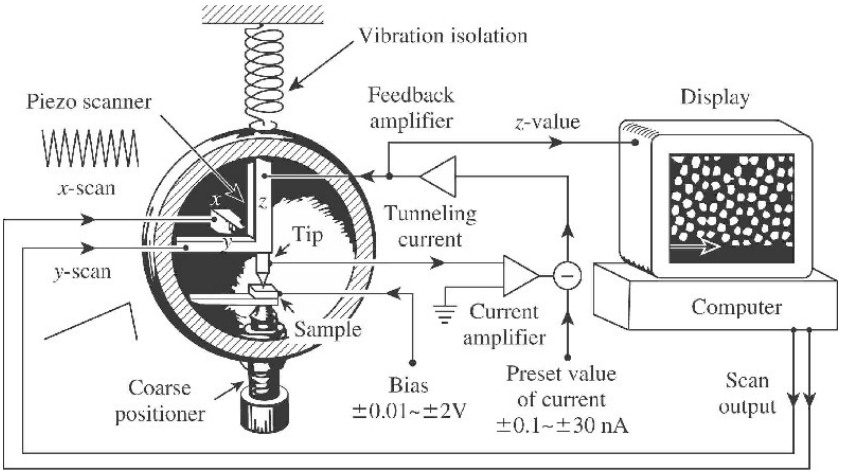


***Figure 20**: Basic scheme for an STM operating in constant current mode. Reproduced from reference.[62]*

It is possible to perform 2 kinds of STM measurements: constant height measurements or constant current measurements. The scheme of Figure 20 shows the principle of operation of an STM in constant current mode. Upon applying a bias voltage between the tip and the sample, a very small tunneling current (generally in the range of a few pA to a few nA) flows, reflecting the tip to surface distance. This tunneling current is then amplified by a current amplifier, converting it to a voltage. This voltage is compared to a reference value and the resulting difference is further amplified to drive the Z piezo. The amplifiers introduce negative feedback, prompting the tip to retract or approach the surface based on the feedback loop, maintaining a stable tunneling current.

As the tip scans the xy plane, a contour plot of the equilibrium z positions is generated for a constant tunneling current. The resulting grayscale image on the screen depicts darker colors for low z values and lighter colors for high z values. This visualization technique allows for the mapping of surface topography using STM.

It is important to note that the STM does not measure the physical height of surface features. For instance, an STM image of an atom adsorbed on a surface will show a perturbation in height at that point. The electrical current transmitted between the tip and the sample is influenced by 2 main factors: (1) the sample geometry and (2) the electrons arrangement within the sample (the electron density, or LDOS), which depends on both the position and the energy.

II.1.4. Scanning tunneling spectroscopy (STS)

In addition to examining the surface topography, STM provides valuable insights into the electronic properties of materials using a technique called Scanning Tunneling Spectroscopy (STS). The theoretical analysis of an electron tunneling through the vacuum barrier has shown that the tunneling current I_t depends on the local density of states (LDOS) of the sample (II. 14) as long as the hypotheses to establish (II. 14) are respected (metallic tip and small bias variation). In the classical operating mode, the tip is positioned at the desired (x, y) location on the sample, the feedback loop is deactivated and the bias

voltage is ramped from V_{start} to V_{end}. This bias voltage ramp is executed by incremented steps (see Figure 21) and it is possible to adjust the time spent on each step (T_{raster}).

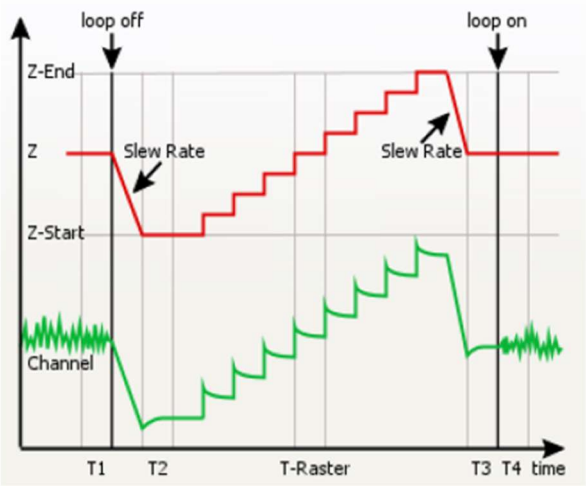


Figure 21: Schematic diagram of spectroscopy, delay and acquisition times. Reproduced from reference.[63]

For each step, the tunnel current is continuously recorded at the maximum frequency of the IV amplifier and one mean value is registered corresponding to $I_t(V_{bias})$. Other parameters can be also modified before starting the spectroscopy, for example, the tip can be brought closer or farther from the surface by modifying its value by an offset distance value ΔZ. The advantage of such a modification is to get a better signal-to-noise ratio. In fact, the tunneling conditions before the spectroscopy are predefined for a fixed value of V_{bias} and these preset conditions are not necessarily ideal during the spectroscopy where V_{bias} is varied. On the instrument used (but these options are commonly available on all control electronics), different stabilization times can be adjusted before and after the regulation cut-off. Numerical derivation of these I_t (V) curves can give access to the LDOS as (II. 14) is derived by $E = eV_{bias}$, we obtain dI_t/dV_{bias} proportional to ρ_s in (II. 15).

$$\frac{dI_t}{dV_{bias}} \propto \frac{T(E_F, z)\, \rho_p(E_F)}{\hbar}\, \rho_s(E) \qquad \text{(II. 15)}$$

However, numerical derivation can induce many artifacts in the curves due to the intrinsic noise of the I_t (V) curve that is not physical information. A technique higher sensitivity consists in directly measuring the dI_t/dV_{bias} experimentally with a lock-in amplifier. For all of these measurements it is important to ensure that the tip is terminated by a metallic apex. To obtain the signature of a metallic tip, the measurement of a known surface state on Au(111) for example is an efficient technique.

II.1.4.1. Principle of the dI/dV measurement with lock-in

The differential conductance dI/dV can also be derived through a different approach by the lock-in amplification technique. This technique is more effective for detecting variations in the $I_t(V)$ curves by direct measurement of the differential conductivity. The lock-in amplifier modulates the bias voltage with a high frequency (generally of the order of 1 kHz) and directly records the $dI_t(V_{bias})/dV_{bias}$ variation. This method leads to a better resolution and a better signal to noise ratio compared to the numerical differentiation of $I_t(V_{bias})$.

A slight signal modulation V_{mod} at frequency w ($V_{mod} = V_0 \sin(wt)$) higher than the frequency of the stepped ramp voltage ($w > \frac{3}{T_{raster}}$ at least, to have a mean of 3 measurements per modulation period) is generated by the lock-in and added to the DC bias voltage leading to a sinusoidal response of the tunneling current. This tunneling current is driven to the input of the lock-in amplifier which detects and locks the component of the signal at the modulated frequency, extracts and amplifies its amplitude ΔI_t. This amplitude and the V_{mod} signal can be simultaneously recorded at each V_b value of the ramp voltage. So, this small and fast voltage temporal variation $V_0 \sin(wt) = \Delta V(t)$ induces a small variation ΔI and acts as a differential perturbation of the current at each bias voltage of the ramp.

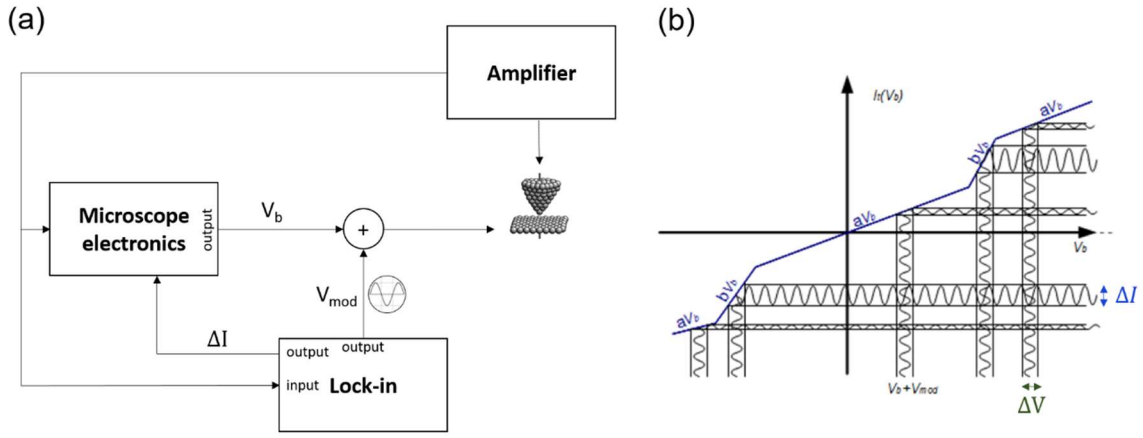


*Figure 22: **(a)** Wiring diagram for experiments with modulated gap voltage. **(b)** Schematic representation of the influence of the variation of the tunneling current on the amplitude of the modulated signal. Schematic reproduced from refrence.[64]*

By normalizing the differential response ΔI_t by ΔV at each bias voltage value, we obtain $\Delta I_t/\Delta V(V_{bias})$ curves which can be approximated by the derivative of $I_t(V_{bias})$ curves, $dI_t(V)/dV\ (V_{bias})$ if ΔV is small enough with respect to the V_b step of the voltage ramp and the frequency w high enough (typically, this involves integrating between 3 and 10 measurements of ΔI_t) with respect to the stepped ramp frequency.

This differential measurement marks any change in the slope of the $I_t(V_{bias})$ curve and therefore, any change in the electronic density of the surface (as we consider a constant density of the metallic tip).

The Figure 22(b) shows a schematic representation of how the convolution of the applied sinusoidal signal and the tunneling current can be used to detect the changes in the $I_t(V_{bias})$ characteristics.

From a practical point of view, the measured tunneling current is noisy due to mechanical variations of the system and intrinsic sources. The lock-in amplifier performs other functions, notably filtering and it is important to properly set the integration times and bias ramp parameters to optimize the signal-to-noise ratio.

To illustrate this principle in the framework of signal analysis, we start from a simplified expression for the tunneling current previously established in (II. 14).

$$I_t(V_{bias} + V_0 \sin(wt)) \propto \int_0^{eV_b + eV_0 \sin(wt)} \rho_s(E)dE \qquad \text{(II. 16)}$$

Due to the small amplitude of the modulation ($V_b \gg V_0$), the tunneling current can be expanded as a Taylor series such as:

$$I_t(V_{bias} + V_0 \sin(wt)) \propto$$
$$I_t(V_b) + V_0 \sin(wt) \times \frac{dI_t(V_{bias})}{dV_{bias}} + \frac{1}{2}\frac{d^2I_t(eV_{bias})}{dV_{bias}^2} V_0^2 \sin^2(wt) + \cdots \qquad \text{(II. 17)}$$

$$I_t(V_{bias} + V_0 \sin(wt)) \propto$$
$$I_t(V_{bias}) + \rho_s(eV_{bias}) eV_0 \sin(wt) + \frac{1}{2}\frac{d\rho_s(eV_{bias})}{dV_{bias}} e^2V_0^2 \sin^2(wt) + \cdots \qquad \text{(II. 18)}$$

Equations (II. 17) and (II. 18) show that the first harmonic is proportional to $dI_t(V_{bias})/dV_{bias}$ and the second harmonic to $d^2I_t(V_{bias})/dV_{bias}^2$. These harmonic frequencies can be extracted by the means of a lock-in amplifier as previously mentioned and this allows a direct measurement of the LDOS.

Both the numerical derivation and the lock-in amplification techniques permit to measure the LDOS at a fixed point on the surface. Measuring it in each point of the surface allows to construct an STS map spatially associated to the STM image (see VI.3.2).

II.2. Non-contact AFM

During this thesis, we worked in collaboration with the IM2NP laboratory in Marseille where Kelvin frequency shift $\Delta f(V_{bias})$ spectroscopies were performed to extract the electrostatic surface potential. These spectroscopies can only be performed on a non-contact Atomic Force Microscope (nc-AFM), which is why the principle of this instrument and the origin of the Kelvin probe force signal will be briefly introduced.

The nc-AFM allows to measure all the interaction forces between a tip and a surface and the Kelvin Probe Force Microscope (KPFM) allows to discriminate among all these forces those which are of electrostatic origin. The KPFM can be seen as a particular operational mode of the nc-AFM that allows for this discrimination.

The objective of this section is to briefly establish the technique at the origin of the quantities measured in these spectroscopies.

II.2.1. Principle of nc-AFM

In nc-AFM, a cantilever oscillating at its natural frequency is used as a force probe. When this cantilever is exposed to a force field, its natural frequency will be modified, shifted. The frequency shift provides information about the presence and the amplitude of the force in the cantilever's environment. When such a cantilever is approached to the surface, different interaction forces between the cantilever and the surface (see Figure 23(b)) modify the frequency and amplitude of oscillation.

These forces depend on the structural, electrical and chemical properties of the surface and therefore provide information on its physical properties. The simultaneous variation of the amplitude and oscillation frequency makes it impossible to extract and regulate the tip-surface distance. This is why in nc-AFM, the amplitude is kept constant on one hand by a control loop that will permanently send an excitation signal to the cantilever. On the other hand, the control loop records the variations of the frequency shift Δf, which serves as a signal to regulate the tip-surface distance by making use of another loop.

This is done in a similar way to what is described for the STM principle, where the tunneling current I_t serves as a signal to regulate the tip-surface distance. Both STM and nc-AFM are implemented on the same type of support and technology. They share the same principles regarding the control of the positioning of the tip with piezoelectric tubes and have similar resolutions. To date, there are microscopes that can perform these 2 types of operations (STM and nc-AFM) and not all the details of the nc-AFM instrumentation will be addressed.

Following this overview, a historical evolution of nc-AFM is presented, tracing its development since its emergence in the 1990s with the pioneering work of T. Albrecht and F. Giessibl.[65,66] Over the past fifteen years, this technique has developed both

instrumentally and theoretically, with an ever-increasing degree of precision, control and understanding of observations.

This technique detects short-range interaction forces between the AFM tip and the surface atoms, enabling chemical identification of the atoms on heterogeneous surfaces. Due to its sensitivity to short-range forces, the nc-AFM is used to manipulate atoms and molecules, particularly at low temperatures (LT) and, with more difficulty, at RT.

An important advancement in the early 2000's was the replacement of the traditional AFM cantilever with a quartz tuning fork on which is mounted a tungsten STM tip.[67] This quartz crystal, similar the ones found in watches, oscillates at low frequencies around 32 kHz and exhibits high sensitivity to short-range forces due to its high stiffness (~1800 N/m). This allows it to oscillate at sub-nanometer amplitudes (ranging between 20-100 pm), which is crucial for detecting local interactions and therefore providing subatomic contrast in imaging.[66]

It is mostly the STM tip on the quartz that allows for the simultaneous measurement of I_t and Δf. It is with this type of tip that we worked at the IM2NP lab microscope. However, the low resonance frequency of the tuning fork makes it a slow technique that requires operation at LT to avoid thermal drift at RT.

Regardless of these challenges, results from IBM's group in Zürich in 2009 comprising high-resolution images of individual molecules using tuning forks encouraged its use.[68]

II.2.2. Fundamentals of non-contact AFM

In this subsection, the relationship between tip-sample forces and frequency shifts as recorded in nc-AFM mode will be discussed. The oscillation dynamics are a critical component in this mode and the cantilever can be treated as an externally driven damped harmonic oscillator.

At a position far from the surface with no effect from external interaction forces, the following equation of motion (II. 19) can be used to represent the oscillation dynamics of the cantilever.[65]

$$\ddot{z}_0(t) + \frac{2\pi f_0}{Q_0}\dot{z}_0(t) + (2\pi f_0)^2 z_0(t) = (2\pi f_0)^2 A_x \cos(2\pi f t) \qquad \text{(II. 19)}$$

$z_0(t)$ is the instantaneous position of the tip, f_0 is the resonant frequency, Q_0 is the quality factor of the cantilever and A_x is the amplitude of the excitation signal. A schematic of an oscillating cantilever over the surface is shown in Figure 23(a).

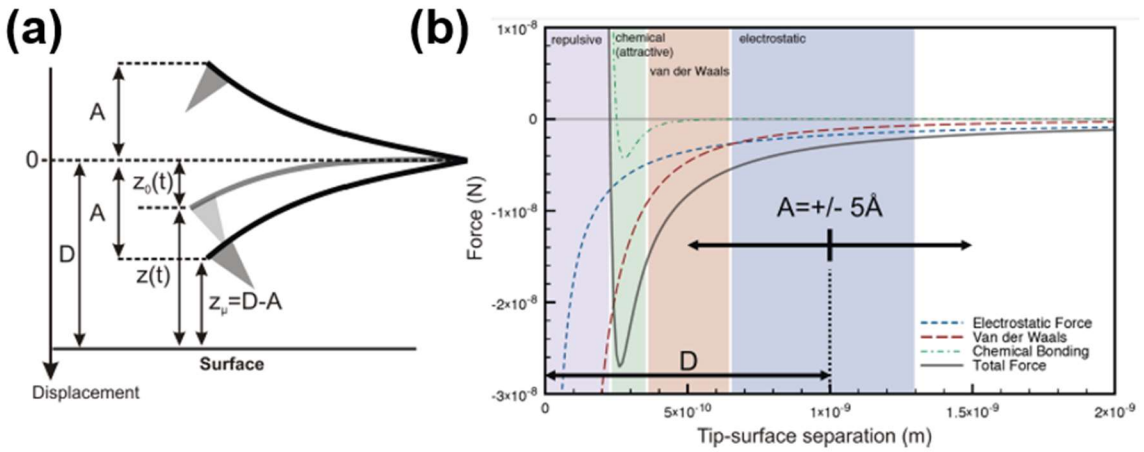


Figure 23: ***(a)*** *Schematic of an oscillating cantilever at its upper and lower turnaround points. D is the distance between the surface and the equilibrium position of the cantilever and z_μ the minimum approach distance of the tip during its oscillation cycle, both are related by the equation $D = z_\mu + A$.* ***(b)*** *Behavior of the interaction force with respect to tip-surface separation D. Adapted from reference.*[69]

When the tip is approached to less than a few nanometers from the surface, it becomes sensitive to attractive interaction forces, such as vdW, electrostatic, magnetic and chemical forces. These forces are short- and long-range and vary in intensity, with electrostatic interactions extending beyond 5 nm and vdW forces beyond 1 nm, while chemical interactions occur within 1 nm (The forces are reported in Figure 23(b)). The total interaction force F_{int} modifies the cantilever's equation of motion, introducing a non-linear force component that affects both the amplitude and phase of the oscillation based on the tip-surface distance. This equation of motion becomes:

$$\ddot{z}_0(t) + \frac{2\pi f_0}{Q_0}\dot{z}_0(t) + (2\pi f_0)^2 z_0(t) = (2\pi f_0)^2 A_x \cos(2\pi f t) + \frac{(2\pi f_0)^2 F_{int}(z(t))}{k_0} \qquad (II.\,20)$$

For nc-AFM, maintaining the amplitude and phase of the oscillator constant at resonance allows for effective decoupling of the conservative ($F_{c,int}$) and the dissipative ($F_{d,int}$) interaction force components. The conservative forces can be expressed as follows:

$$< F_{c,int} > = \frac{1}{2\pi k_0}\int_0^{2\pi} F_{c,int}\,(D - A_0\cos(\theta))\cos(\theta)\,d\theta \qquad (II.\,21)$$

This setup allows determining the resonance frequency shift Δf whose expression is given by $\Delta f = f - f_0$ with respect to the resonance of the free oscillator in (II. 22) and the excitation amplitude expression given in (II. 23).

$$\frac{\Delta f(z)}{f_0} = \frac{< F_{d,int} >}{k_0 A_0} = \frac{1}{2\pi k_0 A_0} \int_0^{2\pi} F_{c,int}\,(D - A_0\cos(\theta))\cos(\theta)d\theta \qquad \text{(II. 22)}$$

$$A_x(z) = A_0\left(1 + \frac{\Delta f(z)}{f_0}\right)\left(\frac{2f_0}{k_0 A_0} < F_{d,int} > + \frac{1}{Q_0}\right) \cong \frac{2}{k_0} < F_{d,int} > \qquad \text{(II. 23)}$$

In this way, Δf provides insights into conservative forces, while A_x describes the dissipative forces. Conservative attractive (repulsive) forces $F_{c,int} < 0$ (> 0) result in a negative (positive) Δf. A negative Δf suggests a non-contact dominant regime, though not 'purely non-contact', as repulsive forces might be involved during a part of the oscillation cycle.

It is important to note that since Δf is a weighted average measurement of the force over the cantilever's oscillation, it is possible for the tip to probe the repulsive regime during a fraction of its oscillation period without the resulting Δf becoming positive. The notion of contact between 2 surfaces occur when repulsive forces start to compensate attractive forces, i.e., at the minimum of the force. Under these conditions, if Δf is negative then the system is in a 'dominant non-contact regime'.[70]

II.3. Kelvin Probe Force Microscopy (KPFM)

II.3.1. Principle of KPFM

The Kelvin probe force microscopy (KPFM) is a surface potential microscopy method adapted to nc-AFM in 1991.[71] By scanning the 2D plane of a surface, the work function can be locally mapped at the atomic or molecular scales and correlated with the sample topography. In an AFM, the sample (s) and the tip (t) are considered as 2 electrodes and are polarized relative to each other by a potential V_{bias} resulting in a capacitance C_{ts}.

Electrostatic forces arise from the tip-surface interface and are related to the differences in work functions between the tip (ϕ_t) and the surface (ϕ_s).

The basic idea of KPFM is to dynamically compensate these forces during scanning. As the tip is oscillating, the tip-to-sample distance varies and thus C_{ts} varies. The tip-sample electrostatic forces are determined by this variation of C_{ts}. The attractive force on the tip is then determined as the derivative of the electrostatic energy of the capacitance C_{ts} with respect to the distance:

$$F_{ts}^{el}(z) = -\frac{1}{2}\left|\frac{\partial C_{ts}(z)}{\partial z}\right| V_{bias}^2 \hat{\mathbf{z}} \qquad \text{(II. 24)}$$

This force varies as the square of the tip-surface potential. The orientation conventions depicted in (Figure 24(a)) defined $\hat{\mathbf{z}}$ as the unit vector in the vertical direction.

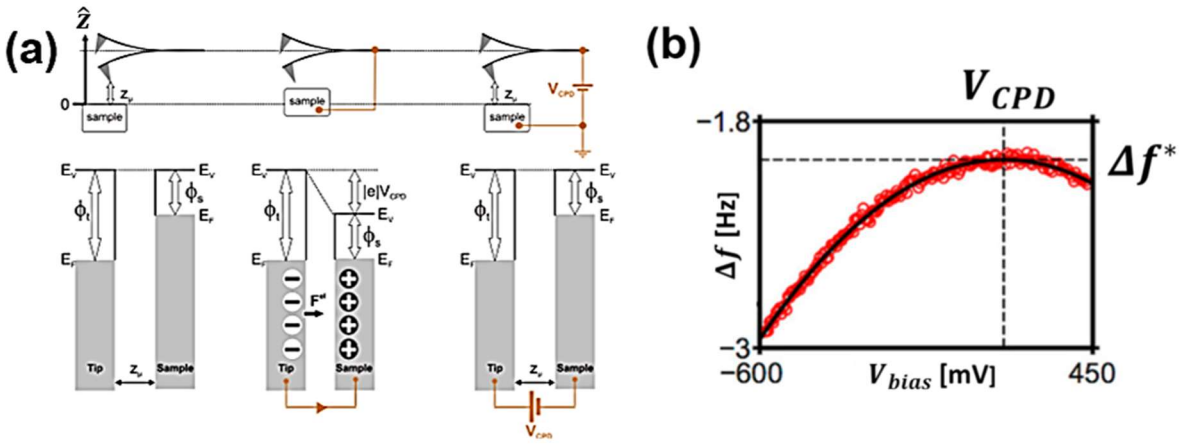


*Figure 24: **(a)** Principle of operation of the KPFM. The electrical contact between 2 electrodes generates a current aligning their Fermi levels. This induces a capacitive component of the attractive force between the tip and the surface. Applying a potential that realigns their vacuum levels compensates for this force, known as the contact potential. Adapted from reference.[70] **(b)** Δf spectroscopic curve schematic, showing its parabolic shape. The maximum value of the frequency shift is Δf^*, value from which the V_{CPD} is deduced. Adapted from earlier work.[72]*

Figure 24(a) shows that the application of a potential that compensates for the difference in work functions between the tip and the surface also compensates for the electrostatic force. As a result, the KPFM technique has become a near-field method for locally mapping the work function difference between the tip and the surface, known as the Contact Potential Difference (CPD) which is from the tip-sample potential:

$$V_{CPD} = \frac{\phi_s - \phi_t}{e} \qquad \text{(II. 25)}$$

To sum up, the electrostatics forces that develop between the tip and the surface are functions of the CPD.

The CPD can be measured independently through $\Delta f = f(V_{bias})$ spectroscopic curves that measure the electrostatic forces. In this case, the tip is positioned at the desired location and height, the z-regulation is stopped, the DC part of the bias is varied and the changes in Δf are measured. The overall curve has a parabolic shape due to (II. 24). V_{CPD} is the potential value that minimizes Δf (the parabola's maximum), i.e., the force. We show this type of measurement in the Chapter VI.

When repeating this measurement at regular intervals on the surface, it is possible to obtain a CPD map of the surface at the atomic scale. The IBM group in Zürich has published an example of this work in 2012.[72]

This type of experiment is more relevant than 'topography and CPD' imaging to probe the short-range regime because stopping the z-regulation helps prevent potential coupling between the forces responsible of topography signals and those responsible for CPD.

In this Thesis work, we made use of the KPFM essentially in the spectroscopic mode, by applying V_{bias} ramps and recording the Δf response. Only one experiment was done on a variable temperature nc-AFM (VT nc-AFM) where the topographic image obtained at a constant Δf and the V_{CPD} are simultaneously recorded (see VI.2.1).

II.3.2. CPD sign and dipole orientation

It is essential to correlate the measured CPD sign with the local charge sign or dipole orientation that induces it.

Equation (II. 25) shows that the CPD sign depends on the electrode to which the modulation is applied: the tip or the surface. It is important to note that if the potential is applied to the tip, the inverse of the CPD is measured, data analysis must therefore be conducted systematically. In the closed-cycle LT-SPM (presented in II.4.2), it is the sample that is polarized and the following data that presents the CPD sign is done with this polarization interpretation.

Let's consider a sample with a CPD reference, CPD_{ref}. On the surface of this sample, there is a local quantity α having a charge 'q' and a dipole 'p'. The direction of the dipole is normal to the surface and its orientation relative to the surface is indicated by an arrow (↑, ↓). According to the classical interpretations of CPD variations:[72–79]

A negative (positive) shift in CPD relative to CPD_{ref} for a surface dipole 'p' pointing outwards from the surface (towards the surface), thus leading to an increase (decrease) in the interface dipole. A negative (positive) shift in CPD relative to CPD_{ref} for a local positive (negative) charge 'q'. These results are summarized in Table 2.

Table 2: Sign of the charge/orientation of the surface dipole as a function of the CPD sign. Reproduced from earlier work.[70]

Local quantity α	**Sign, orientation**	**CPD shift** $\mathbf{V_{CPD,\alpha} - V_{CPD,0}}$
Charge q	+	< 0
	-	> 0
Dipole p	↑	< 0
	↓	> 0

II.4. Experimental setup

The aim of this subsection is to give an overview of the experimental setup used in this thesis work.

II.4.1. LT-STM (CINaM laboratory)

All STM experiments presented in this thesis were performed under ultra-high vacuum (UHV) conditions using a commercial low-temperature STM (Scienta Omicron©) acquired in 2009.

The experimental setup, shown in Figure 25 comprises a preparation chamber and an analysis chamber, allowing the introduction of new tips or samples in the preparation chamber without breaking the UHV conditions in the chamber.

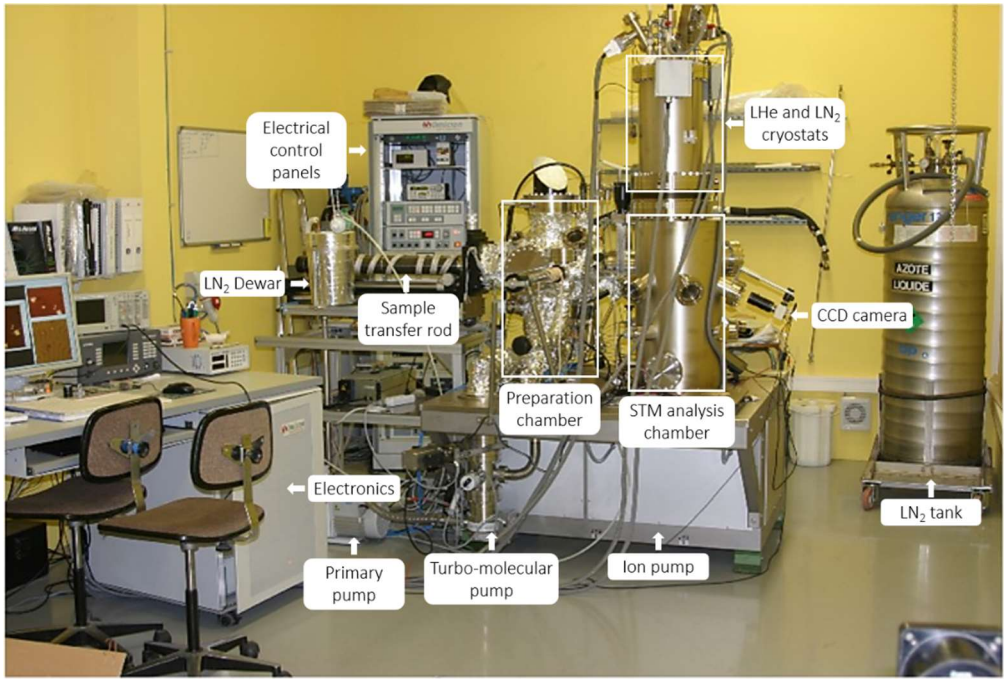


Figure 25: Photography of the LT-STM setup.

A sample transfer rod is used to move new tips and samples from the transfer chamber to the preparation chamber where these tips and samples can be fixed into a manipulator. This manipulator is used to move the sample from the preparation chamber to the analysis chamber which is equipped with several instruments that are detailed in the following. Inside the analysis chamber, tips and samples are transferred into the microscope by the means of a wobble stick, or are placed on a carousel for storage.

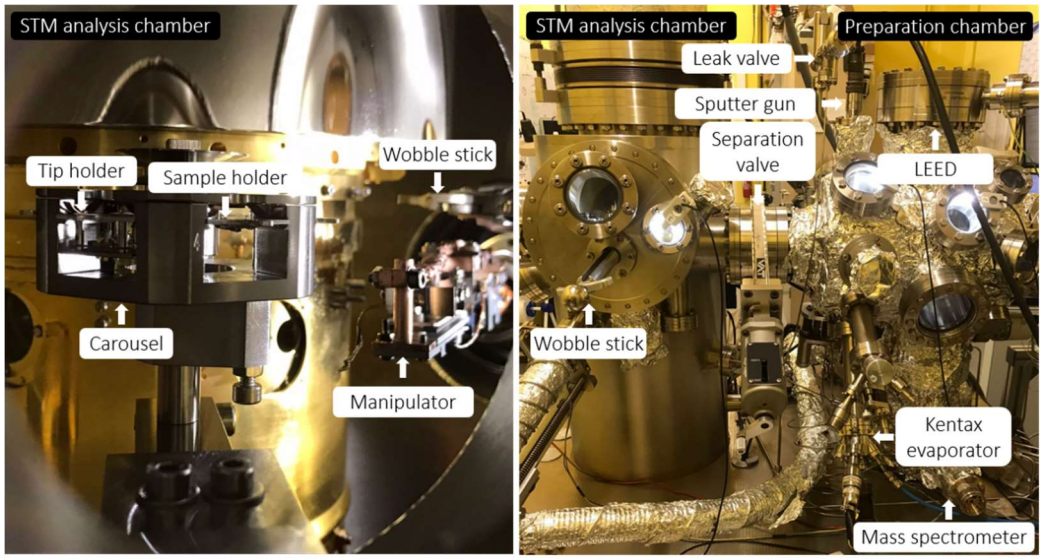


Figure 26: Close-up photography of the components of the LT-STM.

- The preparation chamber:

The preparation chamber is equipped with a pumping system (primary pump, turbo-molecular pump, ion pump and titanium sublimator), a pressure gauge and a mass spectrometer that ensures the maintenance and the control of UHV. It is also equipped with low energy electron diffraction (LEED), a sputter gun, 4 gas lines (Ar, CO, H, N) equipped with leak valves and a commercial organic material effusion cell (Kentax evaporator TCE-BSC). This type of evaporation cell offers significant advantages, primarily due to its exceptional reproducibility in terms of evaporation temperatures and resultant fluxes of evaporated materials. This high level of consistency greatly simplifies and makes possible the repetitive preparation of samples. Additionally, the design of this evaporation source incorporates 3 individual evaporation cells, enabling the storage of multiple compounds.

This chamber serves a dual purpose: it is employed for sample preparation tasks such as surface cleaning and molecular deposition and is utilized in conducting LEED experiments.

- The manipulator:

The manipulator, designed for transferring the sample between the preparation chamber and the analysis chamber incorporates an electron beam sample heater and the capacity for cooling using liquid nitrogen (Omicron© sample heater and cooling upgrade). This facilitates movement of the sample within the preparation chamber, enabling both surface preparation and LEED measurement. The cooling system enables the sample to reach a temperature of 130 K during the preparation process, allowing for the deposition of compounds on a cooled surface. The maximum achievable sample temperature through heating is 1300 K. Temperature monitoring is conducted through a thermocouple in contact with the molybdenum plate on which the crystal is fixed.

- The analysis chamber:

The preparation and analysis chambers are separated by a separation valve, ensuring distinct functionality. In the analysis chamber, a carefully maintained pressure in the range of 10^{-11} torr is upheld through the utilization of an ion pump and a titanium sublimator. Within this chamber, a cryostat is integrated, enabling the cooling of both the sample and the STM tip to liquid nitrogen or liquid helium temperatures.

The outer cryostat is cooled by liquid nitrogen, while the inner cryostat offers the flexibility of cooling with either liquid nitrogen or liquid helium, allowing for tip and sample temperatures of 77 K or 4 K, respectively. Additionally, a carousel is incorporated into the analysis chamber for efficient storage of tips and samples. The movement of samples and tips between the manipulator, carousel and microscope is facilitated by a wobble stick. The sample is oriented downwards on the sample holder. The tip is mounted on a piezoelectric tube, allowing the scanning of the surface in the x- and y-directions on the surface plane and along the z-direction normal to the plane.

The grounded sample remains fixed and stationary, with $-V_{bias}$, the opposite sign of the tunnel voltage set point V_{bias} applied exclusively to the tip during STM measurements. Therefore, in this case, it is as if the sample was polarized at V_{bias}. In this configuration, the electrochemical potential of the tip and the sample $\mu = -eV_{bias}$ is compatible with the scheme of the Figure 19, i.e. for $V_{bias} > 0$ the electron tunnels from the filled states of the tip to the empty states of the surface.

Finally, to enhance precision during the coarse manual approach of the tip over the sample, a CCD camera is strategically positioned in front of one of the windows, offering a close-up view of tip and sample.

II.4.2. LT-STM/nc-AFM (IM2NP laboratory)

This subsection outlines my role as an end user of the equipment in question as part of a collaboration with the Nanostructuration team in IM2NP laboratory in Marseille. This is why only its operational aspects will be focused on rather than technical configuration.

The experiments were performed on a Scienta Omicron© Infinity SPM operating at 8.9 K (Figure 27(a)). The sensor used is a qPlus® tuning fork (Figure 27(c)) having an oscillation amplitude of 200 pm, a frequency of 24 kHz, a spring constant of 2000 N/m and a Q-factor of 33000. The qPlus® quartz tuning fork has a tungsten STM tip that allows for both STM and nc-AFM measurements.

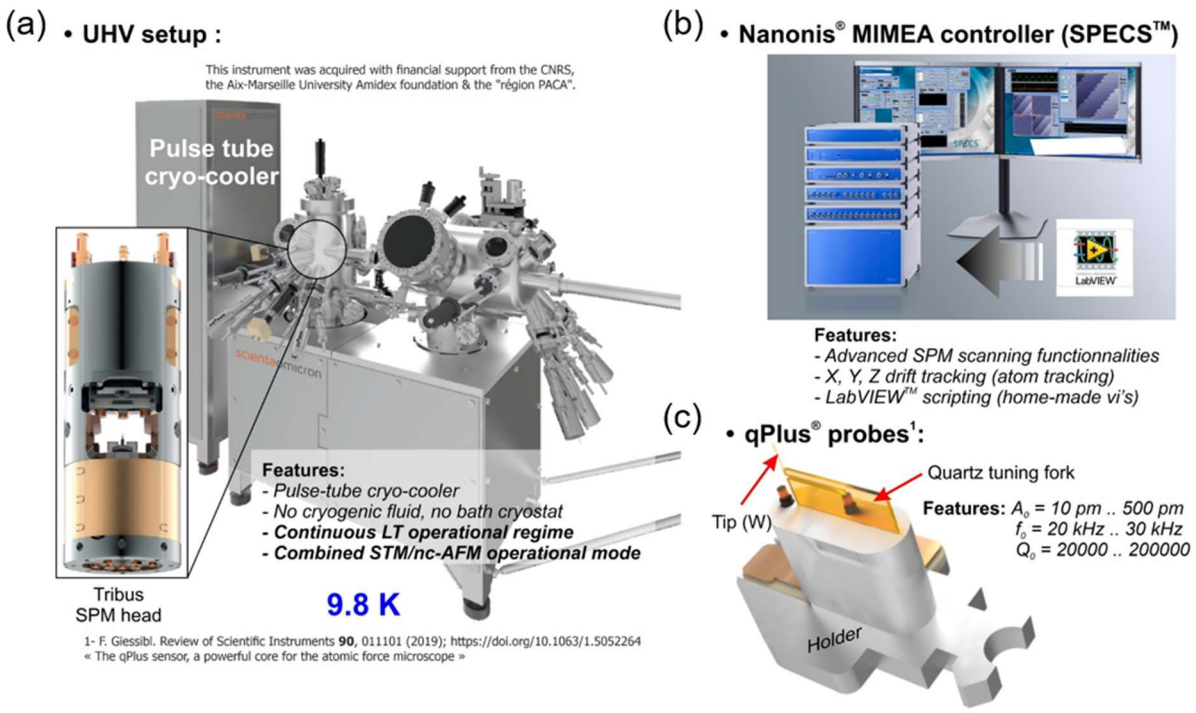


Figure 27: ***(a)*** *The Scienta Omicron© Infinity SPM. It is a pulse tube cooler based on continuous low-temperature SPM (9.8 K), its operational modes combine STM and nc-AFM.* ***(b)*** *The Nanonis® Mimea SPM control system, equipped with atom tracking, drift and tilt control with the possibility to customize applications in LabVIEW™.* ***(c)*** *qPlus® probes, consisting of a quartz tuning fork with a tungsten tip.*

It has a similar preparation chamber and Kentax molecular evaporator as the ones of the LT-STM at CINaM. The images were treated with the free software Gwyddion.[80] The control electronics of the instrument, particularly the Phase-Locked Loop (PLL) which ensures the detection of the frequency f, are key components of the acquisition chain in nc-AFM. The Nanonis® controller (Figure 27(b)) system offers programmable scripts under LabVIEW™, which allows to do precise spectroscopic measurements as well as atom tracking for drift compensation.

The STS maps done in this thesis work were generated on the bare surface of Gr/SiC sample and on molecules deposited on Gr/SiC.

Results presented in Chapter VI, including high resolution images of graphene and spectroscopies as well as spectroscopy maps from Chapter III and Chapter VI have been recorded on this instrument with the collaboration of Dr. Laurent Nony and coworkers.

III. Structural and electrical properties of the substrates

In the context of on-surface molecular assembly, we direct our attention to 2 significant surfaces, HOPG and epitaxial graphene (EG) grown on 4H-SiC(0001) (Gr/SiC(0001)).

HOPG, a synthetic form of graphite, provides an atomically flat and chemically inert surface ideal for the study of molecular adsorption and self-assembly. Similarly, graphene, with its 2D honeycomb lattice of carbon atoms, serves as a platform to explore the intermolecular interactions and molecular arrangements on a 2D surface. Graphene features massless Dirac fermions as charge carriers, enabling high conductivity and unique electronic behavior. It's linear band structure (derivation in Appendix A) intersects at the Dirac point (K points), where the conduction and valence bands meet (illustrated in Figure 37), resulting in its characteristic semi-metallic properties and electron transport governed by relativistic quantum mechanics.[29]

III.1. Substrates preparation

The HOPG substrate is prepared by scotch tape mechanical cleaving in air, followed by annealing at 400 °C for 1 h under UHV. The Gr/SiC(0001) substrate preparation is done by annealing under UHV at 400 °C for 1 h prior to imaging. The 2 substrates mounted on the sample holders are shown in the Figure 28.

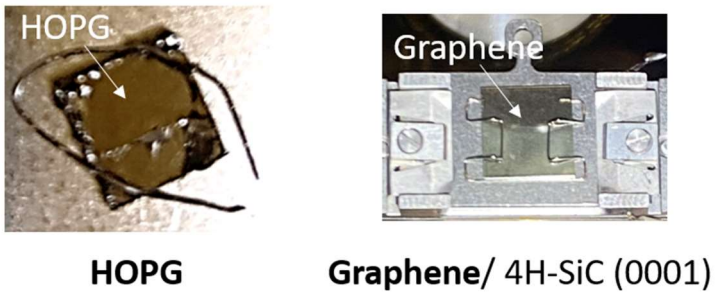


Figure 28: Photographs of the HOPG and Gr/SiC(0001) samples mounted on the Scienta Omicron© sample holders.

III.2. Highly Oriented Pyrolytic Graphite

HOPG surface served as a benchmark substrate of the investigation of self-assembled molecular networks studied by STM.[81–87] HOPG is an sp^2 allotrope of carbon atoms composed of stacked planes of graphene. Each one of these graphene planes consists of carbon atoms arranged in a 2D hexagonal crystal lattice shown in Figure 29(a). Within a single plane of graphene, each carbon atom forms strong covalent bonds with 3 neighboring carbon atoms, creating a robust structure with a C-C bond length of 1.42 Å. The adjacent planes are spaced by 3.35 Å and stabilized by vdW interactions that complement the strong covalent bonds within the planes.[88]

The difference between graphite and HOPG is that the latter is a pyrolytic graphite material having a high degree of preferred crystallographic orientation of the c-axes perpendicular to the surface of the substrate and an angular spread between the graphite sheets measuring less than 1°.[89] This attests to the high-quality crystallinity of the material.

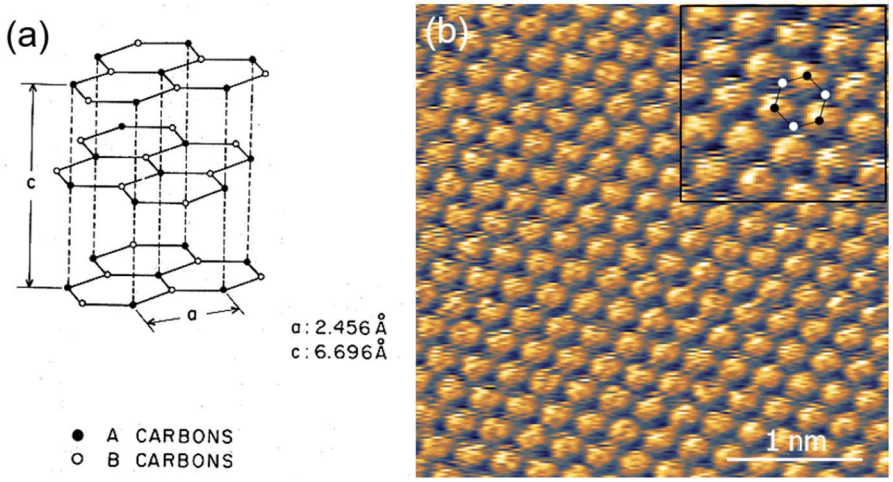


Figure 29: ***(a)*** *The 3D atomic structure of HOPG. 'a' represents the distance between neighboring A-type carbon atoms and 'c' is the distance between 3 consecutive graphene planes. Adapted from earlier work.[88]* ***(b)*** *STM image showing HOPG's atomic resolution. In inset a zoom in with the superimposed hexagon illustrating the location of B-type (black circles) and A-type (white circle) carbon atoms on HOPG. Tunneling conditions: I_t= 6 pA, V_{bias}= 0.8 V.*

In HOPG, the stacking sequence between the graphene planes is the 'AB' or 'Bernal' structure. This structure consists of carbon atoms planes each forming a hexagonal network. These planes are stacked such that half of the carbon atoms (A-type atoms) in one plane are positioned directly above one another in adjacent planes, while the other half (B-type atoms) are situated above the center of a hexagon in the adjacent plane.[88]

This stacking is of significance for the interpretation of the STM images of this material. The sites of B-type atoms have an increased electronic density near the Fermi level which causes them to appear as bright spots. Meanwhile A-type atom sites appear as dark spots since some of their electron density is shared with the underlying carbon atoms.[90]

The A- and B-type carbon atoms that constitute graphene are represented in the inset of Figure 29(b).

III.3. Graphene

III.3.1. Overview on graphene's structural and electronic properties

III.3.1.1. Structural properties of the graphene lattice

The atomic structure of a graphene monolayer (MLG) is shown in Figure 30(a, b). This 2D material is a hexagonal lattice comprising 2 C atoms per unit cell (A-type and B-type C atoms). MLG example is shown in the Figure 30(a), A-type carbons are represented by yellow circles, while B-type carbon atoms are represented by blue circles.

This atom arrangement gives rise to carbon atoms tightly bound in a hexagonal honeycomb lattice with a molecular bond length of 1.42 Å. Each carbon atom has 4 outer-shell electrons, from which 3 are in the sp^2 hybridization state, forming the strong σ-(in-plane) covalent bonds. The fourth electron occupies the p_z orbital which is perpendicular to the crystal plane, whose lateral overlap forms π-bonds.

Many-layer graphene sheets stack in Bernal stacking, as an example, bilayer graphene (BLG) is illustrated in Figure 30(b). The many-layer stacking forms graphite with an interplanar spacing of 3.35 Å. Overall, graphene's hexagonal lattice can be viewed as 2 interleaving triangular lattices with a lattice constant 'a' of 2.46 Å.

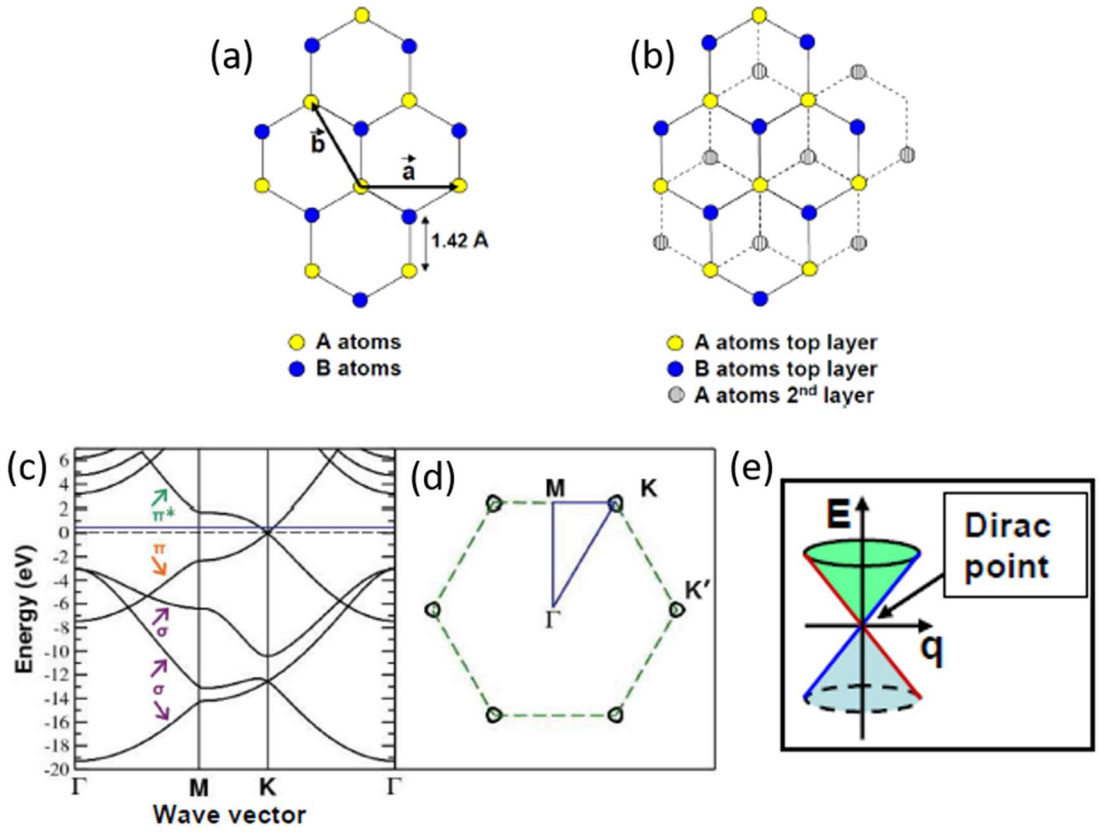


Figure 30: ***(a)*** *Schematic top view of the atomic structure of MLG highlighting the 2 atomic sublattices (A-type and B-type).* ***(b)*** *Top view of the atomic structure of bilayer graphene (BLG) with Bernal stacking.* ***(c)*** *Band structure of MLG obtained from ab-initio calculations. The nature of the bands (σ or π) is indicated.* ***(d)*** *The first Brillouin zone (BZ) of graphene in green dashed lines.* ***(e)*** *Visual representation of the 'Dirac cones' representing the low-energy band structure of graphene close to the K (K') points of the BZ. Adapted from reference.*[91]

III.3.1.2. Electronic band structure of graphene

Graphene's hexagonal lattice has been used to calculate its band structure using a tight-binding approximation obtained from ab initio calculations. The resulting band structure of graphene is presented in Figure 30(c),[92] plotted along specific directions within the 2D Brillouin zone (BZ) depicted in Figure 30(d).

The band structure in Figure 30(c) shows a set of 3 σ bands located rather far in energy (more than 3 eV) below the Fermi level. The low energy electronic states are dominated by the electronic states associated with the π (bonding) and π* (anti-bonding) bands. These bands play a crucial role in the electronic properties of graphene near the Fermi level as they form cones at the K and K' points of the BZ. Around these specific points, the π and π* bands have a linear and isotropic dispersion that looks like a cone rather than a valley. This linear dispersion leads to a unique behavior in graphene, where charge carriers behave like massless Dirac fermions moving at a constant speed regardless of their energy. Thus, this structure is called the Dirac cone and the K and K' points are

referred to as the Dirac points. A sketch of the low-energy band structure E(q), with q being a wavevector measured from or near the Dirac points, is shown in Figure 30(e).

III.3.2. Growth of EG on 4H-SiC(0001)

In 4H-silicon carbide (4H-SiC) the crystal structure is characterized by each silicon 'Si' or carbon 'C' atom forming covalent bonds with 4 nearest neighboring C or Si atoms, respectively, arranged in tetrahedral coordination.

In the nomenclature, the number '4' denotes the number of Si-C bilayers per unit cell and 'H' denotes the hexagonal symmetry. In this case, each bilayer (BL) comprises a plane of C atoms and a plane of Si atoms, with an equal number of atoms.

It is noteworthy that the experiments in this Thesis have been done on a substrate with graphene grown on the outward Si face denoted SiC(0001).

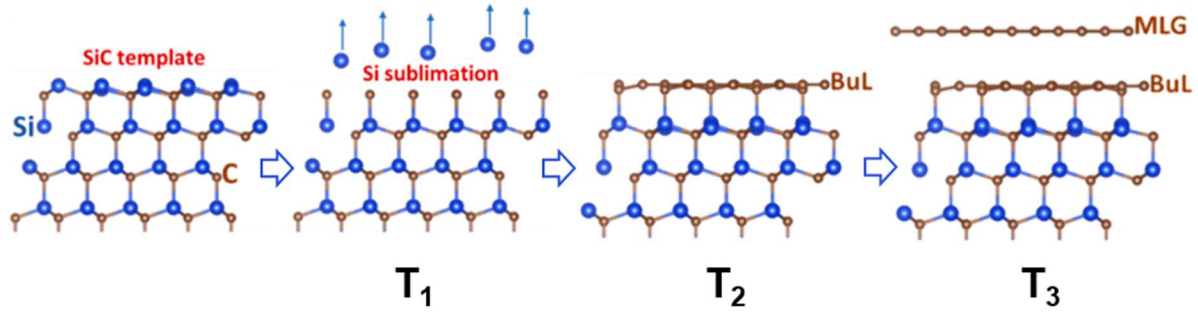


Figure 31: Epitaxial synthesis of MLG. T_1, T_2 and T_3 represent increasing temperature plateau with $T_1 < T_2 < T_3$. Heating a SiC template at temperature T_1 exceeding 1200°C, Si atoms (in blue) start to preferentially sublimate from the SiC, a C-rich layer (C atoms in brown), the inhomogeneous buffer layer (BuL) reconstructs first and gets enriched with carbon atoms until it evolves into a MLG at a temperature T_3. Schematic adapted from earlier work.[93]

The Figure 31 shows a schematic of the MLG surface synthesis resulting from the annealing of a SiC template under a flux of hydrogen under UHV conditions. This template undergoes a $\left(6\sqrt{3} \times 6\sqrt{3}\right)$R30° reconstruction (schematic shown in Figure 33) which is the first stage of graphitization. After heating at temperatures T_1 exceeding 1200°C, silicon atoms start to preferentially sublimate from the SiC surface, producing a first reconstructed C-rich layer, called the buffer layer (BuL). The BuL is inhomogeneous and interacts weakly with the SiC surface by vdW forces.

As the heating continues (the temperature reaches T_2), the carbon layer is further enriched and there is a breaking of the bonds between the C atoms of the BuL and the SiC. This BuL will evolve in a MLG chemically decoupled from the substrate while another BuL is forming underneath it, leading to an epitaxial growth of graphene. If the heating is continued, this BuL will lead to the formation of a new graphene ML and so on.

The graphene samples used in this work have been synthesized in the L2C laboratory in Montpellier by Dr. Périne. Landois and coworkers by following a specific protocol for

the annealing of SiC.[94] The prepared graphene samples underwent a non-uniform annealing process, resulting in areas of bilayer graphene alongside monolayer regions, leading to a surface composed of both MLG and BLG domains. The graphene sample is slightly n-doped and the Dirac energy of graphene is expected to be situated around 420 meV before the Fermi level, as detailed in section III.3.4.[95]

A 6 mm × 6 mm wafer was mounted onto Scienta Omicron© sample holders and secured using springs as shown in the Figure 28. The electrical contact between the graphene and the support is ensured by the contact surface between the springs and the graphene. It turns out that this contact resistance is sufficiently low to ensure electrical continuity between the graphene and the support. We use the term electrical continuity in the sense that this contact resistance did not influence the $I_t(V)$ and dI_t/dV tunneling spectroscopy measurements that will be shown in section III.3.4. The sample is prepared by simple degassing in the preparation chamber of the LT-STM in CINaM by annealing at 400 °C for one hour.

STM images of the surface in 2 different regions on the surface are shown in Figure 32. Figure 32(a) and Figure 32(c) show the same region at large and small scales, respectively, while Figure 32(b) and Figure 32(d) depict another region, also at large and small scales, respectively.

A bright pattern consisting of higher intensity features is apparent at the large scale in Figure 32(a) and Figure 32(b). When imaging at low bias voltage values, the honeycomb pattern is visible for MLG and a triangular structure is visible for BLG. BLG is seen in triangular or threefold symmetry because its layers arrange in AB (Bernal) stacking which distinguishes the 2 carbon atoms in the graphene unit cell (as described in III.2) resulting in a slightly different electronic structure from the one of MLG. The pattern shows a contrast with triangular symmetry due to inequivalent sublattices, meanwhile the lattice vectors remain the same as for MLG (Figure 30(a)).[91,96,97]

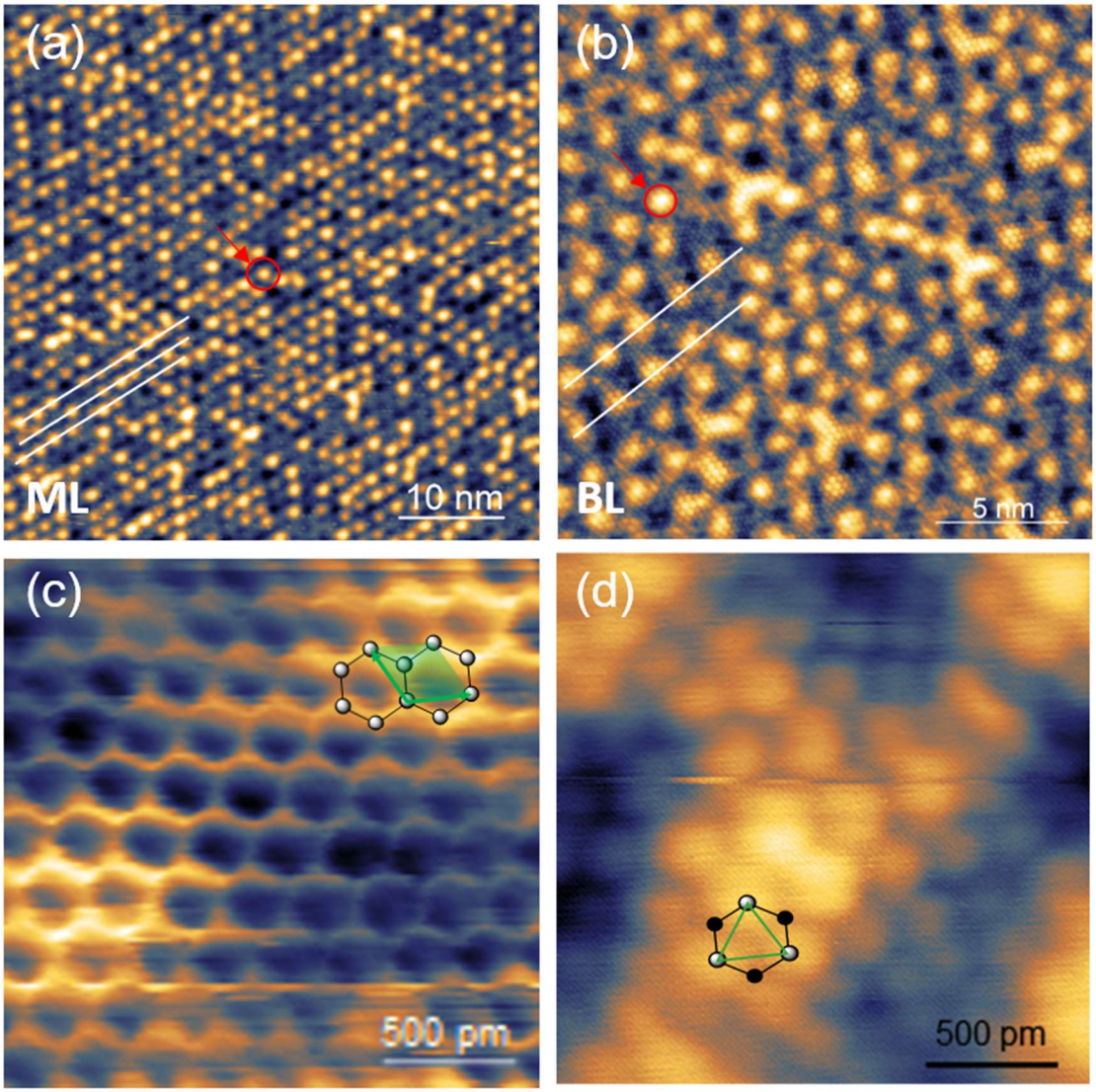


Figure 32: ***(a)*** *STM image of MLG showing bright features at the large scale with an irregular repartition that follows a preferential direction indicated by white lines. A bright feature is highlighted with a red circle and marked by an arrow on the image. Tunneling conditions:* V_{bias} *= 500 mV,* I_t *= 50 pA.* ***(b)*** *STM image of BLG of the bright features that follow a preferential direction indicated by white lines. A bright feature is highlighted with a red circle and shown with an arrow on the image. Tunneling conditions:* V_{bias} *= 480 mV,* I_t *= 10 pA.* ***(c)*** *Close-up STM image that shows the fine honeycomb structure of graphene comprising a periodic contrast of holes. Tunneling conditions:* V_{bias} *= 520 mV,* I_t *= 10 pA.* ***(d)*** *STM image showing the triangular structure of BLG comprised of a periodic contrast of bright spots. Tunneling conditions:* V_{bias} *= 480 mV,* I_t *= 10 pA.*

While imaging at a moderate bias voltage near 500 mV, irregular large bright features emerge for both MLG and BLG, highlighted with a red circle in Figure 32(a, b) respectively. Although the features are arranged in an irregular manner, a preferential direction can be distinguished and is marked by white lines on STM images of Figure 32(a, b).

The bright features find their origin in the $\left(6\sqrt{3} \times 6\sqrt{3}\right)$R30° reconstructed phase of SiC that results in a larger unit cell, specifically $6\sqrt{3} \times 6\sqrt{3}$ times larger than the original SiC unit cell.

The $6\sqrt{3}$ structure can sometimes appear like a 6×6 structure in STM images and is often described as such in the reciprocal space. In STM, (images in the real space), the lattice vectors of the $6\sqrt{3}$ structure are approximately 13 times larger than the lattice constant of SiC. This can be seen as a rotation (often about 30°).of the graphene layer as shown in Figure 33(a) with respect to SiC.[98]

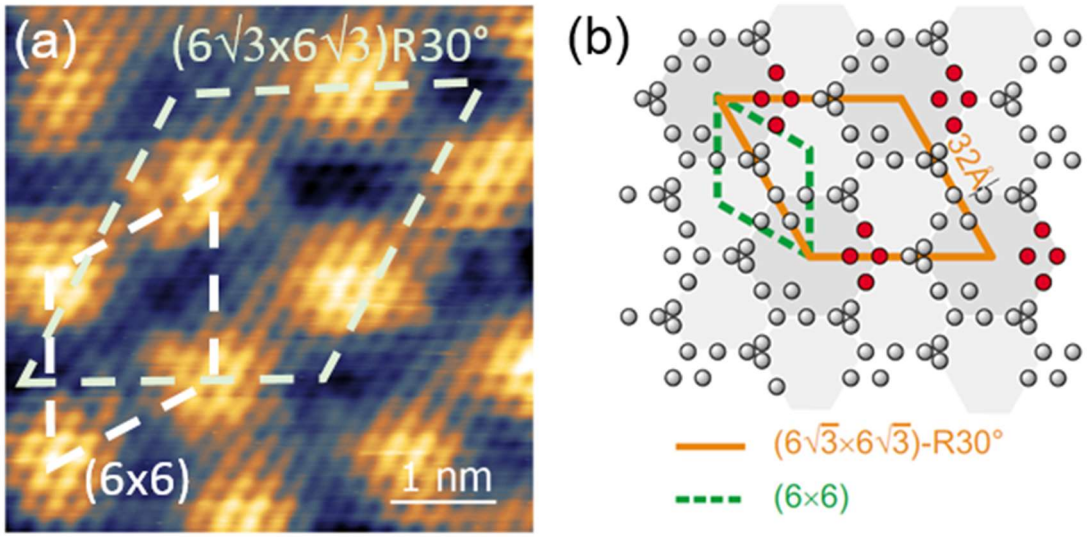


Figure 33: ***(a)*** *STM image of MLG showing the* (6×6) *and the* $(6\sqrt{3} \times 6\sqrt{3})R30°$ *periodicities. Tunneling conditions:* V_{bias} *= 500 mV,* I_t *= 10 pA.* ***(b)*** *Schematic of the arrangement of the atoms or clusters together with the corresponding unit cells dimensions for the different periodicities. Reproduced from reference.*[99]

The Figure 34(a) shows a graphene surface imaged at moderate bias voltage. The tip morphology changes during the scanning in the upward direction and reveals remarkably well the structure of the BuL underneath MLG as shown in the inset of Figure 34(a). Neighboring MLG and BLG imaged with this tip morphology at moderate bias voltages are shown in Figure 34(b) having a step height of 80 pm, a bias dependent value for STM measurements but still in agreement with the literature.[96] The underlying BuL shows a greater roughness than the over the BLG region.

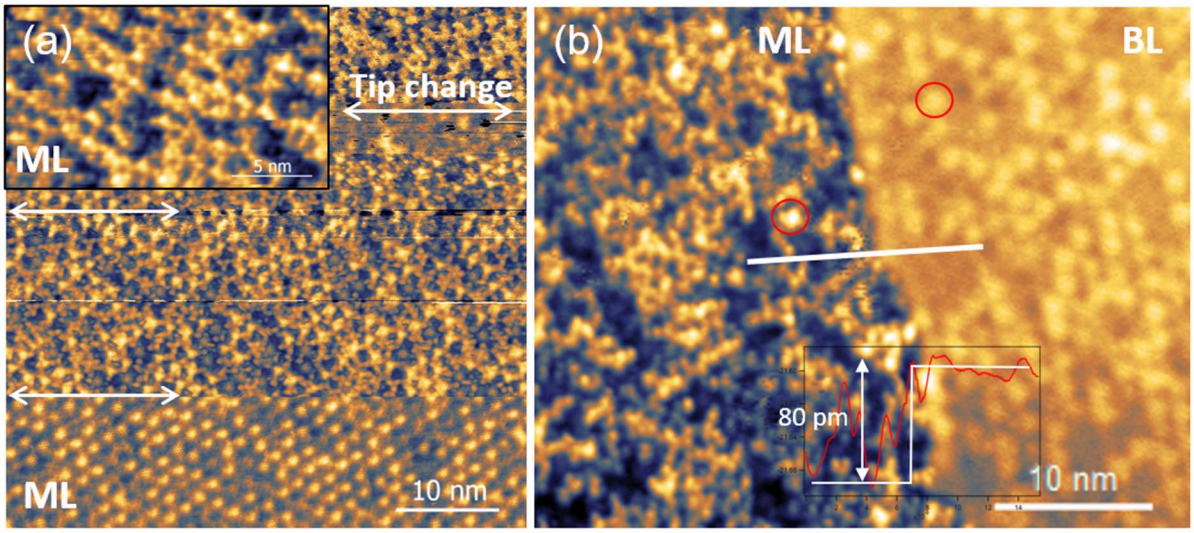


Figure 34: ***(a)*** *STM image of MLG. The tip encounters change during the scan in the upward direction which reveals the BuL structure underneath graphene. The structure of the BuL is shown in the inset. Tunneling conditions:* V_{bias} *= 500 mV,* I_t *= 10 pA.* ***(b)*** *STM image of the boundary of neighboring MLG and BLG. The line profile across the MLG and BLG regions is shown in inset. A bright feature on each layer is highlighted by a red circle. Tunneling conditions:* V_{bias} *= 170 mV,* I_t *= 10 pA. Inset:* V_{bias} *= 390 mV,* I_t *= 10 pA.*

The BuL features appear as different elementary structures, some structures recurring more frequently than others. The most frequent structures are trimer and tetramer features (outlined in Figure 35(a)) as reported in the literature.[100,101] The trimers are oriented and dispersed in different ways on the surface which is likely due to the non-stoichiometric surface carbon segregation which induces disorder during the annealing process. This disordered state is then frozen and stabilized in this condition when the annealing is stopped.

The features in Figure 35(a) are similar to Si adatom structures of the reconstruction of bare Si and SiC surfaces. These features are located below the raised regions of the graphene surface layer and can become transparent under certain imaging conditions.[99]

When imaged from underneath the graphene layer as shown in Figure 35(c, d, e) the tetramer-like features appear as one object, but with the tip closer to the interface the trimer structure can be distinguished as having a transparent adatom in the middle. It appears that this BuL interface is very heterogeneous, and this heterogeneity finds its origin in the nature of the bonds between the atoms of the BuL and SiC, alongside to the amount of segregated carbon atoms as the carbon layer grows denser. When the sublimation process is stopped, we are left with an uncertainty regarding the stage of the growth process, and these bonds find their origin in the dynamic nature of the growing BuL.

A set of STM images in the Figure 35 shows successive STM images of MLG under a slight variation of the bias voltage. The scan direction is indicated by an arrow on the left side of each figure.

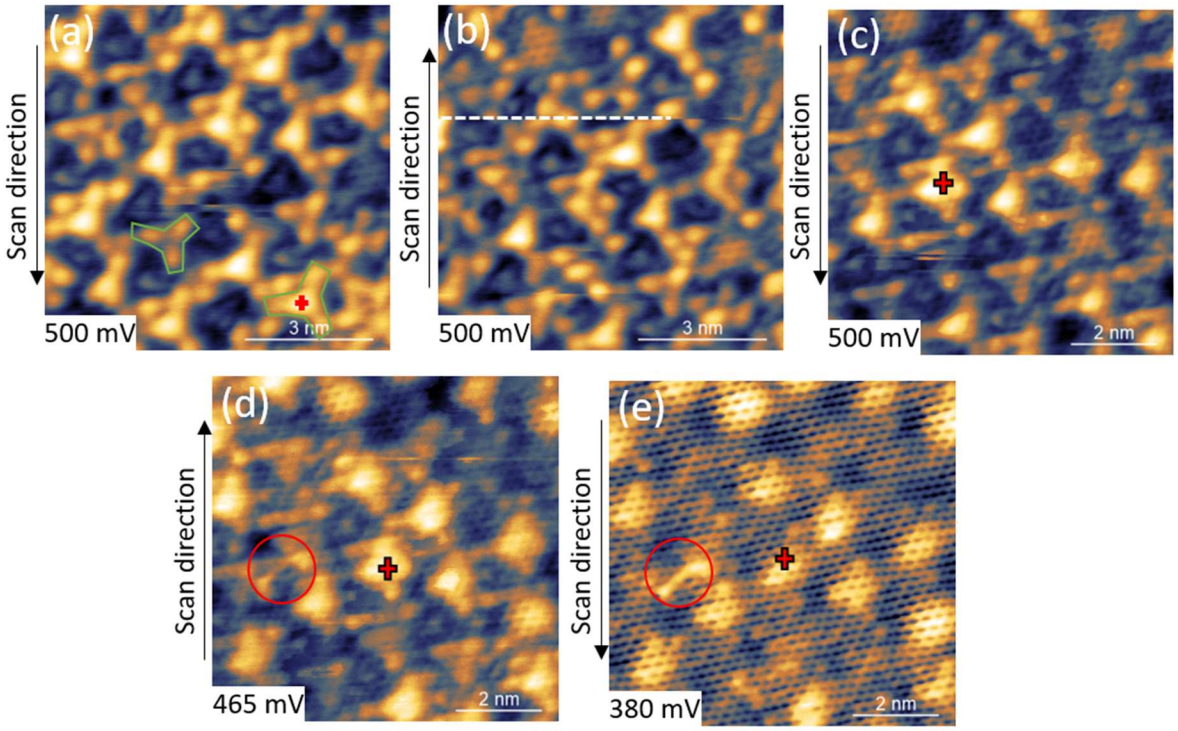


Figure 35: ***STM images of the buffer layer with a varying bias voltage****.* ***(a, b, c)*** *The bright features of the BuL are clearly visible and marked by a plus-shaped red cross. Tunneling conditions:* V_{bias} *= 500 mV,* I_t *= 25 pA.* ***(d)*** *As the bias voltage is decreased, the graphene honeycomb starts to become more visible above the bright features. Tunneling conditions:* V_{bias} *= 465 mV,* I_t *= 25 pA.* ***(e)*** *The honeycomb lattice is clearly visible at this bias voltage.* V_{bias} *= 380 mV,* I_t *= 25 pA.*

Figure 35(a) shows the BuL trimer features delineated in green and tetramer-like features as a trimer with an adsorbate on top, marked by a red cross. While scanning in the upward direction (Figure 35(b)), the tip morphology changes at the white dashed line position and reveals the fine honeycomb lattice situated on top of the BuL which is fully revealed after another scan down in Figure 35(c). The bias voltage is slowly and gradually decreased to 465 mV (see Figure 35(d)) where the bright features become increasingly blurry and the honeycomb lattice slightly more visible.

The Figure 35(e) scanned at a slightly lower bias voltage of 380 mV clearly shows the graphene honeycombs and the BuL features appear more blurred. This set of STM images permits to discern the features of the BuL at a closer-scale, a trimer feature is most prominent on the surface, yet it has random repartition and orientation due to the uncertainty regarding the sublimation process step.

The progressive imaging of graphene over this layer gives information about the layer order and the origin of the bright blurred spots underneath the graphene layer that were previously confused to be a Moiré effect.[102]

The BuL has proven to be heterogeneous (bright irregular features), but still presents some degree of periodicity following the 6 × 6 reconstruction spots visible on the STM images (Figure 33(a)). These bright features primarily consist of trimers and tetramers

and could affect the electronic properties of graphene leading to partial coupling between the layers and hence a change in graphene electronic properties.

A literature review on graphene's electronic properties and their measurement by scanning tunneling spectroscopy will be presented in the following subsection.

III.3.3. Literature overview: STS on Gr/SiC

STS is used to probe the local electronic properties of graphene grown over many substrates. An early STS study conducted in 2008 by Crommie M. et al.[103] on Gr/SiO_2 shows the presence of 2 specific features that are also found in the following publications regarding STS on graphene. First, the differential conductance spectrum shows the expected V-shaped density of states (DOS) (linear behavior). They found that the position of the Dirac point shifts relative to the Fermi level depending on the doping of graphene.

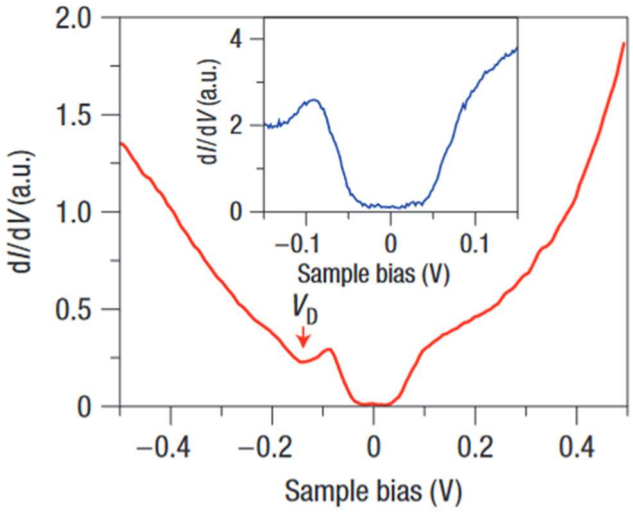


Figure 36: dI/dV spectrum of graphene on SiO_2. The spectrum was acquired at a nominal junction impedance of 5 GΩ (0.5 V, 100 pA). The gap width and the adjacent conductance minimum location (at V_D) were not sensitive to STM tip height over an impedance range of 1–100 GΩ. Inset: A high-resolution dI/dV spectrum emphasizing the central gap-like feature. Reproduced from reference.[103]

Second, they observed the presence of an unexpected ~130 meV pseudogap centered around zero bias. In this publication, the authors give an explanation for the appearance of this pseudogap, which was previously observed but its origin was not elucidated.[104]

To understand the origin of this pseudogap, we have to keep in mind the following concepts:

i. During tunneling transitions between tip and sample states, the conservation of the electronic momentum 'k' is imposed by selection rules.
ii. Electrons with maximum k_z momentum, where 'z' is the direction of tunneling, mainly contribute to the tunneling current.
iii. The probability to elastically tunnel in a surface state depends exponentially on the spatial extension of this state in the z direction (equation II. 6).

However, at graphene's Fermi level, the first empty states are located at the high symmetry K and K′ points, the Dirac point, that is to say, for wave vector components $k_z=0$ ($K=k_{\parallel}$ only) where $k_{||}$ is the in-plane wave vector component.

Even though this electronic state intersects the Fermi level, it is hardly accessible via a tunneling current because of the selection rules on the momentum and because such states tend to decay rapidly in the vacuum region above a surface, their evanescent local density of states (LDOS) is expected to vary as:[103]

$$\mathrm{LDOS}\left(z, k_{||}\right) \propto e^{-\frac{z}{\lambda}}, \lambda^{-1} = \sqrt{\frac{2m\Phi}{\hbar^2} + k_{||}^2} \qquad (3.26)$$

Φ represents the work function, m the electron mass, λ the decay length and $\hbar$ the reduced Planck constant.

The enumerated concepts above contribute to strongly reduce the elastic tunneling at the K point. However, there is a mechanism that implies an electron-phonon interaction which allows the electrons to move to surface states close to the Fermi level. This mechanism has been highlighted for the first time in this publication[103] by analyzing the temperature and tip-sample separation dependence of the tunneling conductance. Using this mechanism, the authors could explain the presence and the size of the pseudogap.

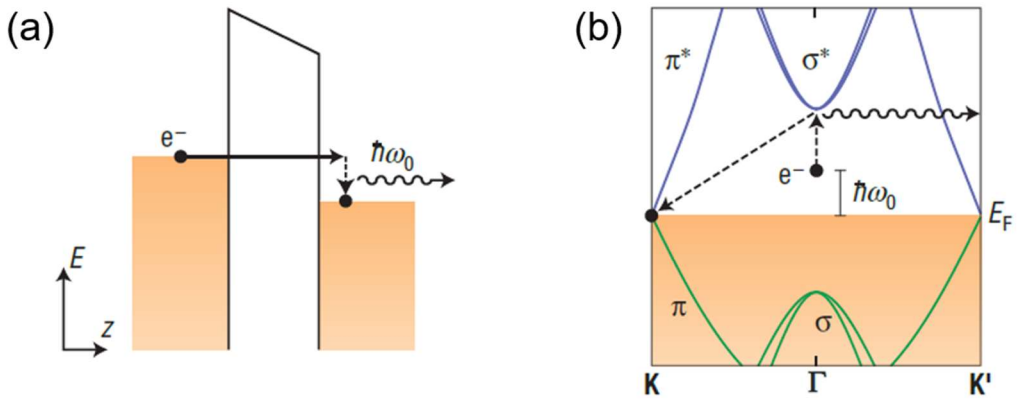


*Figure 37: **(a)** Inelastic electron tunneling due to excitation with energy $\hbar w_0$. **(b)** Wave-vector-dependent inelastic tunneling mechanism involving graphene phonon modes near the K point in the reciprocal space. Adapted from earlier work.[103]*

In their work, the authors show that for an electron to tunnel into the Dirac point (located at the K points), it requires additional momentum, which can be delivered by a phonon excitation. In this mechanism, only the electrons that are provided the threshold energy $\hbar w_0$ (with w_0 the angular frequency of the out-of-plane phonon) can tunnel into the graphene σ^* band (located near the Γ point, as shown in Figure 37(b)). One might

wonder how an electron with approximately 65 meV energy can tunnel to graphene σ^* band, which are located beyond 2 eV. However, this can be explained through a virtual transition, which follows the energy-time uncertainty principle of Heisenberg (illustrated by a dashed arrow in Figure 37(b)). This principle allows the low-energy tunneling electron to explore higher energy states for a very short time. When the electron virtually reaches this state, it has the opportunity to interact with the out-of-plane phonon, exchanging energy and momentum with it. The electron then transitions or tunnels inelastically into an available K point state on the π band through the emission of a K′ point out-of-plane phonon to conserve crystal momentum and energy.

Therefore, above a certain threshold voltage corresponding to the energy of an out-of-plane graphene phonon, an electron-phonon interaction can occur and an inelastic tunneling channel is opened. The out-of-plane acoustical phonon has an energy of about 65 meV which explains the size of the pseudogap. Below this energy, no electron-phonon interactions are possible and the probability for the electron to tunnel in a surface state with only $k_{\parallel}$ momentum is extremely weak. The consequence of this mechanism is that all the tunneling current measured on this substrate originates from inelastic processes.

However, this argument fails to apply to atomically sharp tips. The tip radius R influences the spatial distribution and momentum spread of the tunneling electrons. For example, a sharper tip (smaller R) would mean a broader range of momenta available for tunneling, according to the uncertainty principle, and thus elastic access to the K points will become possible ($\Delta k \sim \hbar/R$). Actually, only one measurements report on graphene on graphite was found where they did not observe a pseudogap, but instead, a linearly increasing conductance away from the Dirac point.[105] In our experiments, we observed variations in the size of the pseudogap depending on the apex of the tip, but never observed its complete absence. The experiment described by the group of Crommie[103] was conducted on Gr/SiO_2. However, other groups working routinely on Gr/SiC(0001)[101] and Gr/SiC($000\bar{1}$)[106,107] observed exactly the same 2 features (shift in the energy of the Dirac point with doping and the presence of a pseudogap). Besides this, other researchers observed a pseudogap at low currents (below 100 pA) that closes at higher currents.[108,109]

Therefore, it is likely that details of the tip-sample geometry can affect the size of the pseudogap at the Dirac energy. These experiments showed that Gr/SiC preserves the intrinsic electronic properties of graphene. The unexpected presence of this pseudogap is related to the measurement technique, in this case the STM, which remains highly sensitive to the momentum of the electronic states in the z direction.

Other measurements, notably in Raman spectroscopy on graphene substrates shows that graphene preserves its electronic properties when synthesized from an SiC substrate.[94]

III.3.4. Single-point STS measurements on graphene

In this thesis, the STS of Gr/SiC(0001) sample was measured on both on the LT-STM of the CINaM lab and the closed-cycle SPM of the IM2NP lab presented in II.4. The results we got were similar on both microscopes, but on the closed-cycle SPM, the sensitivity and the signal-to-noise ratio are enhanced, reason why, we will only present the STS data obtained on the closed-cycle SPM in this manuscript.

Figure 38 shows a single-point STS on Gr/SiC in the energy range [- 0.10 eV, 0.17 eV]. The $I_t(V_{bias})$ spectroscopy is shown in Figure 38(a) and the differential conductivity dI_t/dV is shown in Figure 38(b). The demodulated signal for this spectroscopy is the current, and the lock-in parameters were set to 523 Hz for the frequency, 4 mV for the amplitude. The duration of a V_{bias} step is 505 milliseconds and the total time taken for this 512 pixels' spectroscopy was 34 seconds. The differential conductivity spectrum of Figure 38(b) reveals the presence of a pseudogap of about 50 meV around the Fermi level with an enhancement of the conductance at higher energies (a peak in the conductance is observed around 0.10 eV). This pseudogap varies between 50 mV and 100 mV depending on the apex of the tip and is in accordance with the previously published results.[103,104]

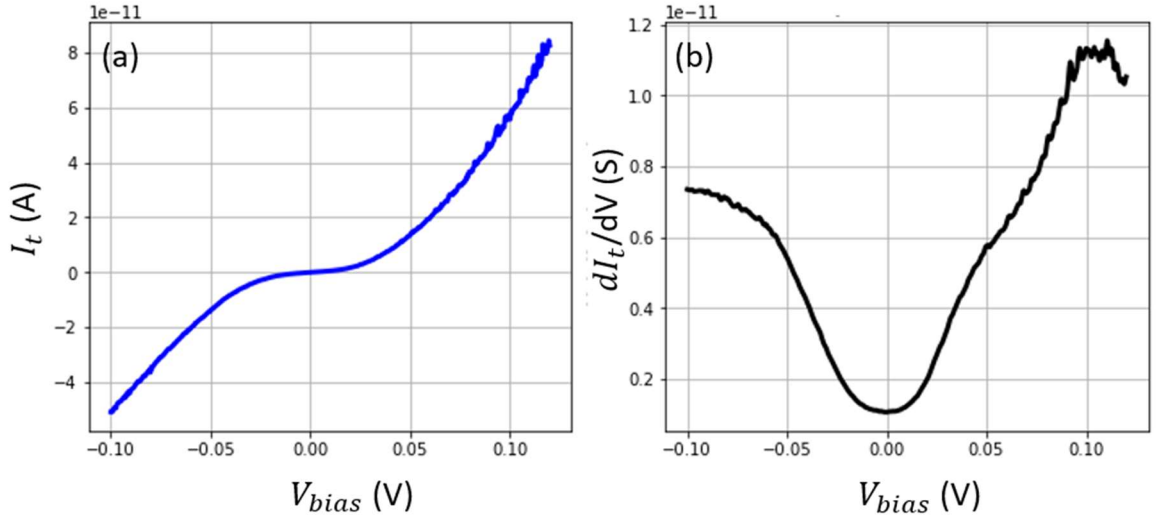


*Figure 38: **(a)** $I_t(V_{bias})$ spectroscopy of a single point on graphene. **(b)** dI_t/dV (V_{bias}) spectrum of a single point on graphene obtained by lock-in technique. Lock-in parameters: V_{mod}= 4 mV, F_{mod}= 523 Hz. Tunneling conditions: V_{bias}= 280 mV, I_t= 87 pA. Stabilization parameters: V_{bias}= 280 mV, I_t= 49 pA.*

To ensure the quality of the tip used in experiments, the tip is prepared on Au(111) surface. The tip quality was checked topographically by an STM image after the tip preparation, where the characteristic herringbone reconstruction of Au(111) is seen as shown in the STM image in the inset of Figure 39. A sharp tip accurately resolves this reconstruction and reveals the arrangement of the surface atoms as well as its atomic and subtle features.

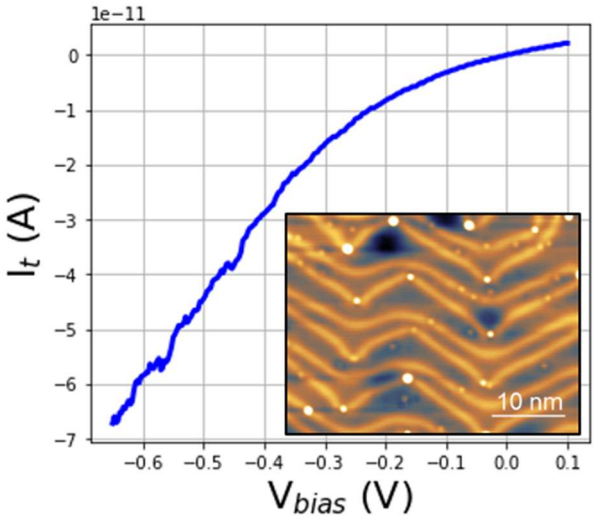


Figure 39: Tunneling spectroscopy performed on clean Au(111). The inset shows an STM image of a clean Au(111) surface.

Following the validation of the sharpness of the tip through the analysis of the morphology of the Au(111) surface, the tip was retracted and the graphene sample was transferred to the STM chamber. After 2 hours of cooling, the sample temperature reached 9.8 K and then STM and STS measurements of the Figure 40 were directly performed on the graphene sample after tip approach.

We must clarify that the lifetime of a clean, gold-coated tip on graphene is generally less than 20 minutes. Therefore, the tip was not prepared on Au prior to all the spectroscopic measurements presented in this manuscript, however, it was prepared on Au for the measurements shown in Figure 40.

The differential conductivity curve shown in Figure 40(b) has a minimum around – 420 meV which could correspond to the Dirac energy. Due to the charge transfer from the SiC substrate, the epitaxial graphene on SiC(0001) is electron doped (n-type) with, in this case, the Fermi energy located at 420 meV above the Dirac energy.[95]

The STM image in Figure 40(c), acquired after performing the spectroscopy, shows the rounded trimer and tetramer features of the underlying BuL confirming the sharpness of the tip.

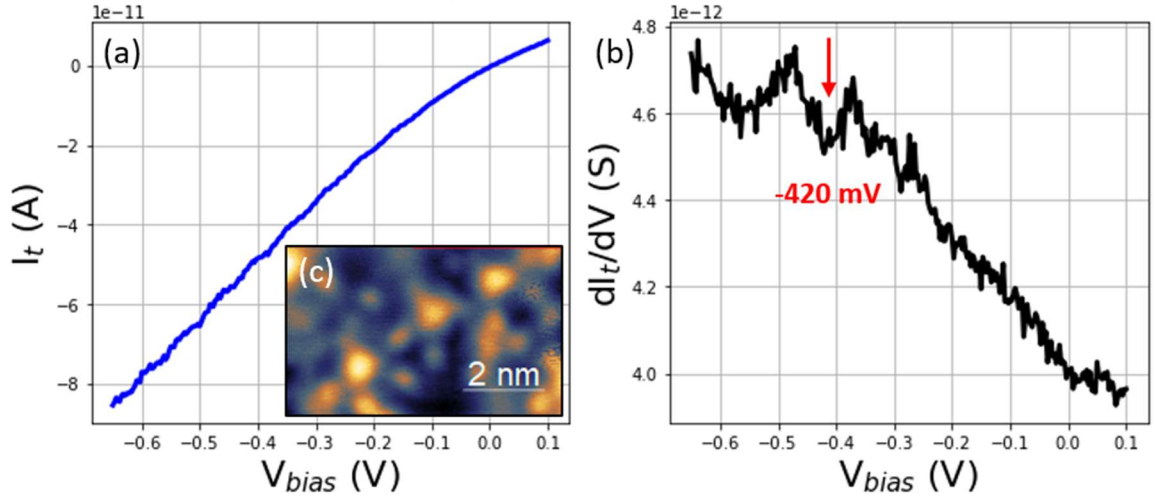


Figure 40: ***(a)*** *$I_t(V_{bias})$ spectroscopy of a single point on graphene in the bias voltage range [-100 mV, -650 mV].* ***(b)*** *dI_t/dV spectrum of a single point on graphene obtained by the lock-in technique. Lock-in parameters: V_{mod}= 20 mV, F_{mod}= 408 Hz. Tunneling conditions: V_{bias}= -760 mV, I_t= 15 pA. Stabilization parameters: V_{bias}= -100 mV, I_t= 15 pA.*

Experimental parameters such as the offset distance between the tip and the sample significantly influence the tunneling current and the electronic states probed in STS. Therefore, in the following section, we explore how variations in tip-sample distance and modulation amplitude affect the resulting STS spectra, providing insights into this dependence on experimental parameters.

III.3.5. Influence of the tip-sample distance and of the modulation amplitude on the STS spectra.

In order to optimize the parameters Z_{offset} and bias modulation V_{mod} of the STS spectra we conduct a preliminary study of the dependence of these parameters on the spectra. The tunneling conductance variation is measured with respect to the tip-sample distance at the same (x, y) point while varying Z_{offset} value. This Z_{offset} value is an additional distance applied to the tip sample-distance after the feedback loop is turned-off and before the STS is recorded. After a few milliseconds of tip stabilization at the spectroscopy conditions of current setpoint I_t= 87 pA and V_{bias}= 120 mV, with the V_{mod} value applied, the feedback loop is turned off. Next, a Z_{offset} is applied and the V_{bias} value is swept from 120 mV to – 100 mV, while recording the current response.

Each spectroscopy of Figure 41 is recorded at the same (x, y) position on the surface with same parameters except for the Z_{offset} (the variable Z_{offset} values are annotated in the Figure 41(a) alongside their corresponding STS curves).

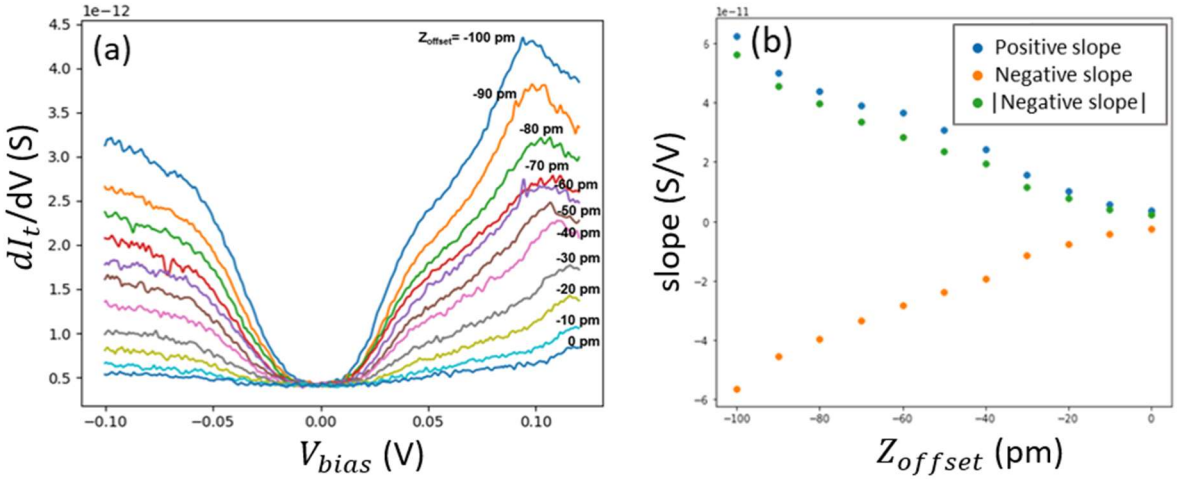


Figure 41: ***(a)*** *Differential conductance dI_t/dV as a function of the bias voltage V_{bias} in the range [120 mV, - 100 mV] for various tip-to-sample distances Z_{offset}. More negative values of Z_{offset} indicate a tip closer to the sample while values approaching zero indicate a tip further away. Lock-in parameters: V_{mod}= 4 mV, F_{mod}= 523 Hz. Stabilization parameters: V_{bias}= 280 mV, I_t= 87 pA.* ***(b)*** *Slope extracted from the linear fitting of the conductance vs Z_{offset}: each dotted point represents the slope at a specific Z_{offset} (color code: blue for the slopes of the curves in the positive bias region, orange for the slopes in the negative bias region and green the absolute values of the slopes from the negative bias region.*

All the STS curves of Figure 41(a) present approximately the same characteristic: a pseudogap presenting a linear dependence of the signal on both sides. The value for the differential conductance decreases exponentially as the tip-sample distance increase.

The tip in closer proximity to the surface allows for a better resolution in probing the electronic structure of graphene, and thus features in the dI_t/dV spectrum are more pronounced such as the sharp peak around 100 meV or the pseudogap at the Fermi energy. To examine the influence of the Z_{offset} on the shape of the spectra, the slope of the linear part of these dI_t/dV curves was extracted. This linear part is located between ~23 mV to 40 mV (Figure 41(b)). The slopes of the dI_t/dV curve were extracted and plotted with respect to the Z_{offset} values. The decrease in the slope with Z_{offset} reflects the decreasing tunneling probability with the increasing distance.

We conducted a second investigation to explore how the tunneling conductance dI_t/dV varies with the amplitude of the applied bias modulation V_0 of the lock-in. For V_{mod} values between 4 mV and 15 mV, the spectra clearly display 2 features: a shoulder around 0.05 V and a peak at 0.1 V. Below these V_{mod} values, the signal-to-noise ratio is too low to clearly distinguish them. Above these values, the integration windows for energy averaging combine the signal from the shoulder and the peak, resulting in a single broad peak. Concerning the larger pseudogap, it decreases with an increase in V_{mod}, but due to the averaging effect, its minimum shifts to positive values.

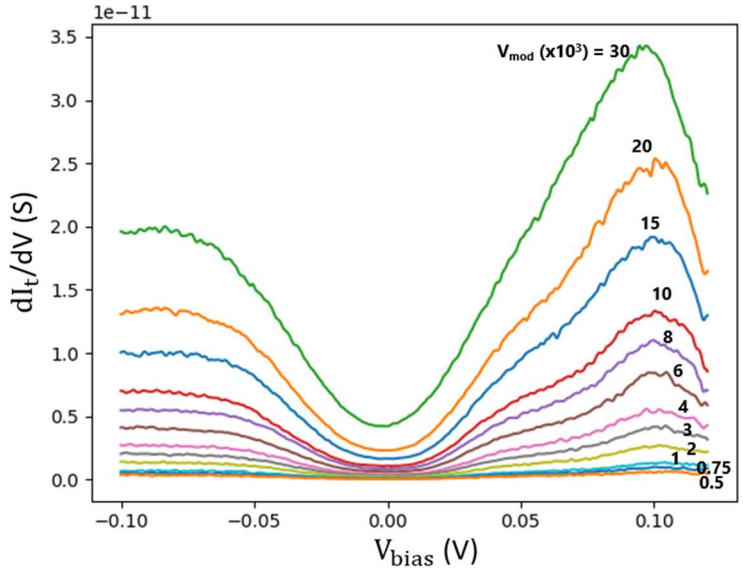


Figure 42: Differential conductance dI_t/dV (V_{bias}) for different values of the amplitude of the modulated bias voltage V_{mod}. (Modulated bias voltage unit in mV)

These examples illustrate the compromise we must consider regarding V_{mod}. A value of V_{mod} that is too low minimizes the averaging effect but also reduces the signal-to-noise ratio. On the other hand, a value that is too high can broaden the features of the spectra and hide some peaks, even if the signal is maximized, thus losing in energy resolution. For the following spectra in this manuscript, we tried to optimize these parameters before recording them.

In the following section, we shift our focus to spatially resolved STS mapping which enables us to visualize how local variations in the electronic structure are manifested across the surface.

III.3.6. Spatial mapping of spectroscopic data

The spatial mapping of spectroscopy measurements is a very demanding technical task, and several conditions must be fulfilled to acquire mappings at the intramolecular scale. A successful spectroscopic mapping that consists of a spectroscopy grid of 20 pixels × 20 pixels and many heights Z (between 5 and 17 in our experiments) requires between 2 to 3 days of acquisition depending on the number of pixels in the grid. A reason for this is that the scanning is done at low temperature for 3 days, therefore the need for a closed-cycle cryostat for the SPM.

There is a non-negligible thermal drift at the intramolecular scale, even at low temperatures which requires thermal drift correction which is done by LabVIEW™ scripting that allows for atom tracking.

In addition to these, the area of interest should present a detectable defect for successful atom tracking. And finally, the apex of the tip should be stable during the time needed for the mapping, another condition that requires working at LT.

The few times where all these criteria are fulfilled, 4D spectroscopy mappings can be obtained.

III.3.6.1. Atom tracking procedure for spectroscopy maps

The 4D spectroscopic mapping procedure consists in overlaying a square grid of predefined $N_i \times N_j \times N_k$ points of coordinates (Xg_i, Yg_j, Zg_k) on the area of interest and in performing a spectroscopic measurement at each point of the grid schematized in Figure 43(a).

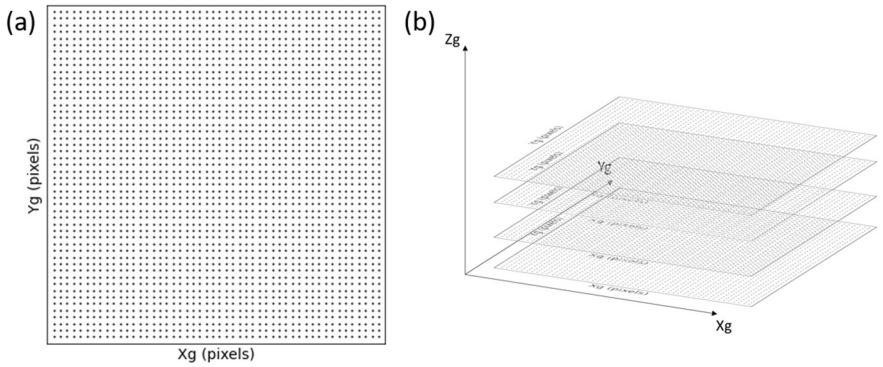


*Figure 43: **(a)** Schematic of a 2D grid of $i \times j$ pixels of coordinates (Xg_i, Yg_i). **(b)** Schematic of the different heights Zg_i of the 2D grids in one spectroscopy experiment.*

This spectroscopy grid can be done for a different number N_k of Z_{offset} from the original Z regulation setpoint (Zg_k) to obtain a 4D mapping schematized in Figure 43(b).

The first 3 dimensions are the spatial dimensions and the 4th one is the spectroscopic measurement. These maps only make sense if each map at Zg_k is acquired in the constant height mode and not in the I_t or Δf constant modes. This prevents mixing the signals originating from the surface properties with the signals originating from the height variations. In other words, the regulation loop is cut off during the mapping.

The mapping requires a lot of time, even though it is done at LT the thermal drift is still present and it is thus necessary to correct the positions (Xg, Yg) of the grid points by making use of atom tracking between each spectroscopic measurement. Figure 44(a) shows the user-defined grid points positions before atom tracking.

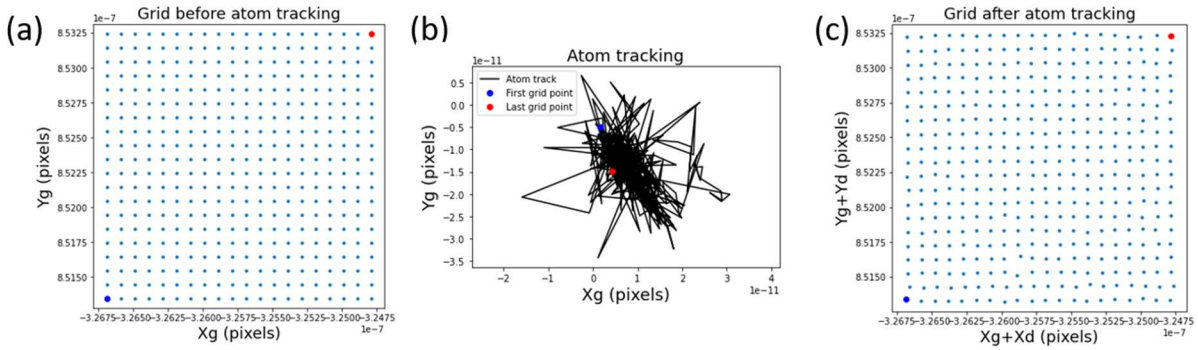


*Figure 44: **(a)** Experimental spectroscopy grid of 20 pixels × 20 pixels before the atom tracking procedure. The first grid point is highlighted in blue and the last grid point is highlighted in red. **(b)** The atom tracking path during the overall spectroscopy. The first grid point is shown by a blue dot and the last grid point is shown by a red dot. **(c)** The corrected grid spots after the atom tracking procedure. The first grid point is highlighted in blue and the last grid point is highlighted in red.*

Atom tracking is a technique implemented by Nanonis™ to locate the peak of a surface defect by the means of the tip performing concentric circles around this defect until it locates the point of maximum of the intensity. This point serves as a reference point on the surface that could be relocated regardless of the thermal drift.

In the 4D spectroscopy program, before starting a spectroscopic grid, the coordinates of the peak of the surface defect are stored as a relative reference for the drift as ($Xd_0 = 0, Yd_0 = 0, Zd_0 = 0$).

The next $i \times j \times k$ atom tracking measurements over the course of the grids will be referenced with respect to the point (0, 0, 0). The Figure 44(b) shows an example of the atom tracking points trajectory in the grid (Xg, Yg) which allows to follow the in-plane evolution of the drift.

All the spectra that make-up a map are done at the same height ($Z_{regulation}+Zg_k$) of the tip, on top of the peak of the defect and thus, fixed and corrected from the Z-drift (which can accumulate during the recording of a spectroscopy) at each atom tracking measurement.

After starting the mapping process, the successive steps for the next $i \times j \times k$ spectroscopic measurements are the following:

i. Atom tracking on the defect for around 20 seconds in order to find the peak intensity of the defect. The (Xd_i, Yd_j, Zd_k) coordinates of the defect position are stored. These coordinates are used as a reference for atom tracking.
ii. The regulation loop is stopped, the $Z_{offset}=Zg_0$ is applied to maintain a constant height Z.
iii. Displacement of the tip to the grid point of coordinates ($Xg_i + Xd_i, Yg_i + Yd_i$) corrected from the drift by atom tracking by (Xd_i, Yd_i).
iv. Spectroscopic measurement: $I(V_{bias})$, dI_t/dV_{bias} or $\Delta f(V_{bias})$ measurement (the spectroscopic mode is chosen before starting the mapping).

a. If the map is done at single height Zg_k, or $N_k = 1$, proceed to i.
b. If the map is done for many heights Zg_k, or $N_k > 1$

- Increment k by 1 (which translates to applying a Z_{offset})
- Proceed with point iv)
- When the last k value is reached, proceed to point i)

These steps ensure a drift correction across all spectra within a map, all relative to the fixed regulation point of atom tracking, which remains constant over the duration of the map. With this procedure, all the spectra at different Zg_k at the same Xg_i, Yg_j are acquired before correcting the drift and recording the spectra at the next Xg_{i+1} and Yg_j point. To provide a mental image, a full Z-rod spectroscopy is acquired at Xg_i, Yg_j, prior to applying the drift correction procedure with atom tracking, in order to save time. Since the number of Zg_k points never exceeded 17, the drift during the Z-rod acquisition was deemed negligible. The Figure 44(c) illustrates the newly acquired grid of 17 points at a single Zg with the corrected positions (Xg + Xd, Yg + Yd) by the described procedure.

III.3.6.2. STS spatial mapping

After the application of the concepts discussed in III.3.6.1, drift-corrected STS maps could be built and used complementary to the single point STS measurements.

The Figure 45(a) shows a small scale STM image of BLG with the triangular bright spots contrast visible (Bernal stacking, discussed in III.3.2). One of its associated differential conductivity maps dI/dV_{map} is shown in Figure 45(b). To obtain these maps, STS spectra were recorded at 256 points across a grid defined by X and Y covering a bias voltage range from V_{bias}= - 0.29 V to V_{bias}= 0.25 V. For each V_{bias} value, a map was generated, representing $dI/dV(V_{bias}, X, Y)$. The X and Y axes correspond to the spatial coordinates of the map, while the color scale indicates the magnitude of the differential conductance at each point, providing a visual representation of the local density of states (LDOS) across the scanned area. As a result, 256 dI/dV maps were constructed. The Figure 45(b) displays the dI/dV map extracted for V_{bias}= - 0.19 V.

The STS map is generated after acquiring the STM image of Figure 45(a) and shows thermal drift between the image acquisition time and the start of the mapping process. The common area between the STM image and the map is delineated on the Figure 45(a, b) by dashed red squares. The STM image of Figure 45(a) shows 3 bright features each marked by a red cross. These features' shape and size correspond to the bright trimer feature of the BuL as detailed earlier in Figure 35. The bright BuL features are also observed as 3 bright features. Additionally, 3 bright features indicated by red arrows on the dI/dV_{map} show outlier data points at positions of the tip where the single point STS presumably failed.

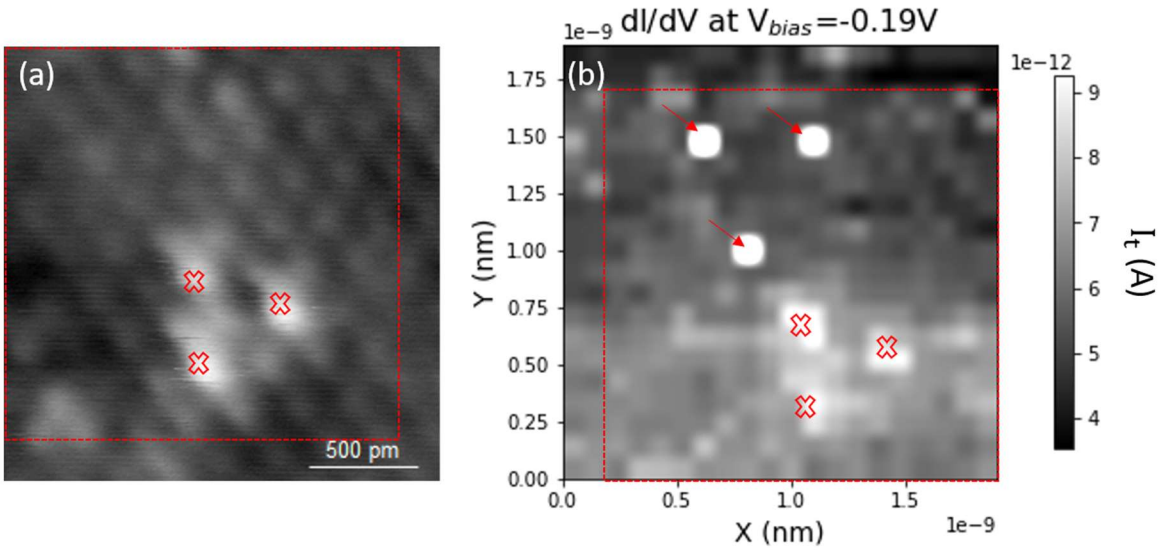


Figure 45: (a) STM image of BLG. 3 bright features are marked by red crosses ('x'), the features size corresponds well to the trimer features associated with the BuL (see Figure 35) Tunneling conditions: V_{bias} =- 0.29 V, I_t = 100 pA. (b) dI/dV_{map} at V_{bias}= - 0.19 V. Number of grid points: X= 20, Y= 20, map dimensions: 2 nm x 2 nm. [- 0.29 V, 0.25 V]

First, the Figure 46(a) extracted at a bias of – 0.19 V shows a dI_t/dV map where 4 points are marked using colored cross ('x') signs. The blue crosses show points of presumably failed spectroscopies. These 3 blue points are labelled by O1, O2 and O3 and another randomly chosen point on BLG is indicated by a black colored cross and is labelled as G1.

The differential conductance spectroscopies measurements corresponding to O1, O2, O3 and G1 are plotted in Figure 46(b).

The spectra for O1, O2 and O3 show a peak at - 0.17 V, a shoulder at - 0.10 V and a dip at zero bias, whereas G1 displays a quite linear behavior around zero bias voltage. For BLG, a closing of the pseudogap is expected, which corresponds well to G1 spectrum.[111]

A comparison of these spectra reveals that O1, O2 and O3 exhibit higher conductance and therefore a higher LDOS compared to G1, which shows lower conductance and a distinct spectral profile. Since the spots corresponding to O1, O2 and O3 are not visible in the STM images at any V_{bias} and their occurrence is localized (neighboring spectroscopies do not display these specific profiles), we hypothesize that they result from a localized and reversible change at the tip apex-likely caused by an adatom that randomly diffused under the tip.

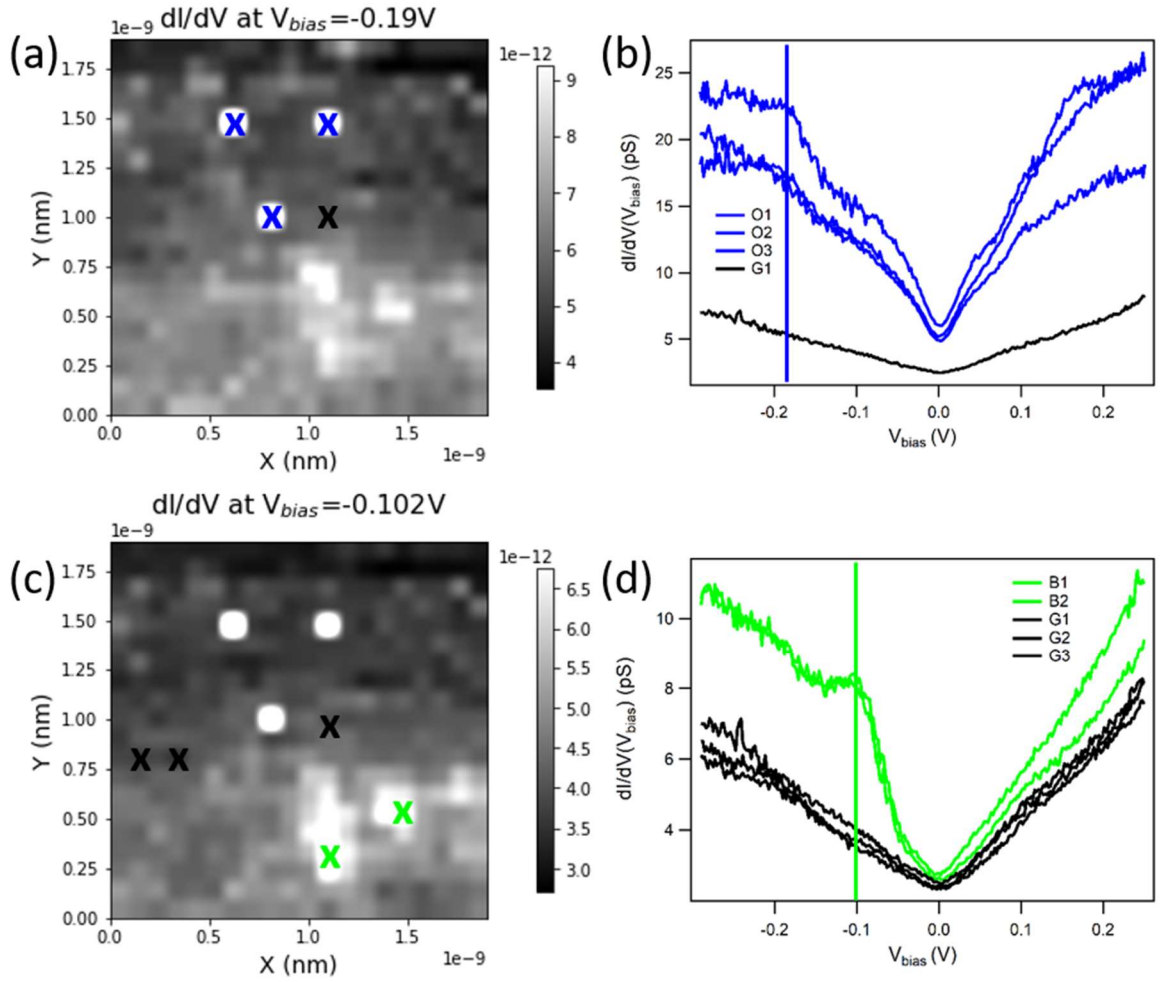


Figure 46: ***(a)*** *dI_t/dV map at V_{bias}= - 0.19 V. The points O1, O2, O3 and G1 indicate the locations on the map where single-point spectroscopies were performed. The white features marked with blue crosses ('x') are likely failed spectroscopies, probably caused by tip accidents during the 4D mapping.* ***(b)*** *Single-point dI_t/dV spectra acquired at O1, O2, O3 (blue) and G1 (black).* ***(c)*** *dI_t/dV map acquired at V_{bias}= - 0.10 V, the points B1 and B2 indicate locations on the map over the bright BuL features and the points G1, G2 and G3 locations over the BLG.* ***(d)*** *Single-point dI_t/dV spectra acquired at B1, B2 (green), G1, G2 and G3 (black).*

In the Figure 46(c) (dI_t/dV map at V_{bias} =- 0.10 V), the bright features associated with the underlying BuL are labelled by B1 and B2, (green crosses) and 3 locations on BLG are labelled by G1, G2 and G3 (black crosses) for comparison. The dI_t/dV spectra at the bright BuL features (B1 and B2) shown in Figure 46(d) exhibit a conductance peak around – 0.10 V, in contrast to the spectra over BLG. All B1, B2, G1, G2 and G3 display a dip at zero bias with no apparent pseudogap and similar conductance values. At positive bias voltage values, all spectra are comparable.

In conclusion, the most notable result is that for the BLG layer, the pseudogap is effectively closed. The LDOS measured near E_F shows a nearly linear behavior. Additionally, a distinct feature around – 0.10 V becomes more apparent when the conductance is measured over a bright feature caused by the underlying BuL. This feature is the only distinguishable contribution of the BuL to the electronic properties of BLG.

III.4. Conclusion

This chapter focused on the modalities of preparation of the substrates of interest in-situ under UHV before deposit: HOPG and Gr/SiC. Graphene's STM images presented a contrast modulation along a crystallographic direction of graphene. This modulation effect was proven to be originating from the graphitic buffer layer randomly growing underneath the graphene layer. We then studied this buffer layer by STM, which showed to be a structurally inhomogeneous layer composed essentially by bright trimer features and small ring features. These features cause the contrast modulation underneath graphene.

By studying graphene by scanning tunneling spectroscopy we first examined the impact of experimental parameters such as tip-sample distance, modulation amplitude, tip morphology on the STS spectra, demonstrating how these factors influence the resolution and interpretation of graphene electronic states. Additionally, we introduced the concept of spatially resolved STS mapping, emphasizing its importance in revealing local variations in the electronic structure across the surface.

By considering all these constraints, we show that the occasional periodicity on graphene induced by the substrate did not affect graphene's intrinsic electronic properties.

IV. Synthesis of zwitterionic molecules

IV.1. Introduction on polymethines

Polymethine dyes are a fascinating class of π-conjugated molecules characterized by a chain of an odd number 'n' of sp^2 hybridized carbon atoms. Electron donating 'D' and/or electron withdrawing groups 'A' or heterocycles border this chain, resulting in neutral, positively charged (cationic), or negatively charged (anionic) dyes.[112–114] A coupled polymethine results from the C-C coupling of 2 polymethine units. The general structures of a polymethine and a coupled polymethine are represented in Figure 47, the ideal polymethine state i.e., the cyanine state, is reached when the 2 bordering groups are adequately balanced.

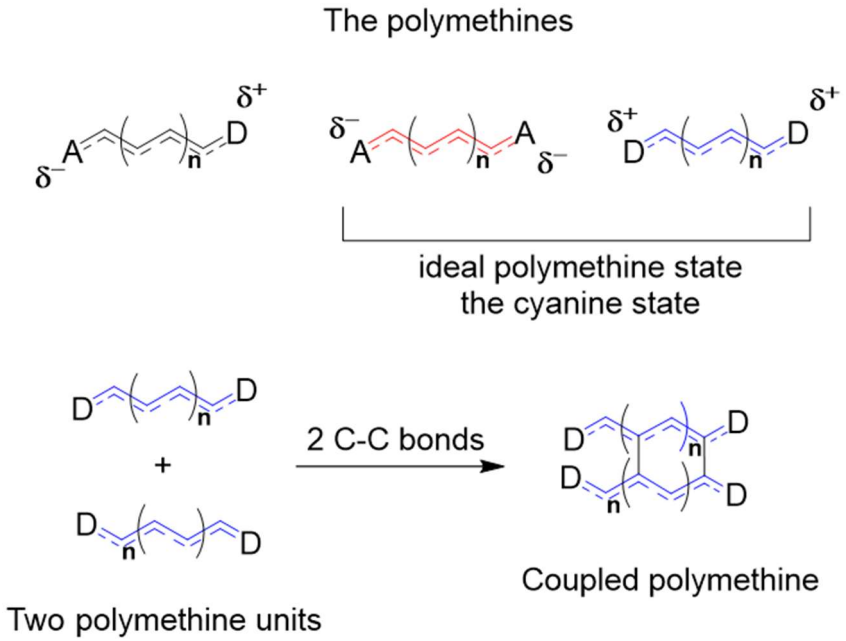


Figure 47: General structure of polymethines with terminal donor (D) and acceptor (A) groups, and of coupled polymethines via C-C bonds.

The conjugated system allows for electron delocalization across the carbon chain, with polymethine chains of variable lengths, which influences the dye's electronic properties and applications.[115] The longer the chain of alternating distribution π-electron density is, the more significant is the redistribution upon light adsorption. This effect contributes to the distinctive deep coloration of the polymethine dyes with respect to other dyes that presents a similar number of π-electrons.

In the 1960s, Dähne and Leupold focused their research on understanding the origin of color in unsaturated organic compounds, uncovering correlations between molecular structure and optical properties.[116] Their work highlighted unique attributes of polymethine structures, with the cyanine state representing an ideal polymethine state that exemplifies the balance and symmetry inherent to this configuration. In this ideal polymethine state, the charge is perfectly delocalized along the conjugated bridge, resulting in a state with equalized bond lengths, therefore, a vanishing bond length alternation (BLA).[117] The BLA is the difference in average bonds lengths that constitute the polymethine chain, between adjacent single and double bonds lengths, this concept is further explained in IV.2.3 and in Figure 56. This bond length equalization is characterized by a sharp and intense electronic absorption band for symmetrical polymethines.

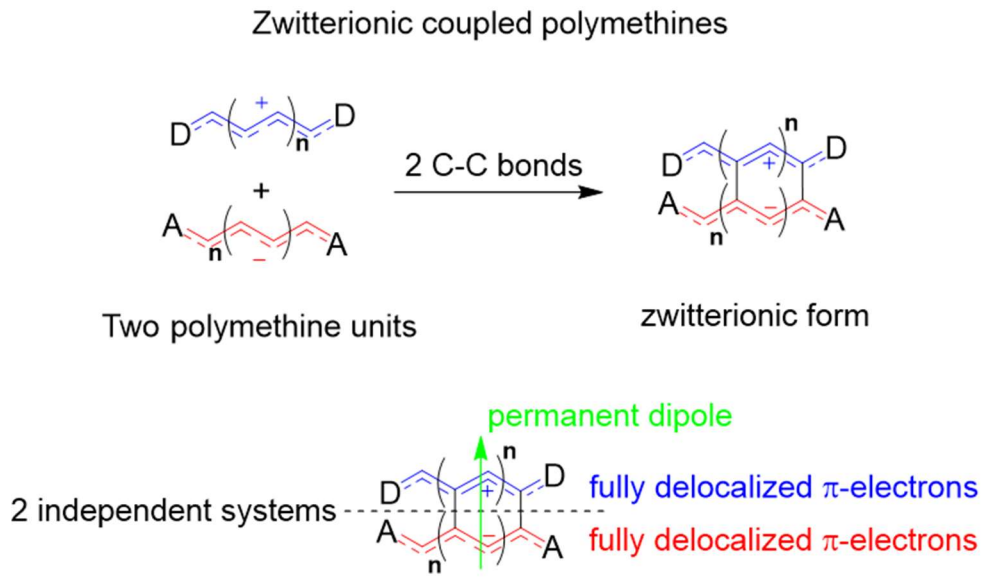


Figure 48: Zwitterionic coupled polymethines formed by coupling of 2 different polymethine units connected by single C-C bonds. These molecules present a permanent dipole moment.

Building on this concept, zwitterionic cyanines form a unique subclass of cyanine dyes, distinguished by the presence of both positive and negative charges within the same molecule. The zwitterionic coupled polymethine consists of 2 independent systems, where the π-electrons are fully delocalized over the polymethine chain. These zwitterionic coupled polymethines present a permanent dipole.

The positive and negative charges are typically delocalized each over a polymethine chain and the attached terminal heterocycles, resulting in a neutral overall charge for the molecule but presenting a significant internal dipole moment.[5,118,119] A recent review article provides a more comprehensive and detailed review on coupled polymethine dyes.[120]

IV.2. Historical milestones in synthesis

IV.2.1. Introduction to transamination and π-zwitterions

The concept of intramolecular charge transfer is central to ground state π-zwitterions, which are fascinating conjugated molecules known for their unique photophysical properties.[121] A zwitterionic form of the monocyclic 2,5-oxoamino-1,4-benzoquinonemonoimines (QZ) was first reported in 2002.[118] These molecules exhibit a stable zwitterionic ground state due to an intramolecular proton transfer, creating 2 distinct 6 π-electron subunits: a positively charged trimethine cyanine and a negatively charged trimethine oxonol, connected by 2 single bonds, as shown in the Figure 49. This configuration ensures a highly stable ground-state electronic structure, preventing the isolation of the canonical isomer (Q).

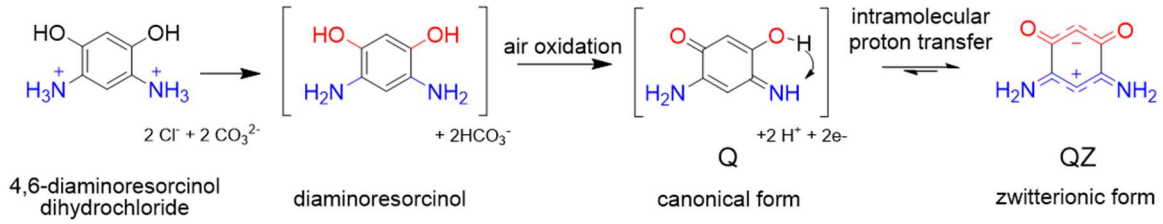


*Figure 49: Transamination procedure towards **QZ** molecules.*

The general transamination procedure to synthesize QZ starting from 4,6-diaminoresorcinol dihydrochloride salt is illustrated in Figure 50. Efficient N-substitution of QZ with alkyl moieties via transamination reactions [5,122] (illustrated in Figure 50) has enabled their use as ditopic bis-bidentate ligands in coordination complexes with notable redox [123–126], catalytic, [127,128] and vapochromic properties.[129]

Adding to the QZ straightforward N-functionalization, their significant intrinsic dipole moment of approximately 10 D makes them highly-suitable for developing molecular films through processes like adsorption or polymerization on metal surfaces and interfaces.[19–23] These molecules were additionally used as interlayers in graphene or MoS_2 transistors.[135,136]

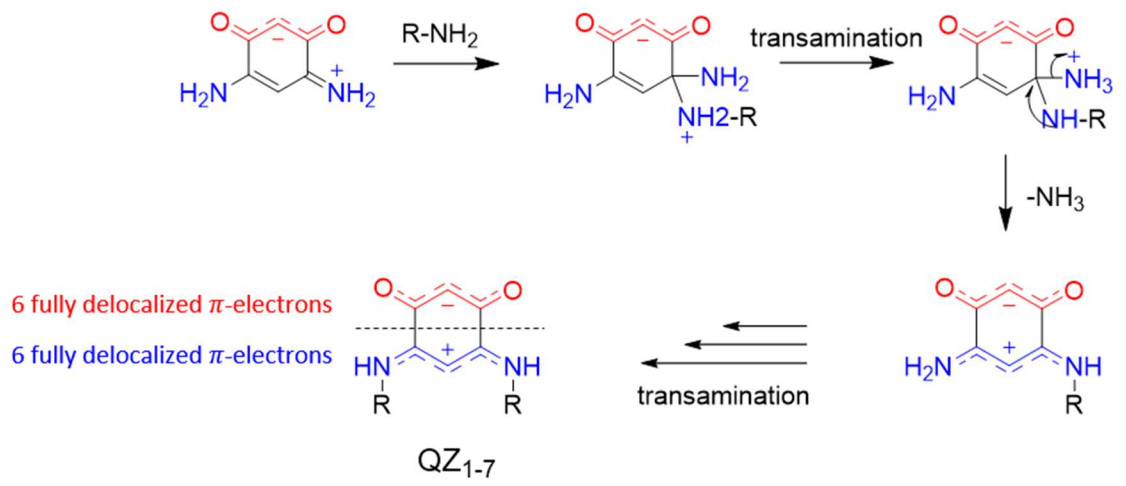


*Figure 50: Transamination procedure to obtain N-substituted **QZ**. **QZ1**: R= CH_2-CH_2-OH; **QZ2**: R= CH_3; **QZ3**: R= $CH(CH_3)CH_2CH_3$; **QZ4**: R= $(CH_2)_3CH_3$; **QZ5**: R= $CH_2CH_2N(CH_3)_2$; **QZ6**: R = C_6H_4-OCH_3; **QZ7**: R= Ph.*

Beyond their many applications, QZ also demonstrated potential in molecular design as metallic complexes. They can be used to create metal complexes, exemplified by the coordination of alkyl-N-substituted QZ with Nickel forming a double-deck assembly of with an interdigitation of the alkyl chains via van der Waals interactions on trichlorobenzene (TCB)/highly oriented pyrolytic graphite (HOPG) surface (see Figure 51).[137]

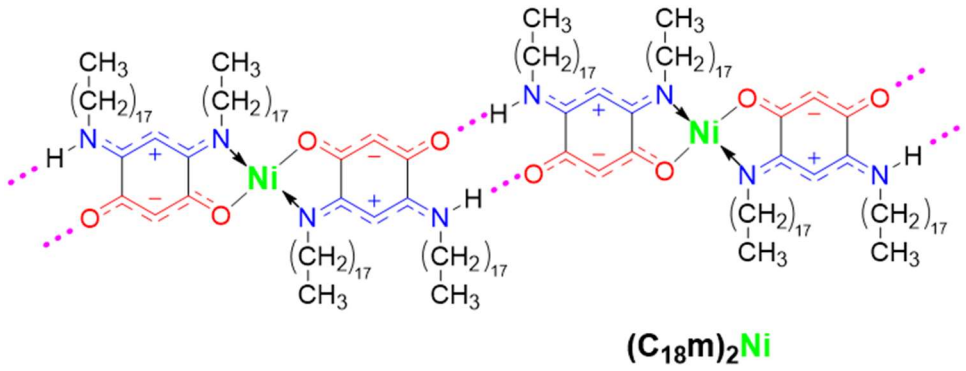


*Figure 51: $C_{18}H_{37}$ group functionalized **QZ**. Charge assisted hydrogen bonds are shown in pink dashed lines. Nickel complex $(C_{18}m)_2Ni$ involving 2 N-substituted **QZ** and one Ni atom. Adapted from reference.[137]*

While synthetic QZ and derivatives have been tailored for various applications, nature provides its own version of these molecules with a rare example of a C-substituted QZ [138,139] the 'dactylocyanine A' molecule, represented in Figure 52 that was reported in 2017 as a blue dye naturally present in the Polynesian marine sponge *Dactylospongia* metachromia. This compound's single crystal structure shown in Figure 52 could be recovered, its trimethine coupled and stable structure could be confirmed.[140]

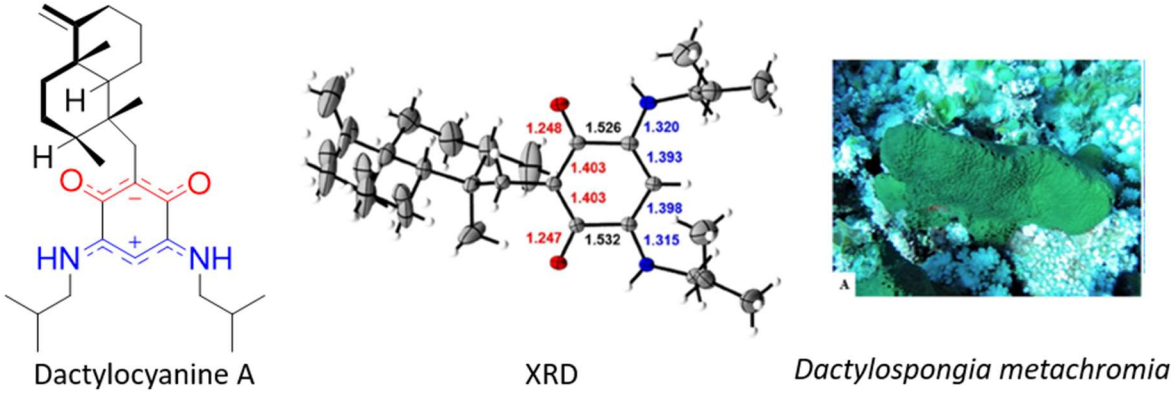


Figure 52: The dactylocyanine A molecule. Single crystal structure (XRD) of dactylocyanine A. The relevant bond lengths are indicated on the structure (in Å). Reproduced from reference.[140] A picture of the sponge metachromia growing exposed to coral reef. Reproduced from reference.[141]

While quinone-based systems offer a pathway to π-zwitterions, another promising strategy involves the design of rigid polycyclic antiaromatic species. These compounds are particularly effective at forming stable ground-state zwitterions, such as tetraazapentacene (ZTAP) [11,14,142] and tetraphenylhexaazaanthracenes (TPHA).[143–146] (see Figure 53)

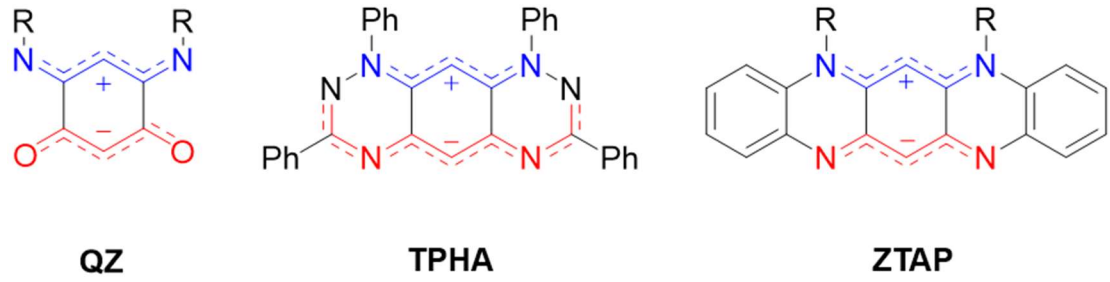


Figure 53: Examples of π-zwitterions. QZ for the 2,5-oxoamino-1,4-benzoquinonemonoimines, TPHA for tetraphenylhexaazaanthracenes and ZTAP for the 5,7-disubstituted-5H,12H-quinoxalino [2,3-b] phenazines zwitterion.

IV.2.2. Advancements in the synthesis of QZ

The first 12π-electron zwitterionic molecule in quinonoid chemistry was reported by Siri and Braunstein in 2002, by the unexpected one-pot synthesis of an unprecedented zwitterionic tert-butyl-substituted aminobenzoquinone, referred to, in this manuscript, as the zwitterionic quinone (QZ), which is recognized in the literature as the zwitterion benzoquinonemonoimine (BQMI) (see Figure 54).[118]

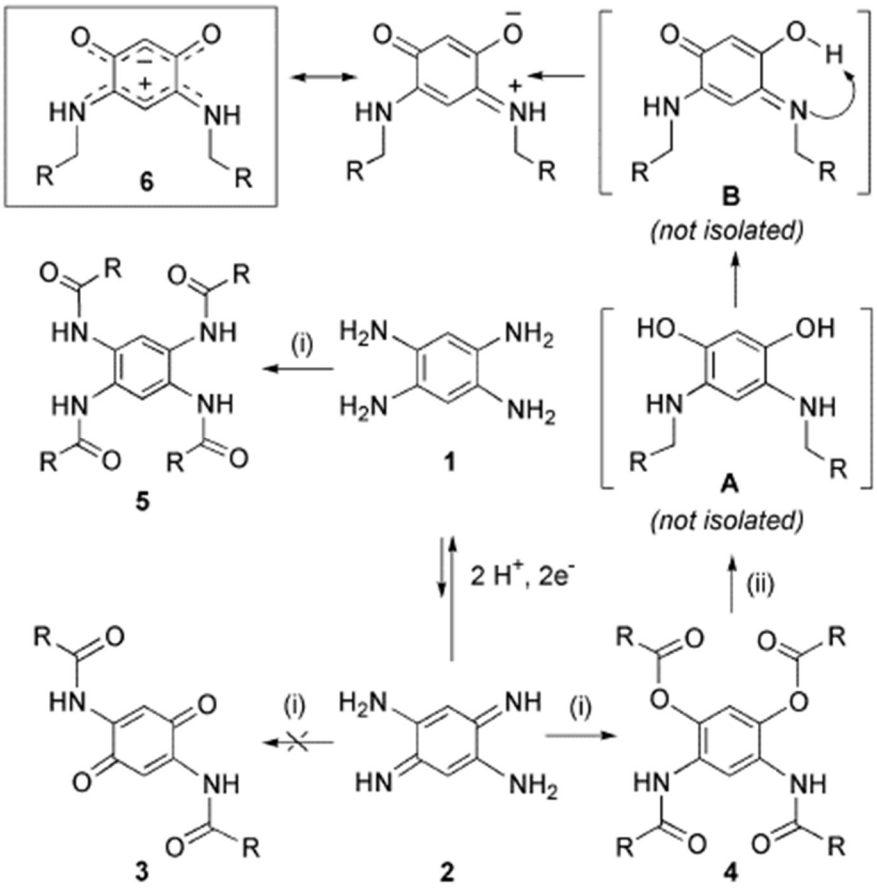


Figure 54: The first synthesis of a zwitterion in quinonoid chemistry from a one pot synthesis of the aromatic N, N, O, O system.[118]

This molecule is described with the N, N, O, O –molecule in which the positive charge is delocalized between the nitrogen atoms and the negative charge is delocalized between the oxygen atoms. In 2005, a new functionalization pathway based on transamination was established, enabling the synthesis of a wide array of alkyl-substituted QZ.[5]

Initially, the deprotonation of the commercially available dihydrochloride salt of 4,6-diaminoresorcinol is carried out in the presence of a base. In the reaction solvent, this compound forms the non-isolated diaminoresorcinol intermediate, while exposed to air it oxidizes to give the unsubstituted zwitterion QZ. When it is exposed to an excess of primary alkylamine or arylamine in solution at room temperature for 30 to 120 minutes, it undergoes transamination, yielding N-alkyl or N-aryl substituted QZ. These zwitterions are purified by simple precipitation and isolated with yields ranging from 72 % to 93 %. It was not until 2009 that the transamination was extended to aromatic amines, allowing for the synthesis of N-substituted aryl QZ derivatives (Figure 55).[122]

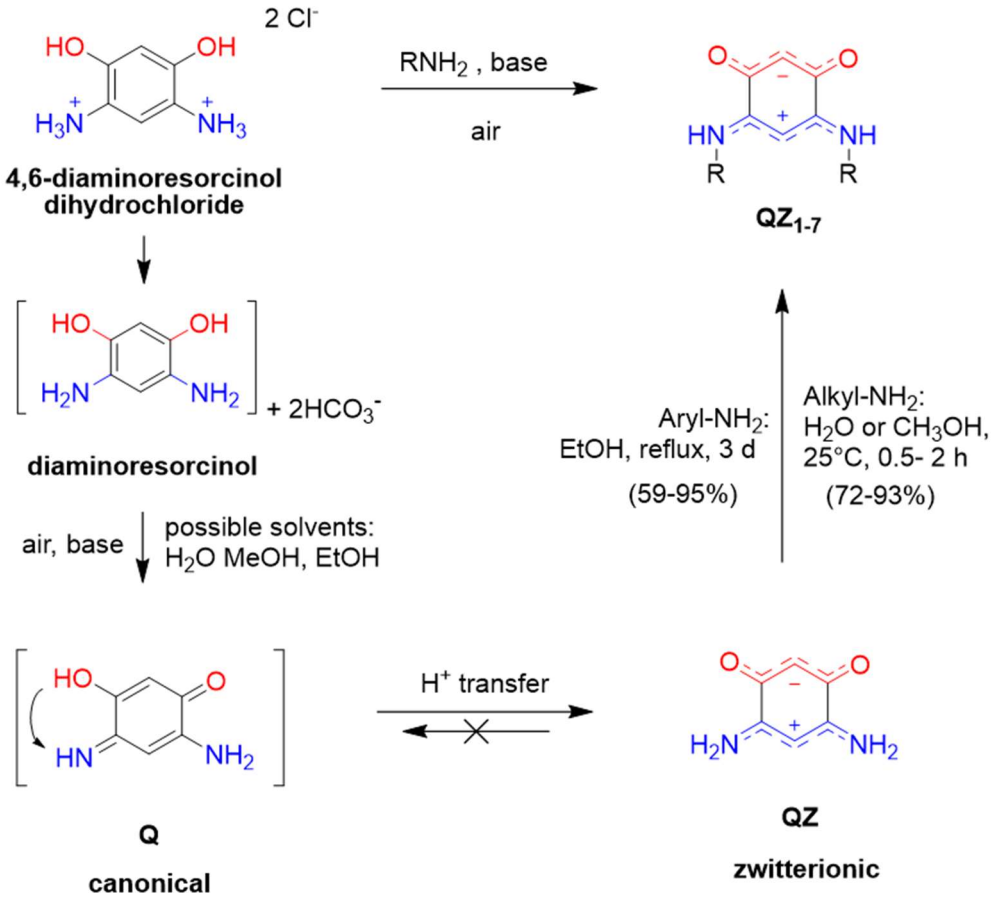


Figure 55: Preparation of ***QZ****.* ***QZ₁****: R= CH_2-CH_2-OH;* ***QZ₂****: R= CH_3;* ***QZ₃****: R= $CH(CH_3)CH_2CH_3$;* ***QZ₄****: R= $(CH_2)_3CH_3$;* ***QZ₅****: R= $CH_2CH_2N(CH_3)_2$;* ***QZ₆****: R = p-C_6H_4-OCH_3;* ***QZ₇****: R= Ph*

In this study, the authors chose the 4-methoxyaniline (*p*-anisidine) as the first arylamine for zwitterion functionalization because the electron-donating methoxy group facilitates transamination. Initially, the reaction was conducted under the same conditions as for alkylamines, but it was unsuccessful. However, by using more severe conditions involving 7 equivalents of 4-methoxyaniline and refluxing in EtOH for 3 days, the desired product was obtained. Similar conditions were applied for aniline, which was added in larger excess (50 equivalents) and the reaction mixture was refluxed for 4 days. The structures QZ_6 and QZ_7 were isolated and purified by precipitation, with respective yields of 59 % and 95 %.

IV.2.3. Structural properties of BQMIs and ZTAP

The isolation of single crystal structures of QZ and ZTAP derivatives shows that these molecules' ground state structure was zwitterionic. In polymethines or coupled polymethines, electrons can delocalize over multiple bonds and the bonds alternate between longer (single bond) and shorter (double bond) lengths, leading to a bond length alternation (BLA).

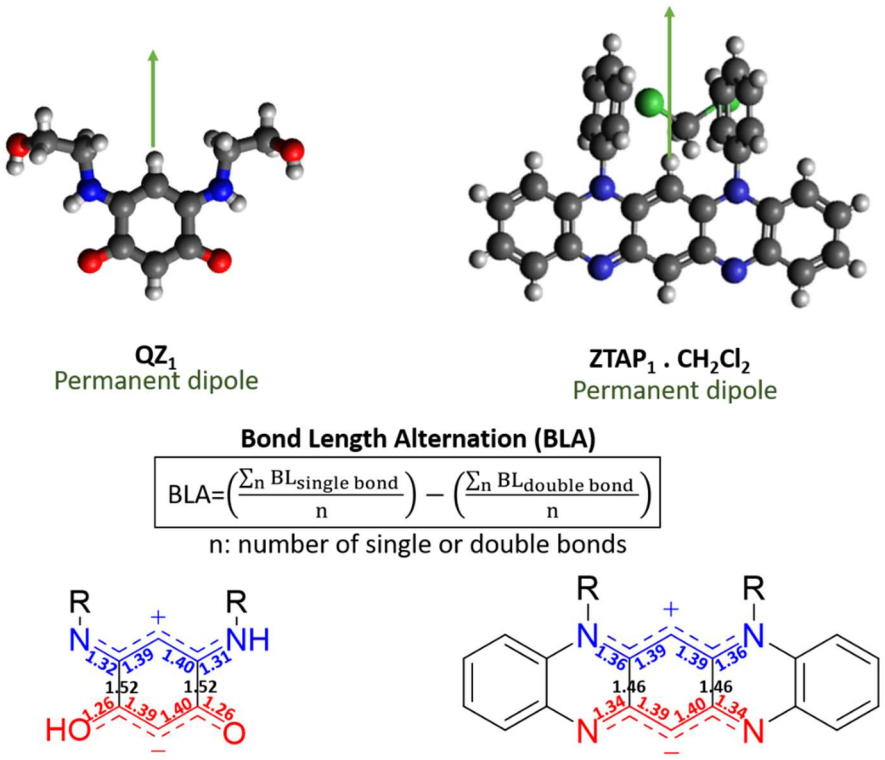


*Figure 56: Single crystal structure of **QZ₁** with R= CH_2-CH_2-OH. The molecule is zwitterionic with low BLA values of 0.005 Å and 0.010 Å for the oxonol and trimethine chains respectively. The BLA formula quantifies the difference between single and double bond lengths in the conjugated system. n is the number of single or double bonds. The **ZTAP₁** molecule is zwitterionic with low BLA values of 0.005 Å for the trimethine chains. The green arrow represents the dipole moment.*

The smaller the BLA (the closer to zero), the strongest the delocalization. As a matter of example, the single crystal structure of QZ_1 shows BLA value of $(1.26 + 1.40) - (1.39 + 1.26) = 0.005$ Å between the oxygen atoms and 0.01 Å between the nitrogen atoms. Additionally, the 2 carbon-carbon bonds linking the 2 polymethine chains of opposite charge have a length which confirms that these bonds are single C-C bonds.

The single crystal structure of $ZTAP_1$ is also represented, and the positively and negatively charged trimethine units presents a BLA value of approximately 0.005 Å, while the 2 carbon-carbon bonds linking the 2 polymethine chains of opposite charges have a length of approximately 1.46 Å and confirms that these bonds are single C-C bonds. The XRD structures of QZ_1 and $ZTAP_1$ confirms the presence of a zwitterionic ground state, with zero bond length alternation (BLA) on each of the 2 six electron π-subunits.

By modifying the peripheral functional groups of these molecules through chemical synthesis, the zwitterionic nature of the molecule and its dipole moment remains intact. The different peripheral groups will lead to different interactions between the molecules, depending on the molecule's geometry and a different resulting dipole moment. If the molecules are adsorbed on a surface, depending on the geometry of adsorption, the interaction with the surface and on the peripheral groups, different assembled structures will arise. This work will focus on understanding the properties of such molecules which present potential in supramolecular design.

In this study, we replicate the synthesis of the QZ derivatives, a process well-established within our team, without deeply delving into their characterization. Additionally, we explore the synthesis of another molecule, ZTAP, whose synthesis pathway was unfamiliar to us and thus examined its properties. The primary goal of synthesizing these compounds is to further investigate their self-assembly capabilities on graphene and HOPG, as discussed in the subsequent chapters.

IV.3. Synthesis conducted in this Thesis

The synthetic pathways to N-substituted QZs involves the transamination of the parent compound with an excess of amine. This method allows for the introduction of aryl or alkyl substituents, providing a straightforward approach to controlling the electronic and optical characteristics of these versatile molecules. Different substituents -R will lead to different supramolecular networks on surfaces, while keeping intact the zwitterionic nature of the molecule.

IV.3.1. Transamination of benzoquinonemonoimine zwitterions

Commercial 4,6-diaminoresorcinol dihydrochloride undergoes aerobic oxidation in air in the presence of a base, here N, N-diisopropylethylamine (DIPEA/Hünig's base) to form the unsubstituted parent zwitterion QZ that is collected by filtration with good yields (93 %).

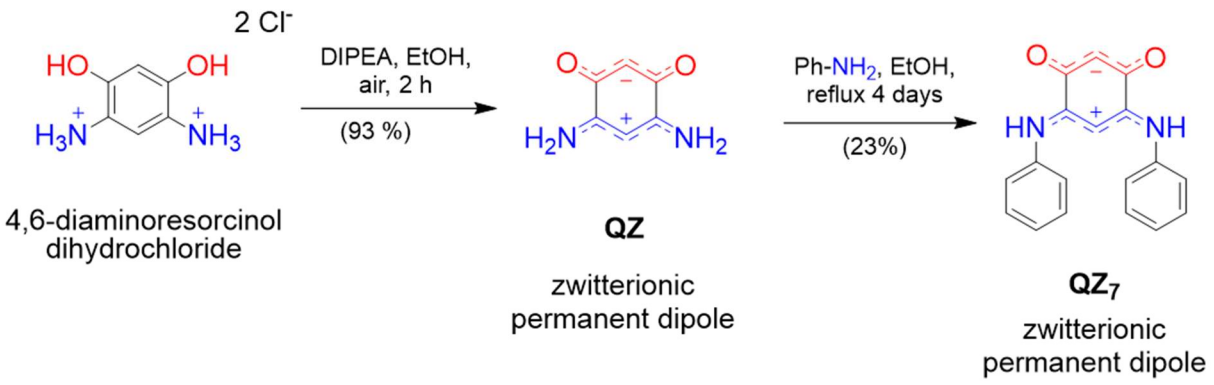


*Figure 57: Synthesis of the zwitterion **QZ** and of its N-phenyl substituted **QZ$_7$** derivative.*

QZ is then reacted through transamination in a protic medium (EtOH) in the presence of a large excess of aniline (50 equivalents) for 4 days to give the QZ_7 compound as a purple powder with 23 % yield.

The QZ_7 compound ^1H NMR spectrum is consistent with the one reported in 2009 by Tamboura F.B and coworkers.[122] The NMR spectrum in Figure 58 shows the presence of

the 2 NH proton signal at δ 10.97 ppm and 2 singlets at δ 5.20 ppm and δ 5.81 ppm characteristic of the 2 protons of the trimethine and oxonol units respectively.

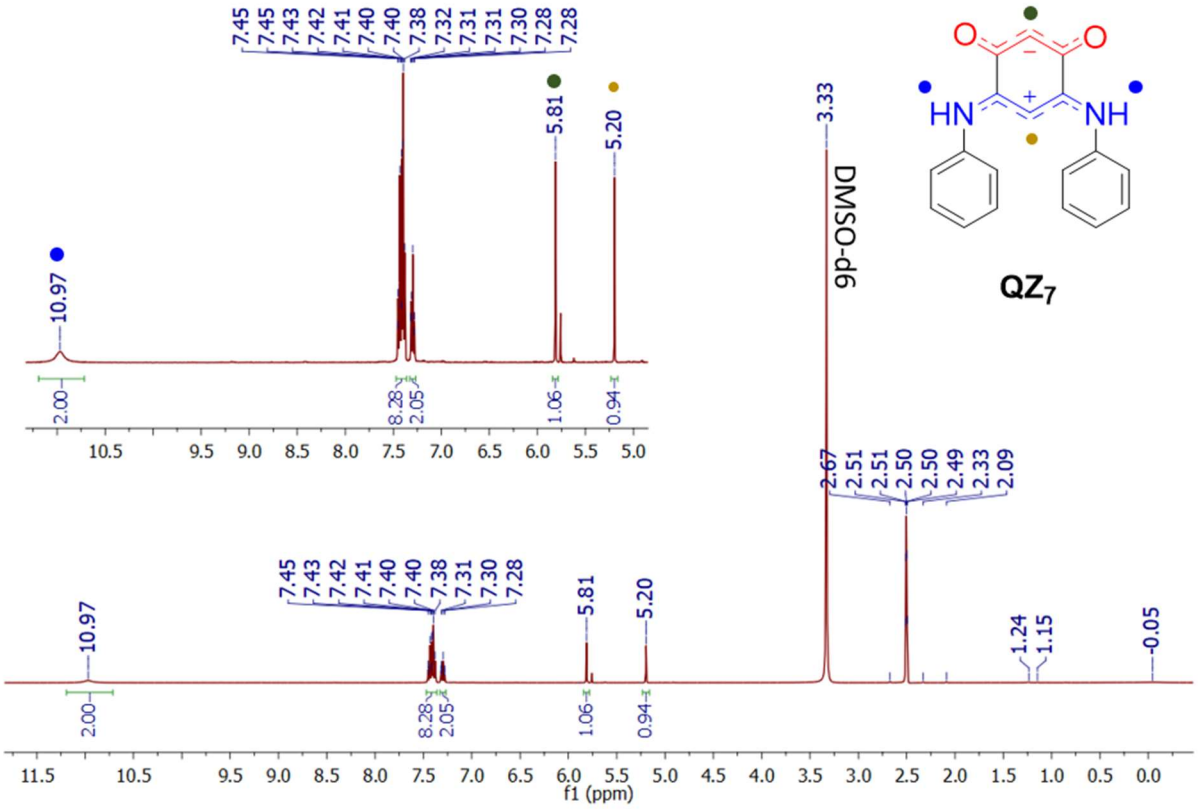


*Figure 58: [1]H NMR spectrum of **QZ7** recorded in DMSO-d6.*

IV.3.2. Synthesis of ZTAP

A regiospecific synthesis of the ZTAP derivatives was first reported by the group of Prof. Panayiotis A. Koutentis.[142] The synthesis pathway (Figure 59) was reproduced in our lab with minor modifications to afford the ZTAP compound derivatives. The general pathway for synthesis of the ZTAP compound is done mainly in 4 steps. The first step is a classical nucleophilic aromatic substitution (SNAr) of an amine on the fluorine atom of the 1-fluoro-4-nitrobenzene to get the substituted nitroaniline X in good yields (51-99 %). The second step is the reduction of X using Zn and NH_4Cl in $MeOH/H_2O$ to afford the compound A in good yields (70-99 %). 2 equivalents of substituted-1,2-benzenediamines A are then condensed on the 1,5-difluoro-2,4-dinitrobenzene through a SNAr of the fluorine atoms to give dinitrobenzene diamines B in good yields (13-93 %). Hydrogenation of the compound B in the presence of Pd/C as catalyst at room temperature gives benzenetetraamines which were successfully isolated in prior studies, however the procedure wasn't replicated in this work. Following the reduction, the mixture was heated in refluxing EtOH in the presence of air, concentrated, then was allowed to cool gradually to room temperature. During this cooling process, a precipitate formed out of the solution. The final product was then collected by filtration and dried

under vacuum to yield the $ZTAP_{1-3}$ derivatives as green powder. The yields vary from 8 % to 71 % depending on 2 factors, the substituent R of ZTAP and the cooling process.

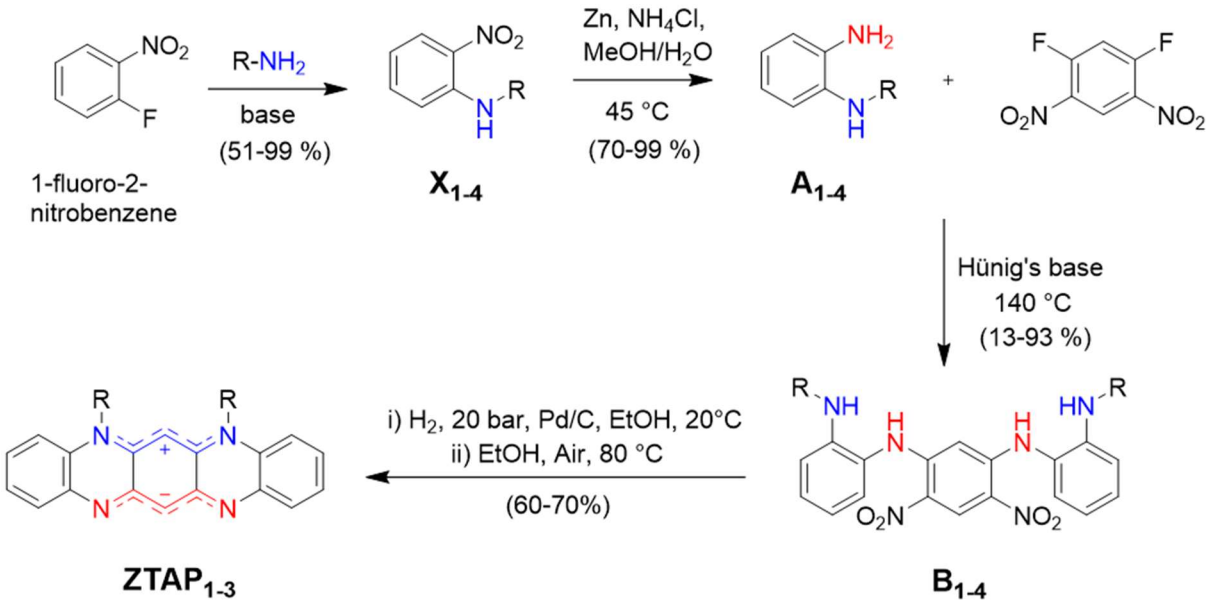


*Figure 59: The synthesis of the **ZTAP** derivatives. **B1**: R= Ph, **B2**: R= p-C_6H_4-O-CH_3, **B3**: R= C_8H_{17}, **B4**: R=p-C_6H_4-Br.*

ZTAP are strong bases and are able to undergo mono- and bis-protonation in solution. In order to ensure the recovery of the free base, drops of 28 vol % ammonia (NH_3) were added to the ethanolic solution after reflux, and before concentration.

IV.3.3. Functionalization of ZTAP

IV.3.3.1. Phenyl group functionalization

The synthesis pathway of $ZTAP_1$ was reproduced with minor modifications to afford the ZTAP compound derivatives. The general pathway for synthesis of the $ZTAP_1$ compound is done mainly in 4 steps, that are shown in Figure 60. The first step is a classical SNAr of aniline on the fluorine atom of the 1-fluoro-4-nitrobenzene in the presence of triethylamine to get the substituted nitroaniline X_1 in good yields (99 %). The second step is the reduction of X_1 using Zn and NH_4Cl in $MeOH/H_2O$ to afford the compound A_1 in good yields (83 %).

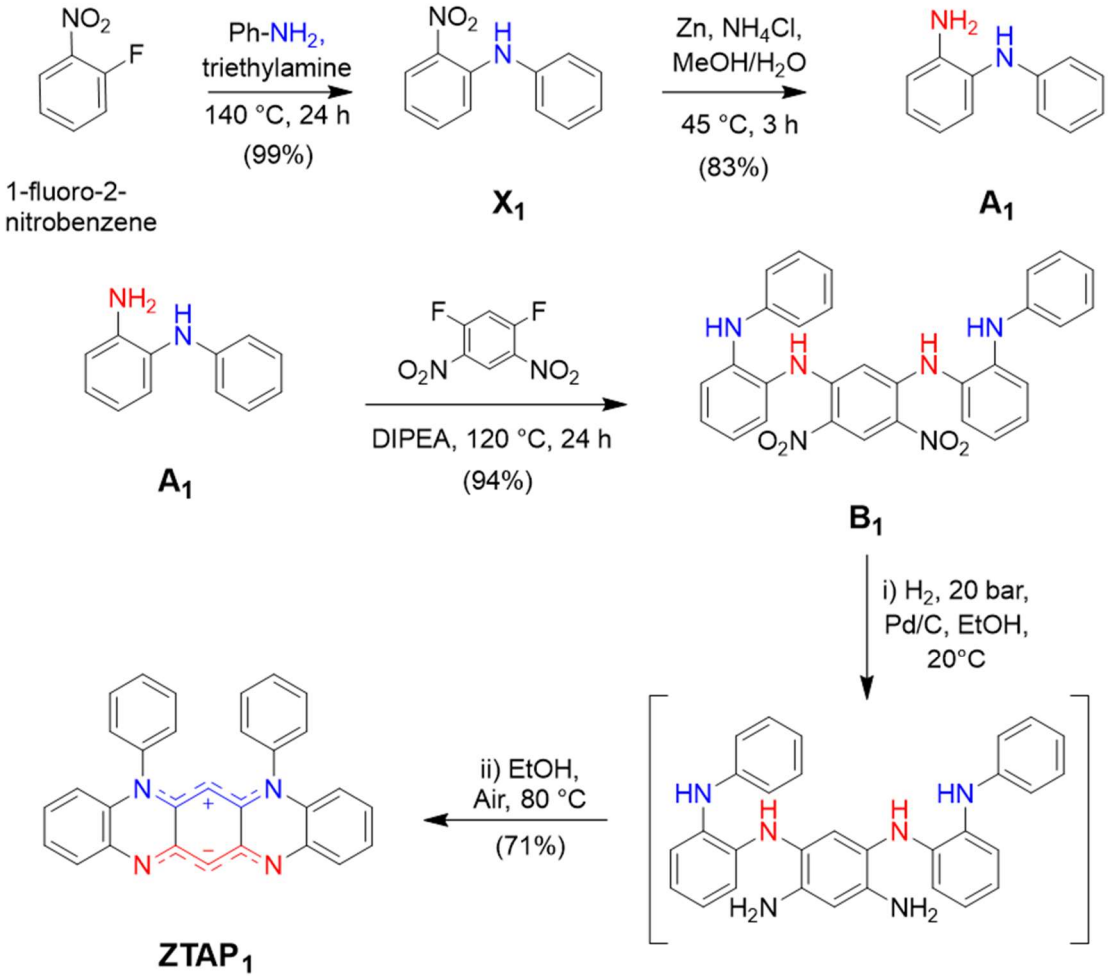


*Figure 60: The synthesis steps of **ZTAP₁**.*

This compound, the substituted-1,2-benzenediamines **A₁** then is reacted with 2 equivalents of 1,5-difluoro-2,4-dinitrobenzene to give dinitrobenzene diamines B_1 in good yields (94 %). Hydrogenation of the compound B_1 in the presence of Pd/C as catalyst at room temperature gives a benzenetetraamine that is not isolated. Following the reduction, the mixture was heated in refluxing EtOH in the presence of air, concentrated, then was allowed to cool gradually to room temperature with the addition of drops of NH_3 to the mixture. During this cooling process, a precipitate formed out of the solution. The final product was then collected by filtration and dried under vacuum to yield the $ZTAP_1$ as a green powder with 71 % yield. Lower yields are obtained depending on the rate of the cooling process, it was observed that yields could go up from 7 % to 71 % with faster cooling. This method did not favor crystal growth of $ZTAP_1$, a compromise must be made by fine tuning the cooling process to enhance the yield and purity of the product. This compound exhibits a very high melting point, and shows decomposition at 360 °C.

IV.3.3.2. Donor-driven functionalization: 4-methoxyphenyl group

In order to synthesize the $ZTAP_2$, which is ZTAP substituted with 4-methoxyphenyl, we modify the first step introduced in IV.3.3.1 by performing a classical SNAr of *p*-anisidine on the fluorine atom of the 1-fluoro-4-nitrobenzene in the presence of DIPEA to get the substituted nitroaniline $\mathbf{X_2}$ in good yield (86 %). Triethylamine could also be used instead of DIPEA to get $\mathbf{X_2}$ (see Figure 61).

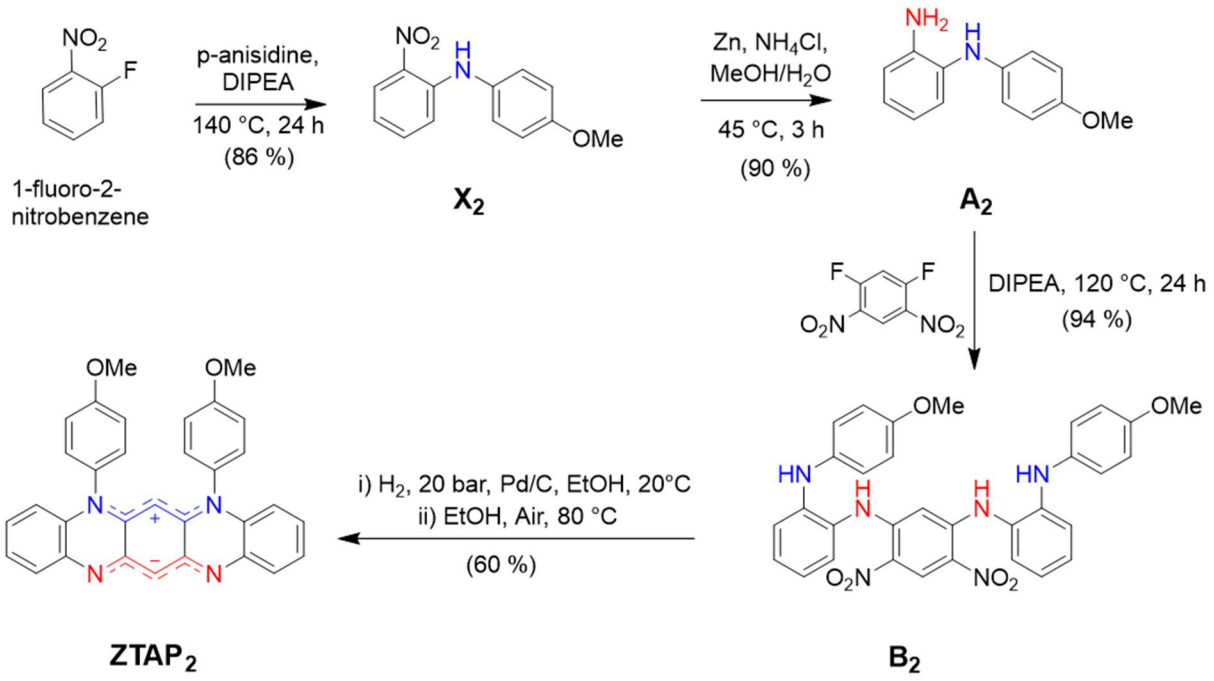


Figure 61: The synthesis steps of ***ZTAP₂***

The reduction and subsequent SNAr methods are unchanged and the compound B_2 is obtained in good yield. Additional purification was necessary to obtain the compound B_2 compared with compound B_1. The explored purification methods include SiO_2 column chromatography (26 % yield) or washing the solid with petroleum ether (96 % yield).

The final hydrogenation step performed was not changed and yielded $ZTAP_2$ as a green powder (60 % yield). This compound also exhibits a very high melting point, and shows decomposition at 360 °C.

IV.3.3.3. Donor-driven functionalization: octyl group

In order to synthesize the $ZTAP_3$, which is N-octyl functionalized ZTAP, we modify the first step introduced in IV.3.3.1 by performing a classical SNAr of octylamine on the fluorine atom to get the substituted nitroaniline X_3 in good yields (99 %). The reduction and subsequent SNAr methods are unchanged and the compound B_3 is obtained in good

yield after additional purification by SiO_2 column chromatography to obtain the compound B_3 in good yields (96 %) (see Figure 62).

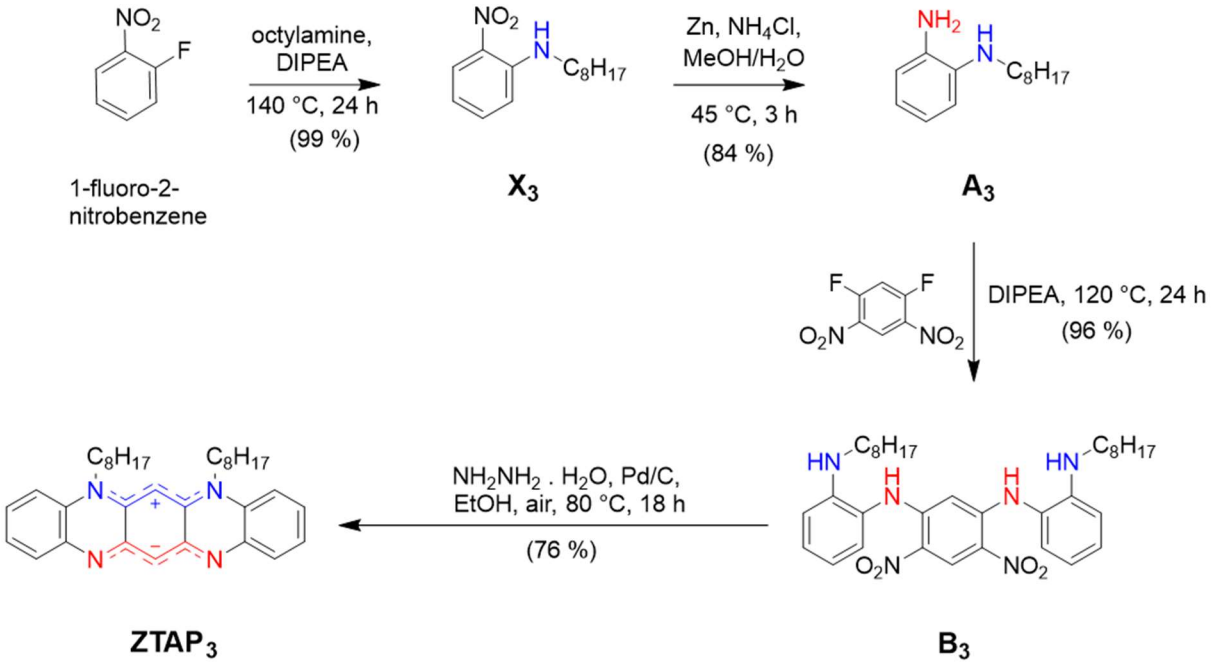


*Figure 62: The synthesis steps of **ZTAP3**.*

The final reduction method with Pd/C was modified by using hydrazine as a milder and safer hydrogen source without the need for high pressure H_2 gas. Compound B_3 and Pd/C were dissolved in absolute EtOH. Hydrazine monohydrate ($NH_2NH_2.H_2O$) was added and the resulting mixture was stirred at 80 °C for 16 hours. The reaction mixture was cooled to room temperature, filtered and the collected fractions were evaporated under reduced pressure. Then the residue was dissolved in absolute EtOH and the solution was stirred at 80 °C for 18 hours in the presence of air. After cooling to room temperature, the mixture was evaporated and the residue was taken up in dichloromethane and washed. The obtained solid was washed with diethyl ether and filtered to afford $ZTAP_3$ as a green powder (76 % yield).

The hydrogenation with Pd/C method used in IV.3.3.1 and IV.3.3.2 was also tried out on A_3 utilizing the same protocol as the one used to get compounds B_1 and B_2, and the synthesis was also successful. The compound $ZTAP_3$ presented a slightly lower yield than with the first method (60 % yield). This compound exhibits a melting point of 204-206 °C.

IV.3.3.4. Acceptor-driven functionalization: 4-bromophenyl groups

In our work, we aimed to functionalize ZTAP phenyl substituents by bromine atoms. Substituting the hydrogen atoms on the para position of the phenyl rings of ZTAP with bromine, could give insight on the donor and acceptor groups effect on the synthesis.

Additionally, the idea of introducing bromine atoms to the ZTAP molecule could be a solution for easier selective substitution post-synthesis. allowing us to anticipate its potential applications in palladium catalyzed chemistry (C-C coupling reactions).

One approach (illustrated in Figure 63) to achieve this outcome is to perform the substitution reaction during the initial synthesis step as follows. The first step consists in the SNAr of now 4-bromoaniline on the fluorine atom of 1-fluoro-4-nitrobenzene to obtain the substituted nitroaniline X_4 in a good yield (95 %).

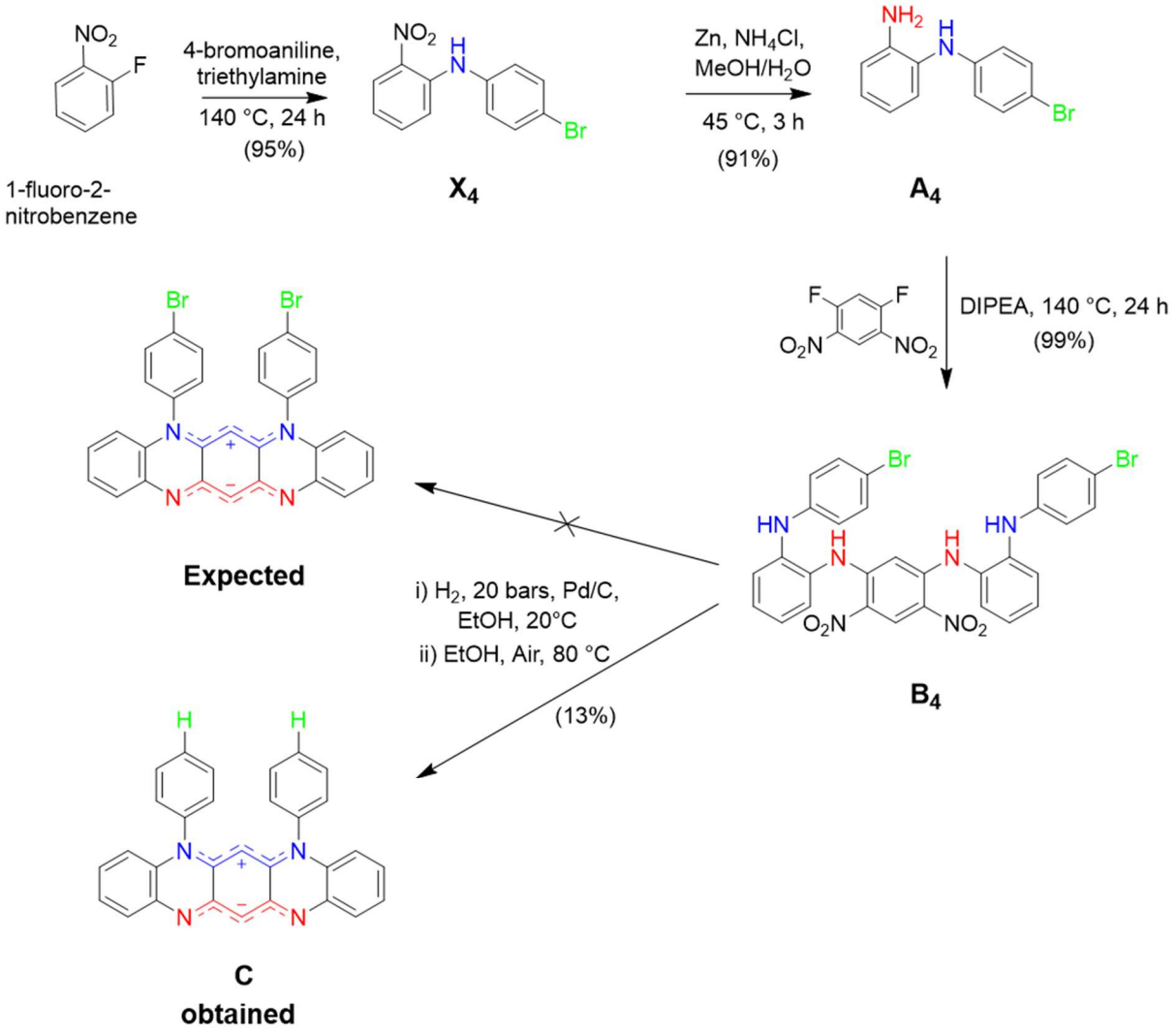


Figure 63: The synthesis steps of B_4 compound. The reduction process resulted in a debromination rather than a cyclisation.

The next reduction step is the one used in IV.3.3.1 which was replicated to afford the N1-(4-bromophenyl)-1,2-benzenediamine compound A_4 (91 %).

A_4 reacts with 2 equivalents of 1,5-difluoro-2,4-dinitrobenzene to give the dinitrobenzene diamines B_4 that could be isolated only once by filtration and washing with solvents. Due to the limited quantity of the isolated compound, complete characterization could not be performed; however, the compound was partially characterized using ^{1}H NMR and mass

spectrometry and the data provides strong evidence for the successful synthesis of B_4 (99 % yield).

Multiple attempts of replicating the synthesis were made, including varying the reaction conditions, ratios and adding an excess of reagent A_4. Despite these efforts, the reaction consistently produced the target compound along with an unidentified mixture of byproducts that could not be separated from the target compound by purification techniques.

These byproducts complicated the isolation and purification process, preventing the acquisition of sufficient pure compound for complete characterization. Despite the ^{13}C NMR spectrum could not be recorded due to material limitations, the available data are consistent with the proposed structure. Further synthesis and isolation are intended to complete the characterizations and to address the challenges encountered in the purification process.

Hydrogenation of the compound B_4 in the presence of Pd/C as catalyst at room temperature gives the benzenetetraamine that were not isolated. Following reduction, the mixture was heated in refluxing EtOH in the presence of air, concentrated, then was allowed to cool gradually to room temperature. During this cooling process, a precipitate formed out of the solution. This precipitate was then collected by filtration and dried under vacuum to yield the compound C which is $ZTAP_1$ as a green powder.

In our attempt to synthesize the 4-bromophenyl substituted ZTAP target compound, we observed an unexpected reductive dehalogenation reaction. In the presence of H_2 gas under pressure and Pd/C as a catalyst at 20 °C, instead of forming the anticipated product, the bromine atoms were removed, resulting in the dehalogenated compound. ^1H NMR and high-resolution mass spectrometry confirmed the removal of bromine atoms and the formation of **$ZTAP_1$**.

IV.3.4. Reactivity

The reactivity of a molecule plays a significant role in defining its chemical behavior and interaction with its environment. This factor could facilitate or not its characterization and it can show if its permanent dipole is conserved in the case of zwitterionic ZTAP. The first subsection will examine the molecule's acid-base behavior, focusing on its response to varying pH conditions.

IV.3.5. Acid-base properties of ZTAP

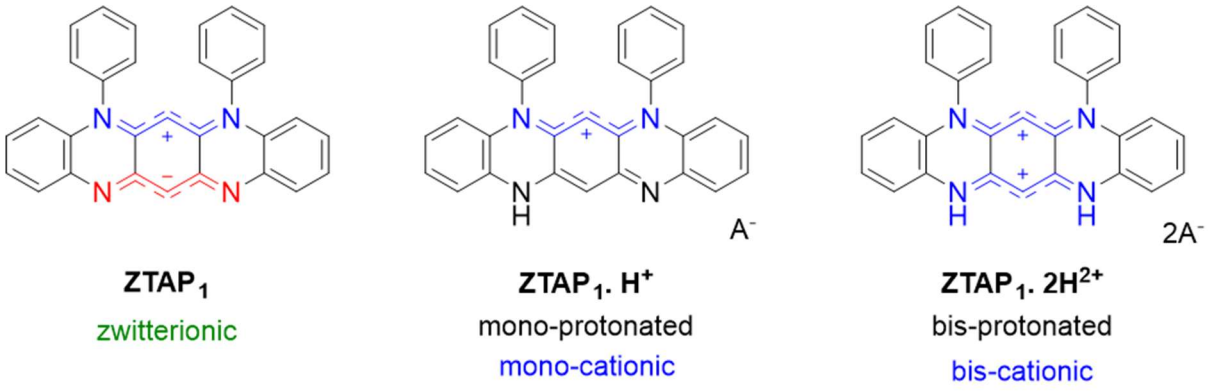


*Figure 64: **ZTAP$_1$** in zwitterionic form. **ZTAP$_1$. H$^+$** in mono-protonated form, A$^-$ is a suitable counterion. **ZTAP$_1$. 2H^{2+}** in bis-protonated form, A$^-$ is a suitable counterion.*

The ZTAP molecules exhibits remarkable adaptability, existing in 3 distinct forms depending on the environmental conditions as illustrated in Figure 64. In the synthetic procedure, drops of a base are added to the ethanolic solution to ensure the precipitation of the green zwitterionic ZTAP as powder, meanwhile the mono-protonated specie (ZTAP. H$^+$) stays in solution in blue color. An excess of a strong, non-nucleophilic acid such as trifluoroacetic acid (TFA) is added to ensure bis-protonation of the ZTAP (ZTAP. 2H^{2+}) molecule in solution.

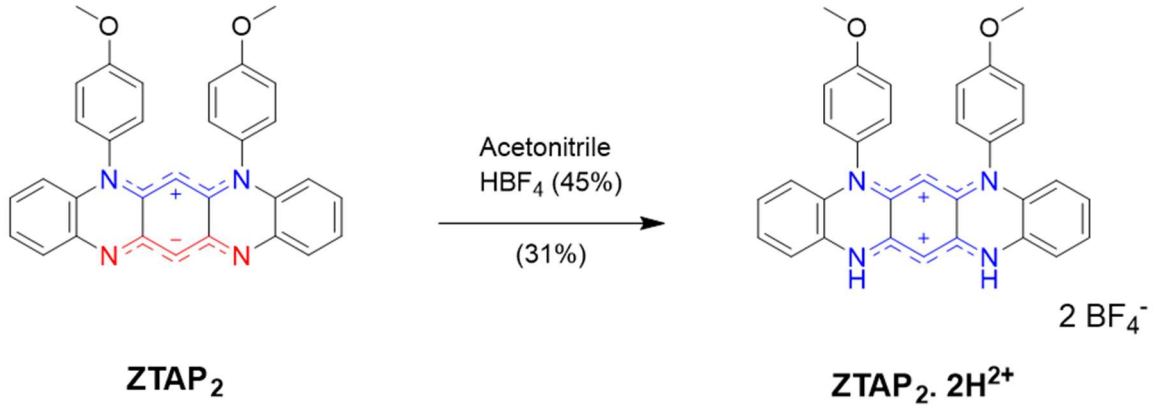


*Figure 65: Preparative bis-protonation of **ZTAP$_2$**.*

Thus, the ZTAP molecule can undergo 2 consecutive protonations in solution, depending on the pH, leading to the formation of a bis-cation with the delocalization of the π-electrons between the 2 nitrogen atoms of each trimethine subunit.

The bis-protonated compound $ZTAP_2.\ 2H^{2+}$ was isolated from 45 % tetrafluoroboric acid (HBF_4) in acetonitrile as a light pink/gold colored powder as shown in Figure 65.

The spectroscopic properties of $ZTAP_2.\ 2H^{2+}$ were studied in many solvents (dichloromethane (DCM), ethanol (EtOH), acetonitrile (ACN), dimethyl sulfoxide (DMSO), tetrahydrofuran (THF) and dimethylformamide (DMF)), the spectra are shown in Figure 66.

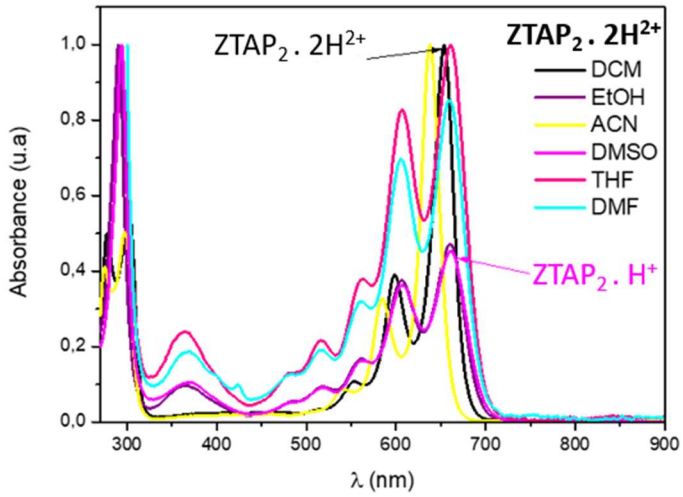


*Figure 66: UV-vis of **$ZTAP_2.2H^{2+}$** in dichloromethane (DCM-black), ethanol (EtOH-purple), acetonitrile (ACN-yellow), dimethyl sulfoxide (DMSO-magenta), tetrahydrofuran (THF-pink), dimethylformamide (DMF-cyan).*

When this bis-cationic molecule is placed in most solvents, an immediate change in absorption spectra is observed. One nitrogen atom tends to rapidly deprotonate in solution. Thus, this molecule in its bis-protonated form acts as a Brønsted-Lowry acid, donating a proton to the solvent.

The UV-vis absorption profile of $ZTAP_2.\ 2H^{2+}$ exhibits a low-energy transition around 660 nm and a high-energy transition near 300 nm in DCM, with the relative peak intensity ratios of 1:0.5, which are consistent in both DCM and ACN. In other solvents, such as DMF and THF, partial deprotonation occurs, leading to the coexistence of mono-cationic and bis-cationic species in solution. This is reflected in the appearance of a new transition around 360 nm. In solvents like EtOH and DMSO, the formation of a mono-cationic derivative is observed, evidenced by a reversed intensity ratio of the high-energy to low-energy transitions (0.5:1) and a further increase in the intensity of the transition around 360nm relative to the maximum low-energy transition.

This observed mono-deprotonation, or partial mono-deprotonation highlights the ZTAP molecules acid-base properties, and the bis-protonated compound acts as a proton donor in most solvents, because even mildly basic solvents can trigger this reaction. This information can be further used to stabilize the molecule in the desired state by controlling its environment.

IV.3.6. Alkylation of ZTAP

To broaden the chemical versatility of ZTAP, we introduce alkyl functionalization on the nitrogen of the outer trimethine. The positive charge of ZTAP is stable and thus the negative charge will get stabilized on the group at the end of the alkyl chain, preventing salt formation while maintaining the zwitterionic nature of the molecule and furthermore stabilizing the cationic structure. The incorporation of alkyl groups into ZTAP structure modulate its photophysical properties.

To improve upon this aspect, 1,4-butane sultone was added in substantial excess to ensure complete reaction with $ZTAP_2$. The reaction was led under argon atmosphere and without solvent, to form the corresponding zwitterionic alkylated compound R-$ZTAP_2$ as a dark blue powder (see Figure 67). The delocalization on the coupled polymethine is disrupted and the position of the negative charge is modified on the molecule.

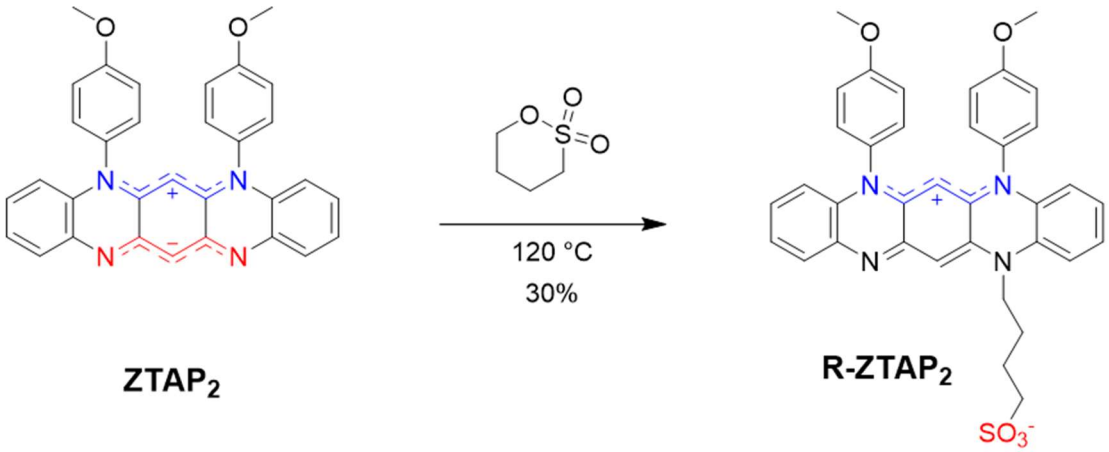


Figure 67: Mono-alkylation of the anionic trimethine part of ***ZTAP2***.

By incorporating the butyl sulfonate group, the solubility was slightly increased compared to $ZTAP_2$ as its ^1H NMR spectrum (shown in Figure 68) could be recorded in $CDCl_3$, but R-$ZTAP_2$ was still not soluble enough to record a ^{13}C NMR. The spectrum shows a doublet signal at δ 3.90-3.93 ppm, assigned to the methoxy groups protons and a singlet at δ 4.83 ppm corresponding to the proton on the positive trimethine unit of R-$ZTAP_2$.

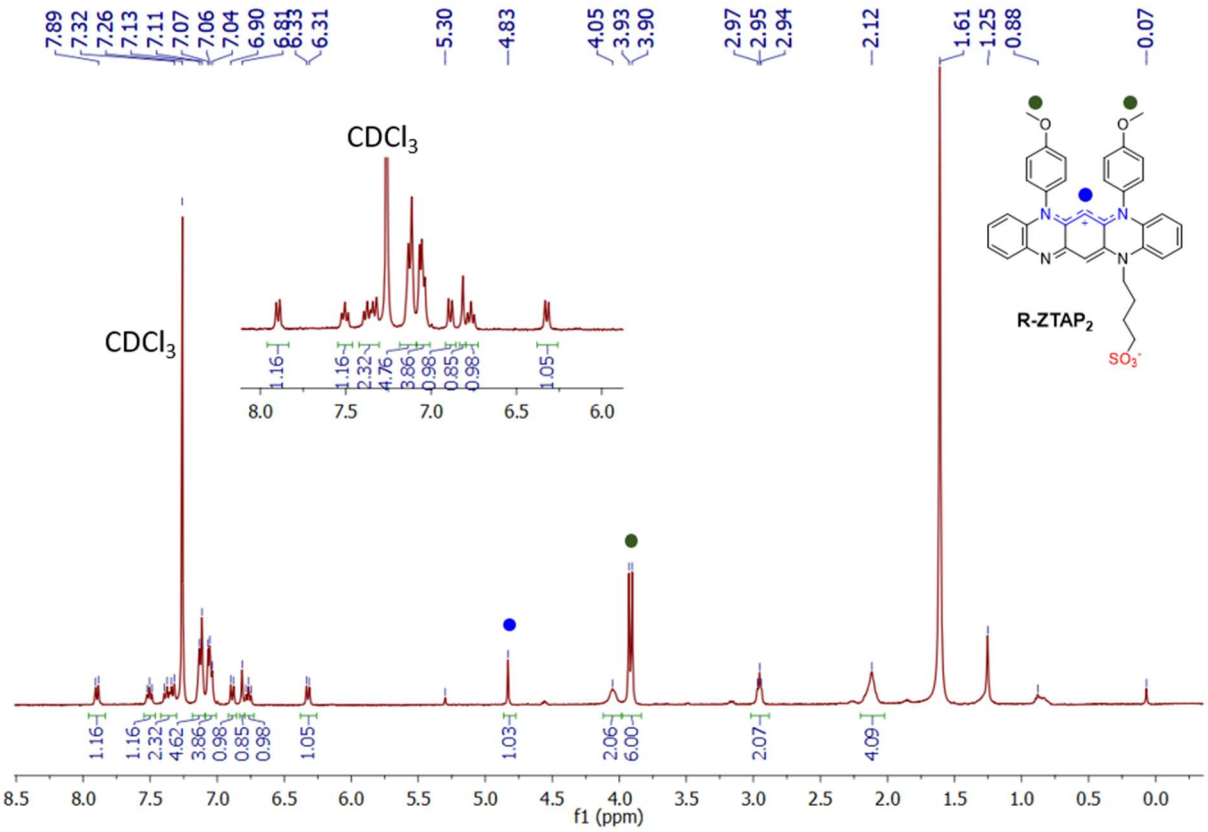


*Figure 68: ^{1}H NMR spectrum of **R-ZTAP$_2$** in $CDCl_3$ (Al_2O_3 basified).*

This modification not only facilitated better dissolution but more accessible overall characterization than for the ZTAP$_{1\text{-}2}$. The overall lower symmetry resulted in a lower, now measurable melting point of 290 °C compared to ZTAP$_2$ which also optimizes its potential performance in subsequent chemical reactions and applications, as an example, it can be more easily sublimated at low pressures for surface deposition.

IV.3.7. Oxidation of ZTAP

The selective bromination of the ZTAP molecule was performed using N-bromosuccinimide (NBS). This molecule is known for facilitating bromination reactions. Despite our goal of achieving bromination, the reaction predominantly resulted in an oxidative process rather than the incorporation of bromine atoms into the ZTAP molecule as shown in Figure 69.

This outcome can be attributed to the dual role of NBS who can also act as an oxidizing agent under certain reaction conditions, in this case, in chloroform at room temperature. This resulted in the efficient selective formation of C-C single bonds caused by the oxidative coupling of 2 ZTAP$_1$ molecular entities on the central carbon atoms of the anionic polymethine group that dimerized to form d-ZTAP$_1$. This product gave a deep blue color in $CHCl_3$ and was obtained in 66 % yield. An analogous d-ZTAP$_1$ compound was

previously obtained and characterized in 2018 by Koutentis and coworkers by the oxidation of **ZTAP$_1$** in the presence of (bis(trifluoroacetoxy)iodo)benzene (PIFA).[6]

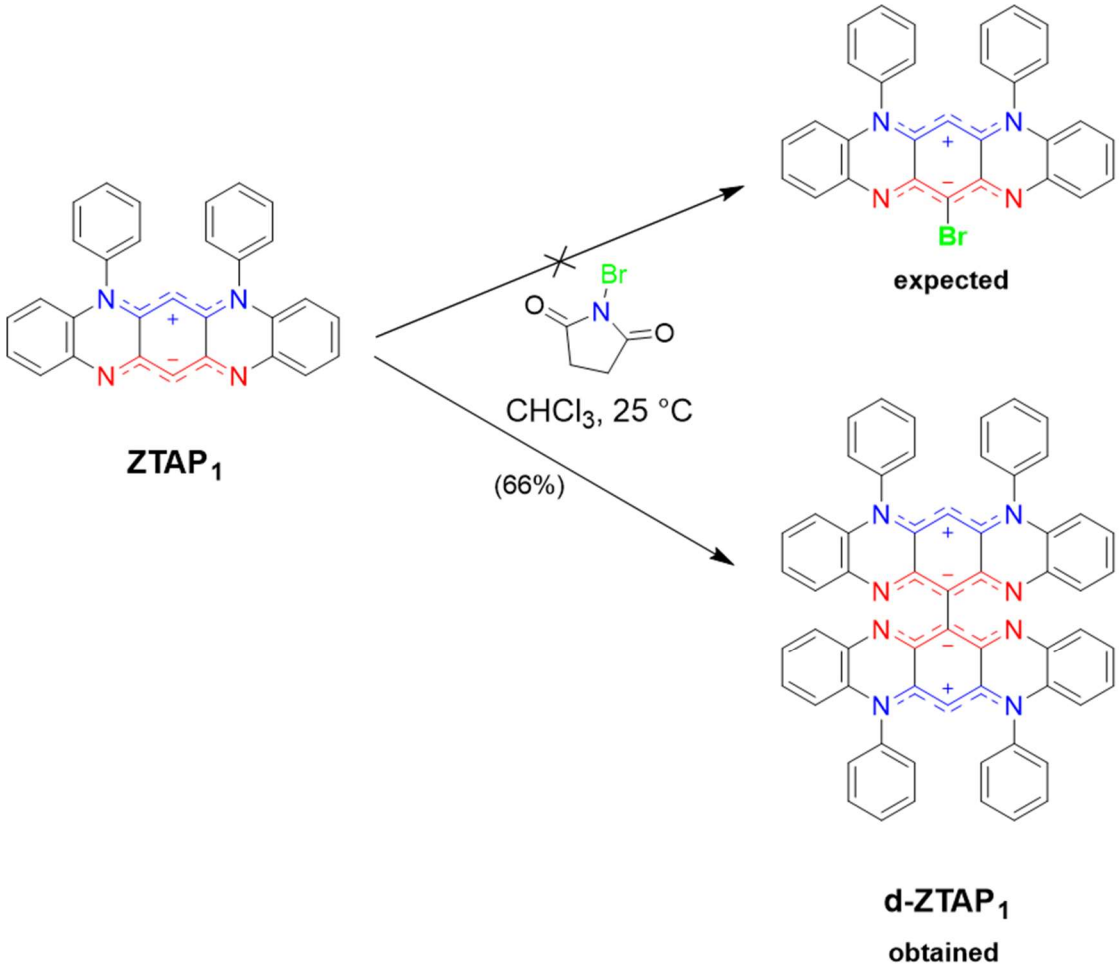


*Figure 69: The synthesis of dimer **d-ZTAP$_1$***

The ^{1}H NMR data collected in deuterated trifluoroacetic acid (TFA-*d*) due to solubility issues supports a symmetrical structure. The ^{1}H NMR data supported the loss of the signal of the anionic central carbon of the trimethine unit of ZTAP$_1$ at 6.16 ppm. This dimer shows high thermal stability with a decomposition point above 340 °C.

IV.3.8. Optical characterization of ZTAP

To initiate the investigation of the optical properties of ZTAP the electronic absorption spectra of the zwitterionic ZTAP$_{1\text{-}3}$, the mono-protonated ZTAP$_{1\text{-}3}$. H$^+$, and the bis-protonated ZTAP$_{1\text{-}3}$. 2H^{2+} derivatives were recorded in dichloromethane (see Figure 70) with the zwitterionic form ensured in solution by the addition of drops of 98 vol % DBU.

The spectrum of ZTAP$_1$ in black line exhibits 3 low-energy absorption bands at 642 nm, 702 nm and a maximum at 762 nm with molar extinction coefficient for the maximum in the order of 3.48x10^4 M^{-1}.cm^{-1} in dichloromethane. Additionally, 2 bands around 420 nm and a band around 300 nm are observed.

With the gradual addition of TFA to the cuvette already containing ZTAP and DBU drops, mono-protonation occurs.

Upon mono-protonation of a nitrogen atom of the anionic trimethine of ZTAP, the polymethine is modified to a cationic polymethine and $ZTAP_1.H^+$ is obtained. A significant blue shift is observed for the low-energy π-π* transitions as the maximum shifts to 669 nm with molar extinction coefficient in the order of $5.22x10^4$ $M^{-1}.cm^{-1}$ in dichloromethane. The color of the solution changes from green to light blue and the n-π* transitions at 420 nm observed for the $ZTAP_1$ are lost and blue shifted.

TFA is added in excess to a cuvette containing $ZTAP_1$ and the color changes from green to dark blue with the bis-protonation of $ZTAP_1$, to get $ZTAP_1.2H^{2+}$, a bis-cationic polymethine. The spectrum shows the most blue shifted bands with the low energy bands being most intense with the maximum shifting towards 657 nm with molar extinction coefficient in the order of $12.64x10^4$ $M^{-1}.cm^{-1}$ in dichloromethane. The spectra for ZTAP are displayed in the Figure 70.

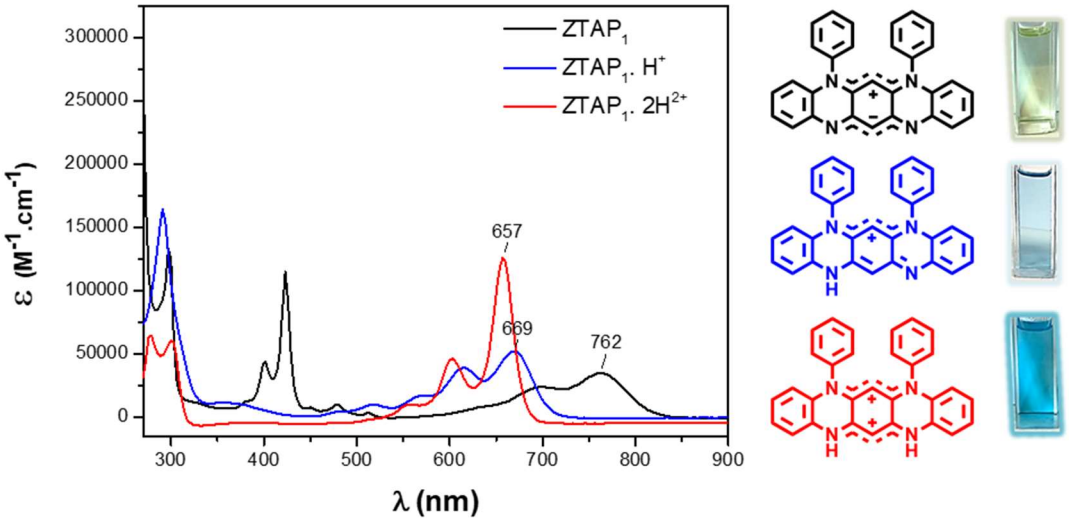


*Figure 70: UV-vis spectra of **$ZTAP_1$**, **$ZTAP_1.H^+$** and **$ZTAP_1.2H^{2+}$** in dichloromethane. Concentration of **$ZTAP_1$** solution of 10^{-6} $mol.L^{-1}$.*

The emission spectrum shown in Figure 71 was recorded for the $ZTAP_1$ in DCM, showing an emission band at approximately 816 nm spanning the NIR region. The Stokes shift $\Delta\bar{\nu}$ is calculated in cm^{-1} using the formula shown in Figure 71 from the emission and absorption bands of $ZTAP_1$. The compound shows a small Stokes shift of 851 cm^{-1}, and the zwitterionic compound showed very weak fluorescence.

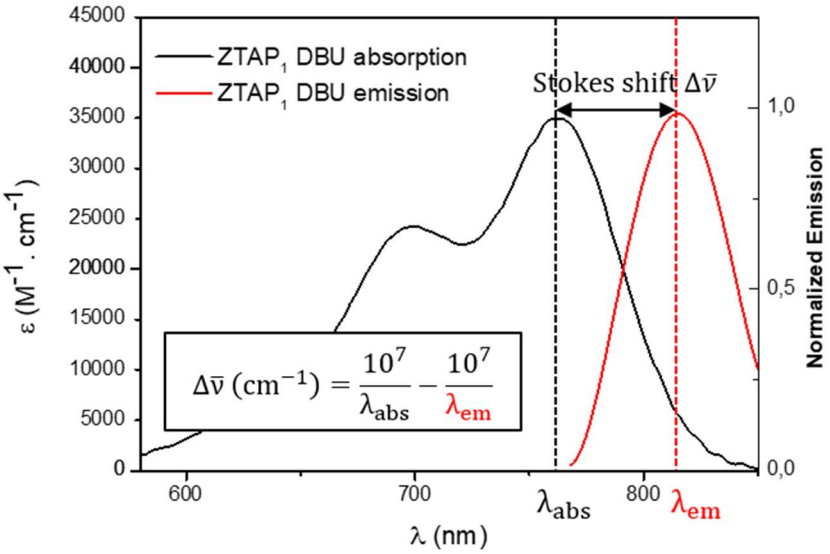


*Figure 71: Absorption and emission spectra of **ZTAP1**. The Stokes shift can be deduced from the maximum wavelength of the absorption and the emission spectra.*

The emission spectra of the mono-protonated cationic specie $ZTAP_1.H^+$ and the bis-cationic specie $ZTAP_1.2H^{2+}$ are plotted in Figure 72. $ZTAP_1.H^+$ shows an increase in the Stokes shift value to 2692 cm^{-1} with a strong increase in fluorescence (Quantum Yield of 11 %). Meanwhile $ZTAP_1.2H^{2+}$ emits before 700 nm and shows a very small Stokes shift 579 cm^{-1} with almost overlapping absorption and emission bands, and presents an increase in fluorescence (Quantum Yield of 16.6 %).

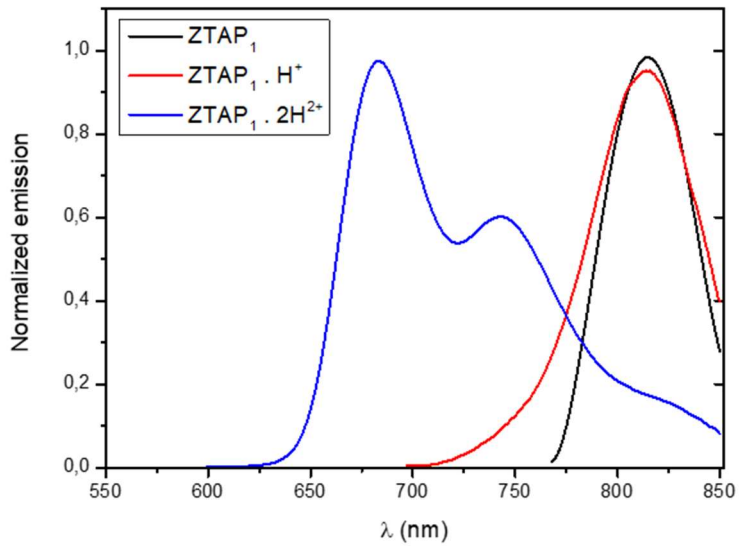


*Figure 72: Normalized emission spectra of **ZTAP1**, **ZTAP1.H+** and **ZTAP1.2H2+** in dichloromethane.*

The Table 3 summarizes the absorption and emission data of $ZTAP_{1\text{-}3}$. The data shows that from all the species, the zwitterionic compound presents the most redshifted absorption maxima and the bis-cationic presents the most blue shifted absorption

maxima. Remarkably low Stokes shift are observed for the bis-cationic compounds $ZTAP_2.2H^{2+}$ and $ZTAP_3.2H^{2+}$ The zwitterionic species also present the weakest fluorescence that increases with mono- or bis-protonation.

*Table 3: Experimental electronic absorption and emission properties of the compounds **ZTAP$_{1-3}$** dissolved in dichloromethane.*

Species	Conditions	λ_{max} [nm] (ε[10^4 M^{-1} .cm^{-1}])	Emission [nm]	Stockes shift [cm^{-1}]	Quantum yields [%]
ZTAP$_1$	**ZTAP$_1$** + DBU	762 (3.48)	814	851	-
ZTAP$_1$ .H$^+$	**ZTAP$_1$** + DBU+ TFA	669 (5.22)	816	2692	11.1
ZTAP$_1$ .2H^{2+}	**ZTAP$_1$** + TFA	657 (12.64)	683	579	16.6
ZTAP$_2$	**ZTAP$_2$** +DBU	759 (1.79)	810	829	-
ZTAP$_2$ .H$^+$	**ZTAP$_2$** +DBU+TFA	675 (2.56)	705	630	11.2
ZTAP$_2$ .2H^{2+}	**ZTAP$_2$** + TFA	657 (6.82)	677	450	6.3
ZTAP$_3$	**ZTAP$_3$** + DBU	768 (2.95)	816	765	-
ZTAP$_3$ .H$^+$	**ZTAP$_3$** + DBU+TFA	666 (10.18)	707	871	10.4
ZTAP$_3$ .2H^{2+}	**ZTAP$_3$** + TFA	657 (3.68)	677	450	7.1

Having explored how the different peripheral functional groups alter the optical properties of the zwitterionic, cationic and bis-cationic polymethines, it is important now to examine how these molecules behave when they form dimers. The UV-vis absorption spectra of ZTAP and d-$ZTAP_1$ are represented in Figure 73. The spectra are normalized to the absorbance value of the band with maximum absorption in the NIR region.

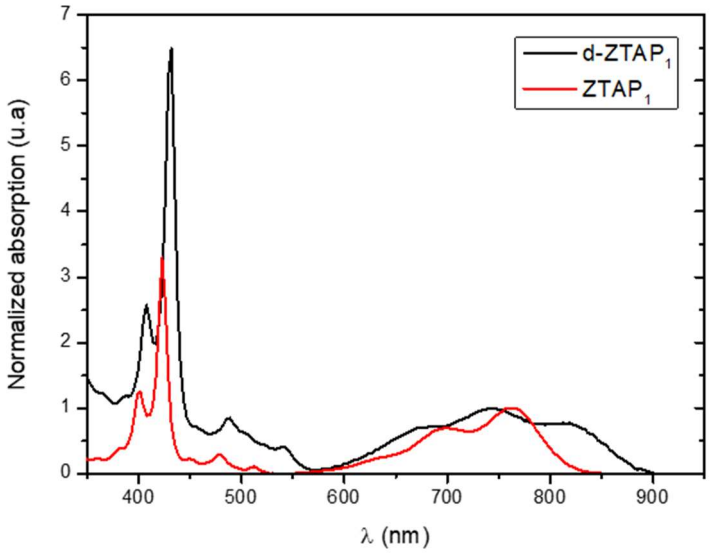


*Figure 73: UV-vis study in dichloromethane of **ZTAP₁** (black), **d-ZTAP₁** (red). The spectra were normalized on the maximum wavelengths λ_{max}. Concentration = 10^{-5} mol.L^{-1}*

The UV-vis spectrum of the dimer d-ZTAP$_1$ shows a red shifted low-energy absorption band with respect to the low-energy band of the spectrum of ZTAP$_1$. This effect is indicative of exciton coupling between the nearly orthogonal azaacene moieties. In fact, when the 2 ZTAP$_1$ molecules are in close proximity, their electron wavefunctions overlap, leading to the coupling of excitons. This interaction results in energy level S_1 splitting, forming 2 distinct energy states: a higher energy state (anti-symmetric combination) and a lower-energy state (symmetric combination) (see Figure 74).

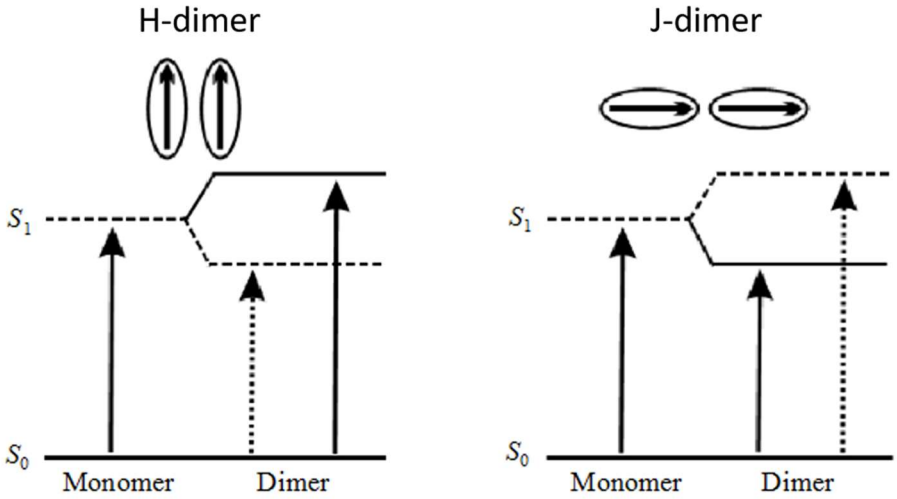


Figure 74: Simplified schematic of exciton theory. H-dimer, J-dimer and corresponding energy levels. Reproduced from earlier work.[147]

The C-C bond between the ZTAP$_1$ monomers permits a twisted conformation of these molecules as a dimer. The d-ZTAP$_1$ molecule condenses in a parallel way (plane-to-plane stacking) to form an H-dimer, or in a head-to-tail arrangement (end-to-end stacking) to form a J-dimer. In J-dimers, transitions to the lower energy excitonic state dominate,

causing a red shift in the absorption spectrum. Meanwhile, for H-dimers, transitions to the higher energy excitonic state dominate, leading to a blue shift in the absorption spectrum. The observed red shift for d-ZTAP$_1$ in Figure 73 confirms that this coupling is strong as observed in J-dimerization.

These results show the impact of molecular interactions and structural modifications on the electronic properties of ZTAP derivatives. The data are summarized in Table 4. It adds to the idea that one can manipulate the molecular properties of a molecule by changing its peripheral functional groups.

*Table 4: Experimental electronic absorption and emission properties of the compounds **ZTAP$_1$, d-ZTAP$_1$** and **R-ZTAP$_2$** dissolved in dichloromethane solution.*

Species	λ_{max} [nm] (ε[10^4 M^{-1}.cm^{-1}])	Stockes shifts [cm^{-1}]	Quantum yields [%]
ZTAP$_1$	762 (3.48)	851	-
d-ZTAP$_1$	819 (0.07)	Not measured	Not measured
R-ZTAP$_2$	666 (1.59)	569	6.7

IV.4. Conclusions

This chapter focused on the synthesis and characterization of a series of molecules, including QZ, ZTAP derivatives, d-ZTAP$_1$, and R-ZTAP$_2$. The primary objective of this work is to design zwitterionic compounds that meet requirements for supramolecular assembly, aiming to create a library of molecules that can be tested and used to modify the molecular packing. By modifying the peripheral functional groups of the **ZTAP** molecule, we maintained their zwitterionic nature while changing the molecule's geometry and reactivity. This is crucial for their self-assembly behavior on surfaces, and these compounds are selected with the intention of better understanding how different the different size of the molecules (tetraazapentacene or quinone), or the different peripheral functional groups impact the molecular arrangement on surfaces as well as the resulting properties.

The synthesis of the QZ derivative followed a straightforward well-established pathway, in contrast to the synthesis of ZTAP, which involved a less familiar process and proved to be challenging. However, their synthesis was a success despite the challenges in synthesis and characterization.

This success provided an opportunity to further characterize the ZTAP molecules and during this process we observed an unexpected oxidation of ZTAP into its dimer form d-ZTAP$_1$, the reductive dehalogenation of ZTAP and showed a novel synthesis of R-ZTAP$_2$.

Looking ahead, the next chapter will make use of the molecules QZ_7 and $ZTAP_1$, that we will refer to as DPQZ and ZTAP respectively. These molecules will be deposited on graphene and graphitic surfaces and their self-assembly behavior will be studied at the atomic scale by scanning tunneling microscopy.

V. DPQZ growth on HOPG and graphene

This chapter will describe a study of the diphenyl functionalized *p*-benzoquinonemonoimine zwitterion (DPQZ), on HOPG and monolayer graphene surfaces. The study is performed by STM and numerical simulations support the results. We show that the molecular phase on both substrates exhibits a structurally identical antiparallel dipole alignment in a head-to-tail dimer configuration structurally characterized at the molecular scale.

The DPQZ molecule, schematically represented in the Figure 75, was synthesized and purified according to established procedures.[148,149]

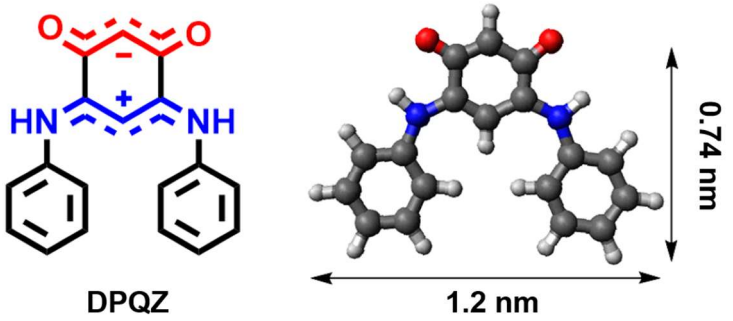


Figure 75: Schematic representation of the di-phenyl p-benzoquinonemonoimine zwitterion molecule DPQZ. The measured dimensions of the molecule in ball and stick model are shown.

V.1. STM study of DPQZ on HOPG and graphene surfaces

All STM experiments and sample preparations were performed under UHV conditions using a commercial low-temperature STM with pressures in the 10^{-11} mbar range. The HOPG surface was prepared by scotch tape mechanical cleaving, followed by annealing at 400 °C for 1 h under UHV. The DPQZ molecules were deposited with high reproducibility by thermal sublimation from a molecular Kentax evaporator with the quartz crucible held at 135 °C. One monolayer (1ML) of these molecules was deposited on a HOPG(0001) surface at room temperature after 8 min of exposure under UHV in the 10^{-10} mbar range during the deposition. The sample was then transferred into the analysis chamber and cooled to liquid nitrogen temperature (78 K). The graphene surface was synthesized *via* 4H-SiC(0001) sublimation at low argon pressure.[94,150] Once introduced in the UHV chamber it was annealing at 400 °C for 1 h before deposition. 1 ML of DPQZ molecules was deposited after 8 min exposure under UHV on a graphene on the 4H-SiC(0001) surface cooled to roughly - 140 °C.

The cleanliness and structural quality of the substrates was checked by STM prior to any deposition. The STM images were obtained in constant current mode at the liquid nitrogen temperature for both the sample and the electrochemical etched tungsten tips. The free software package Gwyddion was used for the analysis of the STM images.[80] All STM images presented are raw acquired data except for standard plane sutransbtraction and one-dimensional Fast Fourier Transform (1D-FFT) filtering at 150 Hz along the horizontal direction.

V.1.1. DPQZ assembly on HOPG

V.1.1.1. Molecular self-assembly of DPQZ

The constant current STM image in Figure 76(a) shows the extended molecular phase with a single orientation after the deposition of DPQZ molecules on HOPG surface. The bright or dark large-scale bent bands visible below the surface are dislocations or stacking defaults on the HOPG surface attributed to the stacking of HOPG sheets. Considering only the molecular layer, this image displays a single phase extended on over more than 400 nm in diameter. This phase comprises multiple domains, all of which have the same orientation (Figure 76(b)). The domain boundaries are marked with red arrows on Figure 76(b). The domains exhibit anisotropic growth behavior with almost uninterrupted growth (several micrometer) in the direction of the red arrows. On the contrary, in the direction of the white lines, their size varies from ~ 9 nm to several tens of nanometers. This anisotropic behavior is discussed further below. In addition to domain walls, periodic

lines of brighter contrast can be distinguished and are highlighted by white lines in Figure 76(b-c).

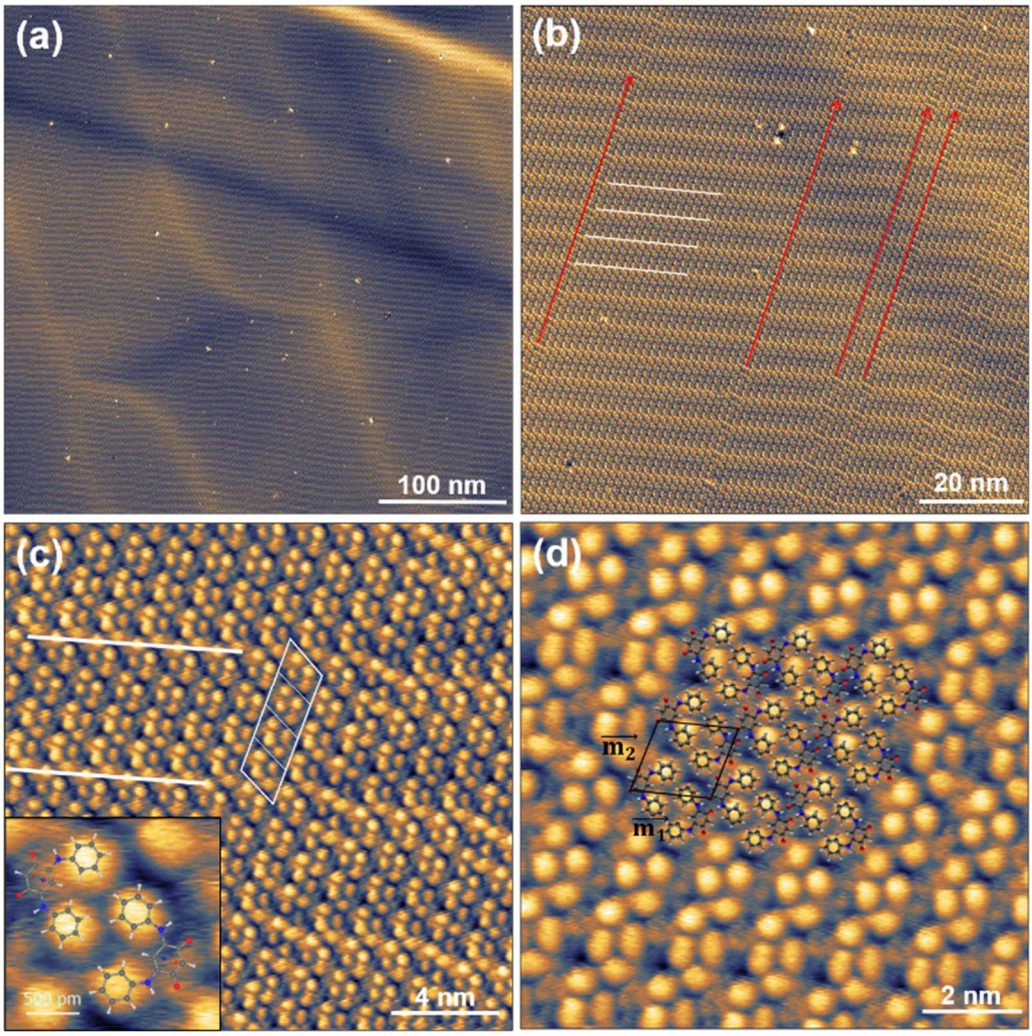


Figure 76: STM images of the same area of DPQZ molecules adsorbed on a HOPG surface at different scales. The images were recorded at a tunneling current of I_t= 2 pA and a sample voltage of V_{bias}= 1.0 V. ***(a)*** *Large scale image showing the extended molecular phase with a single orientation.* ***(b)*** *Domain boundaries highlighted with red arrows and moiré effects are observed on the surface are highlighted by white lines.* ***(c)*** *The predominant molecular motif is highlighted by a white parallelogram.* ***(d)*** *The proposed molecular-scale model.*

Between 2 lines of brighter contrast, one can distinguish 4 identical, periodic motifs highlighted by a white parallelogram (Figure 76(c)). Each motif consists of 4 bright features and 2 dark features (see inset of Figure 76(c)). Given the size and angles of the molecules, we attribute the bright features to the aromatic cores and the darker features to the quinonoid cores of 2 DPQZ molecules.

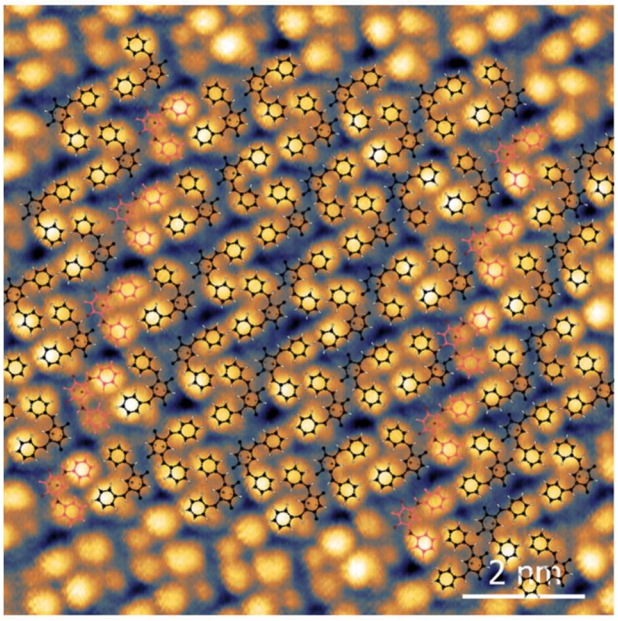


Figure 77: STM image of the monolayer of DPQZ on HOPG surface with the molecular network. The image was recorded at a tunneling current of I_t= 2 pA, and a sample voltage of V_{bias}= - 1.45 V.

The high-resolution STM image in Figure 77 shows the presence of a domain border characterized by a shift in the position of a molecule comprised in a motif. 2 symmetrical and equivalent configurations for the molecular motif are observed leading to mirror domains.

According to this adsorption geometry, the DPQZ self-assemble in a head-to-tail configuration with their dipole moment aligned along $\mathbf{m_1}$. This assembly geometry seems to be guided by NH···O hydrogen bonds following a similar intermolecular interaction reported for zwitterionic quinonemonoimines.[53,122,133,151–154]

V.1.1.2. Epitaxy with the substrate

It is important to note that the origin of the periodic bright lines along $\mathbf{m_1}$, which leads to a moiré pattern, could be a consequence of the lattice mismatch between the molecular network and the HOPG network. To explore this hypothesis, we establish the epitaxial relationship between these 2 networks. True epitaxy implies congruence of adsorbate and substrate lattices at the unit cell level. However, very often, these strict conditions are not met, and one possible alternative is the formation of a HOC superstructure that can be accompanied by a moiré pattern. Commensurate moiré patterns can be viewed as actual superstructures and are described by a unit cell with lattice parameters and a lattice defined through base translation vectors that we will name $\mathbf{a_{moiré}}$ and $\mathbf{b_{moiré}}$.[155] These base translation vectors as well as the molecular lattice translation vectors $\mathbf{m_1}$ and $\mathbf{m_2}$ are associated to the substrate lattice translation vectors $\mathbf{g_1}$ and $\mathbf{g_2}$ by the following relationships:

$$\begin{pmatrix} a_{moiré} \\ b_{moiré} \end{pmatrix} = \begin{pmatrix} a_{1,1} & a_{1,2} \\ a_{2,1} & a_{2,2} \end{pmatrix} \begin{pmatrix} g_1 \\ g_2 \end{pmatrix} \quad (V.1)$$

$$\begin{pmatrix} m_1 \\ m_2 \end{pmatrix} = \begin{pmatrix} b_{1,1} & b_{1,2} \\ b_{2,1} & b_{2,2} \end{pmatrix} \begin{pmatrix} g_1 \\ g_2 \end{pmatrix} \quad (V.2)$$

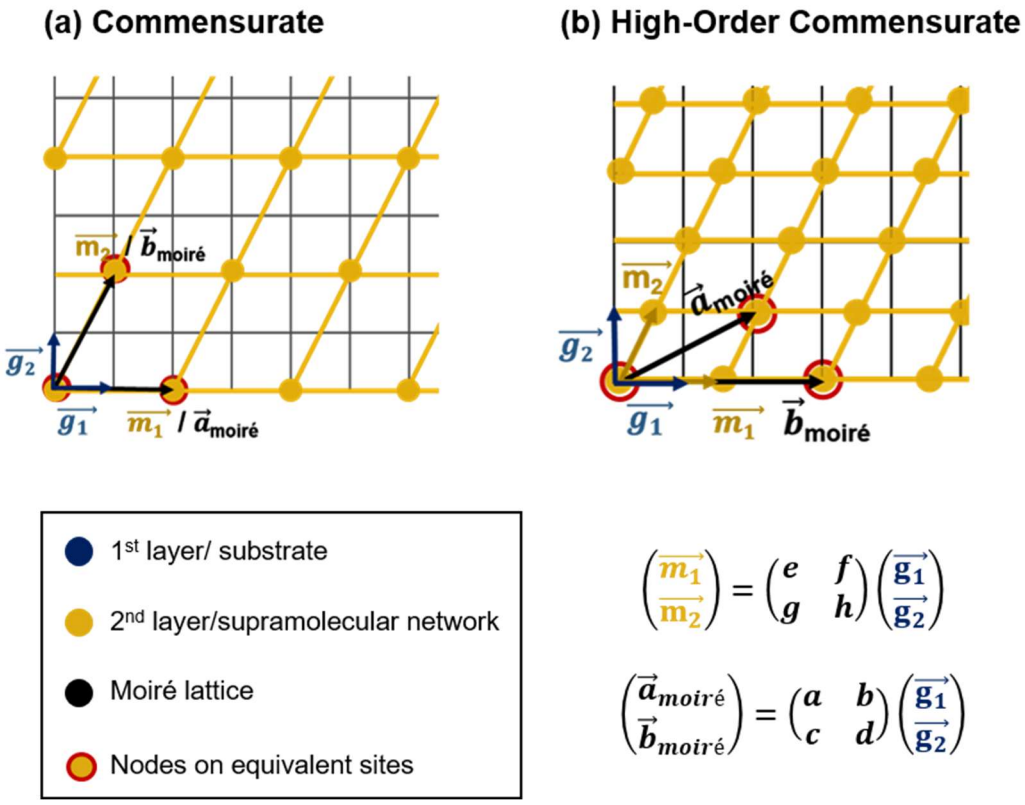


*Figure 78: Scheme illustrating examples of **(a)** commensurate structures and **(b)** high-order commensurate structures.*

To begin with the case where the correlation matrix coefficients of (A.) contain only integer numbers, the layers 1 and 2 are commensurate, and the moiré vectors coincide with the layer 2 or the supramolecular layer. Moving on to the next case, if the correlation matrix in (V. 1) contains only integer values, the superstructure originating from the molecular lattice and HOPG lattice mismatch can be qualified as being of the HOC type.

Additionally, when the network is commensurate (high-order or not); with one of the substrate's crystallographic directions, this case is described as a point-on-line-epitaxy (POL-E). Lastly, the incommensurable networks, where structures are linked by irrational numbers, which prevents commensurability with the substrate over distances compatible with the domain size.

V.1.1.3. Interfacial lattice correlation method

To get the interfacial lattice correlation on HOPG, the identification of diffraction spots using Low Energy Electron Diffraction (LEED) patterns becomes challenging due to the bending of carbon flakes on the surface.

We could compare both structures in real space with atomic resolution by using 2 high-resolution STM images of these networks. However, at the liquid nitrogen temperature, there is distortion of images caused by the thermal drift and creep of the piezo-electric scanner. These distortions are of a nonlinear character and their compensation involves the application of corrections on the vectors' lengths and angles. The error bars on these quantities, which we estimated by comparing images of the HOPG lattice and the molecular lattice acquired separately, lead to error bars > 1 on the correlation matrix coefficients. This prevents us from ensuring the strictly integer character of the coefficients of the correlation matrix, the true epitaxy relationship, and therefore the presence of a commensurate molecular phase. To avoid this, we can compare the 2 lattices in the same STM image. Thus, we deposited less than a monolayer of DPQZ molecules on the HOPG substrate and imaged at the interface between the organic layer and HOPG by STM (Figure 79(a)).

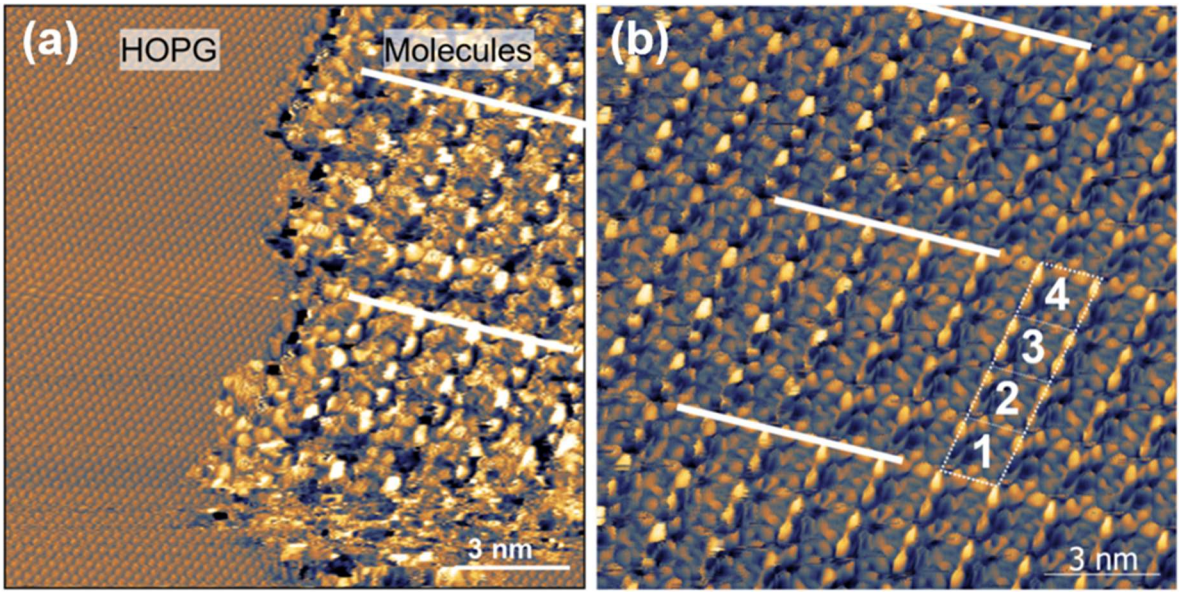


Figure 79: (a) STM image showing less than a monolayer of DPQZ molecules (the right side of the image) on HOPG (the left side of the image) surface with the moiré lines highlighted by white lines. (b) STM image of the molecules zone, white lines highlight the moiré. Between 2 moiré lines, there is 4 labelled identical molecular motifs highlighted by dashed parallelograms. The images were recorded at a tunneling current of I_t = 6 pA, and a sample voltage V_{bias} = 0.8 V.

In Figure 79(a), the molecular layer has a poor resolution because we adjusted the tunneling parameters to obtain atomic resolution on HOPG, which are not suitable to image the molecular layer that possesses a higher tunneling barrier than HOPG. Nevertheless, we can perceive the same molecular phase as the one observed at the

monolayer, which is made up of contrasting lines separated by 4 identical recurrent molecular motifs (see Figure 79(b)).

This poor resolution prevents us from directly acquiring the lattice parameters of the molecular layer; however, the information of the periodic character of the network is preserved and can be extracted.

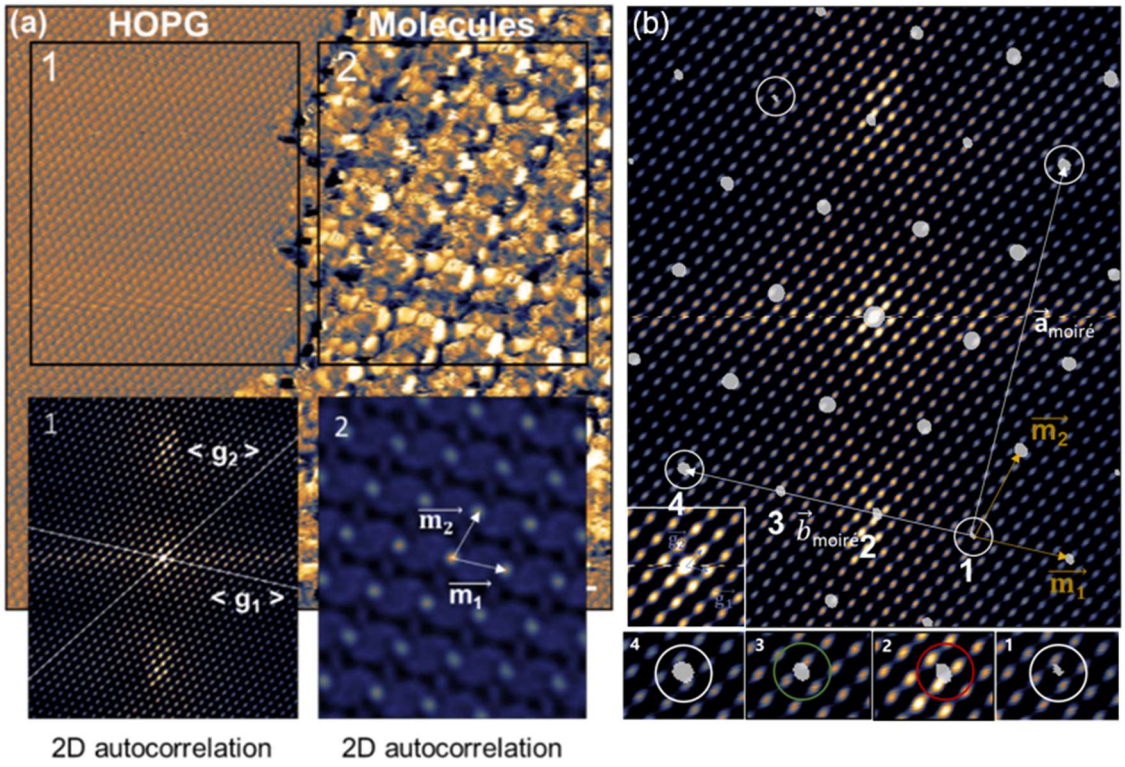


Figure 80: 2D autocorrelation treatment to extract the epitaxial relationship between the supramolecular phase and the HOPG surface. ***(a)*** *STM image on the border between the HOPG and the supramolecular phase. I_t= 6 pA, V_{bias}= 800 mV and of size 15 nm x 15 nm. 2 areas of this image, denoted by '1' and '2', are cropped and their 2D autocorrelation is calculated resulting in the 2 images below where lattice parameters can now be easily extracted.* ***(b)*** *The image resulting from the superposition of the 2 autocorrelation images extracted in (a). The molecular network nodes (white dots) are now clearly identifiable with respect to the HOPG network nodes (smaller yellow dots). In the lower part, a zoom of 4 successive molecular nodes in the* $\boldsymbol{m_1}$ *direction shows that nodes 1 and 4 have identical positions relative to the nodes of the HOPG. This identical molecular node position with respect to HOPG is found on other direction (*$\boldsymbol{a_{moiré}}$*) and is marked with a white circle.*

By using the image in Figure 80(a), we have developed a method that can relate the position of the center of each periodic motif of the molecular layer with respect to the HOPG network. This method consists first, in performing a 2D autocorrelation of 2 parts of this same image, one in the HOPG region and the other in the molecular region. Both parts have identical sizes and lie in the same horizontal band of the image, thus, undergoing the same thermal drift while imaging. Then, the contrast maxima are marked by threshold, and their positions are extracted. It is to be noted that these positions are those of the centers of each motif's features. The superposition of the extracted periodic molecular motif positions and the HOPG autocorrelation image gives the illustration in

Figure 80(b). In this figure, we can identify several molecular nodes whose positions relative to the HOPG nodes are identical: for instance, nodes 1 and 4 in the insets in Figure 80(b). The relative position corresponding to the nodes 1 compared to HOPG is found on the nodes 4 after a translation of vector -3 $\mathbf{m_1}$ ($\mathbf{b_{moiré}}$). It is also found after a vector translation of 4 $\mathbf{m_2}$-$\mathbf{m_1}$ in the $\mathbf{a_{moiré}}$ direction. As we periodically find equivalent positions of the molecular nodes in 2D, we can express the correlation matrix with integer coefficients in (V. 3) and show that the molecular layer assembles according to a 2D HOC phase on HOPG.

$$\begin{pmatrix} a_{moiré} \\ b_{moiré} \end{pmatrix} = \begin{pmatrix} -1 & 4 \\ -3 & 0 \end{pmatrix} \begin{pmatrix} m_1 \\ m_2 \end{pmatrix} = \begin{pmatrix} -14 & 27 \\ -17 & 0 \end{pmatrix} \begin{pmatrix} g_1 \\ g_2 \end{pmatrix} \qquad \text{(V. 3)}$$

The moiré effect is clearly visible on the STM images in the $\mathbf{a_{moiré}}$ direction, and the number '4' in the correlation matrix linked to $\mathbf{m_2}$ matches with the 4 motifs separation between the moiré lines. However, in the $\mathbf{b_{moiré}}$ direction, no periodic modulation of the STM contrast is distinguished, but a study of the height profiles makes it possible to detect a periodicity after 3 molecular motifs in the $\mathbf{b_{moiré}}$ direction (see Figure 81)

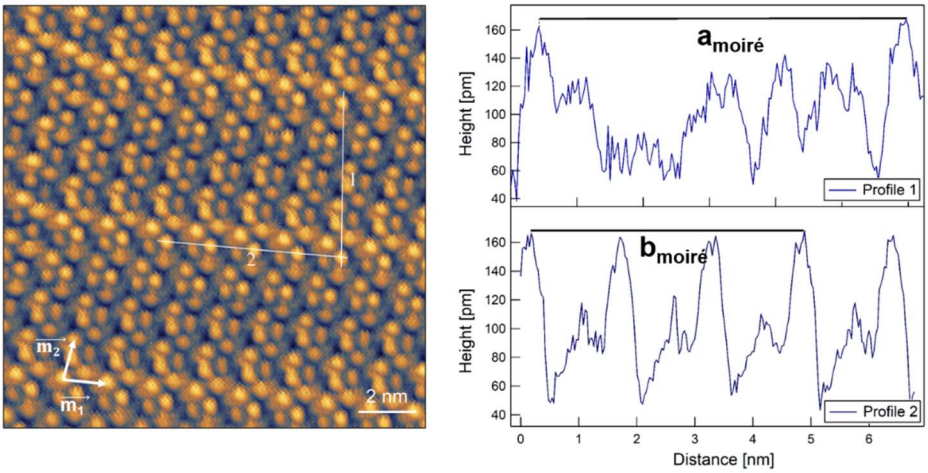


Figure 81: STM image and height profiles of DPQZ monolayer on HOPG. Line profile 1 performed along the $\boldsymbol{a_{moiré}}$ direction indicating a contrast peak after 4 molecular motifs along that direction. Line profile 2 performed along the $\boldsymbol{b_{moiré}}$ direction shows a very small but persistent increase in height after 3 molecular motifs along that direction.

Figure 81 shows an STM image of the adsorbed DPQZ on HOPG with a visible moiré pattern, which appears as brighter molecules features along a certain line. The line profile performed along $\mathbf{a_{moiré}}$ clearly shows a higher amplitude for the height measurement after **4** molecular motifs following $\mathbf{m_2}$ and one molecular motif following - $\mathbf{m_1}$. The line profile along $\mathbf{b_{moiré}}$ shows the structure periodicity in that direction as well as a slight increase in the height profile after 3 $\mathbf{m_1}$. We have to keep in mind that these profile measurements are not enough to prove the existence of a moiré pattern but add to the demonstration in Figure 80.

These results are confirmed by the fact that we found 3 identical molecular domains, rotated by 60° with respect to each other in accordance with the HOPG symmetry. By using (V. 3), we find the following theoretical values of the molecular lattice vectors m_1=1.39 nm and m_2=1.47 nm with an angle θ=77.34°. Taking the average of real space measurement on 3 STM images gives the experimental values $m_{1\text{-exp}}=1.56 \pm 0.2$ nm and $m_{2\text{-exp}}=1.46 \pm 0.2$ nm that makes and angle of $\theta_{exp}=77.09 \pm 1°$. Calibration coefficients $\alpha_{m_1}=m_{1\text{-exp}}/m_1$ and $\alpha_{m_2}=m_{2\text{-exp}}/m_2$ are deduced to be equal to 1.12 and 0.99 respectively.

It is important to keep in mind that the spots of maximum contrast in the autocorrelation image of the molecular phase do not mark the positions of the molecules but the positions of the smallest molecular periodic motif. This motif is composed of a dimer of molecules as illustrated in the inset of Figure 76(c). The high-resolution STM image of Figure 76(d) allow us to determine the relative distance between the molecular dimer and the molecule-molecule distance inside a dimer. These distances provide information about the nature of inter-molecular interactions and allow us to suggest an adsorption model guided by NH···O hydrogen bonds for the supramolecular phase.

The high-resolution STM image in Figure 82(a) highlights the presence of a domain border, which displays a shift in the position of the molecules comprised in the motif. If we name the phenyl rings of one DPQZ molecule of the dimer by '1' and '2' for the left and right rings respectively, we can presume the presence of 2 configurations A and B (inset in Figure 82(a). The configuration A, which is mostly observed, is characterized by the phenyl ring '1' positioned in between 2 phenyl rings of the second molecule of the dimer (to the right). At some point, a new configuration B emerges, and is characterized by conversely the phenyl ring '2' positioned in between 2 phenyl rings of the second molecule of the dimer, the configuration A follows next, and the domain borders consist of the translation of half-a-molecule following $\mathbf{m_2}$. A and B configurations are symmetrical with respect to $\mathbf{m_2}$ and equivalent, so they will give rise to 2 mirror domains A and B.

For example, in Figure 81, we see a succession of close-border domains. By making use of the obtained values of the correlation matrix, we can construct a simple ball and stick model of the arrangement that is shown in Figure 82(b-c), in which the molecules are assumed to be rigid, flat lying on the surface and in which the position of the first dimer of molecules is randomly chosen.

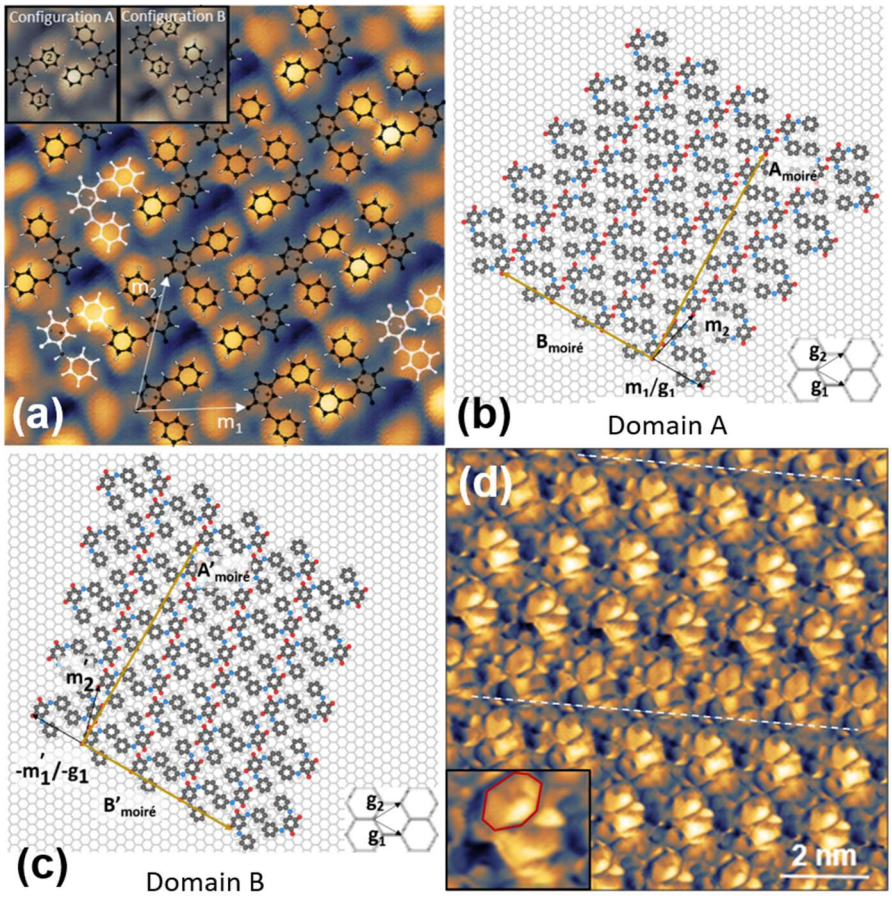


Figure 82: (a) High-resolution STM image highlighting the presence of a domain border (black line), characterized by a shift in the position of the molecules with respect to each other. The numbering of the phenyl rings accentuates this shift. In the molecular domain, the arrangement configuration A is characterized by a dimer with the phenyl ring '2' of the left molecule in between 2 phenyl rings of the right molecule, meanwhile the opposite configuration B happens on the domain border with a phenyl ring '1' of the right molecule between 2 phenyl rings of the left molecule. The image was recorded at a tunneling current of I_t= 2 pA and sample voltage of V_{bias}= - 1.70 V. (b) Suggested ball and stick model of the domain A with molecules assumed to be rigid and lying flat on the surface. This model makes use of the derived correlation matrix coefficients in (V. 3) and assumes a random position of the first dimer of molecules. The HOPG, molecular, and moiré lattice vectors are highlighted on the image. (c) Suggested ball and stick model of the mirror domain B with molecules. (d) High-resolution STM image obtained with a functionalized tip. White dashed lines highlight the moiré, having a different contrast. In the inset, the molecular motif, with a hexagonal-like shaped feature whose dimensions are compatible with a phenyl ring. This suggests a rotation of the phenyl rings out of the plane of the surface. The image was recorded at a tunneling current of I_t=4 pA and a sample voltage of V_{bias}=- 320 mV.

Figure 82(d) shows a high-resolution STM image of the same molecular layer phase obtained with a functionalized tip by an unknown cluster at the apex. The moiré lines of different contrast are highlighted with white dashed lines. The intramolecular resolution in the image clearly shows that the molecular motif encloses a hexagonal-like shaped feature (highlighted in red in the inset), whose dimensions are compatible with the dimensions of a phenyl ring. This feature suggests a rotation of the phenyl rings out of the surface plane. Steric hindrance and repulsive effects must also be considered, which complicates the prediction of the exact arrangement of the molecules on HOPG.

The results of Figure 82 allows to interpret the growth behavior of the 2D organic layer. In the Figure 76, we observe an anisotropic growth of the DPQZ molecules; a large domain extension following $\mathbf{m_2}$ with distances exceeding the micrometer, and smaller distances of the order of ten nanometers following $\mathbf{m_1}$. We can interpret this anisotropy as a response to the asymmetry of energy and directionality of the intermolecular interaction between the directions $\mathbf{m_1}$ and $\mathbf{m_2}$. In the direction $\mathbf{m_1}$, the interaction is related to a phenyl-phenyl interaction with 2 possible equivalent structural configurations (the 2 mirror domains A and B, see Figure 82) between successive molecules, resulting in frequent domain walls depending on which of these configurations is preferred. On the contrary, in the $\mathbf{m_2}$ direction, a much stronger and directive hydrogen-bond type interaction develops between 2 successive molecules without equivalent structural configuration, stabilizing the growth over extended distances into a single direction. This interpretation, as well as its implication on the growth will be further discussed below using the results of the structure calculations.

V.1.2. DPQZ assembly on graphene

DPQZ molecules were deposited on graphene cooled to – 140 °C to ensure the growth of a supramolecular lattice comparable to the HOPG case using the same molecular flux as in the DPQZ/HOPG case.

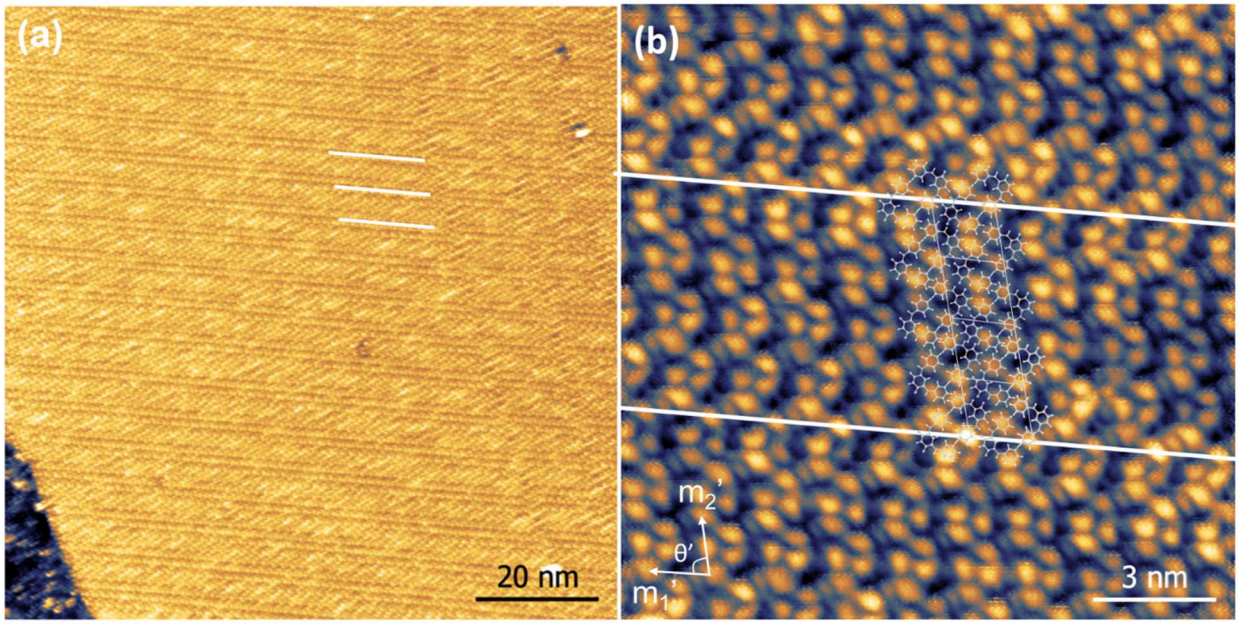


Figure 83: (a) STM image of the DPQZ molecules on graphene, white lines highlight the moiré. The image was recorded at a tunneling current of I_t= 2 pA, and a sample voltage V_{bias}= 1.50 V. (b) STM image of a monolayer of DPQZ molecules on graphene surface with the moiré lines highlighted by white lines. Between 2 moiré lines, 4 molecular motifs are highlighted by white parallelograms. The image was recorded at a tunneling current of I_t= 2 pA and sample voltage of V_{bias}= 0.30 V.

The Figure 83(a) shows a medium scale image of the self-assembled ML resulting from the adsorption of the DPQZ molecules on the graphene substrate. Periodic lines of

different contrast, assumed to be a structural Moiré, are observed and highlighted with white lines. On the high-resolution STM image in Figure 83(b) we see that we can identify 4 repeating units between 2 moiré lines; molecular motifs that enclose features similar to the ones observed on HOPG. We measure the molecular lattice constants to be $m'_{1\text{-exp}}$=1.54 ± 0.10 nm and $m'_{2\text{-exp}}$=1.44 ± 0.16 nm and an angle of 76.1°. These measurements are the average real-space measurements taken from nine images, where the uncertainty is based on the difference between the highest and lowest values measured. By applying the calibration coefficients α_{m_1} and α_{m_2} calculated in the previous subsection, we can correct these values to get $\mathbf{m_1}$'=1.37 nm and $\mathbf{m_2}$'=1.45 nm. These values are in very good agreement with the ones obtained for DPQZ /HOPG.

The similar structural Moiré and motif features, in terms of dimensions and angles, show that the self-assembly on graphene is structurally identical to the one on HOPG.

The findings from earlier publications reveal that HOPG can serve as a model surface for graphene [156–159], and our conclusions regarding the growth mode of the layer on HOPG and the supramolecular phase apply also to DPQZ on graphene/SiC.

To confirm the anisotropic growth interpretation and to explore the possibility for this supramolecular network to induce a periodic surface potential modulation, it is needed to simulate the different interaction energies, and the resulting dipole at the few-molecules scale.

V.2. Computational results

The computational chemistry calculations carried out in this part by Dr. Diego Cortes-Arriagada and Dr. Luis Sanhueza-Vega made it possible to explain the growth mechanism on the 2D self-assembly structure of the DPQZ molecules on graphene surfaces by giving the energetic order of magnitude of the intermolecular interaction and the molecule-substrate interaction and their physical origin.

It was determined that DPQZ molecules tend to self-assemble on graphene surfaces through stacked patterns of C_2 symmetry, influenced by hydrogen bonding and CH···HC interactions between phenyl rings (Figure 84(a)). This behavior aligns with the suggested model (Figure 84(b)) and STM images, indicating a decrease in torsion angle and a nearly flat arrangement of monolayers with strong intermolecular CAHB forces driving the 2D self-assemblies.

The orientation of the DPQZ molecules becomes nearly flat upon adsorption onto graphene, with a significant decrease in the torsion angle between rings, indicating strong intermolecular CAHB driving forces.

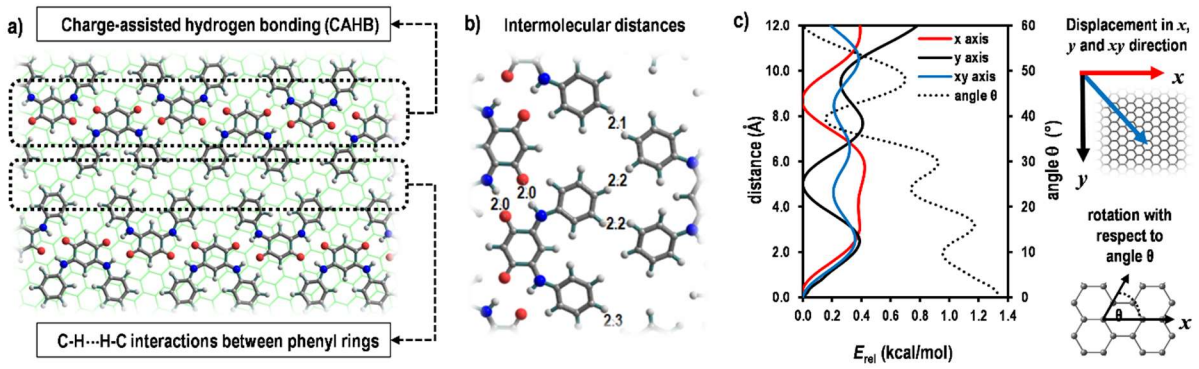


Figure 84: ***(a).*** *Computed adsorption pattern of the 2D self-assembly on graphene.* ***(b)*** *Intermolecular distances (in Å) between dimers on the 2D self-assembly.* ***(c)*** *Relative energy (E_{rel}, in kcal/mol) with respect to the ground state. Displacements of the 2D self-assembly along the x, y and xy direction of graphene. Rotation of the 2D self-assembly occurs with respect to the angle θ formed in benzene type rings of graphene.*

Their study further explored the potential energy landscape of the self-assembly (Figure 84(c)), revealing that metastable states can be reached by bypassing weak energy barriers of up to 0.4 kcal/mol (~ 0.02 eV). This information, in addition to the symmetry of the substrate, explains the presence of domains rotated at 60° from each other.

The stability of the structure is indicated by a binding energy of approximately 1.94 eV per DPQZ molecule, comparable to that of the *p*-benzoquinonemonoimine zwitterion on Cu(111) surfaces.[131] The DPQZ chains are stabilized by CAHBs with binding energies of 0.8 eV per dimer and by weaker CH···HC interactions, which are primarily driven by dispersion forces (van der Waals) in Figure 85(a). This combination of strong CAHBs and weaker dispersion interactions enhances the overall stability and contributes to the anisotropic growth behavior of the molecular assembly.

Detailed analysis of the graphene-DPQZ interface highlighted the interplay between dispersion (53%) and electrostatic effects (Coulomb interactions) (42 %), with both long-range driving forces playing crucial roles in the stability of the self-assembly.

Intermolecular π-π stacking between phenyl rings of DPQZ and benzene rings of the graphene surface contributed significantly to dispersion interactions (green regions in Figure 85(b)), while electrostatic interactions stemmed from the interaction between the activated carbon atoms of graphene and the charged C, O, and N atoms in the zwitterionic DPQZ molecules (green regions in Figure 85(b)). Despite destabilizing steric effects introduced by π-π stacking, (red regions in Figure 85(b)) the stability gained from dispersion and electrostatic effects was more important than destabilizing factors, resulting in stable self-assemblies ($|\Delta E_{dispersion} + \Delta E_{electrostatics}| > \Delta E_{Pauli}$).

Furthermore, the short-range stabilizing effects, i.e., charge transfer and polarization, have slight contributions to the stabilizing energy, with a combined contribution of 5 % per adsorbed dimer. Nevertheless, the graphene surface shows a small reorganization of the electron density upon adsorption resulting in a mutual polarization between graphene and DPQZ at 3.3 Å as shown in Figure 85(c). This matter induces multipole moments on the fragments. Most of the charge rearrangements in the graphene-DPQZ

interface occurs at the polarization step, which leads to electrons accumulating at intramolecular regions with an energy lowering of 0.12 eV per dimer.

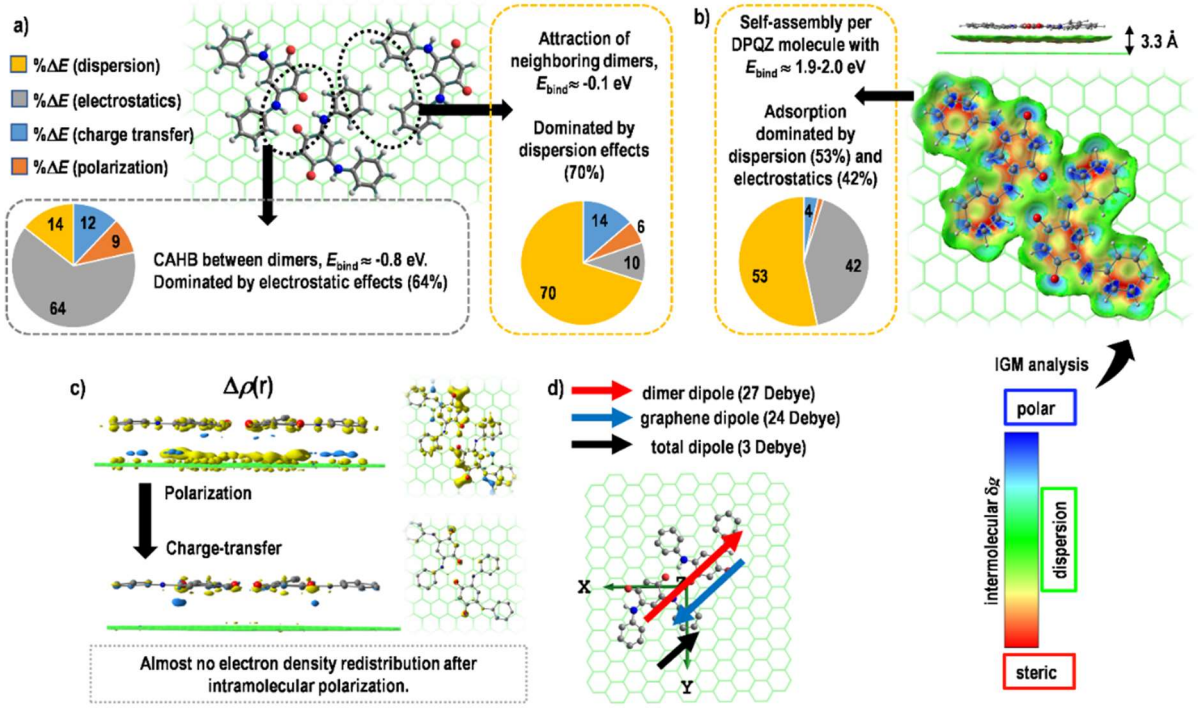


Figure 85: ***(a)*** *Intermolecular interactions between dimers and Absolutely Localized Molecular Orbital Energy Decomposition Analysis (ALMO-EDA) of driving forces.* ***(b)*** *Intermolecular interactions between dimers and graphene, with the quantitative/qualitative ALMO-EDA and Independent Gradient Model (IGM) results of intermolecular interactions.* ***(c)*** *Electron density difference [Δρ(r)] on local domains of the graphene-DPQZ interface and due to charge rearrangements resulting from polarization and charge-transfer effects.* ***(d)*** *Fragmental dipole moment analysis on local domains of the graphene-DPQZ interface.*

Due to a minimal orbital overlap with the gained electron density, weak electron transfer occurs in the graphene → DPQZ direction (~0.05 e per molecule) allocated near to the 2p orbitals of the oxygen atoms which stand for an energy lowering of ~ 0.32 eV per adsorbed dimer.

The electron density rearrangements will be responsible for the enhancement of the intermolecular electrostatic attraction (considering that graphene is non-polar before interaction) and induces a dipole on the graphene surface and adsorbed dimers.

The fragmental dipoles on the graphene and DPQZ dimers have different magnitudes of 23.8 and 27.2 Debye respectively, but are aligned in opposite directions. Consequently, the interface shows local dipoles aligned with the graphene surface plane (~ 3.4 Debye per adsorbed dimer).

Furthermore, the study elucidated the charge reorganization and polarization effects occurring at the graphene-DPQZ interface, leading to induced dipoles aligned with the graphene surface plane.

V.3. Conclusions

By analyzing the high-resolution STM images, we found that the DPQZ molecules physiosorbed in a head to tail self-assembled dimer configuration on HOPG as well as on graphene, with a visible structural Moiré effect. The study of the epitaxial relationship between the molecule lattice and HOPG lattice indicates that the origin of this visible moiré effect is due to the high order commensurability between the 2 layers. ALMO-EDA analyses confirm that the self-assembled DPQZ structure is stabilized by the formation of intermolecular CAHBs between dimers and by the dispersion attraction between the phenyl rings of neighboring molecules. The strong difference of these interactions in terms of directionality, binding energy and equivalent linking fully explains the anisotropic growth of the molecular layer. Although the dipole resulting from a molecular dimer vanishes, the redistribution of the electron density of graphene caused by the adsorption of this dimer breaks the symmetry of the resulting dipole and generates localized dipoles at the interface of approximately 3.4 Debye per dimer. These local dipoles meet one of the requirements for the modulation of the electrostatic surface potential and the engineering of the band structure of graphene.

As a perspective for future work, it could be possible to measure the local modulation of this surface potential at the molecular scale with the Kelvin spectroscopy method as well as the modifications of electronic density induced by the molecular layer.

VI. ZTAP on graphene

This chapter will describe a study of the 5,7-diphenyl-5H,12H-quinoxalino[2,3-b]phenazines (that will be referred to as ZTAP in the manuscript), deposited on graphene/4H-SiC(0001). ZTAP molecule is schematically represented in the Figure 86. The study aims to characterize the morphology and electrical properties of the surface of the resulting surface. The characterization of the system is done by the use of a closed-cycle LT-STM/nc-AFM operating at 8.9 K and a VT-AFM operating at RT.

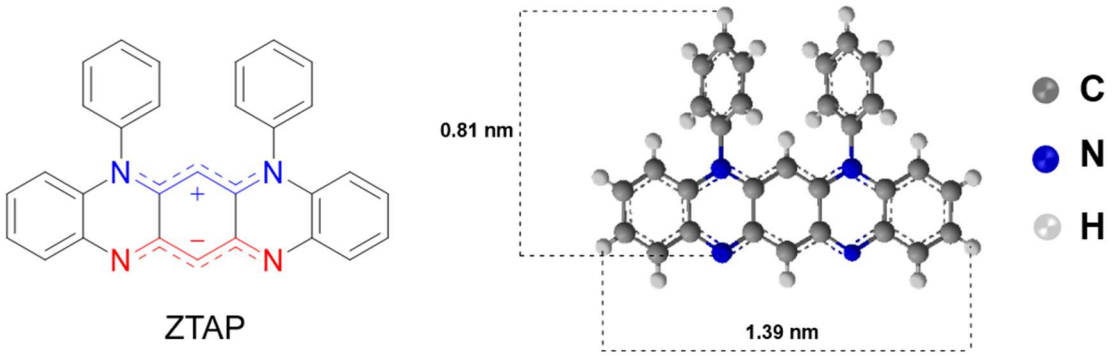


*Figure 86: Schematic representation of the 5,7-diphenyl-5H,12H-quinoxalino[2,3-b]phenazines (**ZTAP**). The dimensions of ZTAP are indicated on the ball and stick model.*

We show that the ZTAP molecular self-assembles in ribbons on graphene and that these molecules present a parallel dipole alignment oriented away from the surface. The dipole moment of ZTAP in this arrangement points away from the surface, modifying the surface potential of graphene, and is measured by Kelvin Probe Force Spectroscopy (KPFS) 4D maps The ZTAP molecule, is synthesized and purified according to an established procedure[160] that is detailed in the Chapter IV.

VI.1. Probing molecular self-assembly by STM

VI.1.1. Experimental Methods

The work was done on the 2 LT microscopes and on the VT-AFM, which were presented in II.4. Nc-AFM measurements, KPFM spectroscopies, and STS measurements were performed at IM2NP lab, while STM measurements were conducted at both CINaM and IM2NP labs.

The ZTAP molecules are deposited on graphene/4H-SiC(0001) with high reproducibility by thermal sublimation from a molecular Kentax evaporator with the quartz crucible held at temperatures ranging between 200°C and 210°C. Approximatively half-monolayer coverage was achieved on graphene substrate held at RT after 20 to 30 min exposure under UHV in the 10^{-10} mbar range during the deposition. The sample was then transferred to the analysis chamber and cooled to liquid helium (LHe) temperature (~ 8.9 K) prior to imaging. The cleanliness and structural quality of the substrates was checked by STM prior to any deposition. All STM images presented in this chapter are raw acquired data except for standard plane subtraction. The V_{CPD} maps were extracted using a Python program in appendix D.

VI.1.2. ZTAP assembly on graphene: STM studies

VI.1.2.1. Molecular self-assembly of ZTAP

The constant current STM image in Figure 87(a) shows that the ZTAP molecules self-assemble in a long-range monolayer on graphene in majority with domain sizes exceeding 400 nm. Smaller domains of uncondensed molecular phases were observed as well. This demonstrates the high mobility of ZTAP on graphene, as it was further evidenced by imaging, as molecules were frequently moving underneath the tip.

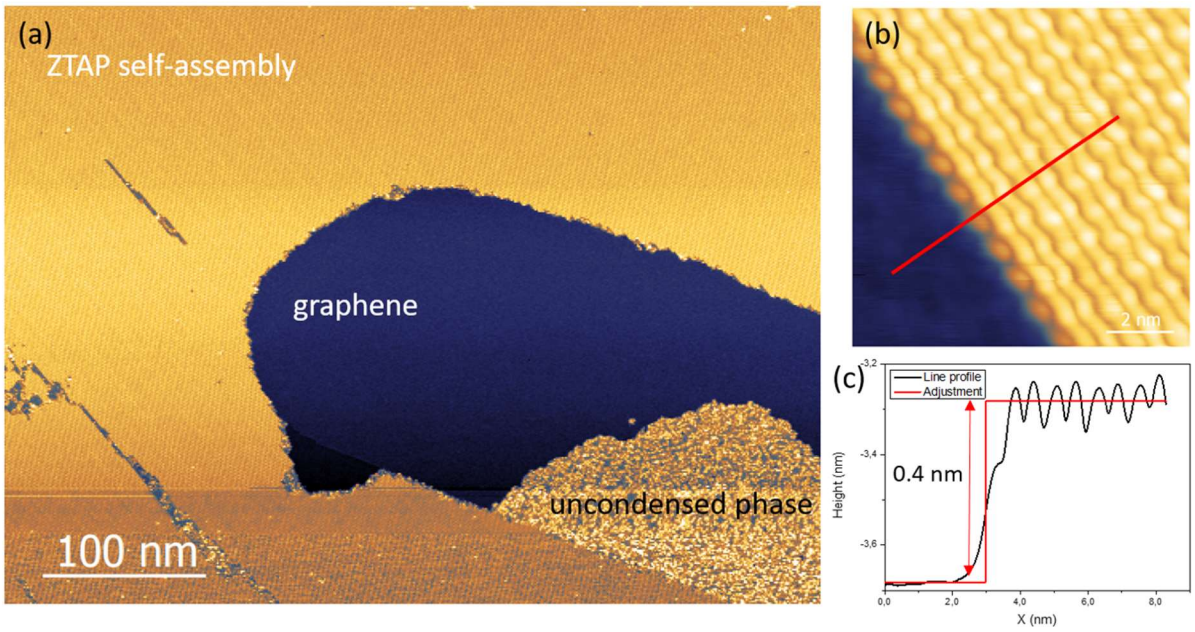


Figure 87: ***(a)*** *STM image of the deposit of ZTAP molecules on graphene. We observe a ML of ZTAP self-assembled and zones were the molecules could not yet condense into a supramolecular phase. Tunneling conditions: V_{bias}= 2.0 V, I_t= 10 pA.* ***(b)*** *STM image of ZTAP and graphene interface. The red line is a line profile. Tunneling conditions: V_{bias}= 2.2 V, I_t= 10 pA.* ***(c)*** *Plot of the line profile height as function of distance of the STM image of (b). The height of the molecule layer is approximately 0.4 nm.*

The monolayer is approximately 0.4 nm high, as shown on the height profile (Figure 87(c)) taken across the boundary between graphene and ZTAP self-assembled layer (Figure 87(b)).

Figure 88 shows 2 STM images of the ZTAP self-assembled phase on graphene, at a closer scale, on different zones of the surface. The unit cell of first layer is shown in Figure 88, where ZTAP organizes in ordered ribbon-like packing, the ribbon borders are delineated by white lines. Within these lines, the molecules assemble in parallel rows, with the number of rows typically ranging from 3 to 5 (3 $\mathbf{m_2}$ to 5 $\mathbf{m_2}$), occasionally extending to 6 or 7 (6 $\mathbf{m_2}$ to 7 $\mathbf{m_2}$). The most frequently observed configuration consists of ribbons composed of 3 rows.

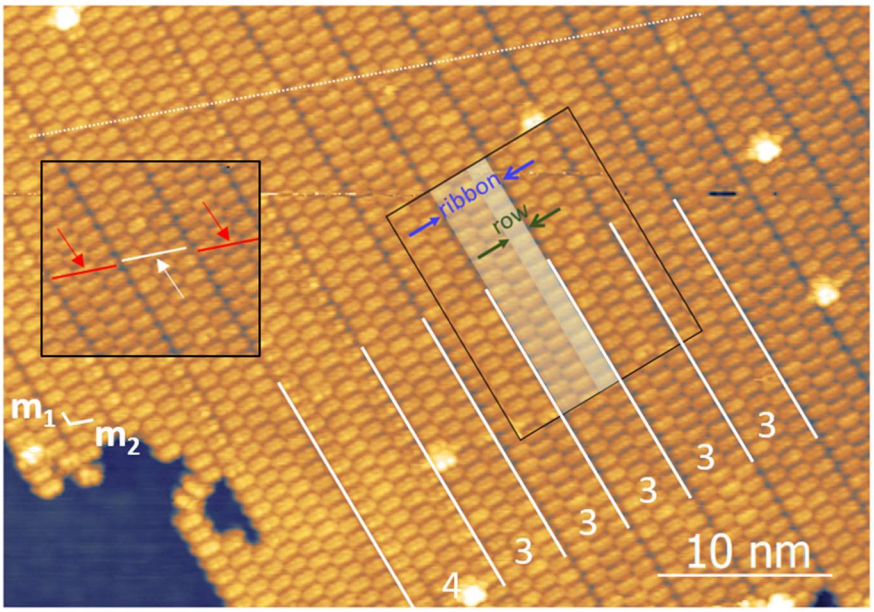


Figure 88: STM image showing a supramolecular assembly of the ZTAP molecules on graphene. White lines delimit ribbon edges and the number indicates the number of rows comprised in a ribbon. The inset shows that not all the ribbons are aligned and do present a shift on certain zones. Red and white lines and arrows show the shift of the ribbons. The molecular unit cell is indicated by ($\boldsymbol{m_1}$,$\boldsymbol{m_2}$). A white dashed line shows that the molecules between successive ribbons are aligned along the direction $\boldsymbol{m_2}$. Tunneling conditions: V_{bias}= 2.1 V, I_t= 10 pA.

After examining various zones on the surface, it is concluded that the ribbons alignment is not homogeneous across the surface. A slight shift of around 80 pm of the molecules is observed following $\mathbf{m_1}$ and is shown by the red arrows in the inset of Figure 88. This shifted distance is smaller than the lattice parameter of graphene, thus, this shift cannot be attributed to an adsorption site hopping.

The intermolecular inter-ribbon distance, will be defined as the separation between consecutive molecules between 2 adjacent ribbons, and the intermolecular intra-ribbon distance as the separation between molecules within a single ribbon. These distances were measured and found to be equal within an error margin of 50 pm. The measurements have been done on multiple height profiles and the error margin was defined as the range between the maximum and the minimum values across the dataset.

The average intermolecular spacing is approximately 1.42 nm along the $\mathbf{m_2}$ direction. Despite the slight measured shift from one ribbon to another, which could be attributed to a contrast effect, the ZTAP molecules are aligned along $\mathbf{m_2}$ between successive ribbons, a white dashed line shows this alignment on the Figure 88. A different type of shift is occasionally observed, for an entire row of molecules along a ribbon in the direction $\mathbf{m_2}$, as shown in the STM image of Figure 89(a).

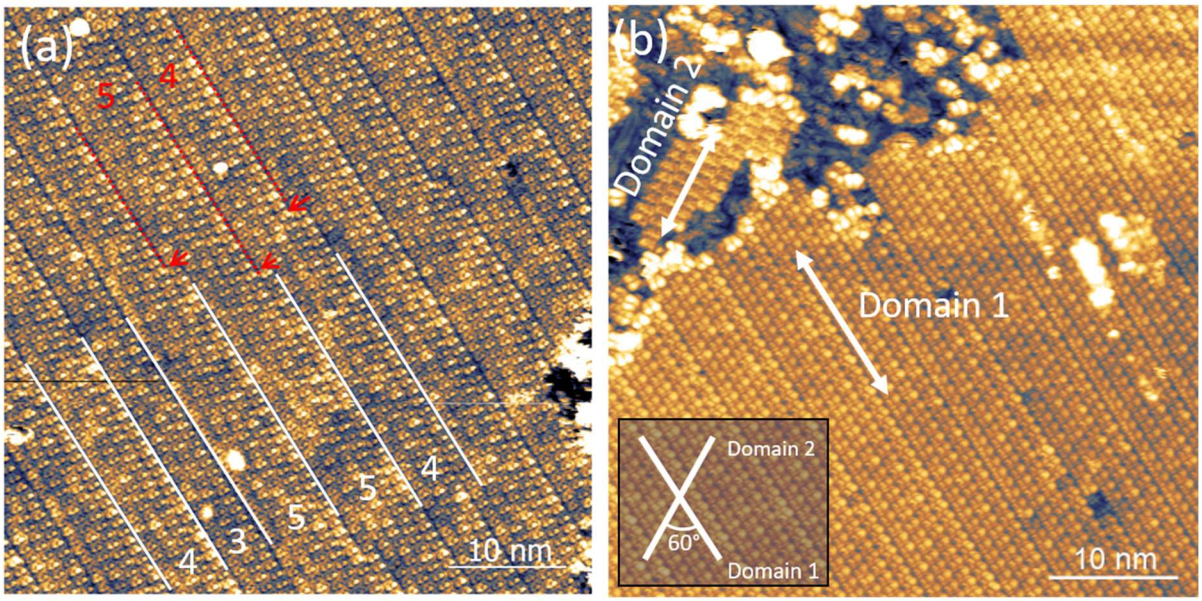


*Figure 89: **(a)** The number of rows in the ribbons is indicated for each row, and a shift to the left of one molecule of the whole ribbon can occur for some ribbons on the surface, red arrows highlight the shift. Tunneling conditions: V_{bias}= 1.3 V, I_t= 10 pA. **(b)** STM image showing the ZTAP supramolecular assembly on graphene. On the upper left corner of the image is a zone where the molecules do not condense in a supramolecular phase. On the same image are shown 2 domains oriented at 60° from each other whose directions are shown in double arrow lines and reproduced in inset. Tunneling conditions: V_{bias}= 1.6 V, I_t= 10 pA.*

Beyond the variation of ribbon row numbers, the surface investigation shows molecular domains that grow in various directions at an angle of 60° relative to each other, reproducing graphene's crystallographic symmetry. This directed growth suggests a point-on-line epitaxy of the ribbons' longitudinal direction $\mathbf{m_1}$ with a crystallographic direction of graphene, which is discussed below in VI.1.2.2. An example of the 2 domain orientations is presented in the STM image of Figure 89(b), the ribbons directions are annotated by double arrows and each direction is assimilated to a domain. The domain 2, present as a minority on the surface, forms a 60° angle with the predominant domain 1, and the remaining portion of the image consists of a molecular uncondensed phase.

Now that the molecular domains composition has been characterized at macroscopic scales and medium scales, we will study the structure at the large and molecular scales in order to understand the slight shift of 80pm in the $\mathbf{m_1}$ direction. The domain 1 at a large scale is shown in Figure 90(a) and the same zone imaged at the closer scale is shown in Figure 90(b). The STM image of Figure 90(a) shows the large domain 1 of the ZTAP ribbons that presents a visual STM chevron superstructure upon 2 successive ribbons,

whose contrast is highlighted in red. This contrast alternates from a ribbon to another and only appears at the large scale. This domain is examined at a close-scale with the help of the STM image of Figure 90(b). At the closer scale, the chevrons contrast disappears and the ribbons are always aligned following $\mathbf{m_2}$ between successive ribbons, thus the 80 pm inter-ribbon shifts observed are attributed to an imaging artefact (see the white arrow following $\mathbf{m_2}$ on the Figure 90(b)).

Figure 90(b) shows a zoom-in on the ribbons, each ribbon comprising 3 rows of a repeating motif. This motif is made of 2 bright features which have a combined diameter of 1 nm (see Figure 90's additional magnified unit cell image).

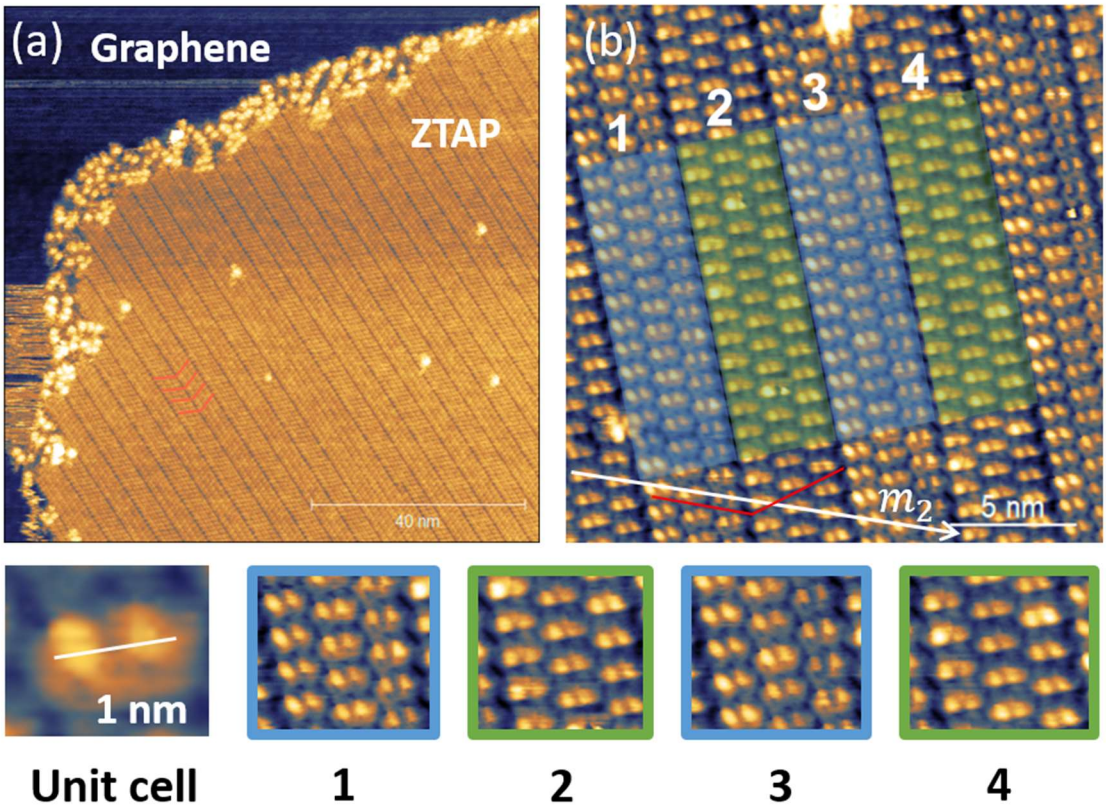


*Figure 90: **(a)** STM image showing a supramolecular assembly of the ZTAP molecules on graphene. A chevron superstructure is apparent and highlighted in red. Tunneling conditions: V_{bias}=2.3 V, I_t= 5 pA. **(b)** Ribbons of molecules each constituted of 3 rows of molecules. Alternate ribbons display a different STM contrast. Ribbons 1 and 3 highlighted in blue display the same contrast and ribbons 2 and 4 highlighted in green display a same contrast but different from the one of 1 and 3. The motif is made of 2 bright features of dimension 1 nm. The alignment of ribbons following the direction m_2 is marked on the image. Tunneling conditions: V_{bias}= 2.7 V, I_t= 5 pA.*

The tip quality in this image allows to distinguish a different intramolecular contrast of the molecules comprised in successive ribbons. Alternate ribbon number displays a slightly different STM contrast (intensity contrast). For example, ribbons labelled by 1 and 3 (highlighted in blue on Figure 90(b)) show the same contrast, and ribbons labelled by 2 and 4 (highlighted in green) show the same contrast but different from the one of ribbons 1 and 3. This slight different contrast is more clearly distinguished from the magnified

additional images in Figure 90, and is at the origin of the chevron artefact seen in Figure 90(a).

To explain this slight contrast difference, we examine a boundary between the molecular domain and graphene (the cropped white rectangle from Figure 91(a)) on which we can more clearly distinguish the ZTAP molecules contrast (see Figure 91(b)). In the Figure 91(b), there are 2 individual molecular rows, one on the left side of the image and another row on the right side of the image, each marked by blue and green arrows respectively.

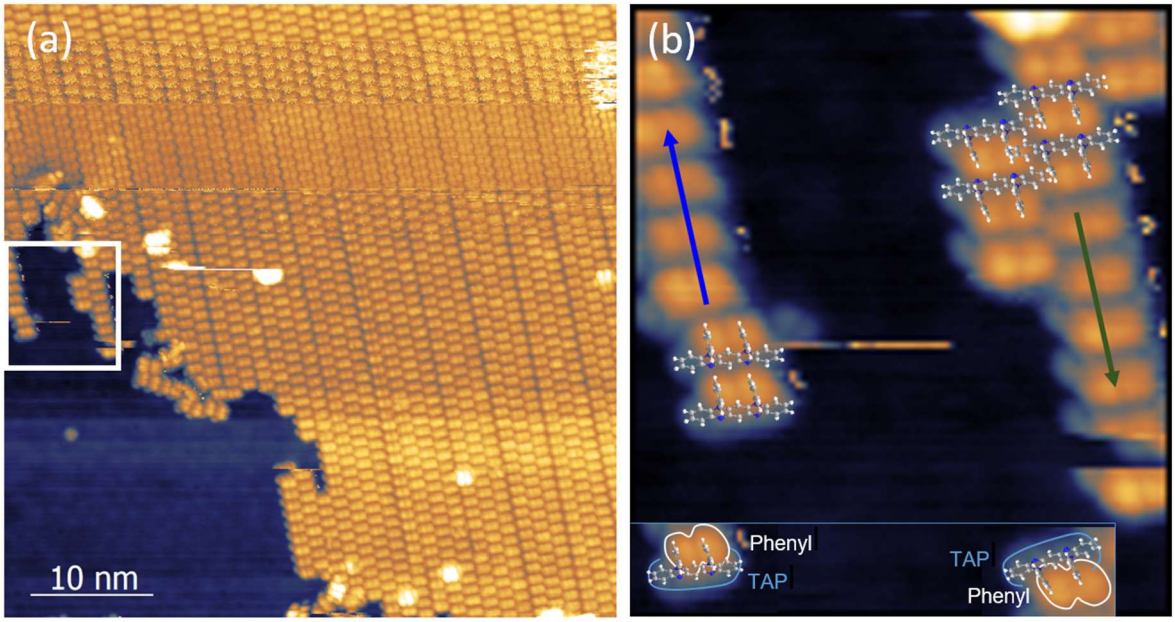


*Figure 91: **(a)** STM image at the interface between the ZTAP and graphene. **(b)** Zoom-in on a zone in the STM image of (a) where the individual molecules contrast is distinguishable. Tunneling conditions: V_{bias}=2.3 V, I_t= 5 pA*

From the Figure 91(b) we can extract the motif for each of these 2 rows, which are magnified in the inset. These motifs correspond to a single ZTAP molecule. The molecular motif is made of 2 bright contrast features and a dark blue contrast feature (shown in the inset of Figure 91(b)). By evaluating their dimensions, we conclude that the dark blue feature represents the zwitterionic core of the tetraazapentacene (TAP) molecule and the 2 bright features represent its 2 N-phenyl peripheral groups. Moreover, there motifs that belong to each row present an opposite motif orientation, which suggests an edge adsorption of ZTAP on graphene, making an angle θ ($\pm\theta$ for blue and green arrows) with the graphene surface (arrows representing the angles of the molecule with the surface are shown in both Figure 91(b) and Figure 92).

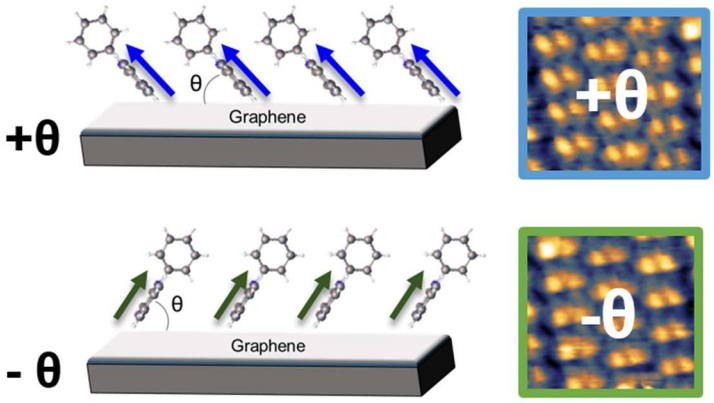


Figure 92: Representative scheme of the configurations $+\theta$ and $-\theta$ for ZTAP assembly on graphene. The blue and green arrows shows that the dipole of the molecule points away from the surface, and θ is the angle the molecule makes with the surface.

Therefore, there is an equivalent and symmetrical adsorption configuration to the adjacent ribbon of molecules (indicated by the green arrow in Figure 91(b) and Figure 92).

The findings in this subsection highlight the fact that the slight shifts of the ZTAP ribbons of the order of 80 pm in the $\mathbf{m_1}$ direction seen in Figure 88(a) is not due to a hopping of the molecule to another adsorption site but it is likely due to the adsorption geometry +θ or –θ of ZTAP on graphene. This also explains the different STM contrasts observed on the STM image of Figure 90(b) and predicts the orientation of the dipoles of ZTAP to be pointing away from the surface.

Given the presence of domain borders with the substrate, we can extend our analysis beyond mere adsorption characterization of the molecules to establish the epitaxial relationship between ZTAP and graphene lattices.

VI.1.2.2. Epitaxy with the substrate

It is possible to find the epitaxial relationship between 2 lattices by overlaying their coordinates and deducing their relative coordinates. The issue in this method resides in the thermal drift that is non-negligible even at 8.9 K. To overcome the issue of thermal drift, both the lattices (in this case, ZTAP and graphene) should coexist in the same STM image. The cross-correlation method used is detailed in this manuscript's section V.1.1.3. It is noteworthy that the STM images in Figure 93 and Figure 94 were rotated while scanning to ensure that the interface between the molecules and the substrate is aligned perpendicularly to the scanning direction. The molecular domain orientation should not be confused to be a different domain orientation than domain 1. The interface between the organic layer and graphene is shown in the Figure 93(a) and the data is processed as follows:

In Figure 93(a), the molecular layer has a poor resolution because of the adjusted tunneling parameters that permit atomic resolution imaging on graphene, are not suitable to image the molecular layer that possesses a higher tunneling barrier than graphene. Region-based contrast enhancement is done on the Figure 93(a) and shown in Figure 93(b) revealing the atomic resolution on graphene.

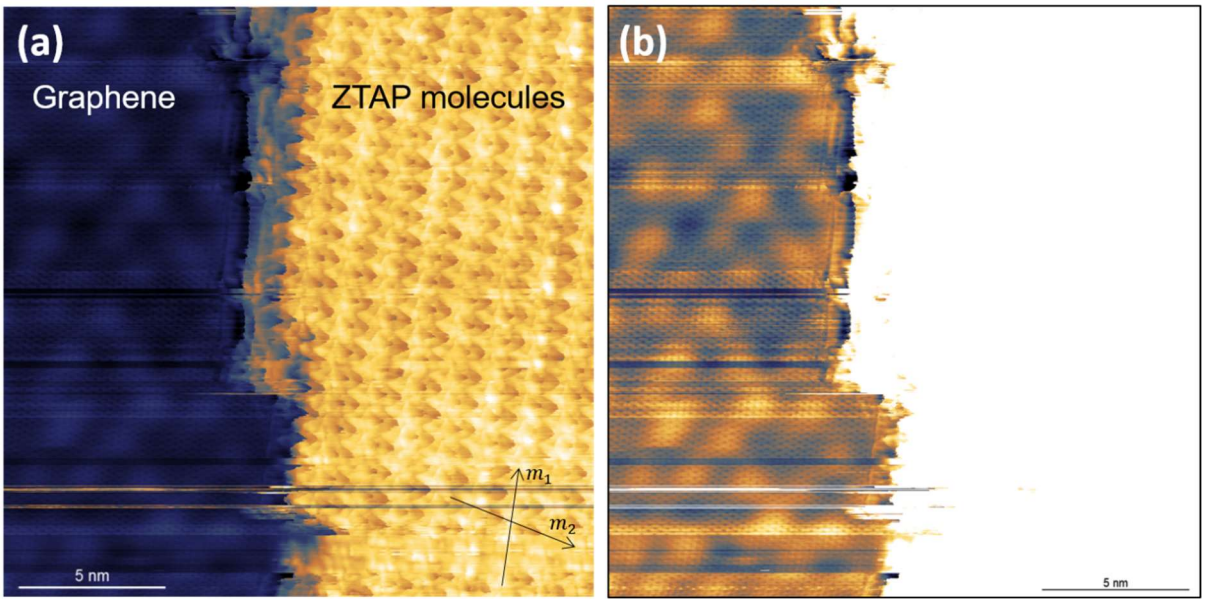


*Figure 93: **(a)** STM image at the interface between graphene and the ZTAP molecules. (b) Saturated contrast for the molecule layer. Tunneling conditions: V_{bias}=1.5 V, I_t= 7 pA.*

The poor resolution prevents the recognition of the structural characteristics of the molecular layer; however, its periodicity is distinguishable. All the ZTAP molecules are aligned following $\mathbf{m_2}$, and no structural defect is present on this part of the image, even if the molecules' boundary is not distinguished, this is also true for the $\mathbf{m_1}$ direction. To extract this periodicity, the autocorrelation of the STM image is performed separately for different zones of the same size, in the same horizontal band (Figure 6(a), inset 1 and inset 2).

The autocorrelation images of each of the lattices are superimposed, and the resulting image of the Figure 94(b) gives the relative position of the molecule lattice nodes with respect to graphene lattice nodes. In this image, the blue dots represent the graphene lattice nodes, and the white dots represent the molecule lattice nodes. Each node symbolizes the center of a motif.

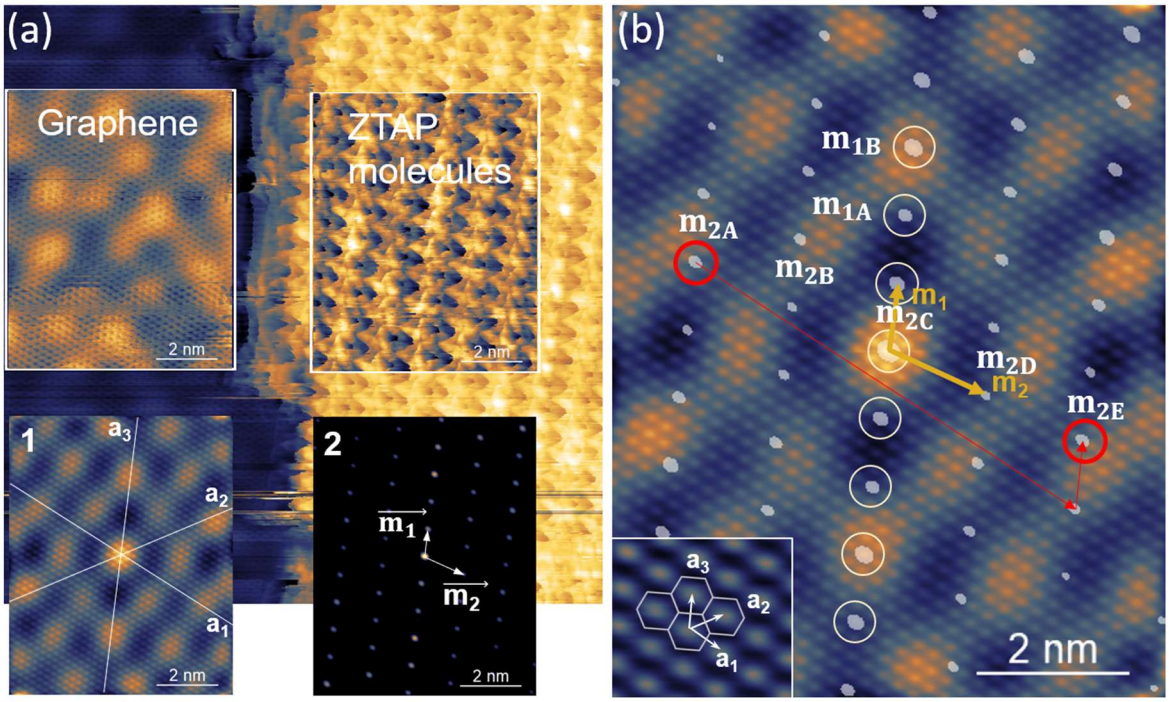


Figure 94: 2D autocorrelation treatment to extract the epitaxial relationship between the supramolecular phase and the graphene surface. ***(a)*** *STM image on the border between the graphene and the supramolecular phase. Tunneling conditions: V_{bias}= 1.5 V, I_t= 7 pA. and of size 20 nm×20 nm. 2 areas of the image are cropped, and their 2D autocorrelation is calculated resulting in the 2 images below, denoted by 1 and 2, where lattice parameters can now be easily extracted.* ***(b)*** *The image resulting from the superposition of the 2 autocorrelation images extracted in (a). The molecular network nodes (white dots) are now clearly identifiable with respect to the graphene network nodes (smaller blue dots). The vectors $\boldsymbol{m_1}$ and $\boldsymbol{m_2}$ of the ZTAP lattice are shown on the figure, as well as the vectors 25 $\boldsymbol{a_1}$+4 $\boldsymbol{a_3}$ which connect 2 equivalent nodes with respect to graphene.*

The subsequent step is to identify molecular nodes positioned on equivalent sites with respect to the graphene lattice nodes in each of the crystallographic directions of the molecular lattice. A zoom-in on labelled molecular nodes of the Figure 94(b) is shown in Figure 95, and a graphene lattice is drawn to scale in order to identify the relative position of the molecule nodes in white with respect to the substrate nodes.

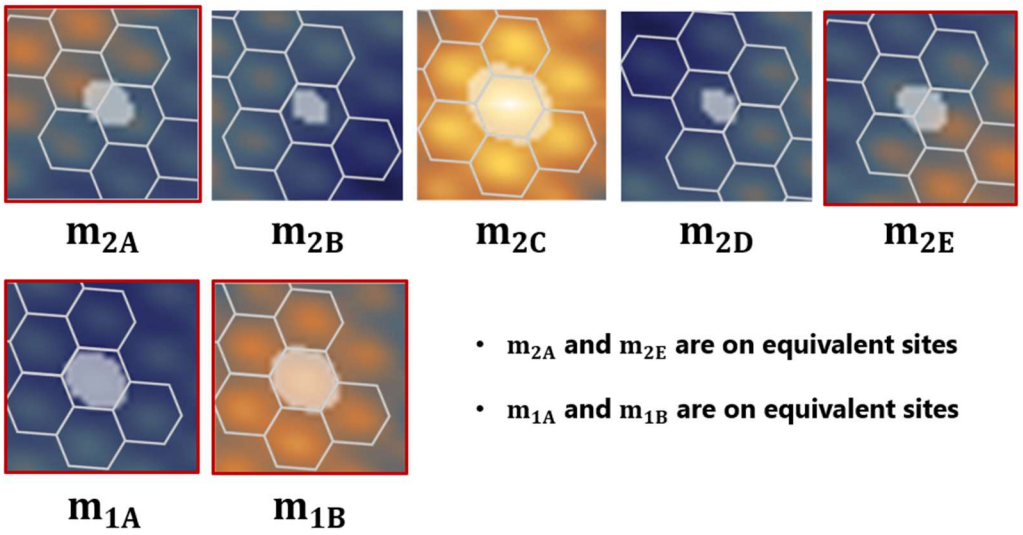


Figure 95: $m_{2A}, m_{2B}, m_{2C}, m_{2D}, m_{2E}$ are zoom-in on specific molecule nodes in the direction m_2 taken from the Figure 94(b)'s autocorrelation image. The graphene lattice is superimposed and the relative position of the molecule nodes with respect to graphene can be compared. The nodes m_{2A} and m_{2E} are on equivalent sites with respect to graphene. m_{1A} and m_{1B}, successive nodes in the direction $\boldsymbol{m_1}$ are on equivalent sites with respect to the graphene lattice.

Following $\mathbf{m_1}$, all molecular nodes are on equivalent sites with respect to the graphene substrate, 2 of these nodes are shown as an illustrative example and are labelled by m_{1A} and m_{1B}. The outcome is a point-on-line epitaxy following the crystallographic direction $\mathbf{a_3}$ of graphene, which is parallel to the direction of growth of the molecules in one ribbon.

Additionally, 2 other nodes labelled by m_{2A} and m_{2E} are observed to be on equivalent sites with respect to graphene following $\mathbf{m_2}$.

And as the distance separating the nodes m_{2A} and m_{2E} is 4 m_2, and the distance separating m_{1A} and m_{1B} is m_1, we can write them as function of graphene's lattice vectors to get the following equations:

$$\begin{cases} \mathbf{m_1} = 0\ \mathbf{a_1} + 4\ \mathbf{a_3} \\ 4\ \mathbf{m_2} = 25\ \mathbf{a_1} + 4\ \mathbf{a_3} \end{cases} \tag{5.1}$$

As a conclusion, the molecular network is high-order commensurate with graphene, with the following correlation matrix translating the epitaxial relationship of ZTAP and graphene:

$$\begin{pmatrix} m_1 \\ m_2 \end{pmatrix} = \begin{pmatrix} 0 & 4 \\ \frac{25}{4} & 1 \end{pmatrix} \begin{pmatrix} a_1 \\ a_3 \end{pmatrix} \tag{5.2}$$

In summary, the STM images study confirms the edge adsorption of **ZTAP** molecules on graphene, with a dipole moment pointing away from the surface. Therefore, there should be an important influence of this dipole on the electrostatic surface potential. The way to measure this electrostatic surface potential at the intramolecular scale, is by using the Kelvin Probe Force Microscope (KPFM) in non-contact AFM mode.

VI.2. ZTAP assembly on graphene: KPFM studies

In nc-AFM, there are several types of interactions forces present between the tip and the sample, including electrostatic forces. These electrostatic forces depend quadratically on the difference between the bias voltage V_{bias} and V_{CPD}, which is the electrostatic contact potential difference (see equation II. 24).

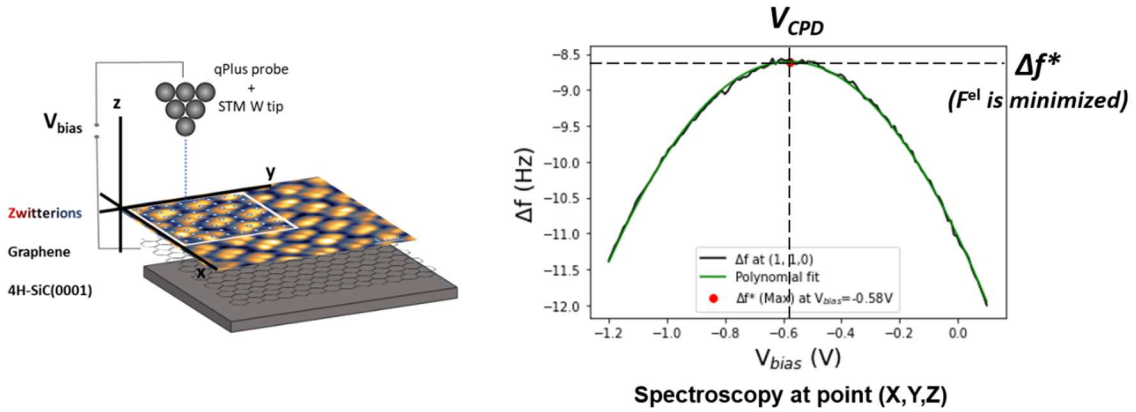


Figure 96: Schematic of the ZTAP on graphene KPFM mapping experiment. The qPlus probe with an STM tungsten tip positioned above the predefined grid points for measurements over the assembled molecules on graphene. The measurements will result in a Kelvin spectroscopy map. On the right, an example of Kelvin spectroscopy parabola acquired at one point (X, Y, Z) of the map, which measures the frequency shift Δf as function of the bias voltage V_{bias}. The maximum of the fitted parabola yields the frequency shift maximum Δf^* and the V_{CPD} for the position (X, Y, Z) of the grid.

This allows determining a value for the electrostatic surface potential relative to the potential of the tip. This quadratic dependence will allow to distinguish among all the forces, isolating the influence of the electrostatic force by varying V_{bias}. The result is Kelvin force spectroscopies as shown in Figure 96, from which 2 quantities can be extracted:

i) The bias voltage at which the electrostatic force is minimized (V_{CPD}).
ii) The value of the electrostatic short-range force at V_{CPD} (Δf^*).

By means of these Kelvin spectroscopies, the V_{CPD} can be calculated by using the equation:

$$V_{CPD} = \frac{\phi_s - \phi_t}{e} \tag{5.3}$$

where ϕ_s and ϕ_t are the sample and tip work functions.

When a V_{CPD} difference is measured between 2 points of the surface, depending on the sign of this difference, it is possible to determine if the surface is more or less locally charged, and determine the sign of the local dipole.

We performed these KPFM measurements on 2 different instruments. First, on a variable temperature atomic force microscope (VT-AFM) in multi-layer regime. Second, in sub-monolayer regime on a closed-cycle LT-STM/nc-AFM by 4D Kelvin probe force spectroscopies (4D-KPFS).

VI.2.1. Multi-layer on VT-AFM

The experiments presented in this subsection were done on a VT-AFM in IM2NP laboratory in Marseille. Dr. Elie Geagea was the operator of the VT-AFM used to obtain the results presented in this subsection. It is important to specify that the molecular evaporator of the VT-AFM, a homemade Knudsen cell, exhibits a higher flux than the Kentax used in the previous experiments. This potentially influences the deposition rate and the resulting molecular deposit characteristics and affects the growth mode of the molecules. The deposition is done on a substrate held at RT during deposition.

Another specification of this equipment is that it operates under classical nc-AFM regulation (feedback loop lock on the Δf signal to maintain it constant) while a second lock-in amplifier lock on the modulation of V_{bias} performs the KPFM measurement. We do not perform spectroscopy on the VT-AFM. The contrast in KPFM image is due to the variation of the V_{CPD}. In other words, a feedback loop maintains this distance based on the measurement of the resultant force. Simultaneously, the bias voltage is modulated by applying a rapidly varying AC voltage to the DC voltage. This modulation induces the parabolic variation of Δf. And the mean value of the V_{CPD} over several modulations is extracted at each point of the image. This value constitutes the V_{CPD} contrast of KPFM of the following figures.

The 300 nm × 300 nm AFM image in Figure 97 shows a few-layer Volmer-Weber growth mode of ZTAP deposited on graphene.

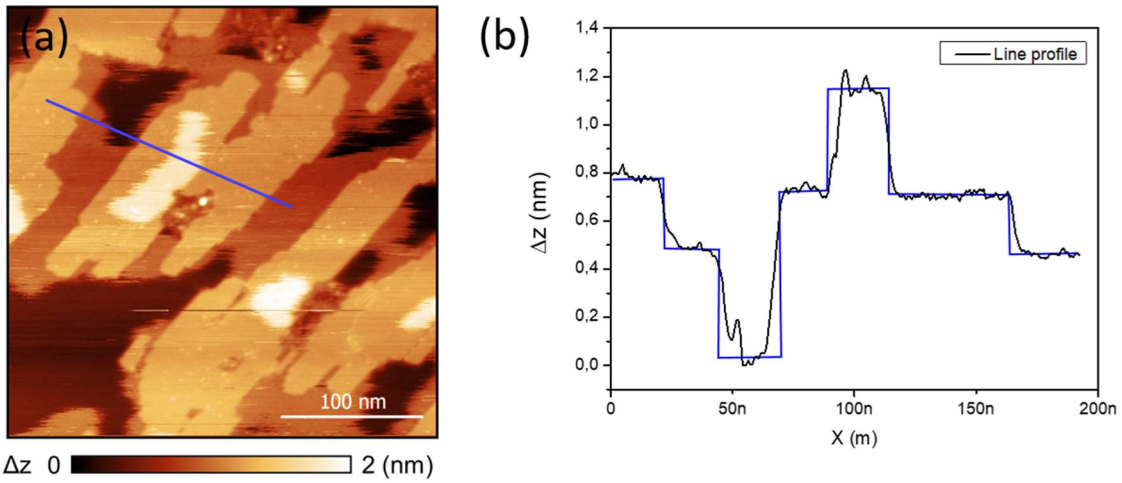


Figure 97: ***(a)*** *Atomic force microscopy (AFM) image showing the topographical surface profile of the many-layer deposit of ZTAP on graphene at RT. The height variations Δz are shown in the color bar below the image.* ***(b)*** *A blue line profile on (a) is plotted showing the relative heights of the different layers.*

The scan shows the formation of distinct molecular islands with different diameters, rather than continuous molecular monolayers. 3 molecular layers form in an island-like manner, prior to full layer completion. A height profile study shown in Figure 97(b) of the topography shows an approximate height of 0.4 nm per layer, which is in good agreement with the topography measurement in Figure 87(c).

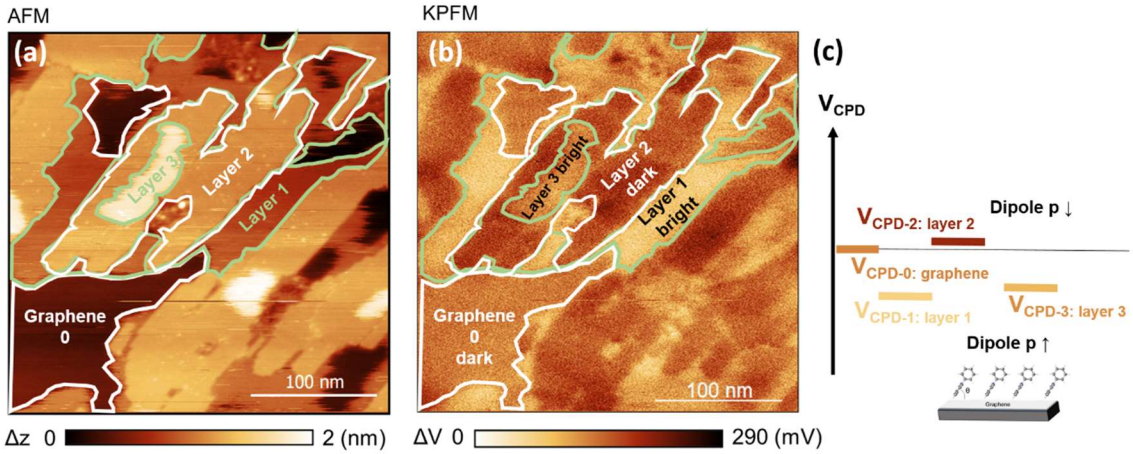


Figure 98: ***(a)*** *Atomic force microscopy (AFM) image showing the topographical surface profile of the many-layer deposit of ZTAP on graphene at RT. The height variations Δz are shown in the scale below the image. The layers are numbered from 0 (graphene) to layer 3 (3rd layer of ZTAP). The images were acquired on a VT-AFM non-contact mode with a cantilever spring constant of 40 N/m and a frequency of 150 kHz.* ***(b)*** *The simultaneously recorded surface potential map KPFM of the same area, highlighting the local variations in surface potential correlated with the topography observed in the AFM image.* ***(c)*** *Comparative scheme for the V_{CPD} and dipole direction for each layer.*

The KPFM in imaging mode provides information on the work function variation across the surface as well as the distribution of surface charges overall dipole orientation of each molecular layer. The KPFM image resulting from the Figure 98(a) shown in Figure 98(b)

shows obvious contrast differences on each layer. The different layers are delimitated by lines of different colors. The green lines and white lines separate successive layers, as an example, the first layer (layer 0) is the graphene layer and the next one (layer 1) is the first molecular layer etc., The lines drawn on the AFM image Figure 98(a) reproduced into the KPFM image of Figure 98(b), allow for direct comparison of the topography with the variations in electrical properties.

The graphene layer is taken as a reference for the CPD value (V_{CPD-0}); the first layer of molecules has a lower V_{CPD-1} value than V_{CPD-0}. The observations are in accordance with the deduced adsorption configuration of dipoles oriented away from the surface (see II.3.2). The layer 2 has a darker contrast and a CPD value V_{CPD-2} approximately close to the value of V_{CPD-0}, this indicates the presence of a very weak dipole pointing towards the surface. Finally, the layer 3 shows a brighter contrast V_{CPD-3} than the one for V_{CPD-0} with a difference of 40 mV, indicating a resulting dipole oriented away from the surface.

This layer-by-layer growth alternates the orientation of the dipoles of the layers and confirms the hypothesis of an edge adsorption of the molecules on graphene. Indeed, for layer 1 the dipoles point away from the surface and we expect a brighter KPFM contrast on this layer with a 75 mV shift of the CPD. For layer 2, the dipole of the layer 1 is compensated by a dipole with an opposite orientation, but as this layer is closer to the tip, its weight in KPFM contrast is slightly enhanced explaining the weak difference of 40 mV between layer 2 and layer 1. Finally, the bright contrast of layer 3 is explained by the sum of 2 layers of dipoles pointing away from the surface (layer 1 and layer 3) separated by one layer of dipoles pointing towards the surface. The V_{CPD-3} value is higher than the V_{CPD-0} value, with a difference of 30 mV between them. A comparative scheme in Figure 98(c) illustrates the CPD sign alongside the corresponding overall dipole sign of the molecule layer.

These measurements give insight on the overall electronic properties of a layer, now to access intramolecular information of the local electronic properties of the first layer of molecules; we use KPFM in the spectroscopy mode on the closed cycle LT-STM/nc-AFM.

VI.2.2. 4D KPFS map: on closed-cycle LT-STM

These spectroscopic measurements were obtained on the closed-cycle LT-STM at the IM2NP lab in Marseille for a collaboration with the Nanostructuration team on this project. This instrument allows for 4D spectroscopy maps (Kelvin probe force spectroscopy maps (KPFS) or scanning tunneling spectroscopy maps (STS)) at the intramolecular scale. These measurements, respectively give information on the modification of the surface potential or the local density of states at the intramolecular scale. Several conditions must be fulfilled to acquire these 4D spectroscopic mappings whose steps are explained in III.3.6.1.

VI.2.2.1. Intramolecular-scale 4D KPFS maps

Figure 99(a) shows an STM image of the ZTAP self-assembled on graphene. To perform a 4D KPFS map, a grid 40 pixels × 40 pixels is placed over this exact imagen and on each pixel of the grid at a point with spatial coordinates (X, Y, Z), the oscillation frequency shift Δf is measured as function of the bias voltage V_{bias} to get the classical KPFS curve shown in Figure 99 (b).

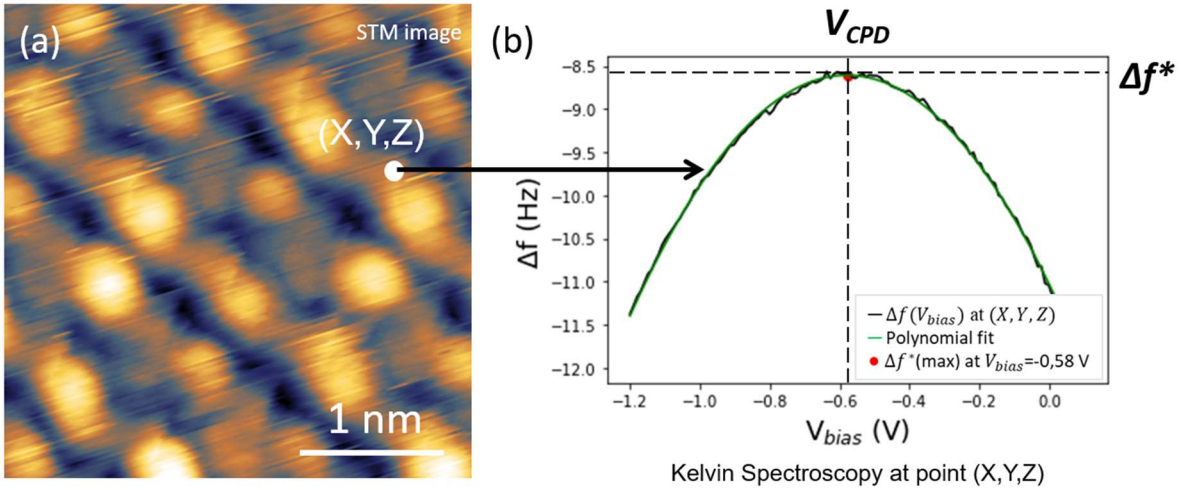


*Figure 99: **(a)** STM image showing the self-assembly of ZTAP on graphene. Tunneling conditions: V_{bias}= 2.5 V, I_t= 10 pA **(b)** Kelvin spectroscopy, where the oscillation frequency Δf is measured as function of bias voltage at one point (X, Y, Z) on the spatial grid on the image in (a). The value of Δf^* the maximum of the parabola can be extracted on each Kelvin spectroscopy curve.*

This map takes about 24 hours to acquire the full set of parabolas for one defined height Z. From this curve, the maximum of the parabola, Δf* is extracted for a given height Z of the tip over the surface. This process is repeated for all the grid points, for a fixed value of Z. Each of the spectroscopies is analyzed by fitting a second-degree polynomial which allows for the extraction of first, the Δf^*, which gives a structural information about the surface, second, the V_{CPD}. For each value of Z, 2 maps can be plotted, the Δf^* $(X, Y)_{map}$ and the V_{CPD} $(X, Y)_{map}$. The Hanning interpolation was applied through Python's imshow function to smooth the Δf (V_{bias}) data edges for a clearer visual representation of the maps. The maps before and after interpolation are shown in Figure 100.

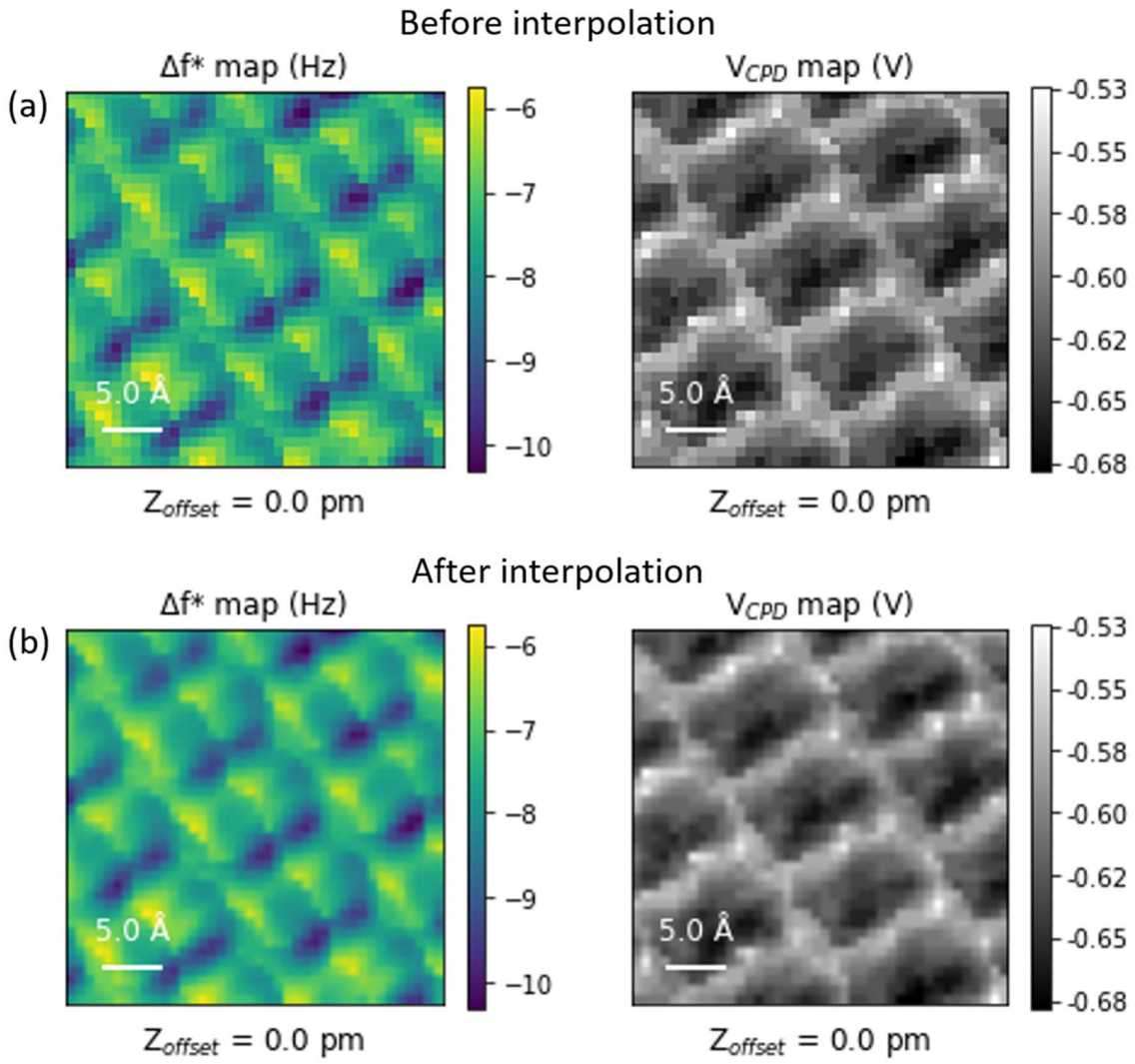


Figure 100: ***(a)*** *Kelvin spectroscopy at a point (X, Y, Z) on the surface, the dotted line in blue represents the raw data, the green solid line represents the data with a polynomial fit and the maximum of Δf defines the value of Δf^*, that is marked with a red dot.* ***(b)*** *Δf^*map of ZTAP on graphene and the contact potential difference (V_{CPD}) map calculated from the raw data. Grid: 40 pixels × 40 pixels. Size in nm²: 3.5 × 3.5.*

The Δf^* map in Figure 101(a) shows a molecular assembly, showing a repeating unit which consists of 2 bright features that correspond to the phenyl functional groups of the ZTAP. This phenyl group signature permit to find the molecules position on the Δf^* map. Note that as the ZTAP molecules present an edge adsorption, the phenyl rings are the closest to the STM tip and thus, the tip should probe the strongest forces for a position above the phenyl groups. The strongest force, means the strongest Δf^* and the darkest contrast. However, what is observed in this Δf^*map is the opposite. This apparent contradiction will be clarified through a complementary study of the KPFS maps as function of Z. The Figure 101(a-b) shows both the Δf^* and V_{CPD} maps.

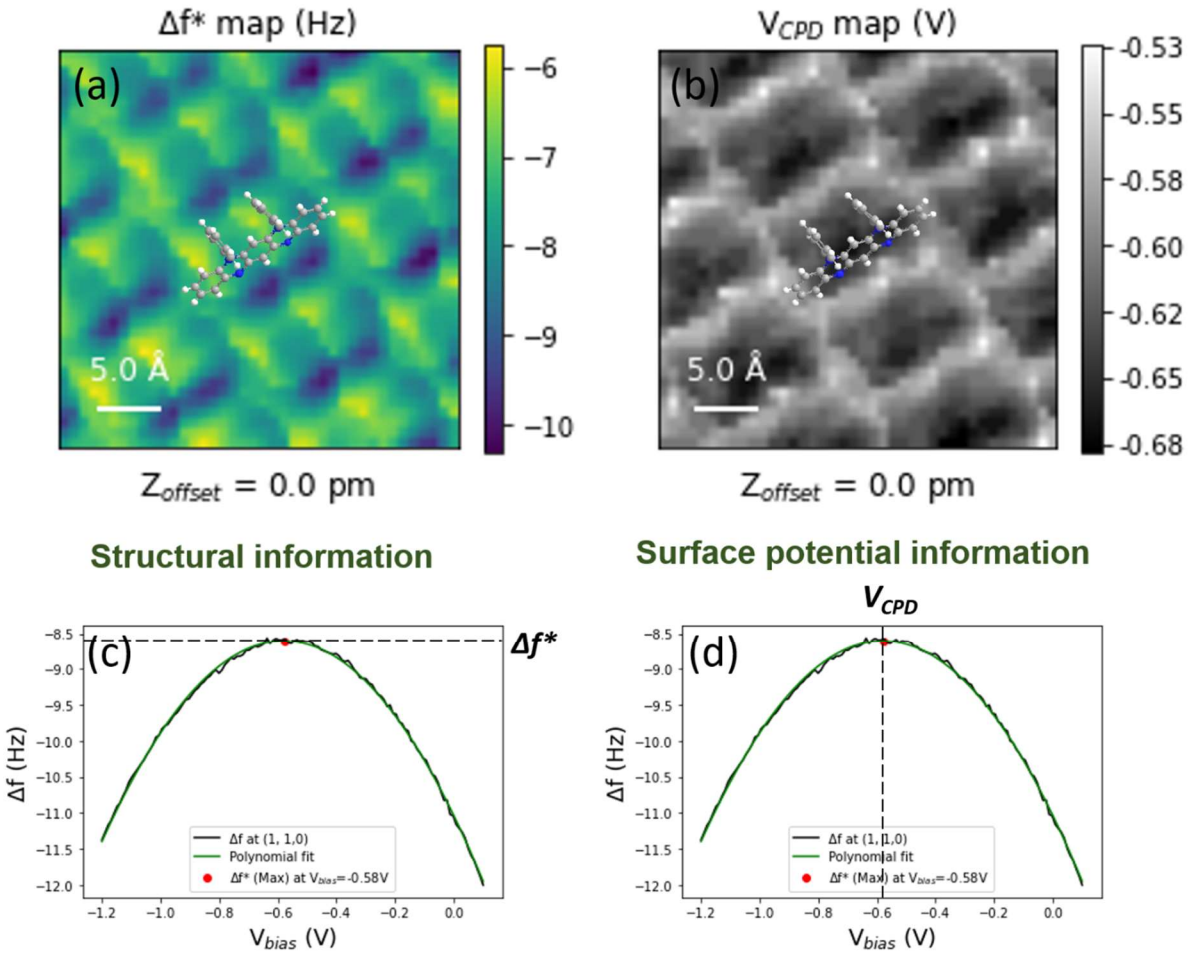


Figure 101: ***(a)*** *Δf^* map, of ZTAP on graphene.* ***(b)*** *Contact potential difference (V_{CPD}) map deduced from (a).* ***(c)*** *Kelvin spectroscopy at a point (X=1, Y=1, Z=0) on the surface, the maximum of Δf defines the value of Δf^*.* ***(d)*** *Kelvin spectroscopy at a point (1, 1, 0) on the surface, the bias voltage for which Δf parabola reaches a maximum, corresponds to V_{CPD}.*

By taking as a reference the Δf* map in Figure 101(a), the ZTAP molecule can be placed on the V_{CPD} map as shown in Figure 101(b). A clear periodic reproducibility of each single molecular V_{CPD} contrast is observed and shows the robustness of the measurement. This V_{CPD} map shows a clear periodic modulation of the surface potential corresponding to the periodicity of the supramolecular layer.

An inhomogeneous dark feature having the lowest V_{CPD} shift is at the position of the zwitterionic core of ZTAP, bordered by white lines (Figure 101(b)). The low values of the V_{CPD} relative to the high values of the borders of the molecule sign the presence of a dipole that orients away from the surface.

A height profile is done on the V_{CPD} map of Figure 102(a), in 2 different directions. The profile 1 is done by passing through the TAP core of the molecule (laterally) following the $\mathbf{m_1}$ direction, and the profile 2 is done approximately along the long axis of the TAP (longitudinally).

The profile 1 in Figure 102(b) shows periodically separated maxima, which are unsymmetrical between the increase and the decrease as during the increase, a shoulder

marked by a red arrow arises. This dissymmetry is probably a signature of the tilt of the molecule, which is not perpendicular to the surface but is inclined at an angle θ to the surface. Along the profile 2, there is again periodic maxima with a more symmetrical profile. These 2 profiles lead to a 2D periodicity for the surface potential.

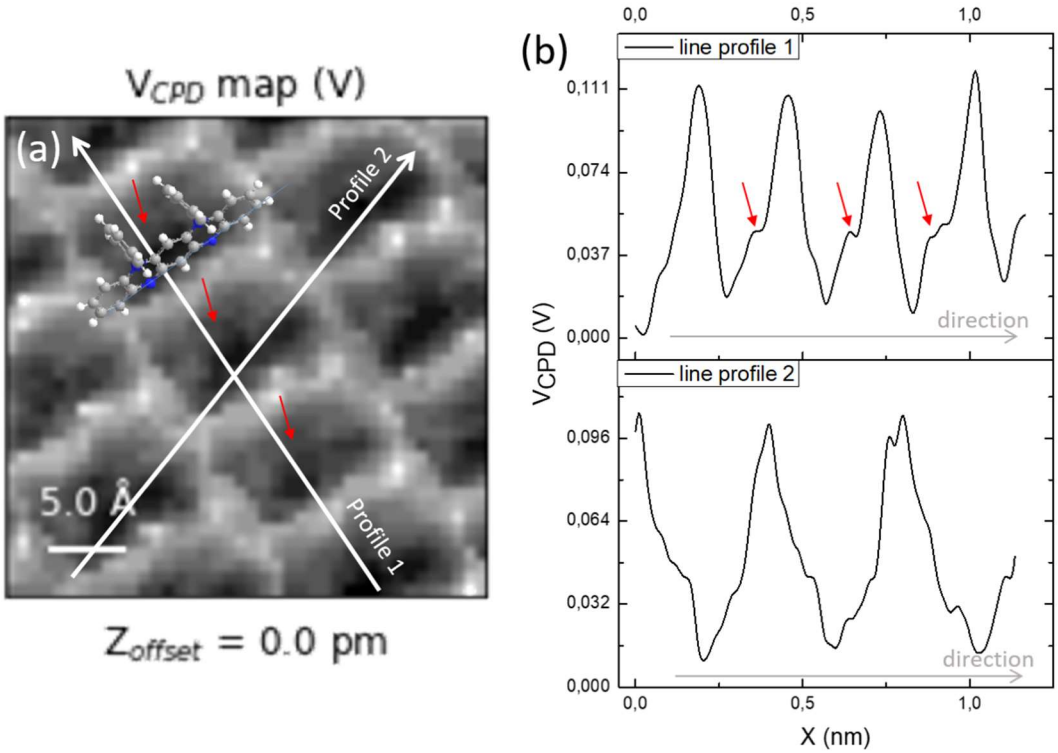


Figure 102: ***(a)*** *Contact potential difference V_{CPD} map with 2 line profiles.* ***(b)*** *Line profile 1 and line profile 2 of the V_{CPD} value as function of the position along the longitudinal (profile 1) in the direction $\boldsymbol{m_1}$ and lateral (profile 2) cuts of the ZTAP assembly on graphene.*

The observations of this subsection show that each molecule preserves its individual dipole (tilted, oriented away from the surface) despite the closeness of the molecular self-assembly, which could have led to stronger dipole-dipole interactions in that case.

VI.2.2.2. Δf^* and V_{CPD} as function of Z_{offset}

It is possible to explore the 3D molecular-scale structure of this potential. A subsequent KPFS experiment is conducted, where the (X, Y) number of points is minimized and the number of Z points is maximized.

This KPFS study, whose results are shown in Figure 103, was conducted on a molecule assembly, and on 5 different heights Z. The map for Z_{offset}= 0 shows similar features to the maps of Figure 101, the 2D periodic ZTAP lattice which modulates periodically the surface potential on the zwitterionic core position of the molecules.

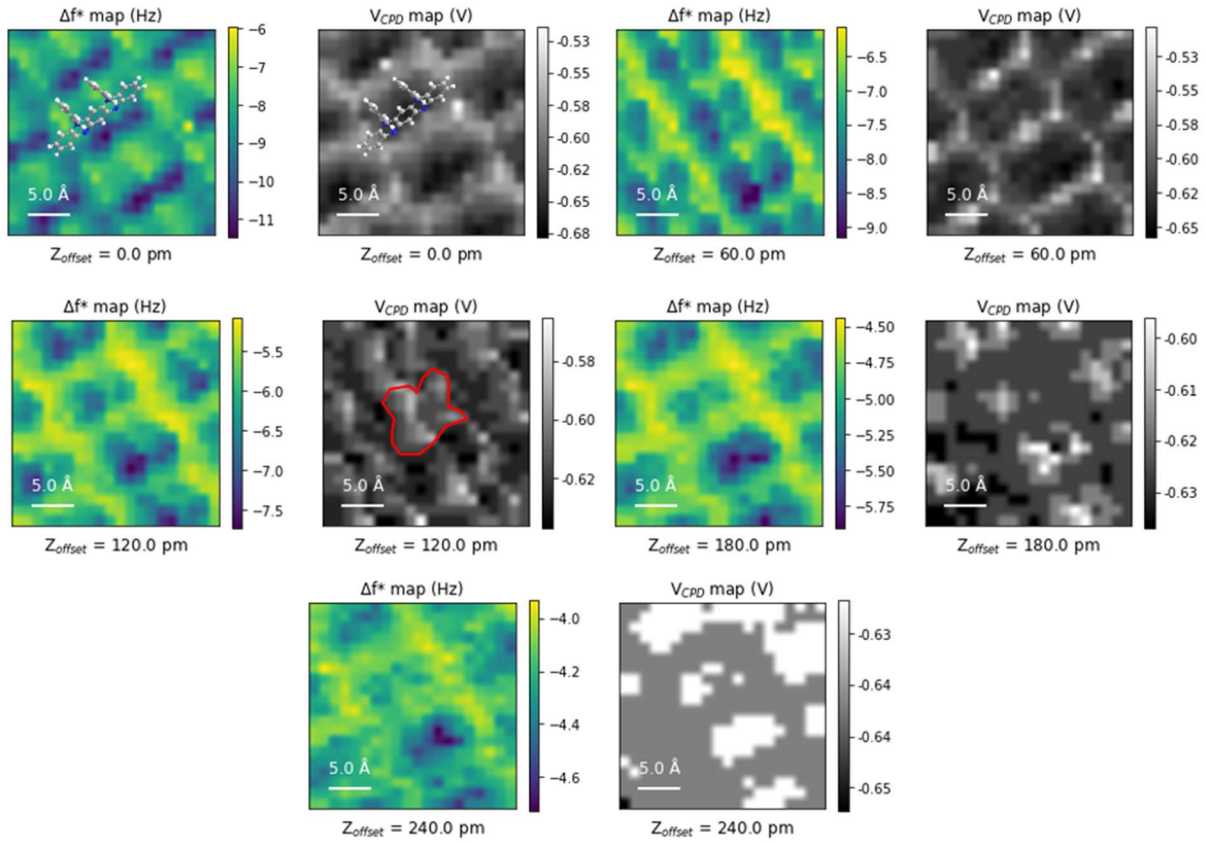


Figure 103: ZTAP on graphene KPFS maps. Δf^* maps (in color) and their corresponding CPD maps (in grey) for each of the 5 different Z_{offset} values whose value is written underneath each map. The smaller the Z_{offset} value, the closer the tip to the surface. Grid 20 pixels x 20 pixels. Image size: 2.74 nm ×2.74 nm, scale bar: 5 Å.

Upon applying a Z_{offset} on the tip position, at a value of 60 pm, the Δf^* map show a contrast inversion between the zwitterionic core and the borders of the molecule. At Z_{offset}= 0 pm, in the Δf^* map, the molecule's center comprises 2 bright spots which correspond to the phenyl substituents and a border of darker contrast, meanwhile at a Z_{offset}= 60 pm, these 2 bright spots contrast becomes darker than the borders of the molecule. At a value for Z_{offset}= 120 pm, the 2 dark spots combine into a single one. This effect becomes even more pronounced when the tip-surface distance further increases as for Z_{offset}= 180 pm. At this distance, the molecule's center contrast appears darker than the borders the 2 dark spots combine into a single one with a contrast that aligns with the fact that the parts of the molecule closer to the tip should result in a darker contrast than the parts further away. When examining the borders of the molecule that are further away from the tip with respect to the phenyl substituents, they likewise follow this contrast inversion between 0 pm and 120 pm. The inversion of contrast is explained by the shift in the electrostatic force regime between the tip and the surface transitioning from a predominantly repulsive regime to an attractive one.

In parallel with these Δf^* mappings, the measurements on the values of V_{CPD} also show a strong contrast evolution between the Z_{offset} values 0 pm and 120 pm. At 0 pm, the same

structure of the V_{CPD} map of Figure 101(b) is found with the dipole effect signature in the center of the molecule via a darker contrast than the one of the borders of the molecule.

This type of contrast is still preserved at 60 pm, although with a weaker contrast for the center of the molecule. However, at 120 pm, the contrast is completely different as 2 bright spots are observed and highlighted in red instead of the dark center and the borders of the molecule present a darker contrast. At this distance from the surface, the signal originating from the molecule's center is lost and replaced with the signal coming from the phenyl substituents of ZTAP. Above 120 pm, Δf^* structural contrast is maintained, the border of the molecules still presents the brightest contrast with respect to the center, however, for the V_{CPD}, all sensitivity is lost as there is less than 30 mV of variation between the maximum and minimum points of the map. The phenyl signature is still faintly discernible as 2 bright spots at 180 pm and is the completely lost at 240 pm. This shows that the KPFM signal as a function of Z_{offset} decays much faster than the Δf^* signal.

With regards to the V_{CPD} contrast, this series of experiments show that the farther the tip-surface distance increases, the more interactions around the tip begin to be integrated. An averaged value of the signal over the molecule is obtained, and this results in the loss of the intramolecular resolution.

An additional KPFS experiment is performed on the same molecular zone to get more information on the evolution of the maps. This experiment consists in the further increasing the number of Z measurements, while decreasing the scan window to fit one molecular motif. The maps obtained from this KPFS experiment are shown in Figure 104 and Figure 105.

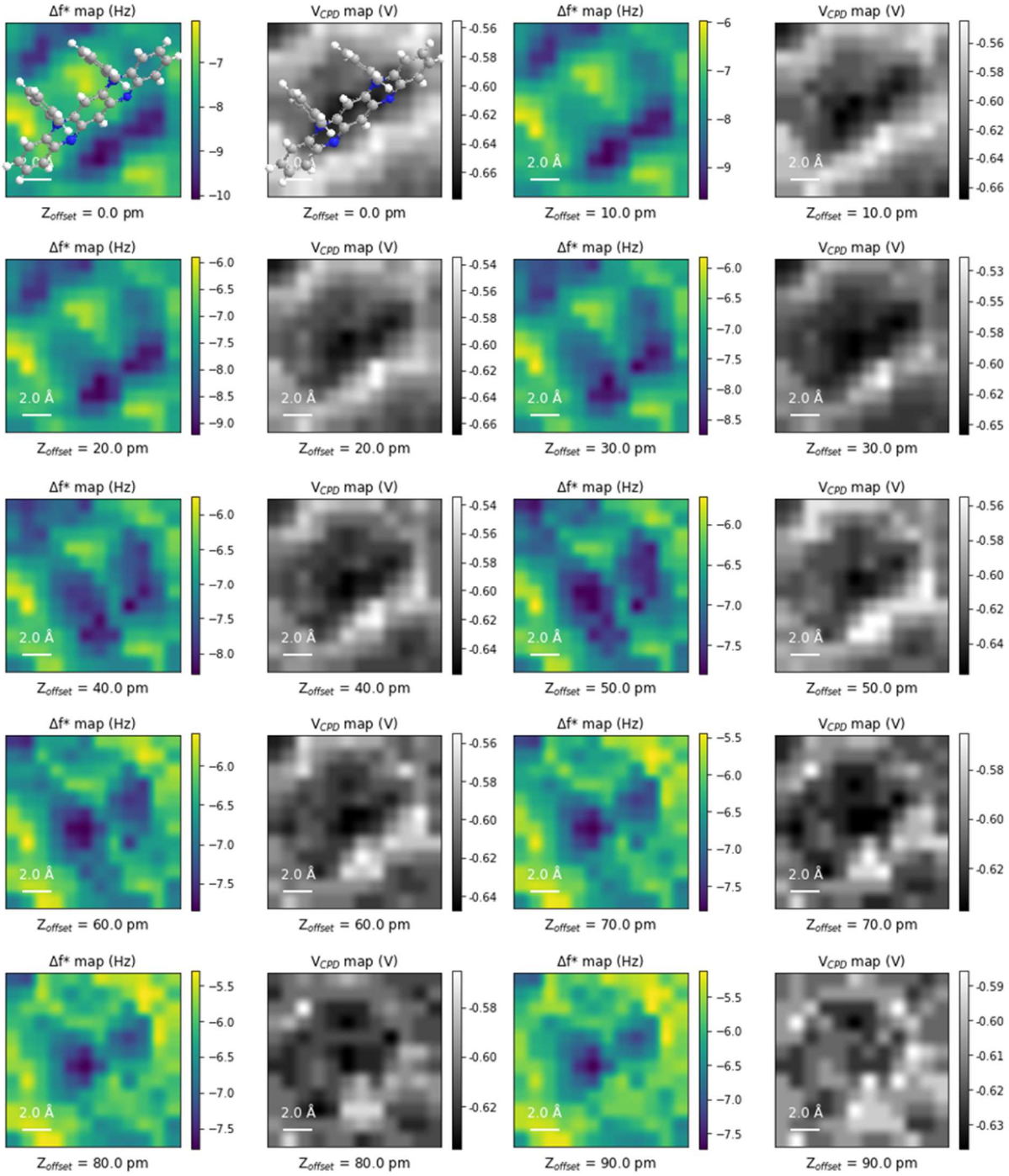


Figure 104: ZTAP on graphene KPFS maps. Δf^* maps (in color) and their corresponding CPD maps (in grey) for each Z_{offset} value. The smaller the value of Z_{offset}, the closer the tip is to the surface. Grid : 12 pixels × 12 pixels. Image size: 1.4 nm × 1.4 nm, scale: 2 Å.

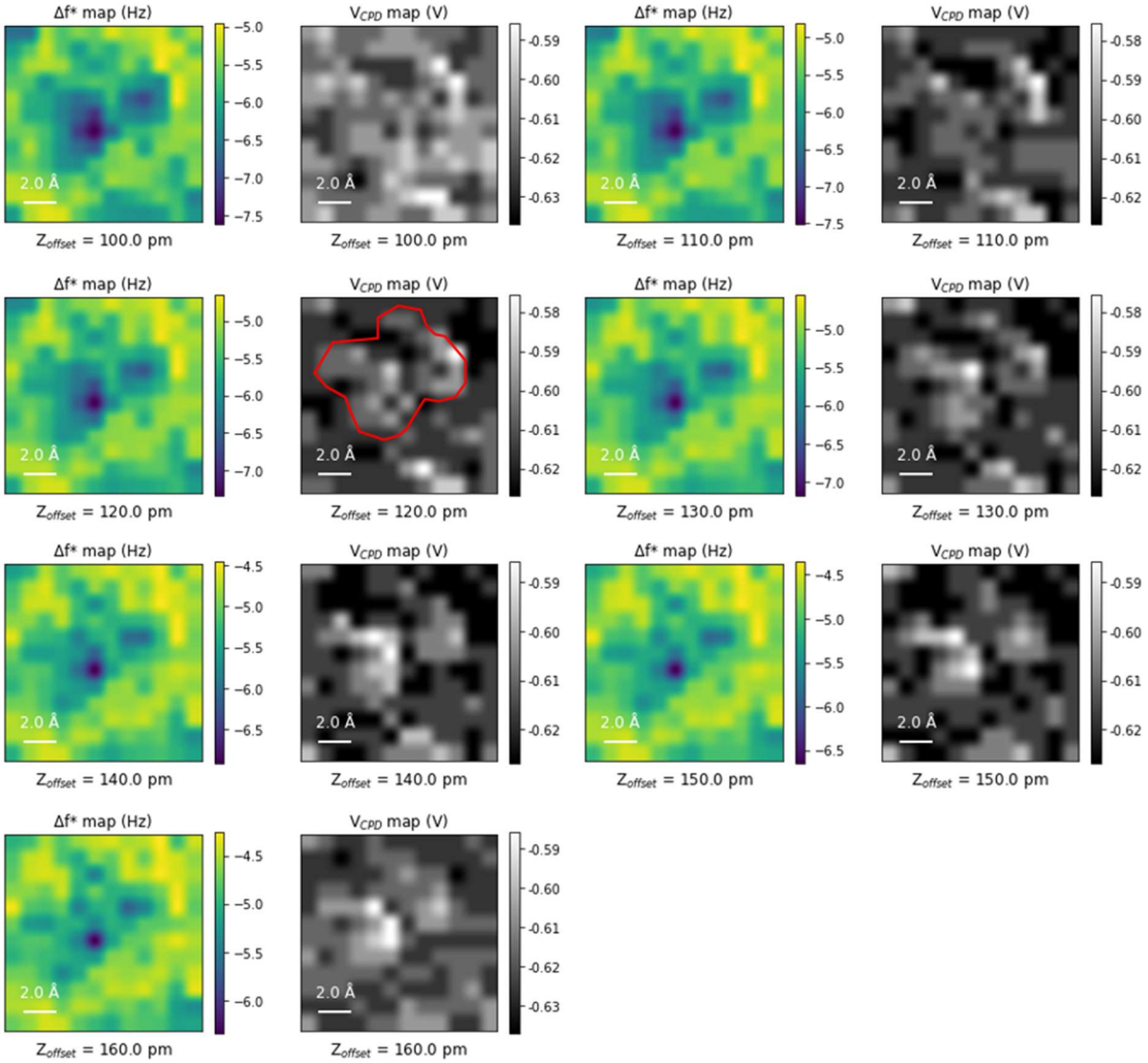


Figure 105: ZTAP on graphene KPFS maps. Δf^* maps (in color) and their corresponding V_{CPD} maps (in grey) for each Z_{offset} value. The smaller the Z_{offset} value, the closer the tip is to the surface. Grid 12 pixels × 12 pixels. Image size: 1.4 nm × 1.4 nm, scale: 2 Å.

Regarding the Δf^* maps, the contrast inversion turning point is observed to be around Z_{offset}= 60 pm, as the borders of the molecule start to show the smallest Δf^* shift (bright contrast) and the area near the zwitterion shows a stronger Δf^* shift (dark contrast). Overall the Δf^* maps, the shift value decreases with the Z_{offset} increase. This is due to the fact that as the tip distance to the molecule is increasing with the Z_{offset} increase, it is becoming less sensitive to the surface forces and at a distance of Z_{offset}= 160 pm, one dark spot is preserved, and reflects averaged values of the overall area of the molecule (border and center of the molecule). Another effect is that, far from the surface, the tip is less sensitive to the electrostatic forces because of the decay of this interaction with distance. These 2 effects (lateral interaction and decay of the interaction with the distance) lead to weaker contrast differences between the center and the border on the maps. This decrease of the interaction with the distance is clearly visible on the Figure 105.

Figure 106(c, d), shows several $\Delta f(V_{bias})$ measurements at different Z_{offset} values, above 2 characteristic points of the molecule; the center where the zwitterionic core of the molecule is present, the coordinates (6, 5) of the grid were chosen to represent this part of the molecule. The second characteristic point of the molecule is at its border, the border means the outer benzenes of the TAP core, thus, a point of coordinates (1, 2) on the grid is chosen to represent this second part of the molecule.

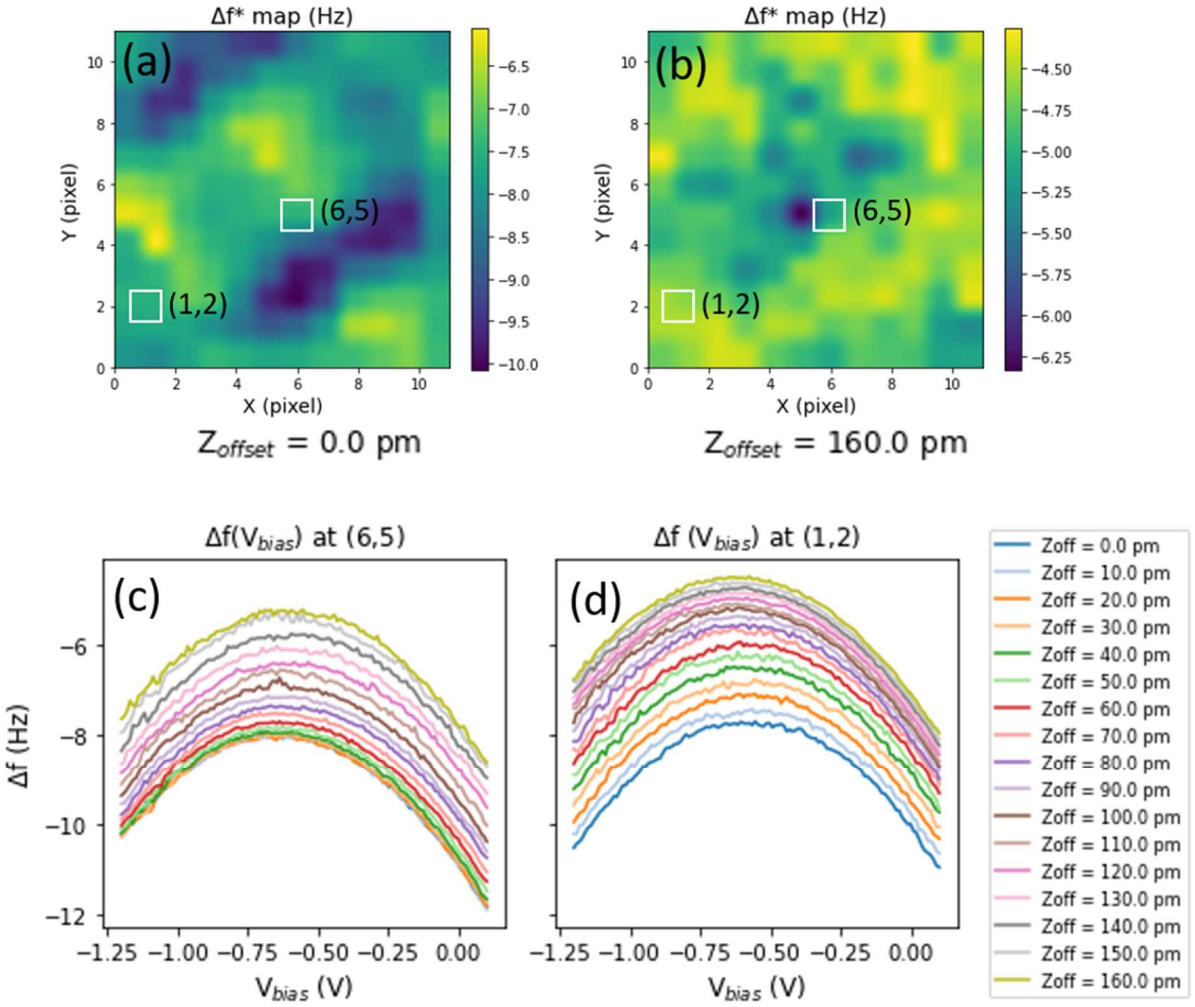


Figure 106: (a) ZTAP on graphene Δf^* map at Z_{offset}=0 pm. 2 pixels of the map at (6,5) and (1,2) are shown by white squares. (b) ZTAP on graphene Δf^* map at Z_{offset}= 160 pm. 2 pixels at (6,5) and (1,2) are shown by white squares. (c) Δf plot as function of V_{bias} at the position (6,5). The curves are constant and progressively shift to the right after 50 pm. (d) Δf plot as function of V_{bias} at (1,2). The curves progressively shift to the left.

The maximum of the parabola in Figure 106(c) for the center point at (6,5) is taken. The evolution of this maximum with Z_{offset} shows an increase in Δf (decrease in |Δf|) starting at 50 pm with a shift to the right, to more positive values of V_{CPD}. Meanwhile, for the molecule borders at (1,2), the V_{CPD} gradually shifts to the left, to more negative values, with the increase of Z_{offset} (Figure 106(d)).

This phenomenon is studied in greater detail; for each $\Delta f(V_{bias})$ measurement, the peak position of the parabola is determined, meaning the V_{CPD} and the corresponding Δf^*. These points are then analyzed as a function of the Z_{offset} for tip positions above the center and above the border and the results are compared in Figure 107.

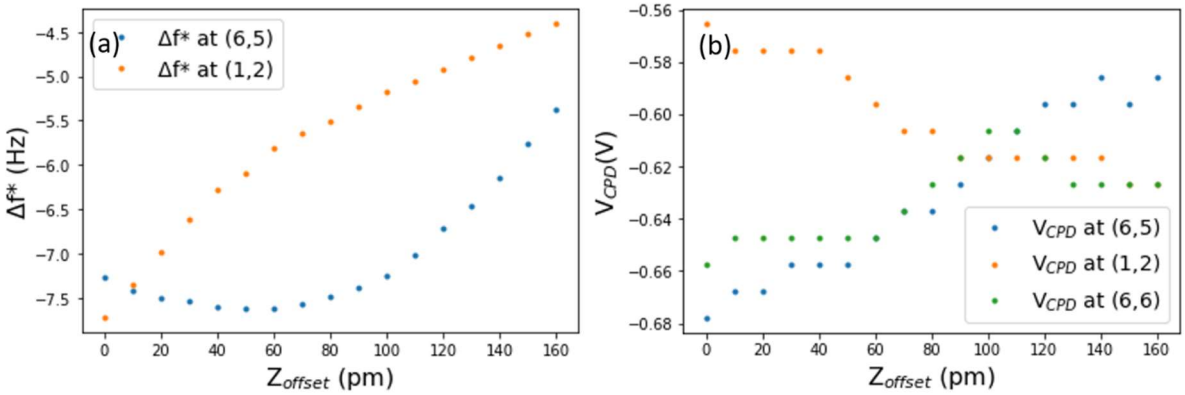


*Figure 107: **(a)** Maxima of the frequency shift Δf^* measured as a function of Z_{offset}. The measurements were conducted on 2 specific points of the KPFM maps shown in Figure 106. These points at (6, 5) and (1, 2) respectively represent the position of the tip over the center of the molecule and its position above a molecule's border. **(b)** The V_{CPD} values recorded as a function of Z_{offset} for the same points as in (a), and another position of the tip (6, 6) over the center of the molecule.*

On the molecule borders (orange dots) at the point (1, 2) of the grid, the plot of Figure 107(a) shows the classical increase in Δf^* signal with the distance in the attractive regime. On the contrary, for the center of the molecule (blue dots) at the point (5, 6) of the grid, the plot of Figure 107(a) follows a U-shaped characteristic force curve with a minimum at 50 pm marking the transition from a dominant repulsive regime to the attractive regime.

Regarding the Figure 107(b), it shows that when the tip is the closest to the molecule (at Z_{offset}= 0 pm) the difference in the value of V_{CPD} shift between the center and the border is maximum (0.12 V). This difference decreases with the distance until it reverses around 100 pm. These findings allow for the interpretation of the contrast inversion observed on the Δf^* maps on the one hand, and to confirm the presence of the dipole of ZTAP while measuring its dependence on Z_{offset} on the other hand.

The following Figure 107 allows for the rationalization of the measurement and explains that contrast inversion.

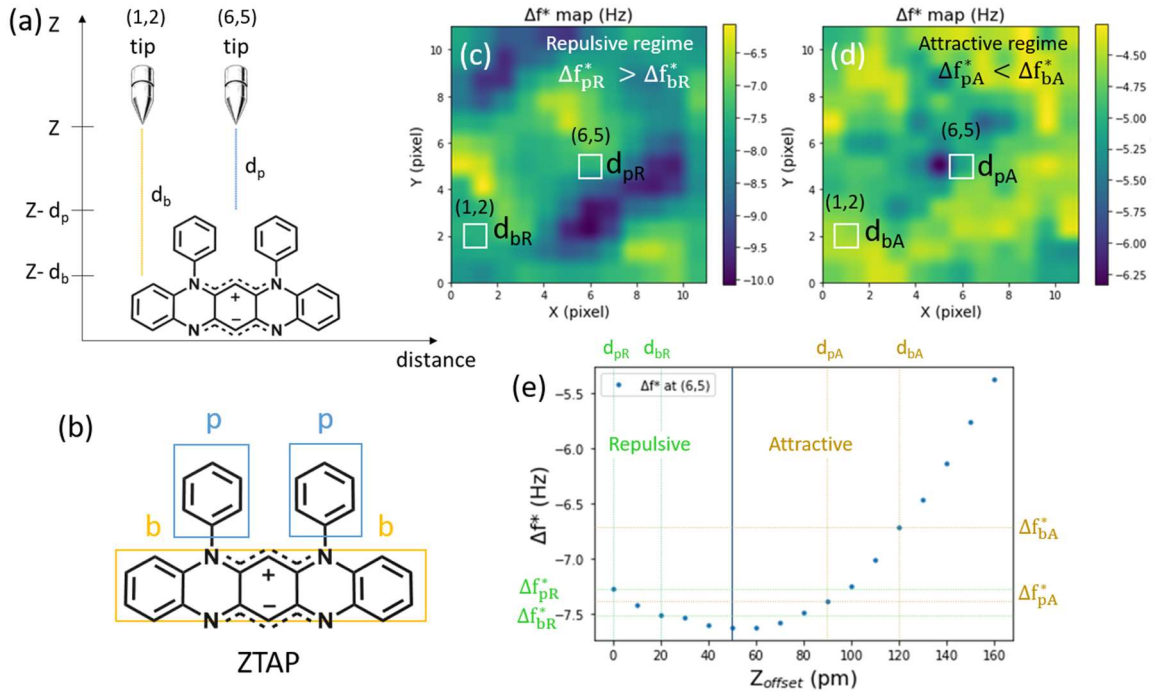


Figure 108: ***(a)*** *Scheme showing the tip position over different parts of ZTAP molecule. When the tip is positioned over the border of the molecule, the distance d_b between the tip and the probed part of the molecule is larger than the distance of the tip when it is positioned over the center of the molecule (over the phenyl substituents) at a distance d_p.* ***(b)*** *The ZTAP molecule can be illustrated as an object having 2 parts of different heights with respect to the tip, the first part 'b' is the border of the molecule highlighted by a yellow rectangle and the second part 'p' are the phenyls rings, each highlighted by a blue rectangle.* ***(c)*** *Δf^* map of the ZTAP molecule for Z_{offset}= 0 pm, in the repulsive regime, 2 pixels, one at a position d_{pR} over the phenyl rings, and another pixel at d_{bR} over the border are shown by white squares. The map contrast shows that $\Delta f^*_{pR} > \Delta f^*_{bR}$.* ***(d)*** *$\Delta f^*$ map of the ZTAP molecule for Z_{offset}= 160 pm, in the attractive regime, 2 pixels, one at a position d_{pA} over the phenyl rings, and another pixel at d_{bA} over the border are shown by white squares.* ***(e)*** *Δf^* as function of Z_{offset} for a position (6, 5) on the map over the center follows a U-shaped characteristic curve with a minimum at Z_{offset}= 50 pm marking the transition from a dominant repulsive regime to the attractive regime.*

The ZTAP molecule can be illustrated as an object having 2 different parts 'b' for border (yellow rectangle) and 'p' for phenyl (blue rectangles) (see Figure 108(b)). Respectively, the different parts 'b' and 'p' of the ZTAP molecule have different heights d_b and d_p with respect to the tip as shown in Figure 108(a). The part 'p' over the center of the molecule (over the phenyl rings) situated at a distance d_p from the tip, the other part, 'b' which represents the border of the TAP core of the molecule around this center. The border represents the external benzene rings of the ZTAP core that lie slightly below at a distance d_b from the tip such that $d_b > d_p$. Generally speaking, in the classical attractive regime (see Figure 108(c)), the probed objects which are closer to the tip, in this case the phenyls, at a distance d_{pA}, lead to a stronger interaction force than the objects further from the tip, in this case, the borders, at a distance d_{bA}. A stronger interaction force results in a smaller Δf^* shift, so for this case, $\Delta f^*_{pA} < \Delta f^*_{bA}$ and the Δf^* maps show the phenyl as having a darker contrast than the border. This arises from the relationship between Δf^* and the tip-

surface distance Z, which is an increasing curve in the attractive regime. For the repulsive regime (see Figure 108(d)), the situation is reversed: the probed objects closer to the tip (d_{pR}) lead to a weaker interaction force than the objects further away from the tip (d_{bR}). A weaker interaction force results in a greater Δf^* shift, and for this case, $\Delta f^*_{pR} > \Delta f^*_{bR}$, and the Δf^* map will show the phenyl as having a brighter contrast than the border. This arises from the relationship between Δf^* and Z, which is a decreasing curve in the repulsive regime (see Figure 108(e)). The origin of the contrast change on Δf^* is now understood as the transition from a repulsive regime to an attractive regime with the gradual increase of Z_{offset}.

Concerning the evolution of the V_{CPD} contrast as function of Z_{offset}, on the border at point (1, 2) the Figure 107(b) shows a classical decrease with increasing Z_{offset} which is explained by an averaging effect in which the sample area that contributes to the V_{CPD} becomes larger with increasing Z_{offset}.[161,162]. The V_{CPD} evolution in the center of the molecule at the points/pixels (6, 5) or (6, 6) as a function of Z_{offset} is also represented in Figure 107(b). The dependence observed for these points can be decomposed in 3 regimes: the first from 0 pm to 50 pm, the second from 50 pm to 120 pm where the dependence is quasi-linear, and the third one from 120 pm to 160 pm where the V_{CPD} contrast gets almost constant.

In the first regime, the tip is sufficiently close to the zwitterionic core of ZTAP for the dominating contrast to be the contrast of the electrostatic dipole, which results in a V_{CPD} value coherent with the dipole orientation. As the tip gets farther from the center of the molecule, the interaction force with the dipole decreases, and as this interaction force has an electrostatic origin, its contribution on the Kelvin signal decreases as well. In the third regime, the tip is sufficiently far for averaging the signal over all the molecule, and tends to be constant and close to V_{CPD} of the border of the molecule.

VI.3. ZTAP assembly on graphene: Scanning Tunneling Spectroscopy

The STS technique introduced in II.1.4 measures the LDOS at a fixed point or at each point of the surface which allows to construct a differential conductance (dI_t/dV) map for each bias voltage value. This is done by delimiting the map area by setting a predefined (X, Y) grid on the surface, and then performing STS measurement at each point of this grid for a fixed value of the tip height Z. The STS maps requirements and conditions were invoked in detail in III.3.6. This technique will be used in this section to map the LDOS of the ZTAP self-assembly on Gr/SiC.

VI.3.1. Scanning tunneling spectroscopy on molecular assembly.

STS was performed over various energy ranges on the ZTAP self-assembled molecular layer. Reliable tunneling spectroscopy requires first ensuring that the tip is perfectly metallic. A metallic tip is usually prepared on a metal surface either by applying high-voltage pulses or by immersing the tip directly into the surface to coat it with metal. The quality of the tip is then checked on the same metallic surface by checking that the tunneling spectrum displays the expected features, such as, for example, the surface state peak observed around - 0.4 V on a Au(111) surface (Figure 21).

On the Gr/SiC(0001) surface, this procedure could not be performed. Attempts were made to prepare the tip on a Au(111) surface and subsequently transfer the graphene sample. However, the time required to locate the suitable area with a molecular layer caused the tip to degrade during the search. It was therefore established that the tip had a metallic character when the STS measurements on graphene exhibited features similar to the spectra presented in the Chapter III specifically a pseudogap of approximately 100 meV width around the Fermi level.

Figure 109 (a) shows an $I_t(V_{bias})$ spectroscopy over an energy range of [- 1.0 V, 2.0 V], obtained at a regulation point on the molecular layer with I_t= 50 pA and V_{bias}= -0.85 V. In Figure 109(b), the numerical derivative of the $I_t(V_{bias})$ spectroscopy reveals 2 resonant tunneling peaks around V_{bias}= - 1.0 V and 1.90 V with respective peak onsets of - 0.8 V and 1.75 V.

As the molecules are not electronically decoupled from the graphene surface, these 2 peaks may correspond to signatures of the molecule's electronic states combined with the surface electronic states.

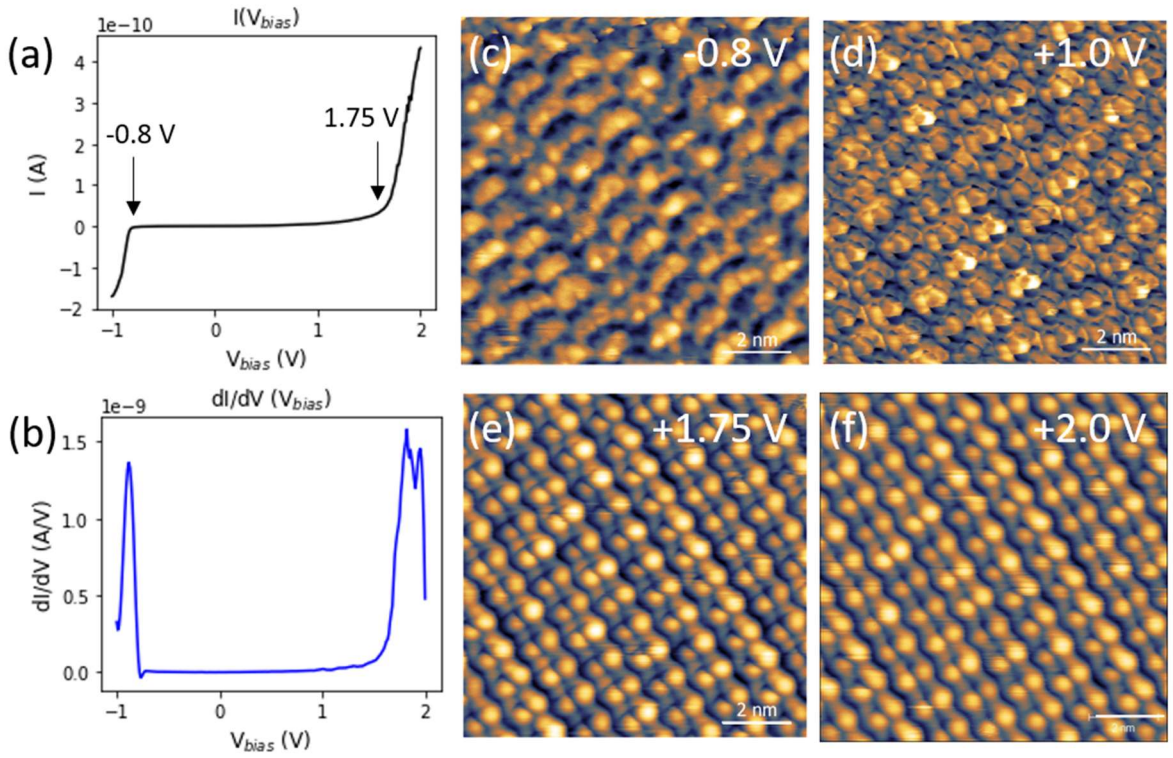


Figure 109: ***(a)*** *Scanning tunneling spectroscopy $I_t(V_{bias})$ from - 1.0 V to 2.0 V obtained on the ZTAP molecular layer, regulation point parameters: I_t= 50 pA, V_{bias}= - 0.85 V.* ***(b)*** *The numerical derivative $dI_t/dV(V_{bias})$ spectroscopy reveals 2 intense peaks at 1.75 V and - 1.0 V. STM images of ZTAP assembly at different bias voltages respectively* ***(c)*** *- 0.80 V,* ***(d)*** *1.0 V,* ***(e)*** *1.75 V and* ***(f)*** *2.0 V. Tunneling conditions: I_t= 3.7 pA. Scale bar= 2 nm.*

STM images of Figure 109(c, d, e, f) are acquired with the same tip, one after the other, at V_{bias} values of respectively - 0.80 V, 1.0 V, 1.75 V and 2.0 V corresponding to before, at, and after the peak around 1.75 V. The molecules contrast evolves significantly around this energy range.

At 1.75 V (Figure 109(e)), the STM image shows rounded bright and broad features reminiscent of molecular orbital lobes. These features are attributed to resonant tunneling through the molecule, where electrons transit into molecular electronic states. This transit leads to an increase in the tunneling current due to 2 main effects: (1) an enhanced number of electronic states with the addition of the molecular orbitals (increase of $\rho_s(E)$) and (2) a smaller distance between the tip and the first accessible electronic state, which is in the molecule above the surface compared to the distance between the tip and the first accessible surface state in graphene.

The smaller distance has a decreasing effect on the exponential term of the transmission coefficient of the tunneling barrier T in equation II.1.

Beyond 2.0 V, the molecules morphology changes again, probably indicating the access to additional states of the molecule.

In the gap region of these peaks as shown by the STM image at a bias voltage value of 1.0 V in Figure 109(d), the features displays polygonal structures having sharp defined angles, indicative of Pauli repulsion imaging.[163]

This type of contrast is characteristic of imaging conditions where the tip is extremely close to the molecule and begins to experience repulsive forces. This behavior can be explained by the rarity of accessible electronic states in this range. To compensate for this low density of states while maintaining the same setpoint current value of 3.7 pA in this case, the tip will get closer to the surface, hence the appearance of the repulsive regime.

The calculation of the electronic states of the isolated ZTAP molecule was performed in previous studies by DFT UB3LYP/6-31G(d).[6] The results for energy of the electronic states with molecular orbitals spatial configurations for the highest occupied molecular orbital (HOMO), lowest unoccupied molecular orbital (LUMO) and the second lowest unoccupied molecular orbital (LUMO+1) are shown in Figure 110.

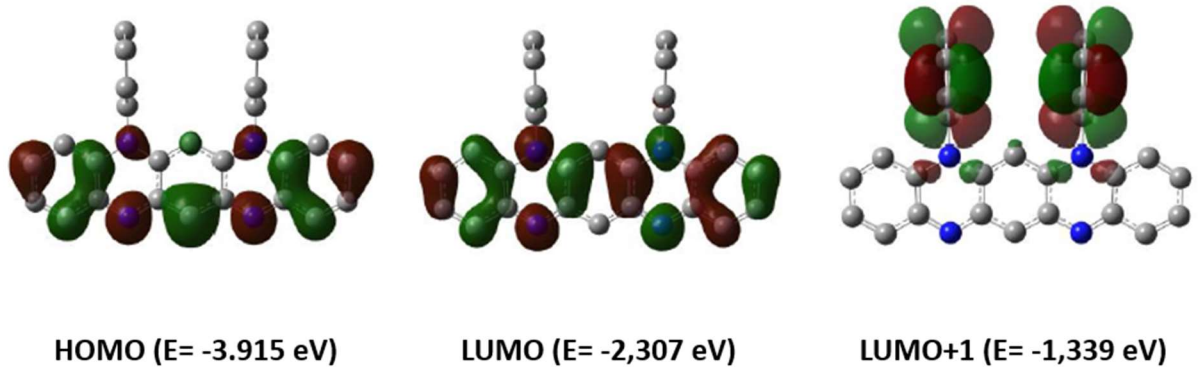


Figure 110: Molecular orbitals for the singlet ground state of ZTAP as calculated with DFT UB3LYP/6-31G(d). Hydrogens are omitted for clarity. Reproduced from earlier work.[6]

It is not possible to strictly compare the DFT calculated electronic orbitals with our STM images because the molecules are on one hand in contact with the conductive graphene surface and on the other hand a part of a compact self-assembly. These 2 characteristics can alter significantly the spatial configuration of their orbitals, as well as their energy position and the energetic width of their electronic states. [164,165]

However, these calculations can guide the interpretation of our STM images combined with the STS spectra, and show the following:

The HOMO of ZTAP supports considerable electron density at the position of its negatively charged cyanine unit. For the LUMO, the electron density is evenly distributed over the TAP core of the ZTAP meanwhile for the LUMO+1, the electronic density is only distributed over the phenyl rings of ZTAP.

The STM image acquired at a bias voltage value of 1.75 V shown in Figure 109(e) shows molecular features compatible with the ones for the LUMO+1 calculation, particularly regarding the electron density repartition as 2 bright spots are observed on the image and represent the phenyls.

The STM image acquired at a bias voltage value of - 0.8 V does not show 2 bright spots per molecule but rather a more heterogeneous distribution of electron density along its TAP core. These features are consistent with the spatial distribution of the HOMO.

The STS peaks in Figure 109(a) can be interpreted as follows: the peak at the energy- -0.8 eV could correspond to the resonance involving tunneling through the HOMO of ZTAP, while the peak around the energy 1.75 eV could indicate a resonance involving tunneling through the LUMO+1 of ZTAP.

The measured energy gap between the HOMO and LUMO+1 is estimated to be 2.55 eV and the calculated gap difference is 2.57 eV. This interpretation implies that we missed the measurement of the electronic state associated with the LUMO situated inherently at a lower energy than the LUMO+1 at 1.75 eV.

In this case, 2 hypotheses are possible: 1) the tunneling current measurement lacks sufficient sensitivity, the tip could be positioned too far during the measurement to detect a variation below 1.75 V. And 2) the tip used is not conductive enough and this interferes with its ability to tunnel in the energy range of [- 0.8 eV, 1.75 eV] and as a result to detect the LUMO. The second hypothesis is regarded as the most plausible one due to the surprising presence of a gap despite the molecules' adsorption on a conductor.

Even if there are no accessible states in ZTAP below 1.75 eV, there should always be accessible states for graphene below this energy where the measurement of a tunneling current is possible. Additionally, the image acquired at tunneling conditions of V_{bias}= 1.0 V showing polygonal features in Figure 109(d) is consistent with a tip functionalized with an insulating aggregate at its apex.

As a result, another set of spectroscopies on the ZTAP assembly was carried out in the V_{bias} range of [- 0.8 V, 0.8 V]. A total of 3 sets were recorded with slightly different tip morphologies and on different sites of the molecule's assembly.

Thus, a set of STS (X, Y) maps on the ZTAP molecules self-assembly on Gr/SiC was conducted at the intramolecular-scale and its principal results will be presented in VI.3.2.

VI.3.2. STS maps

The goal is to understand how the presence of the ZTAP molecules alters the electronic structure of graphene. To achieve this, it is essential to probe the electronic states far from the molecular resonance states, specifically within the ZTAP molecule's gap.

VI.3.3. Energy study of dI/dV spectra

The first set of spectroscopies is conducted in the energy range [-170 meV, 170 meV]. To detect tunneling currents in this energy range, the tip is positioned as close as possible from the surface, the bias voltage amplified and the I/V amplifier tuned to measure extremely low currents. The measurable tunneling current in this range is minimal and it

only reflects the surface's electronic density modified by the presence of the molecules without contributions from the molecular electronic states located at higher energies.

Figure 111 shows a plot of the $dI_t/dV(V_{bias})$ in the energy range [- 0.17 eV, 0.17 eV] and the corresponding gaussian fit (in a red line). In this range, a start of tunneling current increase is detected at 0.17 eV and probably another increase around - 0.17 eV. A gap of 211 meV width is measured between these 2 current peaks.

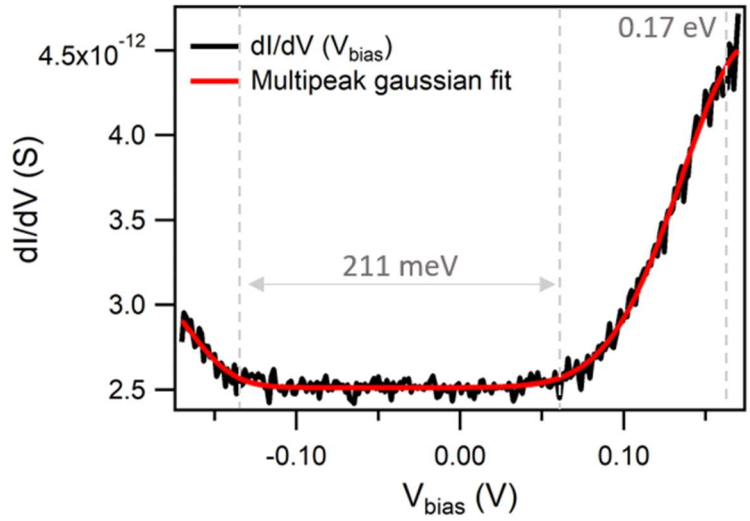


Figure 111: dI_t/dV vs V_{bias} spectrum of a single point on ZTAP self-assembled on graphene in the range [- 0.17 V, 0.17 V]. Lock-in Parameters: Z_{offset}= - 180 pm, V_{mod}= 11 mV, F_{mod}= 434 Hz, V_{bias}= 370 mV, I_t= 129 pA.

The peak around 0.17 eV is the threshold for the tunnel current detection at the smallest tip-molecule/graphene distance. During the measurements, the tip is positioned above the molecule's height (around 0.8 nm) and the measured current exponentially decays with the distance causing it to drop below the sensitivity of the IV amplifier, and in this case only the noise of the instrument is measured.

Figure 112(a) shows a second set of $dI_t/dV(V_{bias})$ spectroscopies in the energy range [0 eV, 0.5 eV] and its corresponding gaussian multipeak fit (red line). This spectroscopy was acquired with a different tip morphology than the one presented in Figure 111. The peak around 0.13 eV could correspond to the threshold for the tunnel current detection at the smallest tip-graphene distance observed around 0.17 eV in the spectroscopy in Figure 111.

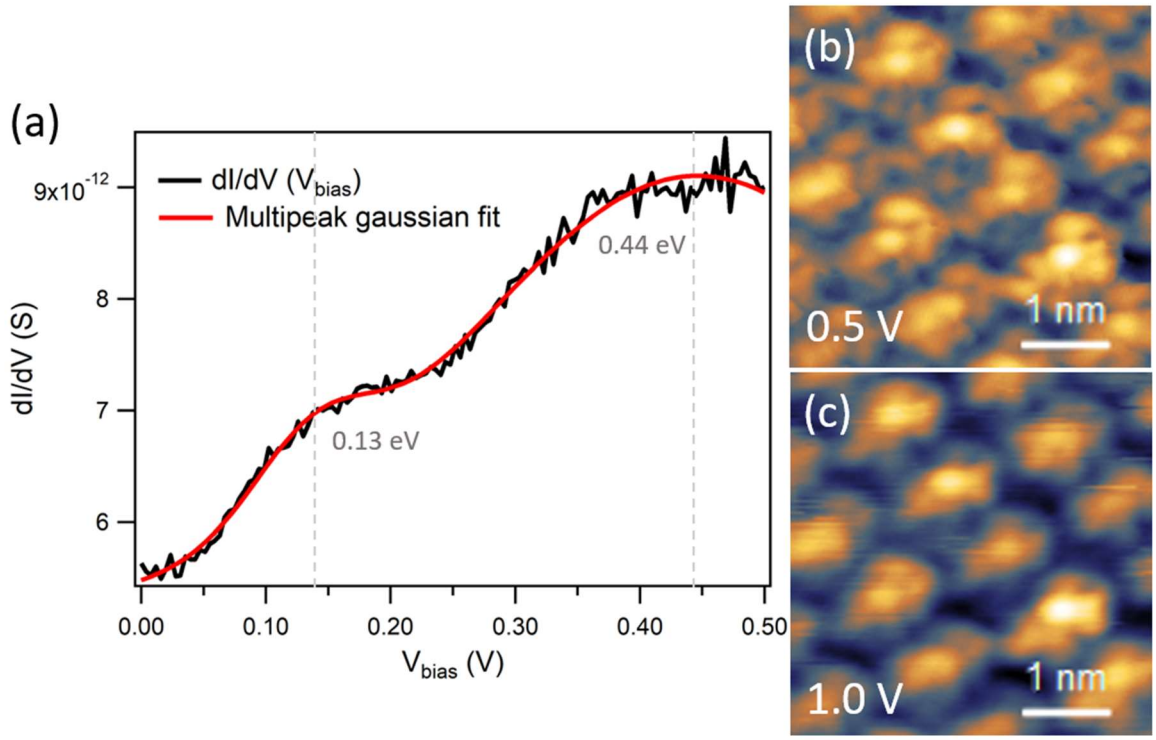


Figure 112: ***(a)*** *dI_t/dV vs V_{bias} spectrum of a single point on ZTAP self-assembled on graphene in the range [0 V, 0.5 V]. Lock-in Parameters: Z_{offset}= - 150 pm, V_{mod}= 20 mV, F_{mod} = 434 Hz, V_{bias}= 500 mV, I_t= 102 pA.* ***(b)*** *STM image of ZTAP self-assembly on Gr/SiC. Tunneling conditions: V_{bias}= 0.5 V, I_t= 23 pA.* ***(c)*** *STM image of ZTAP self-assembly on Gr/SiC. Tunneling conditions: V_{bias}= 1.0 V, I_t= 23 pA.*

Another peak is observed around 0.45 eV and can be attributed to either another graphene state at a higher energy or it can be attributed to the LUMO molecular resonant state combined with graphene's electronic states at this energy. With only this piece of information, no conclusion can be done on the nature of this peak.

A third set of spectroscopies was performed on the ZTAP molecules assembly in an energy range that spans the positive and negative bias voltage values ranging from [- 0.85 eV, 0.85 eV]. The tip used is slightly different from the previous spectroscopy set, the $dI_t/dV(V_{bias})$ plot and its corresponding gaussian multipeak fit are shown in Figure 113(a).

To achieve this, the tip is retracted slightly further compared to its position in the spectroscopy set shown in Figure 112(a). This adjustment avoids saturating the IV amplifier at higher bias voltages. The IV amplifier's sensitivity is reduced at lower bias voltages but gains in dynamics towards higher bias voltages (0.85 V). Reason why this spectroscopy does not exhibit the same profile as the spectroscopies shown in Figure 111 and Figure 112(a) towards the low bias voltage values (the peak around 0.17 V is no longer visible). This spectroscopy reveals an initial increase of intensity around - 0.80 V also observed as a peak in the spectroscopy shown in Figure 109(a), this peak signs the molecule's HOMO molecular resonant state combined with graphene's electronic states at this energy.

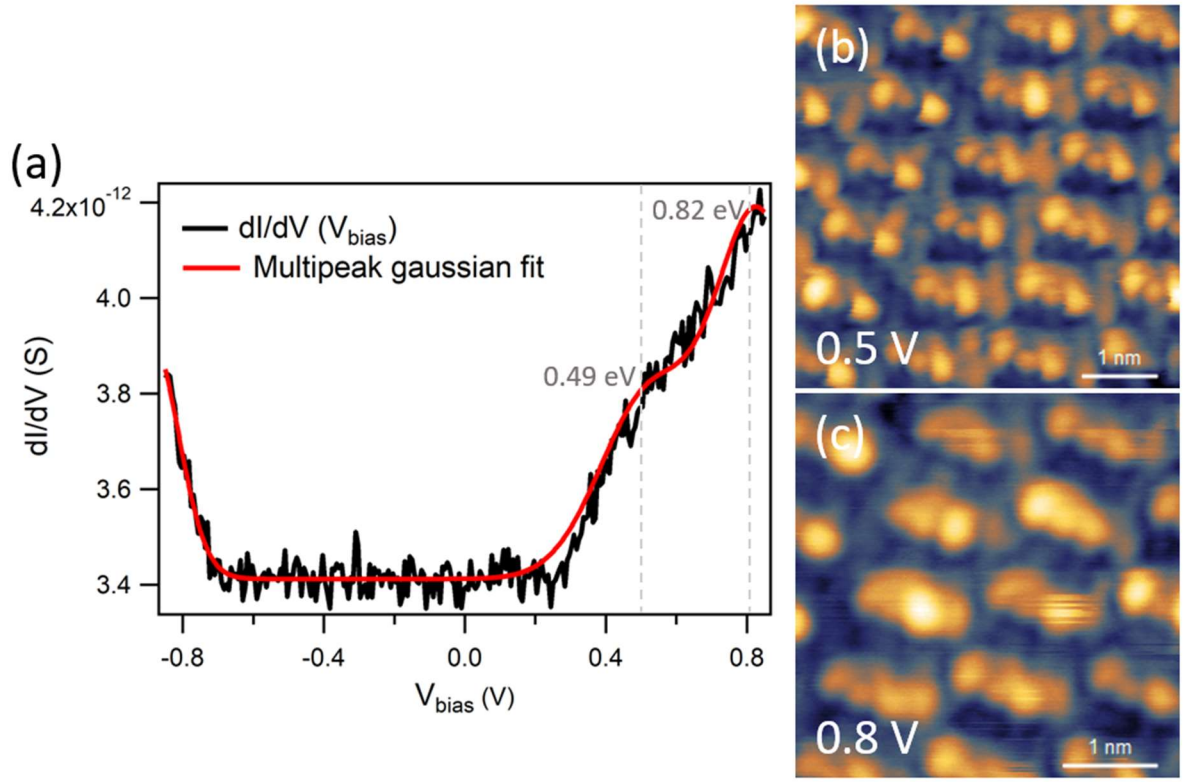


Figure 113: ***(a)*** *dI_t/dV vs V_{bias} spectrum of a single point on ZTAP self-assembled on graphene in the range [-0.85 V, 0.85 V]. Lock-in Parameters: Z_{offset} = - 120 pm, V_{mod} = 15 mV, F_{mod} = 434 Hz, V_{bias} = 850 mV, I_t = 82 pA.* ***(b)*** *STM image of ZTAP self-assembly on Gr/SiC. Tunneling conditions: V_{bias} = 0.5 V, I_t = 26 pA.* ***(c)*** *STM image of ZTAP self-assembly on Gr/SiC. Tunneling conditions: V_{bias} = 0.8 V, I_t = 22 pA.*

Another peak is observed around 0.49 V that could be associated to the one measured around 0.45 eV in the spectroscopy of Figure 112(a). A third peak is observed around 0.82 eV and could also sign the ZTAP LUMO molecular resonant state in addition to the graphene electronic states at this energy.

STM images acquired with the 2 different tip morphologies at the different bias voltage values around the peak values could be an additional supporting information for the attribution of the peaks around 0.45 eV and 0.80 eV (Figure 112(b-c) and Figure 113(b-c)).

The STM image of Figure 113(b) acquired at a V_{bias} value of 0.5 V shows a molecular unit composed of 4 small lobes with an uneven repartition in electronic density. This morphology is compared to the image acquired with a different STM tip in Figure 112(b). However, the latter does not represent a discernible molecular structure. Consequently, the 2 images are not comparable, and no definitive conclusions can be drawn, as neither aligns with the molecular morphology predicted by calculations in Figure 110.

In contrast, the STM image in Figure 113(c) acquired at a bias voltage of 0.80 V displays a molecular unit having bright lobes more rounded morphology. When compared to Figure 112(c), acquired with a different tip at a higher bias voltage of 1.0 V, the 2 images appear to be similar, both showing a regular repartition of electronic density localized in the TAP core of the ZTAP molecule.

By adding the information acquired from the energy-dependent study with the resulting STM images, a preliminary overall attribution of the observed peaks can be made. These results are summarized in Figure 114, where the curves' maxima are normalized and their minima reset to zero. This approach focuses only on the energetic positions of the peaks, disregarding their intensities, to facilitate direct comparison between the spectra.

The analysis begins with the peak around - 0.85 eV, which is attributed to the HOMO molecular resonant state of ZTAP combined with the electronic states of graphene at this energy. The current increase observed around -0.17 eV is likely due to a graphene electronic state, labeled as 'a' in the figure. Another significant threshold of intensity increase, observed between 0.13 eV and 0.17 eV, is also associated with a graphene electronic state and is labeled as 'b'. Another graphene state is identified in the range of 0.44 eV to 0.49 eV, labelled as 'c' in the figure.

The peak at approximately 0.80 eV is attributed to the LUMO molecular resonant state combined with graphene electronic states at this energy. This attribution is supported with the recorded STM images around the bias voltage value 0.80 V, which shows a regular distribution of electronic density localized at the TAP core of the ZTAP molecule. Although differences between the experimental and calculated energy differences between molecular electronic states are not usually comparable, the hypothesis can be further supported by the measured HOMO-LUMO transition energy of 1.82 eV compared the calculated value of 1.61 eV.

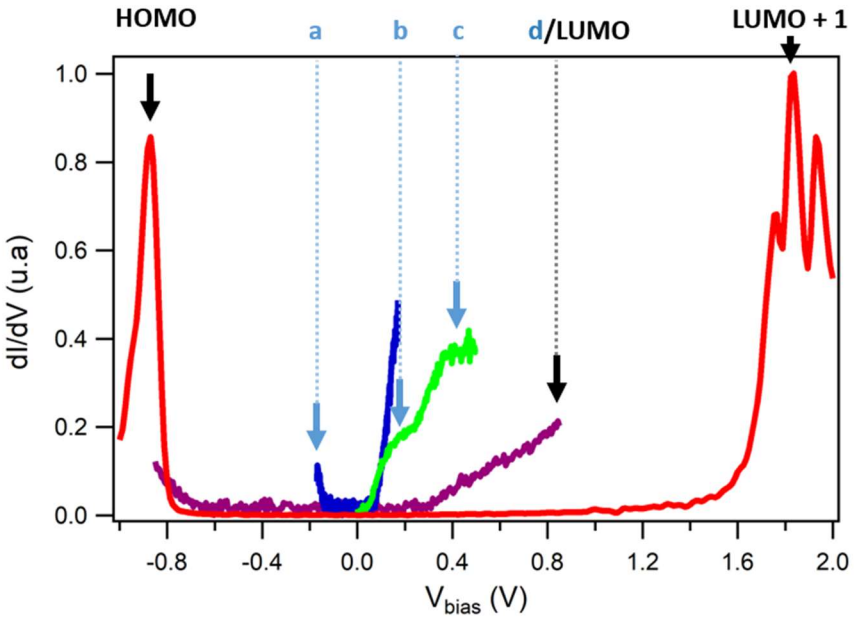


Figure 114: Differential conductivity spectroscopies acquired for different energy ranges and different tip heights. The curves' intensity maxima are normalized and their minima reset to zero for comparison between the spectra.

VI.3.4. Spatial study of STS maps

I(V) and dI/dV(V_{bias}) mapping on a grid of 50 pixels × 50 pixels was conducted on the ZTAP molecule's self-assembly on Gr/SiC. The bias voltage range extends from [- 0.17 V, 0.17 V] for these maps.

The dI/dV and I_{map} under study was acquired at 0.17 eV. At this low energy, a graphene electronic state is probed rather than a molecular resonant state of ZTAP, making the molecules indistinguishable at this energy. However, the map reveals bright spots that correspond to the periodicity of the molecular assembly.

The dI/dV map that will be studied is the one acquired at V_{bias} value of 0.17 eV. At this low energy a graphene electronic state can be probed, not the molecular resonant state, the molecules will not be distinguishable at this energy. Thus, the electronic contribution from the graphene substrate dominates the signal, rather than the molecular states. However, this map shows periodic bright spots that have the periodicity of the ZTAP molecular assembly, suggesting how the molecular assembly influences the graphene electronic structure. Their periodic arrangement modulates the graphene state, resulting in the periodic features observed in the map.

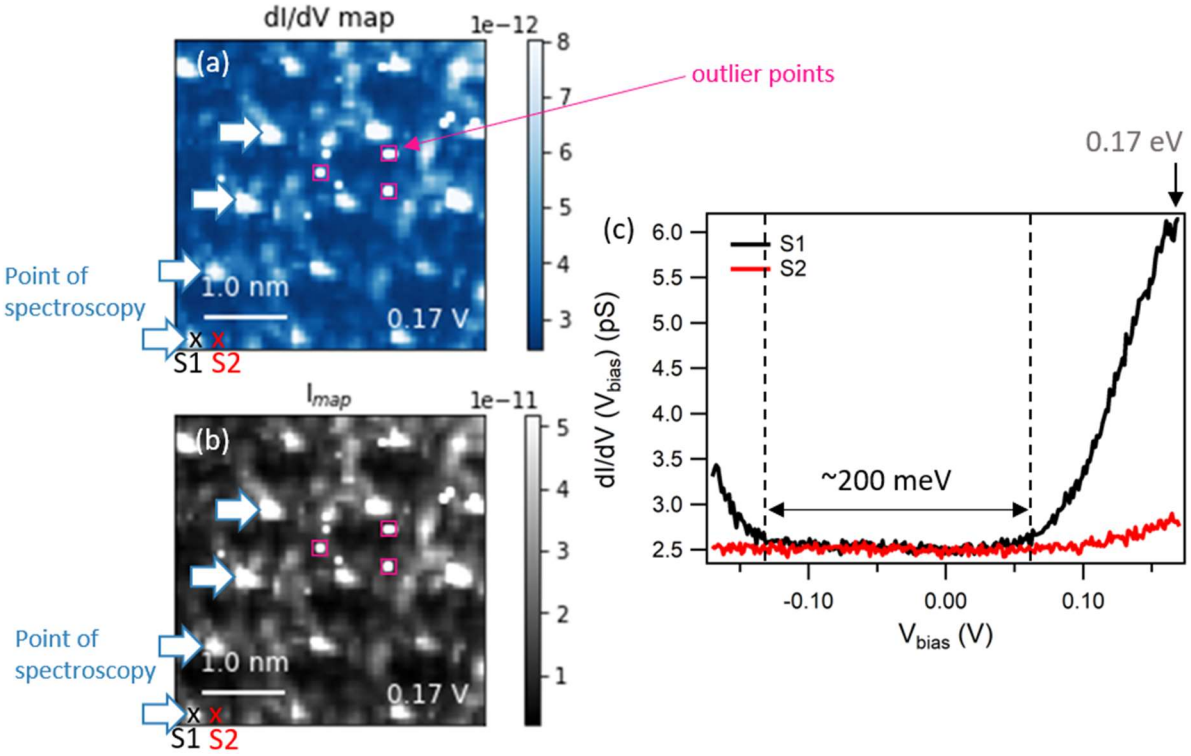


Figure 115: ***(a)*** *Differential conductivity dI/dV map of ZTAP on graphene at V_{bias}= 0.17 V. Bright spots showing outlier data points are highlighted by pink squares. (b) I_{map} of ZTAP on graphene at V_{bias}= 0.17 V. Bright spots showing outlier data points are highlighted by pink squares* ***(c)*** *dI/dV single spectroscopy measurement was performed at a bright spot on the map, labeled as S1 and marked with a black cross ('x'). Another dI/dV single spectroscopy measurement was conducted at a dark spot on the map, labeled by S2 and marked with a red cross ('x'). Lock-in Parameters: V_{mod}= 11 mV, F_{mod} = 434 Hz, V_{bias}= 370 mV, I_t= 18 pA.*

The LDOS is probed on this map on the bright spots, and the resultant dI/dV curve in Figure 115(c) shows the presence of a 200 meV pseudogap around the fermi energy with a localized effect due to the adsorbed molecules.

The LDOS then starts to increases around - 0.15 V and 0.07 V and these values could correspond to energy positions of graphene states modified by the molecules near the Fermi level. These results show a strong heterogeneity in the spatial distribution of the electronic states at 0.17 eV with periodic localized areas of high contrast. This distribution is periodic and follows the molecular lattice periodicity. In the next subsection, we will focus on localizing the ZTAP positions within this map.

VI.3.4.1. Molecules' recognition on the STS maps

To locate the ZTAP molecules on the differential conductivity map of Figure 115 we start by locating ZTAP position on an STM image. The Figure 116(a) shows an STM image acquired under conditions that allow to clearly see the molecule's position such as at a bias voltage of 850 mV, where the TAP core is visible. This image was acquired right after the map acquisition and presents negligible thermal drift. On this image will be superposed the dI/dV map of Figure 116(b) with the STM image done after the map acquisition to locate the position of ZTAP as shown in Figure 116(c).

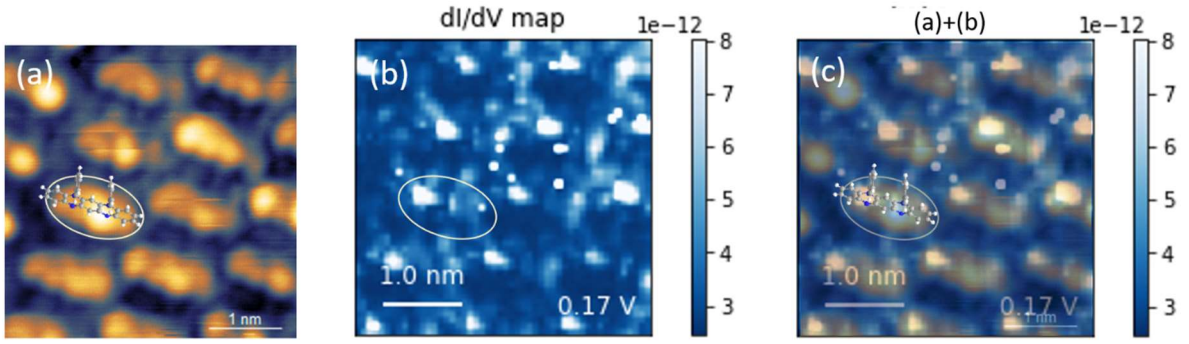


*Figure 116: **(a)** STM image of ZTAP self-assembly on graphene. Tunneling conditions: V_{bias}= 850 mV, I_t=100 pA. One molecule is circled in white. **(b)** Differential conductivity dI/dV of ZTAP on graphene at V_{bias}= 0.17 V. Lock-in Parameters: V_{mod}= 11 mV, F_{mod} = 434 Hz, V_{bias}= 370 mV, I_t= 18 pA. **(c)** Superposition of the image in (a) and the map in (b).*

This superposition allows to associate the bright spots to a specific region of the molecule. Thus, the Figure 116(c) shows that the bright spot corresponds to an azaacene ring of ZTAP, probably at the position near the nitrogen atoms of the molecule represented in blue on the ball and stick model of ZTAP overlaid on the Figure 116(c).

VI.3.4.2. Analysis of the outlier data points

To ensure a clear data analysis, we will begin with an examination of specific points on the map that exhibit an exceptionally bright contrast, appearing as isolated dots at random positions on the surface. These points are present on all the set of maps acquired at the bias voltages ranging from [- 0.17 V, 0.17 V].

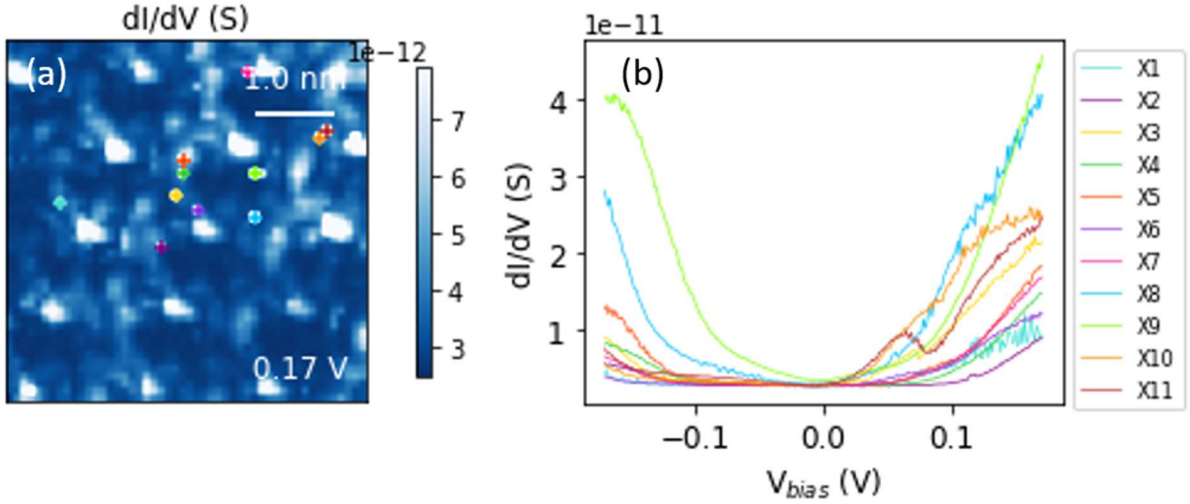


Figure 117: ***(a)*** *dI/dV map of ZTAP self-assembly on graphene. The colored '+' signs indicate outlier data points that exhibit a bright contrast, these points are labelled by X1 to X11. The highlighted data points are considered anomalies and are excluded from further analysis. Lock-in Parameters:* V_{mod}*= 11 mV,* F_{mod} *= 434 Hz,* V_{bias}*= 370 mV,* I_t*= 18 pA.* ***(b)*** *Differential conductance curves corresponding to the outlier data points marked in (a). the curves illustrate the suppression of the pseudogap for the green and blue curves, the smaller gap of the orange curve, and the larger pseudogap observed in the remaining curves.*

These points are classified as outliers and will be excluded from further analysis of the map to avoid confusion. Examples of these outlier data points are marked with colored plus signs '+', labelled from X1 to X11 in the legend of Figure 117(b).

The differential conductance curves of the outlier points are shown in Figure 117(b). We exclude these single STS from analysis because they correspond to a punctual modification of the apex of the tip.

VI.3.4.3. STS maps on the different parts of ZTAP molecule

Having identified and excluded the outlier data points, the analysis proceeds by the study the STS curves corresponding to the points located beneath the various parts of the ZTAP molecule. The analysis of the STS data will mirror the previous examination, concentrating on the map and dI/dV curves corresponding to the colored data points now labelled from S1 to S7.

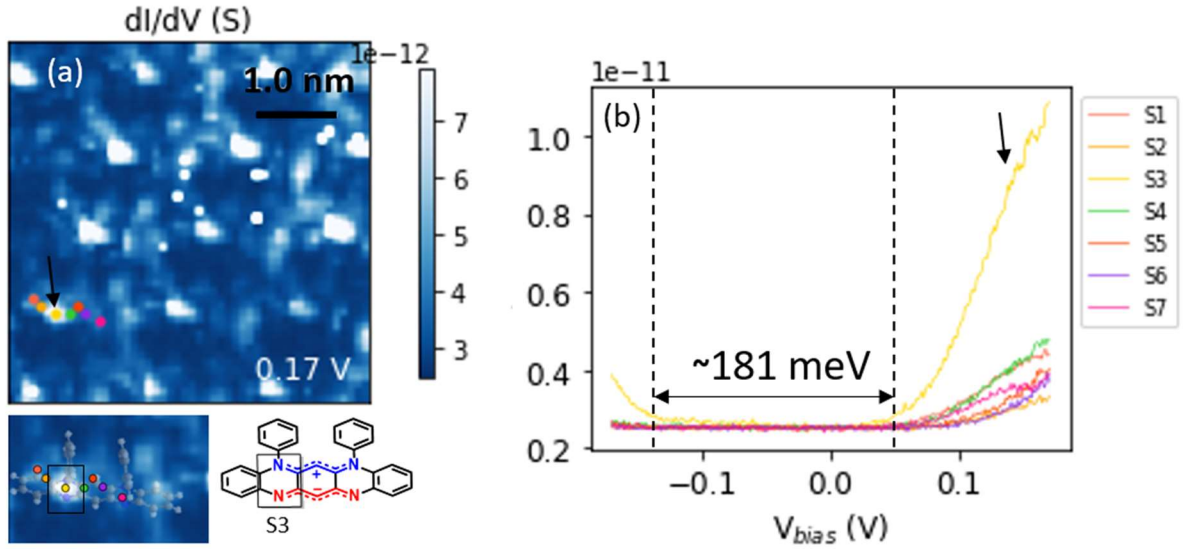


*Figure 118: **(a)** dI/dV map showing the distribution of data points beneath specific areas of the ZTAP molecule, with colored dots indicating the analyzed data points labelled by S1 to S7. These points correspond to regions of interest for further analysis. Lock-in Parameters: V_{mod}= 11 mV, F_{mod} = 434 Hz, V_{bias}= 370 mV, I_t= 18 pA. **(b)** dI/dV measurements corresponding to data points marked in (a). The curves reveal variations in the pseudogap for the magenta spot corresponding to the S3 part of the molecule shown in inset.*

This map shows a periodic bright feature indicated by a yellow dot and an arrow, its differential conductivity spectrum is labelled by S3 in yellow color in Figure 118.

The S3 spectrum of the ZTAP molecule shows a pseudogap of width 181 meV, with peak onsets near 0.05 V and - 0.13 V.

In contrast, the other spectroscopies over the other parts of the molecule display greater pseudogap widths extending from 220 meV to 280 meV, with the latter's onsets at the energy of 0.11 eV for the positive bias region.

We observe asymmetry in pseudogap widths and onset positions between positive and negative bias voltages. These features could arise from overlapping contributions of molecular resonances, graphene states and the dipoles at the interface.

The bright spot emerges in regions where the molecules assembly is commensurate with the substrate in the $\mathbf{m_1}$ direction. This ZTAP self-assembled arrangement is probably responsible for the modulation of the electronic structure, and the STS maps are an additional indicator of the molecular-substrate registry.

VI.4. Conclusion

This chapter demonstrated the complementary use of KPFM, STS and STM for characterizing molecular assemblies on surfaces. Each technique provided unique insights into the morphology, electronic structure and assembly behavior of the system.

The ZTAP molecules physiosorbed in ribbons of alternating symmetrical adsorption configuration as observed from the analysis of high-resolution STM images. An epitaxial relationship study between the ZTAP self-assembly's lattice and graphene lattice showed that the ZTAP form a high-order commensurate superstructure with graphene.

Coupling KPFM and 4D KPFS studies on this ZTAP network with the results acquired from STM images enables the mapping of surface potential variations. The results confirm the resultant dipole orientation pointing away from the graphene surface for the monolayer, and alternates with the number of layers. The surface dipole effect could be mapped at the intramolecular scale for a molecular assembly.

For the monolayer, this dipole periodically modulates the electrostatic surface potential of graphene on the position of the zwitterionic core of the molecules.

In addition, STS energy study and spatial study provided information about the electronic states of the assembly. At tip positions far from the surface, the differential conductance spectra gave insights into the key molecular resonant states coupled with the graphene electronic states such as HOMO, LUMO and LUMO+1, as well as their spatial alignment with the structural features observed on the STM images. The electronic states near the Fermi level were examined by performing differential conductivity maps in narrow energy windows and with the tip held the closest possible from the surface. Bright periodic features having the periodicity of the molecular assembly emerge on the maps showing a periodic modulation of the electronic structure of graphene on the molecule lattice nodes.

This work can be further enhanced to address current limitations and extract more precise data to build a more comprehensive picture of the system. STS mappings should be conducted on both graphene and ZTAP assembly using the same tip morphology across various energy windows to uncover potential shifts in graphene states. These experimental efforts complemented by computational simulations could offer a more precise interpretation of this system.

General Conclusion

The research question at the heart of this thesis was whether it is possible to induce the modulation of the surface potential of graphene by depositing an organic molecular layer, specifically a zwitterionic molecular layer, and whether this could lead to modifications in the material's electronic structure.

The results of this study provide a clear affirmative answer. By depositing QZ and ZTAP zwitterionic molecules on graphene, we successfully observed the formation of a large-scale superlattice, which directly influences the graphene's band structure.

This self-assembly of DPQZ molecules results in a molecular dipole aligned with the graphene surface, while ZTAP molecules adopt an inclined dipole orientation that more significantly impacts the surface potential. Low-temperature 4D KPFM mapping revealed a modulation of up to 150 mV in the local contact potential difference (LCPD), directly correlated with the molecular dipoles. This demonstrates the ability of organic molecular layers to modify the electrostatic properties of graphene.

Through careful control of the molecular size and peripheral functional groups, we were able to tune the lattice parameter size and the molecular assembly geometry, creating a periodic interaction with the underlying graphene structure. These findings offer evidence that zwitterionic molecules can effectively alter the surface potential of graphene, answering the research question in the affirmative.

This work has laid a solid foundation for exploring the potential of zwitterionic molecular layers in modifying the electronic properties of graphene. Further experiments could focus on fabricating small devices of zwitterions on graphene and studying the transport properties at various temperature ranges, enabling the investigation of the molecular freezing effects. Subsequently, Raman spectroscopy could be conducted on the heterostructures to extract critical information about the graphene's doping levels and the strain induced by the molecular network. This analysis could also provide valuable insights into the molecular ordering and may reveal unique Raman signatures arising from the presence of the superlattice. Simultaneously, theoretical simulations focused on modeling the graphene/molecule interface will be essential to enhance the interpretation of the experimental results.

Bibliography

(1) Cao, Y.; Fatemi, V.; Fang, S.; Watanabe, K.; Taniguchi, T.; Kaxiras, E.; Jarillo-Herrero, P. Unconventional Superconductivity in Magic-Angle Graphene Superlattices. *Nature* **2018**, *556* (7699), 43–50. https://doi.org/10.1038/nature26160.

(2) Zheng, Z.; Ma, Q.; Bi, Z.; de la Barrera, S.; Liu, M.-H.; Mao, N.; Zhang, Y.; Kiper, N.; Watanabe, K.; Taniguchi, T.; Kong, J.; Tisdale, W. A.; Ashoori, R.; Gedik, N.; Fu, L.; Xu, S.-Y.; Jarillo-Herrero, P. Unconventional Ferroelectricity in Moiré Heterostructures. *Nature* **2020**, *588* (7836), 71–76. https://doi.org/10.1038/s41586-020-2970-9.

(3) Siri, O.; Braunstein, P. Unprecedented Zwitterion in Quinonoid Chemistry. *Chem. Commun.* **2002**, No. 3, 208–209. https://doi.org/10.1039/b107828n.

(4) Braunstein, P.; Siri, O.; Taquet, J.; Rohmer, M.-M.; Bénard, M.; Welter, R. A 6π + 6π Potentially Antiaromatic Zwitterion Preferred to a Quinoidal Structure: Its Reactivity Toward Organic and Inorganic Reagents. *J. Am. Chem. Soc.* **2003**, *125* (40), 12246–12256. https://doi.org/10.1021/ja0354622.

(5) Yang, Q.-Z.; Siri, O.; Braunstein, P. First Transamination Reactions for the One-Pot Synthesis of Substituted Zwitterionic Quinones. *Chemical Communications* **2005**, No. 21, 2660–2662. https://doi.org/10.1039/B501926E.

(6) Zissimou, G. A.; Kourtellaris, A.; Koutentis, P. A. Oxidation of Isodiphenylfluorindine: Routes to 13-Oxoisodiphenylfluorindinium Perchlorate and Fluorindine Cruciform Dimers. *Organic Letters* **2018**, *20* (3), 844–847.

(7) Hapala, P.; Švec, M.; Stetsovych, O.; van der Heijden, N. J.; Ondráček, M.; van der Lit, J.; Mutombo, P.; Swart, I.; Jelínek, P. Mapping the Electrostatic Force Field of Single Molecules from High-Resolution Scanning Probe Images. *Nat Commun* **2016**, *7* (1), 11560. https://doi.org/10.1038/ncomms11560.

(8) Wickenburg, S.; Lu, J.; Lischner, J.; Tsai, H.-Z.; Omrani, A. A.; Riss, A.; Karrasch, C.; Bradley, A.; Jung, H. S.; Khajeh, R.; Wong, D.; Watanabe, K.; Taniguchi, T.; Zettl, A.; Neto, A. H. C.; Louie, S. G.; Crommie, M. F. Tuning Charge and Correlation Effects for a Single Molecule on a Graphene Device. *Nat Commun* **2016**, *7* (1), 13553. https://doi.org/10.1038/ncomms13553.

(9) Goronzy, D. P.; Ebrahimi, M.; Rosei, F.; Arramel; Fang, Y.; De Feyter, S.; Tait, S. L.; Wang, C.; Beton, P. H.; Wee, A. T. S.; Weiss, P. S.; Perepichka, D. F. Supramolecular Assemblies on Surfaces: Nanopatterning, Functionality, and Reactivity. *ACS Nano* **2018**, *12* (8), 7445–7481. https://doi.org/10.1021/acsnano.8b03513.

(10) Gobbi, M.; Bonacchi, S.; Lian, J. X.; Liu, Y.; Wang, X.-Y.; Stoeckel, M.-A.; Squillaci, M. A.; D'Avino, G.; Narita, A.; Müllen, K.; Feng, X.; Olivier, Y.; Beljonne, D.; Samorì, P.; Orgiu, E. Periodic Potentials in Hybrid van Der Waals Heterostructures Formed by Supramolecular Lattices on Graphene. *Nat Commun* **2017**, *8* (1), 1–8. https://doi.org/10.1038/ncomms14767.

(11) Wudl, F.; Koutentis, P. A.; Weitz, A.; Ma, B.; Strassner, T.; Houk, K. N.; Khan, S. I. Polyazaacenes: New Tricks for Old Dogs. *Pure and Applied Chemistry* **1999**, *71* (2), 295–302. https://doi.org/10.1351/pac199971020295.

(12) Sawicka, A.; Skurski, P.; Simons, J. An Excess Electron Binding to the `purple' Zwitterion Quinonoid. *Chemical Physics Letters* **2002**, *362* (5), 527–533. https://doi.org/10.1016/S0009-2614(02)01078-3.

(13) Constantinides, C. P.; Koutentis, P. A.; Schatz, J. A DFT Study of the Ground State Multiplicities of Linear vs Angular Polyheteroacenes. *Journal of the American Chemical Society* **2004**, *126* (49), 16232–16241.

(14) Guevara-Level, P.; Pascal, S.; Siri, O.; Jacquemin, D. First Principles Investigation of the Spectral Properties of Neutral, Zwitterionic, and Bis-Cationic Azaacenes. *Phys. Chem. Chem. Phys.* **2019**, *21* (41), 22910–22918. https://doi.org/10.1039/C9CP04835A.

(15) Kunkel, D. A.; Hooper, J.; Simpson, S.; Miller, D. P.; Routaboul, L.; Braunstein, P.; Doudin, B.; Beniwal, S.; Dowben, P.; Skomski, R.; Zurek, E.; Enders, A. Self-Assembly of Strongly Dipolar Molecules on Metal Surfaces. *The Journal of Chemical Physics* **2015**, *142* (10), 101921. https://doi.org/10.1063/1.4907943.

(16) Whitesides, G. M.; Mathias, J. P.; Seto, C. T. Molecular Self-Assembly and Nanochemistry: A Chemical Strategy for the Synthesis of Nanostructures. *Science* **1991**, *254* (5036), 1312–1319. https://doi.org/10.1126/science.1962191.

(17) Barth, J. V.; Costantini, G.; Kern, K. Engineering Atomic and Molecular Nanostructures at Surfaces. *Nature* **2005**, *437* (7059), 671–679. https://doi.org/10.1038/nature04166.

(3) *Metastable state | Phase transition, Kinetic energy, Equilibrium | Britannica*. https://www.britannica.com/science/metastable-state.

(19) Barth, J. V. Molecular Architectonic on Metal Surfaces. *Annual Review of Physical Chemistry* **2007**, *58*, 375–407. https://doi.org/10.1146/annurev.physchem.56.092503.141259.

(20) Minkin, V. I. Glossary of Terms Used in Theoretical Organic Chemistry. *Pure and Applied Chemistry* **1999**, *71* (10), 1919–1981. https://doi.org/10.1351/pac199971101919.

(21) Uvarov, E. B.; Isaacs, A. The Penguin Dictionary of Science; 1972.

(22) Arunan, E.; Desiraju, G. R.; Klein, R. A.; Sadlej, J.; Scheiner, S.; Alkorta, I.; Clary, D. C.; Crabtree, R. H.; Dannenberg, J. J.; Hobza, P.; Kjaergaard, H. G.; Legon, A. C.; Mennucci, B.; Nesbitt, D. J. Defining the Hydrogen Bond: An Account: (IUPAC Technical Report) Sponsoring Body: IUPAC Physical and Biophysical Chemistry Division: See More Details on p. 1630. https://doi.org/10.1515/iupac.83.0501.

(23) Głowacki, E. D.; Irimia-Vladu, M.; Bauer, S.; Sariciftci, N. S. Hydrogen-Bonds in Molecular Solids – from Biological Systems to Organic Electronics. *J. Mater. Chem. B* **2013**, *1* (31), 3742–3753. https://doi.org/10.1039/C3TB20193G.

(9) Pihko, P. M. *Hydrogen Bonding in Organic Synthesis*; John Wiley & Sons, **2009**.

(25) Ciesielski, A.; Szabelski, P. J.; Rżysko, W.; Cadeddu, A.; Cook, T. R.; Stang, P. J.; Samorì, P. Concentration-Dependent Supramolecular Engineering of Hydrogen-Bonded Nanostructures at Surfaces: Predicting Self-Assembly in 2D. *J. Am. Chem. Soc.* **2013**, *135* (18), 6942–6950. https://doi.org/10.1021/ja4002025.

(26) Kühnle, A. Self-Assembly of Organic Molecules at Metal Surfaces. *Current Opinion in Colloid & Interface Science* **2009**, *14* (2), 157–168.

(27) Novoselov, K. S.; Geim, A. K.; Morozov, S. V.; Jiang, D.; Zhang, Y.; Dubonos, S. V.; Grigorieva, I. V.; Firsov, A. A. Electric Field Effect in Atomically Thin Carbon Films. *Science* **2004**, *306* (5696), 666–669. https://doi.org/10.1126/science.1102896.

(28) Novoselov, K. S.; Fal′ko, V. I.; Colombo, L.; Gellert, P. R.; Schwab, M. G.; Kim, K. A Roadmap for Graphene. *Nature* **2012**, *490* (7419), 192–200. https://doi.org/10.1038/nature11458.

(29) Geim, A. K.; Novoselov, K. S. The Rise of Graphene. *Nature Mater* **2007**, *6* (3), 183–191. https://doi.org/10.1038/nmat1849.

(30) MacLeod, J. M.; Rosei, F. Molecular Self-Assembly on Graphene. *Small* **2014**, *10* (6), 1038–1049. https://doi.org/10.1002/smll.201301982.

(31) Wang, Y.-L.; Ren, J.; Song, C.-L.; Jiang, Y.-P.; Wang, L.-L.; He, K.; Chen, X.; Jia, J.-F.; Meng, S.; Kaxiras, E.; Xue, Q.-K.; Ma, X.-C. Selective Adsorption and Electronic Interaction of F 16 CuPc on Epitaxial Graphene. *Phys. Rev. B* **2010**, *82* (24), 245420. https://doi.org/10.1103/PhysRevB.82.245420.

(32) Zhang, Z.; Huang, H.; Yang, X.; Zang, L. Tailoring Electronic Properties of Graphene by π–π Stacking with Aromatic Molecules. *J. Phys. Chem. Lett.* **2011**, *2* (22), 2897–2905. https://doi.org/10.1021/jz201273r.

(33) Kong, L.; Enders, A.; Rahman, T. S.; Dowben, P. A. Molecular Adsorption on Graphene. *J. Phys.: Condens. Matter* **2014**, *26* (44), 443001. https://doi.org/10.1088/0953-8984/26/44/443001.

(34) Mao, H. Y.; Lu, Y. H.; Lin, J. D.; Zhong, S.; Wee, A. T. S.; Chen, W. Manipulating the Electronic and Chemical Properties of Graphene via Molecular Functionalization. *Progress in Surface Science* **2013**, *88* (2), 132–159. https://doi.org/10.1016/j.progsurf.2013.02.001.

(35) Tang, Q.; Zhou, Z.; Chen, Z. Graphene-Related Nanomaterials: Tuning Properties by Functionalization. *Nanoscale* **2013**, *5* (11), 4541–4583. https://doi.org/10.1039/C3NR33218G.

(36) Liu, H.; Liu, Y.; Zhu, D. Chemical Doping of Graphene. *Journal of materials chemistry* **2011**, *21* (10), 3335–3345.

(37) Cho, J.; Smerdon, J.; Gao, L.; Süzer, Ö.; Guest, J. R.; Guisinger, N. P. Structural and Electronic Decoupling of C60 from Epitaxial Graphene on SiC. *Nano Lett.* **2012**, *12* (6), 3018–3024. https://doi.org/10.1021/nl3008049.

(38) Nair, M. N.; Mattioli, C.; Cranney, M.; Malval, J.-P.; Vonau, F.; Aubel, D.; Bubendorff, J.-L.; Gourdon, A.; Simon, L. STM Studies of Self-Assembled Tetrathiafulvalene (TTF) Derivatives on Graphene: Influence of the Mode of Deposition. *J. Phys. Chem. C* **2015**, *119* (17), 9334–9341. https://doi.org/10.1021/acs.jpcc.5b00857.

(24) Wang, Y.-L.; Ren, J.; Song, C.-L.; Jiang, Y.-P.; Wang, L.-L.; He, K.; Chen, X.; Jia, J.-F.; Meng, S.; Kaxiras, E.; Xue, Q.-K.; Ma, X.-C. Selective Adsorption and Electronic Interaction of F16CuPc on Epitaxial Graphene. *Phys. Rev. B* **2010**, *82* (24), 245420. https://doi.org/10.1103/PhysRevB.82.245420.

(40) Wang, Q. H.; Hersam, M. C. Room-Temperature Molecular-Resolution Characterization of Self-Assembled Organic Monolayers on Epitaxial Graphene. *Nature Chem* **2009**, *1* (3), 206–211. https://doi.org/10.1038/nchem.212.

(41) Karmel, H. J.; Garramone, J. J.; Emery, J. D.; Kewalramani, S.; Bedzyk, M. J.; Hersam, M. C. Self-Assembled Organic Monolayers on Epitaxial Graphene with Enhanced Structural and Thermal Stability. *Chem. Commun.* **2014**, *50* (64), 8852–8855. https://doi.org/10.1039/C4CC02761B.

(42) Fang, Y.; Nguyen, P.; Ivasenko, O.; Aviles, M. P.; Kebede, E.; Askari, M. S.; Ottenwaelder, X.; Ziener, U.; Siri, O.; Cuccia, L. A. Charge-Assisted Hydrogen Bond-Directed Self-Assembly of an Amphiphilic Zwitterionic Quinonemonoimine at the Liquid–Solid Interface. *Chem. Commun.* **2011**, *47* (40), 11255. https://doi.org/10.1039/c1cc14085j.

(43) Routaboul, L.; Braunstein, P.; Xiao, J.; Zhang, Z.; Dowben, P. A.; Dalmas, G.; Da Costa, V.; Félix, O.; Decher, G.; Rosa, L. G.; Doudin, B. Altering the Static Dipole on Surfaces through Chemistry: Molecular Films of Zwitterionic Quinonoids. *J. Am. Chem. Soc.* **2012**, *134* (20), 8494–8506. https://doi.org/10.1021/ja212104b.

(44) Simpson, S.; Kunkel, D. A.; Hooper, J.; Nitz, J.; Dowben, P. A.; Routaboul, L.; Braunstein, P.; Doudin, B.; Enders, A.; Zurek, E. Coverage-Dependent Interactions at the Organics–Metal Interface: Quinonoid Zwitterions on Au(111). *J. Phys. Chem. C* **2013**, *117* (32), 16406–16415. https://doi.org/10.1021/jp403384h.

(45) Sun, K.; Zhao, B.; Murugesan, V.; Kumar, A.; Zeng, K.; Subbiah, J.; Wong, W. W. H.; Jones, D. J.; Ouyang, J. High-Performance Polymer Solar Cells with a Conjugated Zwitterion by Solution Processing or Thermal Deposition as the Electron-Collection Interlayer. *J. Mater. Chem.* **2012**, *22* (45), 24155. https://doi.org/10.1039/c2jm35221d.

(46) Denawi, H.; Koudia, M.; Hayn, R.; Siri, O.; Abel, M. On-Surface Synthesis of Spin Crossover Polymeric Chains. *J. Phys. Chem. C* **2018**, *122* (26), 15033–15040. https://doi.org/10.1021/acs.jpcc.8b04171.

(47) Dowben, P. A.; Kunkel, D. A.; Enders, A.; Rosa, L. G.; Routaboul, L.; Doudin, B.; Braunstein, P. The Dipole Mediated Surface Chemistry of P-Benzoquinonemonoimine Zwitterions. *Top Catal* **2013**, *56* (12), 1096–1103. https://doi.org/10.1007/s11244-013-0075-5.

(48) Kong, L.; Perez Medina, G. J.; Colón Santana, J. A.; Wong, F.; Bonilla, M.; Colón Amill, D. A.; Rosa, L. G.; Routaboul, L.; Braunstein, P.; Doudin, B.; Lee, C.-M.; Choi, J.; Xiao, J.; Dowben, P. A. Weak Screening of a Large Dipolar Molecule Adsorbed on Graphene. *Carbon* **2012**, *50* (5), 1981–1986. https://doi.org/10.1016/j.carbon.2011.12.055.

(49) Yuan, M.; Tanabe, I.; Bernard-Schaaf, J.-M.; Shi, Q.-Y.; Schlegel, V.; Schurhammer, R.; Dowben, P. A.; Doudin, B.; Routaboul, L.; Braunstein, P. Influence of Steric Hindrance on the Molecular Packing and the Anchoring of Quinonoid Zwitterions on Gold Surfaces. *New J. Chem.* **2016**, *40* (7), 5782–5796. https://doi.org/10.1039/C5NJ03251B.

(50) Rosa, L. G.; Velev, J.; Zhang, Z.; Alvira, J.; Vega, O.; Diaz, G.; Routaboul, L.; Braunstein, P.; Doudin, B.; Losovyj, Y. B.; Dowben, P. A. Approaching an Organic Semimetal: Electron Pockets at the Fermi Level for a *p* -benzoquinonemonoimine Zwitterion. *Physica Status Solidi (b)* **2012**, *249* (8), 1571–1576. https://doi.org/10.1002/pssb.201147426.

(51) Xiao, J.; Zhang, Z.; Wu, D.; Routaboul, L.; Braunstein, P.; Doudin, B.; Losovyj, Y. B.; Kizilkaya, O.; Rosa, L. G.; Borca, C. N.; Gruverman, A.; Dowben, P. A. The Interface Bonding and Orientation of a Quinonoid Zwitterion. *Phys. Chem. Chem. Phys.* **2010**, *12* (35), 10329–10340. https://doi.org/10.1039/C003996A.

(52) Fang, Y.; Cibian, M.; Hanan, G. S.; Perepichka, D. F.; De Feyter, S.; Cuccia, L. A.; Ivasenko, O. Alkyl Chain Length Effects on Double-Deck Assembly at a Liquid/Solid Interface. *Nanoscale* **2018**, *10* (31), 14993–15002. https://doi.org/10.1039/C8NR04220A.

(53) Kunkel, D. A.; Simpson, S.; Nitz, J.; Rojas, G. A.; Zurek, E.; Routaboul, L.; Doudin, B.; Braunstein, P.; Dowben, P. A.; Enders, A. Dipole Driven Bonding Schemes of Quinonoid

Zwitterions on Surfaces. *Chem. Commun.* **2012**, *48* (57), 7143–7145. https://doi.org/10.1039/C2CC32462H.

(54) Kunkel, D. A.; Simpson, S.; Nitz, J.; Rojas, G. A.; Zurek, E.; Routaboul, L.; Doudin, B.; Braunstein, P.; Dowben, P. A.; Enders, A. Dipole Driven Bonding Schemes of Quinonoid Zwitterions on Surfaces. *Chem. Commun.* **2012**, *48* (57), 7143. https://doi.org/10.1039/c2cc32462h.

(55) Kong, L.; Routaboul, L.; Braunstein, P.; Park, H.-G.; Choi, J.; Córdova, J. P. C.; Vega, E.; Rosa, L. G.; Doudin, B.; Dowben, P. A. Adsorption of TCNQH-Functionalized Quinonoid Zwitterions on Gold and Graphene: Evidence for Dominant Intermolecular Interactions. *RSC Adv.* **2013**, *3* (27), 10956. https://doi.org/10.1039/c3ra40930a.

(56) Yokoyama, T.; Takahashi, T.; Shinozaki, K.; Okamoto, M. Quantitative Analysis of Long-Range Interactions between Adsorbed Dipolar Molecules on Cu(111). *Phys. Rev. Lett.* **2007**, *98* (20), 206102. https://doi.org/10.1103/PhysRevLett.98.206102.

(57) Binnig, G.; Rohrer, H.; Gerber, Ch.; Weibel, E. Surface Studies by Scanning Tunneling Microscopy. *Phys. Rev. Lett.* **1982**, *49* (1), 57–61. https://doi.org/10.1103/PhysRevLett.49.57.

(58) *The Nobel Prize in Physics 1986*. NobelPrize.org. https://www.nobelprize.org/prizes/physics/1986/summary/%3E/.

(59) Calogero, G. A Van Der Waals Density Functional Study of N-Doped Graphene/Ir(111) for Chemical Identification of Individual Atoms with STM and AFM, 2015. https://doi.org/10.13140/RG.2.2.35138.07360.

(60) Bardeen, J. Tunnelling from a Many-Particle Point of View. *Phys. Rev. Lett.* **1961**, *6* (2), 57–59. https://doi.org/10.1103/PhysRevLett.6.57.

(61) Tersoff, J.; Hamann, D. R. Theory and Application for the Scanning Tunneling Microscope. *Phys. Rev. Lett.* **1983**, *50* (25), 1998–2001. https://doi.org/10.1103/PhysRevLett.50.1998.

(62) Chen, C. J. *Introduction to Scanning Tunneling Microscopy Third Edition*; Oxford University Press, 2021.

(63) GmbH, O. N.; Hoffmann-Millack, B. *MATRIX Application Manual for SPM*; 2014.

(64) Lelaidier, T. Organic Semiconductor Characterisation by Scanning Tunnelling Microscopy and Optical Spectroscopy. These de doctorat, Aix-Marseille, 2016. https://theses.fr/2016AIXM4032 (accessed 2024-06-01).

(65) Giessibl, F. J. Advances in Atomic Force Microscopy. *Rev. Mod. Phys.* **2003**, *75* (3), 949–983. https://doi.org/10.1103/RevModPhys.75.949.

(66) Giessibl, F. J. Atomic Resolution on Si(111)-(7×7) by Noncontact Atomic Force Microscopy with a Force Sensor Based on a Quartz Tuning Fork. *Applied Physics Letters* **2000**, *76* (11), 1470–1472. https://doi.org/10.1063/1.126067.

(67) Albrecht, T. R.; Akamine, S.; Carver, T. E.; Quate, C. F. Microfabrication of Cantilever Styli for the Atomic Force Microscope. *Journal of Vacuum Science & Technology A* **1990**, *8* (4), 3386–3396. https://doi.org/10.1116/1.576520.

(68) Gross, L.; Mohn, F.; Moll, N.; Liljeroth, P.; Meyer, G. The Chemical Structure of a Molecule Resolved by Atomic Force Microscopy. *Science (New York, N.Y.)* **2009**, *325* (5944). https://doi.org/10.1126/science.1176210.

(69) Burke, S. A. *Building Foundations for Molecular Electronics: Growth of Organic Molecules on Alkali Halides as Prototypical Insulating Substrates*; McGill University, 2008.

(70) Nony, L. Applications de La Microscopie de Force Dynamique En Mode Non-Contact : Structures Supramoléculaires Sur Surfaces Isolantes et Microscopie de Sonde de Kelvin, 2013.

(71) Nonnenmacher, M.; o'Boyle, M.; Wickramasinghe, H. K. Kelvin Probe Force Microscopy. *Applied physics letters* **1991**, *58* (25), 2921–2923.

(72) Mohn, F.; Gross, L.; Moll, N.; Meyer, G. Imaging the Charge Distribution within a Single Molecule. *Nat Nanotechnol* **2012**, *7* (4), 227–231. https://doi.org/10.1038/nnano.2012.20.

(73) Terris, B. D.; Stern, J. E.; Rugar, D.; Mamin, H. J. Contact Electrification Using Force Microscopy. *Phys. Rev. Lett.* **1989**, *63* (24), 2669–2672. https://doi.org/10.1103/PhysRevLett.63.2669.

(74) Stomp, R.; Miyahara, Y.; Schaer, S.; Sun, Q.; Guo, H.; Grutter, P.; Studenikin, S.; Poole, P.; Sachrajda, A. Detection of Single-Electron Charging in an Individual InAs Quantum Dot by Noncontact Atomic-Force Microscopy. *Phys. Rev. Lett.* **2005**, *94* (5), 056802. https://doi.org/10.1103/PhysRevLett.94.056802.

(75) Azuma, Y.; Kanehara, M.; Teranishi, T.; Majima, Y. Single Electron on a Nanodot in a Double-Barrier Tunneling Structure Observed by Noncontact Atomic-Force Spectroscopy. *Phys. Rev. Lett.* **2006**, *96* (1), 016108. https://doi.org/10.1103/PhysRevLett.96.016108.

(76) Milde, P.; Zerweck, U.; Eng, L. M.; Abel, M.; Giovanelli, L.; Nony, L.; Mossoyan, M.; Porte, L.; Loppacher, C. Interface Dipole Formation of Different ZnPcCl8 Phases on Ag(111) Observed by Kelvin Probe Force Microscopy. *Nanotechnology* **2008**, *19* (30), 305501. https://doi.org/10.1088/0957-4484/19/30/305501.

(77) Gross, L.; Mohn, F.; Liljeroth, P.; Repp, J.; Giessibl, F. J.; Meyer, G. Measuring the Charge State of an Adatom with Noncontact Atomic Force Microscopy. *Science* **2009**, *324* (5933), 1428–1431. https://doi.org/10.1126/science.1172273.

(78) Nony, L.; Bocquet, F.; Loppacher, C.; Glatzel, T. On the Relevance of the Atomic-Scale Contact Potential Difference by Amplitude-Modulation and Frequency-Modulation Kelvin Probe Force Microscopy. *Nanotechnology* **2009**, *20* (26), 264014. https://doi.org/10.1088/0957-4484/20/26/264014.

(79) Barth, C.; Hynninen, T.; Bieletzki, M.; Henry, C. R.; Foster, A. S.; Esch, F.; Heiz, U. AFM Tip Characterization by Kelvin Probe Force Microscopy. *New J. Phys.* **2010**, *12* (9), 093024. https://doi.org/10.1088/1367-2630/12/9/093024.

(80) Nečas, D.; Klapetek, P. Gwyddion: An Open-Source Software for SPM Data Analysis. *Open Physics* **2012**, *10* (1), 181–188. https://doi.org/10.2478/s11534-011-0096-2.

(81) Li, J.; Zu, X.; Qian, Y.; Duan, W.; Xiao, X.; Zeng, Q. Advances in Self-Assembly and Regulation of Aromatic Carboxylic Acid Derivatives at HOPG Interface. *Chinese Chemical Letters* **2020**, *31* (1), 10–18. https://doi.org/10.1016/j.cclet.2019.04.032.

(82) Peng, X.; Xiao, Y.; Mu, B.; Deng, K.; Tian, W.; Xiao, X.; Li, X.; Zeng, Q. Programmable Binary Crystallization Behaviors Assisted by Hydrogen Bond on HOPG Surface. *Applied Surface Science* **2021**, *565*, 150529. https://doi.org/10.1016/j.apsusc.2021.150529.

(83) Unlu, I.; Dixon, A. D. C.; Brozik, J. A.; Hipps, K. W. Alkynyl Linkers as a Design Tool to Gain Control over the Self-Assembly of Meso-Substituted Porphyrins on HOPG. *Langmuir* **2020**, *36* (18), 4897–4907. https://doi.org/10.1021/acs.langmuir.0c00179.

(84) Samorí, P.; Severin, N.; Simpson, C. D.; Müllen, K.; Rabe, J. P. Epitaxial Composite Layers of Electron Donors and Acceptors from Very Large Polycyclic Aromatic Hydrocarbons. *J. Am. Chem. Soc.* **2002**, *124* (32), 9454–9457. https://doi.org/10.1021/ja020323q.

(85) Shen, X.; Wei, X.; Tan, P.; Yu, Y.; Yang, B.; Gong, Z.; Zhang, H.; Lin, H.; Li, Y.; Li, Q.; Xie, Y.; Chi, L. Concentration-Controlled Reversible Phase Transitions in Self-Assembled Monolayers on HOPG Surfaces. *Small* **2015**, *11* (19), 2284–2290. https://doi.org/10.1002/smll.201402645.

(86) Snegir, S.; Dappe, Y. J.; Sysoiev, D.; Huhn, T.; Scheer, E. Nonuniform STM Contrast of Self-Assembled Tri-n-Octyl-Triazatriangulenium Tetrafluoroborate on HOPG. *ACS Omega* **2023**, *8* (41), 38766–38772. https://doi.org/10.1021/acsomega.3c06454.

(87) Yan, Q.; Meng, T.; Luo, W.; Sun, L.; Zeng, Q.; Xu, H. Co-Assembly Behaviors of Flavonol Derivatives Induced by a Pyridine Derivative on HOPG via Hydrogen Bonding and Van Der Waals Forces. *Langmuir* **2022**, *38* (28), 8651–8656. https://doi.org/10.1021/acs.langmuir.2c01076.

(88) Tatar, R. C.; Rabii, S. Electronic Properties of Graphite: A Unified Theoretical Study. *Phys. Rev. B* **1982**, *25* (6), 4126–4141. https://doi.org/10.1103/PhysRevB.25.4126.

(89) Fitzer, E.; Kochling, K.-H.; Boehm, H. P.; Marsh, H. Recommended Terminology for the Description of Carbon as a Solid (IUPAC Recommendations 1995). *Pure Appl. Chem.* **1995**, *67* (3), 473–506. https://doi.org/10.1351/pac199567030473.

(90) Zeinalipour-Yazdi, C. D.; Pullman, D. P. A New Interpretation of the Scanning Tunneling Microscope Image of Graphite. *Chemical Physics* **2008**, *348* (1), 233–236. https://doi.org/10.1016/j.chemphys.2008.03.019.

(91) Varchon, F. Propriétés électroniques et structurales du graphène sur carbure de silicium. phdthesis, Université Joseph-Fourier - Grenoble I, 2008. https://theses.hal.science/tel-00371946 (accessed 2024-11-05).

(92) Cooper, D. R.; D'Anjou, B.; Ghattamaneni, N.; Harack, B.; Hilke, M.; Horth, A.; Majlis, N.; Massicotte, M.; Vandsburger, L.; Whiteway, E.; Yu, V. Experimental Review of Graphene. *International Scholarly Research Notices* **2012**, *2012* (1), 501686. https://doi.org/10.5402/2012/501686.

(93) Norimatsu, W.; Kusunoki, M. Epitaxial Graphene on SiC{0001}: Advances and Perspectives. *Phys. Chem. Chem. Phys.* **2014**, *16* (8), 3501–3511. https://doi.org/10.1039/C3CP54523G.

(94) Landois, P.; Wang, T.; Nachawaty, A.; Bayle, M.; Decams, J.-M.; Desrat, W.; Zahab, A.-A.; Jouault, B.; Paillet, M.; Contreras, S. Growth of Low Doped Monolayer Graphene on SiC(0001) via Sublimation at Low Argon Pressure. *Phys. Chem. Chem. Phys.* **2017**, *19* (24), 15833–15841. https://doi.org/10.1039/C7CP01012E.

(95) Coletti, C.; Riedl, C.; Lee, D. S.; Krauss, B.; Patthey, L.; Von Klitzing, K.; Smet, J. H.; Starke, U. Charge Neutrality and Band-Gap Tuning of Epitaxial Graphene on SiC by Molecular Doping. *Phys. Rev. B* **2010**, *81* (23), 235401. https://doi.org/10.1103/PhysRevB.81.235401.

(96) Wong, S. L.; Huang, H.; Chen, W.; Wee, A. T. S. STM Studies of Epitaxial Graphene. *MRS Bulletin* **2012**, *37* (12), 1195–1202. https://doi.org/10.1557/mrs.2012.204.

(97) Omidian, M.; Néel, N.; Manske, E.; Pezoldt, J.; Lei, Y.; Kröger, J. Structural and Local Electronic Properties of Clean and Li-Intercalated Graphene on SiC(0001). *Surface Science* **2020**, *699*, 121638. https://doi.org/10.1016/j.susc.2020.121638.

(98) Van Bommel, A. J.; Crombeen, J. E.; Van Tooren, A. LEED and Auger Electron Observations of the SiC(0001) Surface. *Surface Science* **1975**, *48* (2), 463–472. https://doi.org/10.1016/0039-6028(75)90419-7.

(99) Riedl, C.; Starke, U.; Bernhardt, J.; Franke, M.; Heinz, K. Structural Properties of the Graphene-SiC(0001) Interface as a Key for the Preparation of Homogeneous Large-Terrace Graphene Surfaces. *Phys. Rev. B* **2007**, *76* (24), 245406. https://doi.org/10.1103/PhysRevB.76.245406.

(100) Rutter, G. M.; Guisinger, N. P.; Crain, J. N.; Jarvis, E. A. A.; Stiles, M. D.; Li, T.; First, P. N.; Stroscio, J. A. Imaging the Interface of Epitaxial Graphene with Silicon Carbide via Scanning Tunneling Microscopy. *Phys. Rev. B* **2007**, *76* (23), 235416. https://doi.org/10.1103/PhysRevB.76.235416.

(101) Veuillen, J.-Y.; Hiebel, F.; Magaud, L.; Mallet, P.; Varchon, F. Interface Structure of Graphene on SiC: An Ab Initio and STM Approach. *Journal of Physics D: Applied Physics* **2010**, *43* (37), 374008.

(102) Chang, C. S.; Tsong, I. S. T.; Wang, Y. C.; Davis, R. F. Scanning Tunneling Microscopy and Spectroscopy of Cubic β-SiC(111) Surfaces. *Surface Science* **1991**, *256* (3), 354–360. https://doi.org/10.1016/0039-6028(91)90877-U.

(103) Zhang, Y.; Brar, V. W.; Wang, F.; Girit, C.; Yayon, Y.; Panlasigui, M.; Zettl, A.; Crommie, M. F. Giant Phonon-Induced Conductance in Scanning Tunnelling Spectroscopy of Gate-Tunable Graphene. *Nature Phys* **2008**, *4* (8), 627–630. https://doi.org/10.1038/nphys1022.

(104) Brar, V. W.; Zhang, Y.; Yayon, Y.; Ohta, T.; McChesney, J. L.; Bostwick, A.; Rotenberg, E.; Horn, K.; Crommie, M. F. Scanning Tunneling Spectroscopy of Inhomogeneous Electronic Structure in Monolayer and Bilayer Graphene on SiC. *Applied Physics Letters* **2007**, *91* (12), 122102. https://doi.org/10.1063/1.2771084.

(105) Li, G.; Luican, A.; Andrei, E. Y. Scanning Tunneling Spectroscopy of Graphene on Graphite. *Phys. Rev. Lett.* **2009**, *102* (17), 176804. https://doi.org/10.1103/PhysRevLett.102.176804.

(106) Lagoute, J.; Joucken, F.; Repain, V.; Tison, Y.; Chacon, C.; Bellec, A.; Girard, Y.; Sporken, R.; Conrad, E. H.; Ducastelle, F.; Palsgaard, M.; Andersen, N. P.; Brandbyge, M.; Rousset, S. Giant Tunnel-Electron Injection in Nitrogen-Doped Graphene. *Phys. Rev. B* **2015**, *91* (12), 125442. https://doi.org/10.1103/PhysRevB.91.125442.

(107) Bouatou, M.; Chacon, C.; Lorentzen, A. B.; Ngo, H. T.; Girard, Y.; Repain, V.; Bellec, A.; Rousset, S.; Brandbyge, M.; Dappe, Y. J.; Lagoute, J. Visualizing In-Plane Junctions in Nitrogen-Doped Graphene. *Advanced Functional Materials* **2022**, *32* (47), 2208048. https://doi.org/10.1002/adfm.202208048.

(108) Geringer, V.; Subramaniam, D.; Michel, A. K.; Szafranek, B.; Schall, D.; Georgi, A.; Mashoff, T.; Neumaier, D.; Liebmann, M.; Morgenstern, M. Electrical Transport and Low-Temperature Scanning Tunneling Microscopy of Microsoldered Graphene. *Applied Physics Letters* **2010**, *96* (8), 082114. https://doi.org/10.1063/1.3334730.

(109) Deshpande, A.; Sham, C.-H.; Alaboson, J. M. P.; Mullin, J. M.; Schatz, G. C.; Hersam, M. C. Self-Assembly and Photopolymerization of Sub-2 Nm One-Dimensional Organic Nanostructures on Graphene. *J. Am. Chem. Soc.* **2012**, *134* (40), 16759–16764. https://doi.org/10.1021/ja307061e.

(110) Kowalczyk, P. J. Investigation of STM Tip Influence on the Recorded Position of the Shockley Surface State on Au(1 1 1). *Surface Science* **2009**, *603* (5), 747–751. https://doi.org/10.1016/j.susc.2008.12.033.

(111) Lauffer, P.; Emtsev, K.; Graupner, R.; Seyller, T.; Ley, L.; Reshanov, S.; Weber, H. Atomic and Electronic Structure of Few-Layer Graphene on SiC (0001) Studied with Scanning Tunneling Microscopy and Spectroscopy. *Physical Review B—Condensed Matter and Materials Physics* **2008**, *77* (15), 155426.

(112) Mishra, A.; Behera, R. K.; Behera, P. K.; Mishra, B. K.; Behera, G. B. Cyanines during the 1990s: A Review. *Chem. Rev.* **2000**, *100* (6), 1973–2012. https://doi.org/10.1021/cr990402t.

(113) Bouit, P.-A.; Di Piazza, E.; Rigaut, S.; Le Guennic, B.; Aronica, C.; Toupet, L.; Andraud, C.; Maury, O. Stable Near-Infrared Anionic Polymethine Dyes: Structure, Photophysical, and Redox Properties. *Organic Letters* **2008**, *10* (19), 4159–4162. https://doi.org/10.1021/ol801416n.

(114) Kulinich, A. V.; Ishchenko, A. A. Merocyanine Dyes: Synthesis, Structure, Properties and Applications. *Russ. Chem. Rev.* **2009**, *78* (2), 141–164. https://doi.org/10.1070/RC2009v078n02ABEH003900.

(115) Pascal, S.; Haefele, A.; Monnereau, C.; Charaf-Eddin, A.; Jacquemin, D.; Le Guennic, B.; Maury, O.; Andraud, C. On the Versatility of Electronic Structures in Polymethine Dyes. In *Optics and Photonics for Counterterrorism, Crime Fighting, and Defence X; and Optical Materials and Biomaterials in Security and Defence Systems Technology XI*; SPIE, 2014; Vol. 9253, pp 306–316.

(116) Dähne, S. Systematik Und Begriffserweiterung Der Polymethinfarbstoffe. *Zeitschrift für Chemie* **1965**, *5* (12), 441–451. https://doi.org/10.1002/zfch.19650051202.

(117) Zollinger, H. *Color Chemistry: Syntheses, Properties, and Applications of Organic Dyes and Pigments*; John Wiley & Sons, 2003.

(118) Siri, O.; Braunstein, P. Unprecedented Zwitterion in Quinonoid Chemistry. *Chemical communications* **2002**, No. 3, 208–209.

(119) Braunstein, P.; Siri, O.; Taquet, J.; Rohmer, M.-M.; Bénard, M.; Welter, R. A 6π + 6π Potentially Antiaromatic Zwitterion Preferred to a Quinoidal Structure: Its Reactivity Toward Organic and Inorganic Reagents. *J. Am. Chem. Soc.* **2003**, *125* (40), 12246–12256. https://doi.org/10.1021/ja0354622.

(120) Mourot, B.; Jacquemin, D.; Siri, O.; Pascal, S. Coupled Polymethine Dyes: Six Decades of Discoveries. *Chem Rec* **2024**, e202400183. https://doi.org/10.1002/tcr.202400183.

(121) Beverina, L.; Pagani, G. A. π-Conjugated Zwitterions as Paradigm of Donor–Acceptor Building Blocks in Organic-Based Materials. *Acc. Chem. Res.* **2014**, *47* (2), 319–329. https://doi.org/10.1021/ar4000967.

(122) Tamboura, F. B.; Cazin, C. S. J.; Pattacini, R.; Braunstein, P. Reactions of Amines with Zwitterionic Quinoneimines: Synthesis of New Anionic and Zwitterionic Quinonoids. *Eur. J. Org. Chem. 2009* (20), 3340–3350. https://doi.org/10.1002/ejoc.200900154.

(123) Braunstein, P.; Bubrin, D.; Sarkar, B. Synthesis of Bis(Phosphinoferrocenyl) Copper Complexes from Zwitterionic Quinonoid Ligands and Their Structural and Redox Properties. *Inorg. Chem.* **2009**, *48* (6), 2534–2540. https://doi.org/10.1021/ic802042w.

(124) Das, H. S.; Das, A. K.; Pattacini, R.; Hübner, R.; Sarkar, B.; Braunstein, P. First Structurally Characterized Mono- and Dinuclear Ruthenium Complexes Derived from Zwitterionic Quinonoid Ligands. *Chem. Commun.* **2009**, *29*, 4387–4389. https://doi.org/10.1039/B907710C.

(125) Paretzki, A.; Pattacini, R.; Huebner, R.; Braunstein, P.; Sarkar, B. Stabilising a Quinonoid-Bridged Dicopper(I) Complex by Use of a Dppf (Dppf = (Diphenylphosphino)Ferrocene) Backbone. *Chem. Commun.* **2010**, *46* (9), 1497–1499. https://doi.org/10.1039/B921731B.

(126) Deibel, N.; Hohloch, S.; Sommer, M. G.; Schweinfurth, D.; Ehret, F.; Braunstein, P.; Sarkar, B. Electrochromic Platinum(II) Complexes Derived from Azobenzene and Zwitterionic Quinonoid Ligands: Electronic and Geometric Structures. *Organometallics* **2013**, *32* (24), 7366–7375. https://doi.org/10.1021/om4009179.

(127) Hohloch, S.; Braunstein, P.; Sarkar, B. Ruthenium Hydride Complexes with Zwitterionic Quinonoid Ligands – Isomer Separation, Structural Properties, Electrochemistry, and Catalysis. *European Journal of Inorganic Chemistry* **2012**, *3*, 546–553. https://doi.org/10.1002/ejic.201101091.

(128) Yang, Q.-Z.; Kermagoret, A.; Agostinho, M.; Siri, O.; Braunstein, P. Nickel Complexes with Functional Zwitterionic N,O-Benzoquinonemonoimine-Type Ligands: Syntheses, Structures, and Catalytic Oligomerization of Ethylene. *Organometallics* **2006**, *25* (23), 5518–5527. https://doi.org/10.1021/om060600s.

(129) Kar, P.; Yoshida, M.; Shigeta, Y.; Usui, A.; Kobayashi, A.; Minamidate, T.; Matsunaga, N.; Kato, M. Methanol-Triggered Vapochromism Coupled with Solid-State Spin Switching in a Nickel(II)-Quinonoid Complex. *Angewandte Chemie* **2017**, *129* (9), 2385–2389. https://doi.org/10.1002/ange.201611085.

(130) Routaboul, L.; Braunstein, P.; Xiao, J.; Zhang, Z.; Dowben, P. A.; Dalmas, G.; Da Costa, V.; Félix, O.; Decher, G.; Rosa, L. G.; Doudin, B. Altering the Static Dipole on Surfaces through Chemistry: Molecular Films of Zwitterionic Quinonoids. *J. Am. Chem. Soc.* **2012**, *134* (20), 8494–8506. https://doi.org/10.1021/ja212104b.

(131) Kunkel, D. A.; Simpson, S.; Nitz, J.; Rojas, G. A.; Zurek, E.; Routaboul, L.; Doudin, B.; Braunstein, P.; Dowben, P. A.; Enders, A. Dipole Driven Bonding Schemes of Quinonoid Zwitterions on Surfaces. *Chem. Commun.* **2012**, *48* (57), 7143–7145. https://doi.org/10.1039/C2CC32462H.

(132) Fang, Y.; Nguyen, P.; Ivasenko, O.; Aviles, M. P.; Kebede, E.; Askari, M. S.; Ottenwaelder, X.; Ziener, U.; Siri, O.; Cuccia, L. A. Charge-Assisted Hydrogen Bond-Directed Self-Assembly of an Amphiphilic Zwitterionic Quinonemonoimine at the Liquid–Solid Interface. *Chem. Commun.* **2011**, *47* (40), 11255–11257. https://doi.org/10.1039/c1cc14085j.

(133) Dowben, P. A.; Kunkel, D. A.; Enders, A.; Rosa, L. G.; Routaboul, L.; Doudin, B.; Braunstein, P. The Dipole Mediated Surface Chemistry of P-Benzoquinonemonoimine Zwitterions. *Top Catal* **2013**, *56* (12), 1096–1103. https://doi.org/10.1007/s11244-013-0075-5.

(134) Kong, L.; Routaboul, L.; Braunstein, P.; Park, H.-G.; Choi, J.; Córdova, J. P. C.; Vega, E.; Rosa, L. G.; Doudin, B.; Dowben, P. A. Adsorption of TCNQH-Functionalized Quinonoid Zwitterions on Gold and Graphene: Evidence for Dominant Intermolecular Interactions. *RSC Adv.* **2013**, *3* (27), 10956–10961. https://doi.org/10.1039/c3ra40930a.

(135) Boulet, I.; Pascal, S.; Bedu, F.; Ozerov, I.; Ranguis, A.; Leoni, T.; Becker, C.; Masson, L.; Matkovic, A.; Teichert, C.; Siri, O.; Attaccalite, C.; Huntzinger, J.-R.; Paillet, M.; Zahab, A.; Parret, R. Electrical Monitoring of Organic Crystal Phase Transition Using MoS 2 Field Effect Transistor. *Nanoscale Adv.* **2023**, *5* (6), 1681–1690. https://doi.org/10.1039/D2NA00817C.

(136) Mahmood, A.; Yang, C.-S.; Jang, S.; Routaboul, L.; Chang, H.; Ghisolfi, A.; Braunstein, P.; Bernard, L.; Verduci, T.; Dayen, J.-F.; Samorì, P.; Lee, J.-O.; Doudin, B. Tuning Graphene Transistors through Ad Hoc Electrostatics Induced by a Nanometer-Thick Molecular Underlayer. *Nanoscale* **2019**, *11* (42), 19705–19712. https://doi.org/10.1039/C9NR06407A.

(137) Fang, Y.; Cibian, M.; Hanan, G. S.; Perepichka, D. F.; De Feyter, S.; Cuccia, L. A.; Ivasenko, O. Alkyl Chain Length Effects on Double-Deck Assembly at a Liquid/Solid Interface. *Nanoscale* **2018**, *10* (31), 14993–15002. https://doi.org/10.1039/C8NR04220A.

(138) Canard, G.; Chen, Z.; Suryaningtias, A.; Jean, M.; Vanthuyne, N.; Giorgi, M.; Roussel, C.; Siri, O. Regioselective Addition of DDQ on a Quinoid Ring: An Entry into Chiral Zwitterionic Bridging Ligands. *New J. Chem.* **2018**, *42* (10), 8247–8252. https://doi.org/10.1039/C7NJ03765A.

(139) Braunstein, P.; Siri, O.; Taquet, J.; Yang, Q.-Z. Regioselective Carbon–Carbon Bond Formation Reactions between TCNE or TCNQ and a Quinonoid Ring. *Angewandte Chemie* **2006**, *118* (9), 1421–1425. https://doi.org/10.1002/ange.200502574.

(140) Bonneau, N.; Chen, G.; Lachkar, D.; Boufridi, A.; Gallard, J.-F.; Retailleau, P.; Petek, S.; Debitus, C.; Evanno, L.; Beniddir, M. A.; Poupon, E. An Unprecedented Blue Chromophore Found in Nature Using a "Chemistry First" and Molecular Networking Approach: Discovery of Dactylocyanines A–H. *Chemistry – A European Journal* **2017**, *23* (58), 14454–14461. https://doi.org/10.1002/chem.201702336.

(141) Maslin, M.; Gaertner-Mazouni, N.; Debitus, C.; Joy, N.; Ho, R. Marine Sponge Aquaculture towards Drug Development: An Ongoing History of Technical, Ecological, Chemical Considerations and Challenges. *Aquaculture Reports* **2021**, *21*, 100813. https://doi.org/10.1016/j.aqrep.2021.100813.

(142) Koutentis, P. A. Regiospecific Synthesis of 5, 7-Disubstituted Quinoxalino [2, 3-b] Phenazines. *ARKIVOC.* **2002**, *6*, 175–191.

(143) Hutchison, K.; Srdanov, G.; Hicks, R.; Yu, H.; Wudl, F.; Strassner, T.; Nendel, M.; Houk, K. N. Tetraphenylhexaazaanthracene: A Case for Dominance of Cyanine Ion Stabilization Overwhelming 16π Antiaromaticity. *J. Am. Chem. Soc.* **1998**, *120* (12), 2989–2990. https://doi.org/10.1021/ja973558o.

(144) Langer, P.; Bodtke, A.; Saleh, N. N. R.; Görls, H.; Schreiner, P. R. 3,5,7,9-Tetraphenylhexaazaacridine: A Highly Stable, Weakly Antiaromatic Species with 16 π Electrons. *Angewandte Chemie International Edition* **2005**, *44* (33), 5255–5259. https://doi.org/10.1002/anie.200500831.

(145) Constantinides, C. P.; Zissimou, G. A.; Berezin, A. A.; Ioannou, T. A.; Manoli, M.; Tsokkou, D.; Theodorou, E.; Hayes, S. C.; Koutentis, P. A.

Tetraphenylhexaazaanthracenes: 16π Weakly Antiaromatic Species with Singlet Ground States. *Org. Lett.* **2015**, *17* (16), 4026–4029. https://doi.org/10.1021/acs.orglett.5b01923.

(146) Zissimou, G. A.; Constantinides, C. P.; Manoli, M.; Pieridou, G. K.; Hayes, S. C.; Koutentis, P. A. Oxidation of Tetraphenylhexaazaanthracene: Accessing a Scissor Dimer of a 16π Biscyanine. *Org. Lett.* **2016**, *18* (5), 1116–1119. https://doi.org/10.1021/acs.orglett.6b00222.

(147) Bhopate, D.; Kim, K.; Mahajan, P.; Gore, A.; Patil, S.; Majhi, S.; Naik, G.; Liang, T.; Ahemad, J.; Yu, Y. Fluorescent Chemosensor for Quantitation of Multiple Atmospheric Gases. *Journal of Nanomed Nanotechnol* **2017**, *8* (2), 1–9.

(148) Tamboura, F. B.; Cazin, C. S. J.; Pattacini, R.; Braunstein, P. Reactions of Amines with Zwitterionic Quinoneimines: Synthesis of New Anionic and Zwitterionic Quinonoids. *Eur. J. Org. Chem. 2009* (20), 3340–3350. https://doi.org/10.1002/ejoc.200900154.

(149) Siri, O.; Braunstein, P. Unprecedented Zwitterion in Quinonoid Chemistry. *Chemical Communications* **2002**. https://doi.org/10.1039/b107828n.

(150) Wang, T.; Huntzinger, J.-R.; Bayle, M.; Roblin, C.; Decams, J.-M.; Zahab, A.-A.; Contreras, S.; Paillet, M.; Landois, P. Buffer Layers Inhomogeneity and Coupling with Epitaxial Graphene Unravelled by Raman Scattering and Graphene Peeling. *Carbon* **2020**, *163*, 224–233. https://doi.org/10.1016/j.carbon.2020.03.027.

(151) Fang, Y.; Nguyen, P.; Ivasenko, O.; Aviles, M. P.; Kebede, E.; Askari, M. S.; Ottenwaelder, X.; Ziener, U.; Siri, O.; Cuccia, L. A. Charge-Assisted Hydrogen Bond-Directed Self-Assembly of an Amphiphilic Zwitterionic Quinonemonoimine at the Liquid–Solid Interface. *Chem. Commun.* **2011**, *47* (40), 11255. https://doi.org/10.1039/c1cc14085j.

(152) Routaboul, L.; Braunstein, P.; Xiao, J.; Zhang, Z.; Dowben, P. A.; Dalmas, G.; Da Costa, V.; Félix, O.; Decher, G.; Rosa, L. G.; Doudin, B. Altering the Static Dipole on Surfaces through Chemistry: Molecular Films of Zwitterionic Quinonoids. *J. Am. Chem. Soc.* **2012**, *134* (20), 8494–8506. https://doi.org/10.1021/ja212104b.

(153) Simpson, S.; Kunkel, D. A.; Hooper, J.; Nitz, J.; Dowben, P. A.; Routaboul, L.; Braunstein, P.; Doudin, B.; Enders, A.; Zurek, E. Coverage-Dependent Interactions at the Organics–Metal Interface: Quinonoid Zwitterions on Au(111). *J. Phys. Chem. C* **2013**, *117* (32), 16406–16415. https://doi.org/10.1021/jp403384h.

(154) Yuan, M.; Tanabe, I.; Bernard-Schaaf, J.-M.; Shi, Q.-Y.; Schlegel, V.; Schurhammer, R.; Dowben, P. A.; Doudin, B.; Routaboul, L.; Braunstein, P. Influence of Steric Hindrance on the Molecular Packing and the Anchoring of Quinonoid Zwitterions on Gold Surfaces. *New J. Chem.* **2016**, *40* (7), 5782–5796. https://doi.org/10.1039/C5NJ03251B.

(155) Spitzer, S.; Helmle, O.; Ochs, O.; Horsley, J.; Martsinovich, N.; Heckl, W. M.; Lackinger, M. What Can Be Inferred from Moiré Patterns? A Case Study of Trimesic Acid Monolayers on Graphite. *Faraday Discuss.* **2017**, *204*, 331–348. https://doi.org/10.1039/C7FD00113D.

(156) Le Liepvre, S.; Du, P.; Kreher, D.; Mathevet, F.; Attias, A.-J.; Fiorini-Debuisschert, C.; Douillard, L.; Charra, F. Fluorescent Self-Assembled Molecular Monolayer on Graphene. *ACS Photonics* **2016**, *3* (12), 2291–2296. https://doi.org/10.1021/acsphotonics.6b00793.

(157) Li, B.; Tahara, K.; Adisoejoso, J.; Vanderlinden, W.; Mali, K. S.; De Gendt, S.; Tobe, Y.; De Feyter, S. Self-Assembled Air-Stable Supramolecular Porous Networks on Graphene. *ACS Nano* **2013**, *7* (12), 10764–10772. https://doi.org/10.1021/nn4039047.

(158) Du, P.; Jaouen, M.; Bocheux, A.; Bourgogne, C.; Han, Z.; Bouchiat, V.; Kreher, D.; Mathevet, F.; Fiorini-Debuisschert, C.; Charra, F.; Attias, A.-J. Surface-Confined Self-Assembled Janus Tectons: A Versatile Platform towards the Noncovalent Functionalization of Graphene. *Angewandte Chemie International Edition* **2014**, *53* (38), 10060–10066. https://doi.org/10.1002/anie.201403572.

(159) MacLeod, J. M.; Lipton-Duffin, J. A.; Cui, D.; De Feyter, S.; Rosei, F. Substrate Effects in the Supramolecular Assembly of 1,3,5-Benzene Tricarboxylic Acid on Graphite and Graphene. *Langmuir* **2015**, *31* (25), 7016–7024. https://doi.org/10.1021/la5048886.

(160) Koutentis, P. A. Regiospecific Synthesis of 5,7-Disubstituted Quinoxalino[2,3-b]Phenazines. *Arkivoc* **2002**, *2002* (6), 175–191. https://doi.org/10.3998/ark.5550190.0003.616.

(161) Gross, L.; Mohn, F.; Liljeroth, P.; Repp, J.; Giessibl, F. J.; Meyer, G. Measuring the Charge State of an Adatom with Noncontact Atomic Force Microscopy. *Science* **2009**, *324* (5933), 1428–1431. https://doi.org/10.1126/science.1172273.

(162) Walch, H.; Leoni, T.; Guillermet, O.; Langlais, V.; Scheuermann, A.; Bonvoisin, J.; Gauthier, S. Electromechanical Switching Behavior of Individual Molecular Complexes of Cu and Ni on NaCl-Covered Cu(111) and Ag(111). *Physical Review B: Condensed Matter and Materials Physics (1998-2015)* **2012**, *86* (7). https://doi.org/10.1103/PhysRevB.86.075423.

(163) Weiss, C.; Wagner, C.; Kleimann, C.; Rohlfing, M.; Tautz, F. S.; Temirov, R. Imaging Pauli Repulsion in Scanning Tunneling Microscopy. *Phys. Rev. Lett.* **2010**, *105* (8), 086103. https://doi.org/10.1103/PhysRevLett.105.086103.

(164) Repp, J.; Meyer, G.; Stojković, S. M.; Gourdon, A.; Joachim, C. Molecules on Insulating Films: Scanning-Tunneling Microscopy Imaging of Individual Molecular Orbitals. *Phys. Rev. Lett.* **2005**, *94* (2), 026803. https://doi.org/10.1103/PhysRevLett.94.026803.

(165) Soe, W.-H.; Manzano, C.; De Sarkar, A.; Chandrasekhar, N.; Joachim, C. Direct Observation of Molecular Orbitals of Pentacene Physisorbed on Au(111) by Scanning Tunneling Microscope. *Phys. Rev. Lett.* **2009**, *102* (17), 176102. https://doi.org/10.1103/PhysRevLett.102.176102.

(166) Castro Neto, A. H. The Electronic Properties of Graphene. *Rev. Mod. Phys.* **2009**, *81* (1), 109–162. https://doi.org/10.1103/RevModPhys.81.109.

(167) *7.7: Quantum Tunneling of Particles through Potential Barriers*. Physics LibreTexts. https://phys.libretexts.org/Bookshelves/University_Physics/University_Physics_(OpenStax)/University_Physics_III_-_Optics_and_Modern_Physics_(OpenStax)/07%3A_Quantum_Mechanics/7.07%3A_Quantum_Tunneling_of_Particles_through_Potential_Barriers (accessed 2024-08-31).

(168) Kehrmann, F.; Duret, A. Ueber Ein Isomeres Des Diphenylfluorindins. *Berichte der deutschen chemischen Gesellschaft* **1898**, *31* (2), 2442–2444. https://doi.org/10.1002/cber.189803102213.

(169) Zhang, P.; Terefenko, E. A.; McComas, C. C.; Mahaney, P. E.; Vu, A.; Trybulski, E.; Koury, E.; Johnston, G.; Bray, J.; Deecher, D. Synthesis and Activity of Novel 1-or 3-(3-Amino-1-Phenyl Propyl)-1, 3-Dihydro-2H-Benzimidazol-2-Ones as Selective Norepinephrine Reuptake Inhibitors. *Bioorganic & medicinal chemistry letters* **2008**, *18* (23), 6067–6070.

(170) Wolfe, J. P.; Tomori, H.; Sadighi, J. P.; Yin, J.; Buchwald, S. L. Simple, Efficient Catalyst System for the Palladium-Catalyzed Amination of Aryl Chlorides, Bromides, and Triflates. *J. Org. Chem.* **2000**, *65* (4), 1158–1174. https://doi.org/10.1021/jo991699y.

(171) Willard, H. H.; Manalo, G. D. Derivatives of Diphenylamine as Oxidation-Reduction Indicators in Alkaline Solution. *Anal. Chem.* **1947**, *19* (3), 167–170. https://doi.org/10.1021/ac60003a011.

(172) 傅尧; 郭靖; 李闯. Heterogeneous Catalyst and Method for Preparing 2, 5-Furandimethylamine from 5-Hydroxymethylfurfural. CN113976131B, March 10, 2023. https://patents.google.com/patent/CN113976131B/en (accessed 2024-07-26).

(173) Chattopadhyay, P.; Rai, R.; Pandey, P. S. Two-Step Synthetic Route to 10-Substituted Isoalloxazines. *Synthetic Communications* **2006**, *36* (13), 1857–1861. https://doi.org/10.1080/00397910600602552.

(174) Takizawa, S.; Montes, V. A.; Anzenbacher, P. Phenylbenzimidazole-Based New Bipolar Host Materials for Efficient Phosphorescent Organic Light-Emitting Diodes. *Chem. Mater.* **2009**, *21* (12), 2452–2458. https://doi.org/10.1021/cm9004954.

(175) Ruiz, A. T.; Bousquet, M. H. E.; Pascal, S.; Canard, G.; Mazan, V.; Elhabiri, M.; Jacquemin, D.; Siri, O. Small Panchromatic and NIR Absorbers from Quinoid Zwitterions. *Org. Lett.* **2020**, *22* (20), 7997–8001. https://doi.org/10.1021/acs.orglett.0c02926.

(176) *Metastable state | Phase transition, Kinetic energy, Equilibrium | Britannica*. https://www.britannica.com/science/metastable-state.

Appendix

A. Electronic properties of graphene

Reference [166]

Graphene is made out of carbon atoms arranged in hexagonal structure (see Figure 119). The structure can be seen as a triangular lattice with a basis of 2 atoms per unit cell. The lattice vectors can be written as:

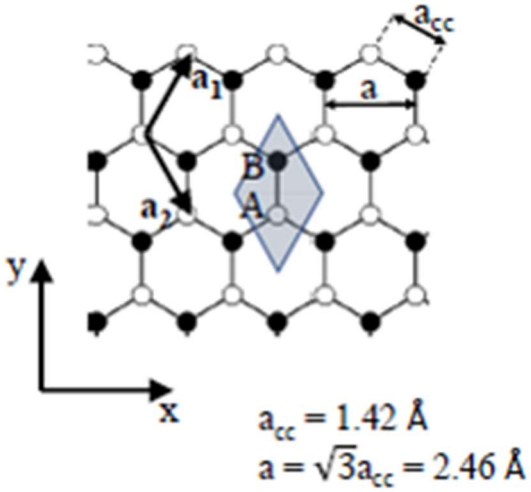


Figure 119: Crystal structure of graphene in the real space. 'a' represents the lattice parameter and 'a_{cc}' the distance between 2 consecutive carbon atoms.

$$a_1 = \frac{a}{2}(3,\sqrt{3}),\ a_2 = \frac{a}{2}(3,-\sqrt{3}) \qquad (A.1)$$

Where a= 1.42 Å is the carbon-carbon distance. The reciprocal-lattice vectors are given by:

$$b_1 = \frac{2\pi}{3a}(1,\sqrt{3}),\ b_2 = \frac{2\pi}{3a}(1,-\sqrt{3}) \qquad (A.2)$$

Of particular importance for the physics of graphene are the 2 points K and K′ at the corners of the graphene Brillouin zone (BZ), these are named Dirac points. Their positions in momentum space are given by

$$K=\left(\frac{2\pi}{3a},\frac{2\pi}{3\sqrt{3}a}\right),\ K'=\left(\frac{2\pi}{3a},-\frac{2\pi}{3\sqrt{3}a}\right) \quad (A.3)$$

The 3 nearest-neighbor vectors in real space are given by:

$$\delta_1=\frac{a}{2}(1,\sqrt{3}),\ \delta_2=\frac{a}{2}(1,-\sqrt{3}),\ \delta_3=-a(1,0) \quad (A.4)$$

The tight-binding Hamiltonian for electrons in graphene considering that electrons can hop to both nearest and next-nearest neighbor atoms, is expressed as (units are such as $\hbar = 1$):

$$H=-t\sum_{\ll i,j\gg}(a_i^{\dagger}b_j+b_j^{\dagger}a_i) \quad (A.5)$$

Where $a_j(a_i^{\dagger})$ annihilates (creates) an electron with spin on site R_i on sublattice A (an equivalent definition is used for sublattice B), t ($\sim$ 2.8 eV) is the nearest neighbor hopping energy (hopping between different sublattices).

Using Bloch's theorem, the wave function for an electron in a periodic potential can be expressed as:

$$\psi(\mathbf{r})=e^{i\mathbf{k}.\mathbf{r}}u(\mathbf{r}) \quad (A.6)$$

Where $\boldsymbol{k}$ is the wave vector and $u(\mathbf{r})$ has the periodicity of the lattice.

Transforming the Hamiltonian into reciprocal space and using the basis of Bloch states for the A and B sublattices, we get a $2x2$ Hamiltonian matrix:

$$H(k)=\begin{pmatrix}0 & -tf(\mathbf{k})\\ -tf^{*}(\mathbf{k}) & 0\end{pmatrix} \quad (A.7)$$

where

$$f(k)=1+e^{-ik.a_1}+e^{-ik.a_2} \quad (A.8)$$

To find the energy eigenvalues, we solve the eigenvalue problem $H(\mathbf{k})\psi=E\psi$ which leads to deriving the energy band having the form:

$$E(\mathbf{k})=\pm t|f(\mathbf{k})| \tag{A. 9}$$

Near the Dirac points $\mathbf{K}$ and $\mathbf{K}'$ in the Brillouin zone, we can approximate $f(\mathbf{k})$ using a linear expansion. For instance, around $\mathbf{K}=\left(\frac{4\pi}{3a},0\right)$, we have: $\mathbf{k}=\mathbf{K}+\mathbf{q}$, with $|\mathbf{q}|\ll|\mathbf{K}|$.

In this region: $f(\mathbf{k})\approx\frac{3a}{2}(q_x\text{-}iq_y)$ thus, $|f(\mathbf{k})|\approx\frac{3a}{2}|\mathbf{q}|$.

Substituting back, the energy dispersion relation near the Dirac points becomes:

$$E(\mathbf{k})\approx\pm\hbar v_F|\mathbf{q}| \tag{A. 10}$$

$\mathbf{k}$ is the momentum measured relatively to the Dirac points and v_F is the Fermi velocity, given by $v_F=\frac{3ta}{2}$, with value $v_F\cong1\times10^6$ m/s.

Now, using this dispersion relation, we derive the density of states (DOS) for graphene $g(E)$ is defined as the number of available electronic states per unit energy per unit area:

$$g(E)=\frac{dN}{dE} \tag{A. 11}$$

Where N is the number of states with energy less than E, $N(E)=g_sg_v\left(\frac{A}{(2\pi)^2}\right)\pi k^2$.

g_s and $g_v$are the spin degeneracy (= 2) and the valley degeneracy (= 2 due to the 2 Dirac points) respectively, and A is the area of the graphene sheet.

The number of states becomes:

$$N(E)=4\left(\frac{A}{(2\pi)^2}\right)\pi\left(\frac{E}{\hbar v_F}\right)^2 \tag{A. 12}$$

Thus, the density of states of graphene near the Dirac points is:

$$g(E)=\frac{2E}{\pi(\hbar v_F)^2} \tag{A. 13}$$

The linear dependence of the DOS on energy is a characteristic feature of graphene's electronic structure, reflecting its unique band structure and massless Dirac fermion behavior.

B. Particle tunneling in a unidimensional potential barrier

The Figure 120 schematically displays a particle of energy E passing through a potential barrier with a constant height U_0 and width z_0. In that case, 3 regions (labelled I, II and III) are available for the particle:

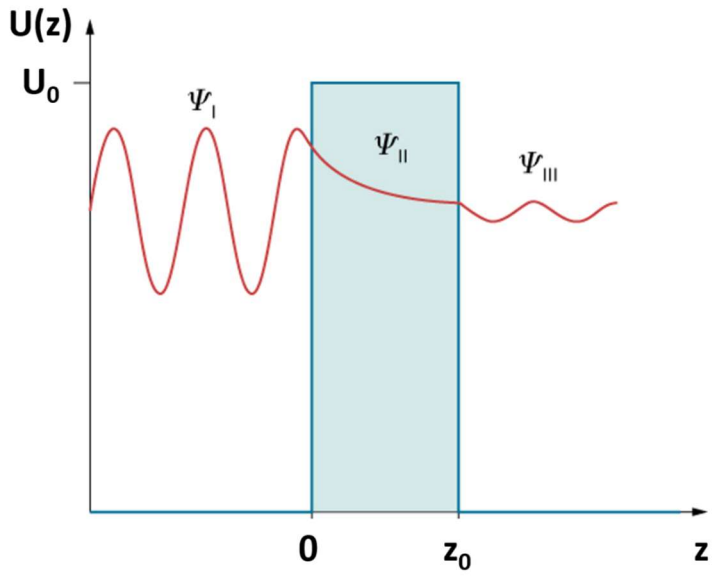


Figure 120: 3 types of solutions to the stationary Schrödinger equation for the quantum-tunneling problem: Oscillatory behavior in regions I and III where a quantum particle moves freely, and exponential decay behavior in region II (the barrier region) where the particle moves in the potential U_0.Reproduced from reference.[167]

The unidimensional time independent Schrödinger equation for a wave function is given by the following equation:

$$H\Psi = \left[-\frac{\hbar^2}{2m}\frac{d^2}{dz^2} + U(z)\right]\Psi(z) = E\Psi(z) \qquad (A.14)$$

With H being the Hamiltonian of the system, $\hbar = \frac{h}{2\pi}$ the reduced Plank constant, m the mass of the particle, U(z) the height of the potential step, E the energy of the particle, and $\Psi(z)$ the particle wave function.

Assuming the particle comes from - ∞ and that it cannot be reflected at + ∞, this particle is described by the following wave functions which are solutions of the time independent Schrödinger equation:

$$\begin{cases} \Psi_I(z) = Ae^{ik_I z} + Be^{-ik_I z} \\ \Psi_{II}(z) = Ce^{ik'_{II} z} \\ \Psi_{III}(z) = Ee^{ik_{III} z} \end{cases} \quad (A.15)$$

From these equations it is possible to calculate wave vectors for each region using the time independent Schrödinger equation. 2 cases are observed depending on the energy of the particle: In the first case where $E > U_0$, values for wave vectors are:

$$\begin{cases} k_I = \sqrt{\dfrac{2mE}{\hbar^2}} \\ k'_{II} = \sqrt{\dfrac{2m(E - U_0)}{\hbar^2}} \\ k_{III} = \sqrt{\dfrac{2mE}{\hbar^2}} = k_I \end{cases} \quad (A.16)$$

After the determination of B, C, D, and E as a function of A by using the conditions of continuous functions and derivatives at the boundaries ($z = 0$ and $z = z_0$), the reflection ($R = \frac{|B|^2}{|A|^2}$), and the transmission ($T = \frac{|E|^2}{|A|^2}$) coefficients can be calculated to be:

$$\begin{cases} R = \dfrac{|B|^2}{|A|^2} = \dfrac{(k_I^2 - k_{II}^2)^2 \sin^2(k_{II} z_0)}{4k_I^2 k_{II}^2 (k_I^2 - k_{II}^2)^2 \sin^2(k_{II} z_0)} \\ T = \dfrac{4k_I^2 k_{II}^2}{4k_I^2 k_{II}^2 + (k_I^2 - k_{II}^2)^2 \sin^2(k_{II} z_0)} \end{cases} \quad (A.17)$$

In quantum mechanics, a particle with an energy higher than the height of the potential barrier has a non-zero probability to be reflected, unlike in the classical case.

Now if we consider the energy of the particle lower than the potential barrier height ($E < V_0$), wave functions solutions of the Schrödinger equation for different regions are:

$$\begin{cases} \Psi_I(z) = Ae^{ik_I z} + Be^{-ik_I z} \\ \Psi_{II}(z) = Ce^{-k'_{II} z} + De^{k'_{II} z} \\ \Psi_{III}(z) = Ee^{ik_I z} \end{cases} \quad (A.18)$$

And the associated wave vectors:

$$\begin{cases} k_I = \sqrt{\dfrac{2mE}{\hbar^2}} \\ k'_{II} = \sqrt{\dfrac{2m(U_0 - E)}{\hbar^2}} \\ k_{III} = \sqrt{\dfrac{2mE}{\hbar^2}} = k_I \end{cases} \quad (A.19)$$

Once again by using the conditions at the boundary it is possible to calculate reflection ($R = \frac{|B|^2}{|A|^2}$), and transmission coefficients ($T = \frac{|E|^2}{|A|^2}$):

$$\begin{cases} R = \dfrac{|B|^2}{|A|^2} = \dfrac{(k_I^2 - k_{II}'^2)^2 \sinh^2(k'_{II} z_0)}{(k_I + k'_{II}) \sinh^2(k'_{II} z_0) + 4k_I^2 k_{II}'^2} \\ T = \dfrac{4k_I^2 k_{II}'^2}{(k_I + k'_{II}) \sinh^2(k'_{II} z_0) + 4k_I^2 k_{II}'^2} \end{cases} \quad (A.20)$$

Unlike classical mechanics, a particle with a total energy E lower than the potential barrier height ϕ has a non-zero probability of tunneling through this barrier. This is the principle used in STM. In the classically forbidden region, the wave function ψ decays exponentially via:

$$\Psi(z) = \Psi(0) \times \exp - \frac{\sqrt{2m(\phi - E)}z}{\hbar} \quad (A.21)$$

where m is the mass of the particle and $\hbar = 1{,}05 \times 10^{-34}$J.s.

In STM, the barrier is given by the vacuum gap between the sample and the tip. Then, the tunneling current I_t can be calculated by considering the density of states of the sample, $\rho_s(E_F)$, at the Fermi edge:

$$I_t \propto V\rho_s(E_F)\exp\left[-2\frac{\sqrt{2m(\phi - E)z}}{\hbar}\right] \propto V\rho_s(E_F)e^{-1.025\sqrt{\phi z}} \qquad (A.22)$$

Where the barrier height ϕ is in eV and z in angstrom units. With a typical barrier height of ϕ=5 eV, which corresponds to the work function of gold, the tunneling current decays by an order of magnitude when the vacuum gap is changed by 1 Å.

C. Experimental methods

Data processing and STM image treatment

The free software package Gwyddion was used for the analysis of the STM images.[80]

Python was used to process the KPFS and STS data curves, CPD and dI/dV maps.

General remarks and analysis conditions for synthesis

All reagents and anhydrous solvents were purchased from Alfa Aesar or Sigma Alrich and were used without further purification. Column chromatography was performed using silica gel (60-120 mesh), alumina 90 basic (63-200 μm, Beckmann grade III). Analytical thin layer chromatography (TLC) was performed on precoated silica gel-60 F254 (0.5 mm) aluminum plate. Visualization of the spots on TLC plates was achieved by exposure to UV light. Filter aid was performed using Celite® AW standard Supercel® or Celite® type 545. Unless otherwise specified, the desired product was dried under vacuum (< 10 mbar) over 5 hours at room temperature.

^{1}H NMR spectra were recorded on a on a JEOL ECS400 spectrometer operating at 400 MHz, respectively. **^{13}C NMR** spectra were recorded on a JEOL ECS400 spectrometer operating at 100 MHz, respectively. Chemical shifts are reported in delta (δ) units, expressed in parts per million using the residual protonated solvent as an internal standard (For proton: $CDCl_3$, 7.26 ppm; DMSO-d_6, 2.50 ppm; Acetone-d_6, 2.05 ppm, TFA-d, 11.5 ppm. For ^{13}C: $CDCl_3$, 77.0 ppm; DMSO-d_6, 39.4 ppm; Acetone-d_6, 30.8 ppm). The multiplicity of signals is designated by the following abbreviations: s, singulet; br s, broad signal; d, doublet; t, triplet; br t, broad triplet; q, quartet; quint, apparent quintet; sext, apparent sextet; m, multiplet. Coupling constants, *J*, are reported in Hz.

Mass spectrometry (MS) was performed on 3200 QTRAP (Applied Biosystems SCIEX) or SYNAPT G2 HDMS (Waters). High-resolution mass spectrometry (HRMS) analysis was performed on a SYNAPT G2 HDMS (Waters).

Melting points (Mp) were measured in open capillary tubes with a STUART SMP30 melting points apparatus and are reported uncorrected in °C.

Absorption spectra were measured on a Varian Cary 50 UV-vis or on an Agilent Cary 5000 UV-vis-NIR or on a Perkin-Elmer Lambda EZ 210 UV-vis spectrophotometer. All spectra were measured using quartz cuvette 2 or 4 side and carried out with spectroscopic grade solvents.

Luminescence. Emission spectra were measured using a Horiba-Jobin Yvon Fluorolog-3 spectrofluorimeter equipped with a three-slit double-grating excitation and a spectrograph emission monochromator with dispersions of 2.1 nm mm^{-1} (1200 grooves

per mm). A 450 W xenon continuous wave lamp provided excitation. The luminescence of diluted solutions was detected at right angle using 10 mm quartz cuvettes.

Fluorescence quantum yields Φ were measured in diluted solutions with an optical density lower than 0.1 using the following equation:

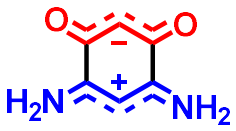
$$\frac{\Phi_x}{\Phi_r} = \left(\frac{\mathrm{A}_r(\lambda)}{\mathrm{A}_x(\lambda)}\right)\left(\frac{n_x^2}{n_r^2}\right)\left(\frac{\mathrm{D}_x}{D_r}\right)$$

where A is the absorbance at the excitation wavelength (λ), n the refractive index and D the integrated intensity. 'r' and 'x' stand for reference and sample. The fluorescence quantum yields were measured in DCM relative to Oxazine 725 Perchlorate in EtOH (Φ = 11 %). The excitation wavelength used was 590 nm.

Synthetic protocols and characterization

QZ

Compound QZ



QZ

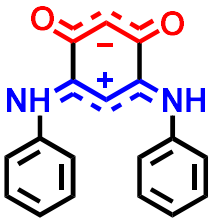
Chemical Formula: $C_6H_6N_2O_2$
Molecular Weight: 138,13

In a round bottom flask, 4,6-diaminoresorcinol hydrochloride (2.0 g, 9.4 mmol, 1 equiv.) was dissolved in absolute EtOH (15 mL). *N*,*N*-diisopropylethylamine (2.4 g, 3.3 mL, 18.8 mmol, 2 equiv.) was added and the mixture was stirred for 2 hours at room temperature in the presence of air. The resulting suspension was filtered on a sintered glass funnel, the purple solid was washed with EtOH (3 × 5 mL) and water (3 x 5 mL) finally dried under vacuum to afford the pure product as a purple solid in 93.4 % yield (120 mg, 8.93 mmol).

^{1}H NMR (400 MHz, DMSO-d$_6$) δ = 9.18 (s, 2H), 8.41 (s, 2H), 5.62 (s, 1H), 4.91 (s, 1H).

The characterizations are in accordance with the previously reported data.[118]

Compound QZ$_7$



QZ$_7$

Chemical Formula: $C_{18}H_{14}N_2O_2$
Molecular Weight: 290,32

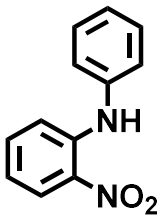
Aniline (3.3 mL, 36 mmol) was added to an EtOH (20 mL) suspension of parent zwitterion **QZ** (0.100 g, 0.72 mmol). The reaction mixture was heated to reflux for 4 days. The mixture was cooled down to room temperature, and the crude solid was washed with diethyl ether (3 × 40 mL) then with dichloromethane. The product was obtained as a black solid (59 mg, 23 %).

^{1}H NMR (**400 MHz, DMSO-d$_6$**) δ 10.97 (s, 2H), 7.42 (m, 8H), 7.33 – 7.27 (m, 2H), 5.81 (s, 1H), 5.20 (s, 1H).

The characterizations are in accordance with the previously reported data.[122]

ZTAP

Compound X_1



X_1

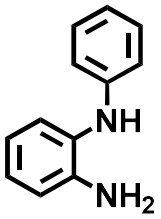
Chemical Formula: $C_{12}H_{10}N_2O_2$
Molecular Weight: 214,2221

To a stirred mixture of 1-fluoro-2-nitrobenzene (1.49 mL, 14.1 mmol) and Aniline (2.22 mL, 14.1 mmol), triethylamine (1.95 mL, 14.1 mmol) was added, and the reaction mixture was heated to 140 °C for 24 hours and then allowed to cool at ca. 20 °C. The mixture was then diluted with DCM and the organic phase was washed by diluted HCl (10 %) to remove unreacted amines. The organic layer was washed with a saturated solution of NaCl, separated, dried over anhydrous Na_2SO_4, filtered, and then evaporated to afford the final compound **X1** as an orange powder (3 g, 14 mmol, 99 % yield).

^{1}H NMR (400 MHz, $CDCl_3$) δ= 9.49 (s, 1H), 8.21 (dd, *J* = 8.6, 1.5 Hz, 1H), 7.42 (dt, *J* = 9.2, 1.8 Hz, 2H), 7.39 – 7.34 (m, 1H), 7.29 (s, 1H), 7.27 (s, 1H), 7.25 – 7.21 (m, 2H), 6.77 (m, *J* = 1H).

The characterizations are in accordance with the previously reported data. [168]

Compound A_1



A_1

Chemical Formula: $C_{12}H_{12}N_2$
Molecular Weight: 184,24

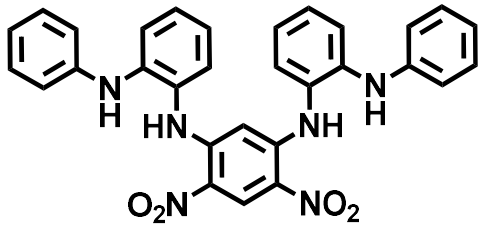
To a stirred mixture of **X_1** (0.7g, 3.23 mmol) and NH_4Cl (1.72 g, 32.3 mmol) in MeOH (25 mL) and H_2O (12.5 mL) at ca 20 °C, under argon, Zn powder was added in one portion (1.05 g, 16.15 mmol), and the reaction mixture was heated to 45 °C for 3 hours and then allowed to cool at ca. 20 °C. The mixture was filtered through a Celite® pad to remove Zn

residues, then dissolved in DCM. The organic layer was washed successively by a saturated solution of $NaHCO_3$, water and a saturated solution of NaCl before being dried over anhydrous Na_2SO_4, filtered, and then evaporated. The residue was purified via silica gel column chromatography with Petroleum ether/EtOAc 3:7 as eluent (Rf = 0.38) to afford compound **A_1** as dark red oil (490 mg, 3.23 mmol, 83 % yield).

^{1}H NMR (400 MHz, $CDCl_3$) δ = 7.17 – 7.10 (m, 2H), 7.07 (dd, *J* = 7.8, 1.4 Hz, 1H), 6.95 – 6.89 (m, 1H), 6.83 (dd, *J* = 7.9, 1.5 Hz, 1H), 6.79 – 6.73 (m, 2H), 6.73 – 6.67 (m, 1H), 6.62 (td, *J* = 7.5, 1.5 Hz, 1H), 6.44 (s, 1H), 4.44 (s, 2H).

The characterizations are in accordance with the previously reported data. [169]

Compound B_1



B_1

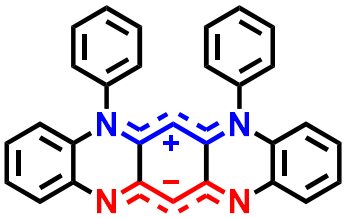
Chemical Formula: $C_{30}H_{24}N_6O_4$
Molecular Weight: 532,56

To a stirred mixture of **A_1** (470 mg, 2.5 mmol) in absolute EtOH (8 mL) and N,N-diisopropylethylamine (DIPEA or Hünig's base) (5 mmol, 1 mL) at ca 20 °C, under argon, 1,5-difluoro-2,4-dinitrobenzene (250 mg, 1.25 mmol) was added in one portion and the reaction mixture was heated to reflux for 24 h and then allowed to cool at ca. 20 °C. The red precipitate was filtered through a Celite® pad, washed with hot water, then by cold EtOH, and dried under vacuum to afford the compound **B_1** as a red powder (668 mg, 52 %).

^{1}H NMR (400 MHz, DMSO-d_6) δ 9.42 (s, 2H), 8.97 (s, 1H), 7.60 (s, 2H), 7.13 (m, 10H), 6.93 – 6.71 (m, 8H), 6.01 – 5.90 (m, 1H).

The characterizations are in accordance with the previously reported data. [142]

Compound ZTAP$_1$



ZTAP$_1$

Chemical Formula: $C_{30}H_{20}N_4$
Molecular Weight: 436,51

METHOD 1:

To a stirred solution of compound **B$_1$** (205 mg, 0.38 mmol) in absolute EtOH (40 mL) at *ca*. 20 °C under argon, Pd/C (200 mg) was added in one portion. The mixture was stirred for 20 minutes under argon then transferred to an autoclave that was evacuated and flushed with dihydrogen 3 times (2 bars). The reaction mixture was then left to stir under an atmosphere of hydrogen (20 bars) for 12 hours. TLC monitoring showed the complete consumption of the starting material and the Pd/C was filtered through a Celite® pad and washed with DCM to dissolve the red precipitate. All solvents were then evaporated to get a brown oil, which was then directly solubilized in absolute EtOH and left to stir under reflux at *ca* 20 °C at air. Hydrochloric acid (36 %, 2 mL) was added dropwise and the color of the reaction mixture became purple then dark blue. The mixture was left to stir under reflux for 4 h, then left to cool at *ca* 20 °C. The mixture was made basic by the addition of ammonia (28 %, 2.48 mL) and the color of the reaction instantly turned to dark green. The purple precipitate was then washed with hot water (60 °C), by cold EtOH and dried under vacuum to afford **ZTAP$_1$** as a dark green powder (28 mg, 17 %).

METHOD 2:

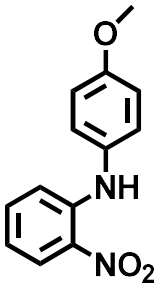
To a stirred solution of compound **B$_1$** (177 mg, 0.33 mmol) in absolute EtOH (30 mL) at *ca*. 20°C under argon, Pd/C (5 %, 200 mg) was added in one portion. The mixture was stirred for 20 minutes then transferred to an autoclave that was evacuated and flushed with dihydrogen 3 times (2 bar). The reaction mixture was then left to stir under an atmosphere of dihydrogen (20 bar) for 12 hours. TLC monitoring showed the complete consumption of the starting material and the Pd/C was filtered through a Celite® pad and washed with hot EtOH to dissolve the precipitated amine. The brown ethanolic solution was heated under reflux until its color turned to green. It was then concentrated and left to cool down on the bench. The dark green precipitate was then filtered and washed with cold EtOH and dried to afford **ZTAP$_1$** as a dark green powder (116 mg, 71 %).

^{1}H NMR (400 MHz, TFA-d) δ = 7.78 (d, *J* = 6.2 Hz, 6H), 7.67 (d, *J* = 6.8 Hz, 4H), 7.50 (t, *J* = 7.4 Hz, 2H), 7.41 (s, 1H), 7.37 (d, *J* = 6.5 Hz, 4H), 6.90 (d, *J* = 8.6 Hz, 2H), 5.54 (s, 1H).

HRMS (ESI) calculated for $C_{30}H_{20}N_4^+$ ([M+H]$^+$) 437.1761, found 437.1759.

The characterizations are in accordance with the previously reported data. [6,142]

Compound X2 N-(4-methoxyphenyl)-2-nitrobenzenamine



X2

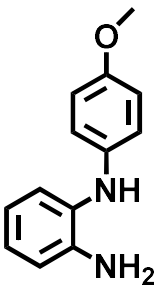
Chemical Formula: $C_{13}H_{12}N_2O_3$
Molecular Weight: 244,25

To a stirred mixture of 1-fluoro-2-nitrobenzene (1.49 mL, 14.1 mmol) and *p*-anisidine (1.73 g, 14.1 mmol) in a sealed tube, DIPEA (7.36 mL, 42.3 mmol) was added, and the reaction mixture was heated to 140 °C for 24h, and then allowed to cool at ca. 20 °C. The mixture was diluted with DCM and successively washed 2 times by dilute HCl (10 %) to remove the unreacted amines. The organic phase was then washed successively by saturated solutions of $NaHCO_3$ and NaCl, dried over anhydrous $Na_2SO_{4(s)}$, filtered, and evaporated to obtain a dark red solid that was triturated in pentane to afford the desired product as a wine-red powder (2.99 g, 86 % yield). Rf = 0.93 (Petroleum Ether: Ethyl Acetate/4:1).

^{1}H NMR (400 MHz, $CDCl_3$) δ = 9.40 (s, 1H), 8.19 (dd, *J* = 8.6, 1.5 Hz, 1H), 7.32 (t, *J* = 7.8 Hz, 1H), 7.19 (t, *J* = 6.0 Hz, 2H), 7.00 (d, *J* = 8.6 Hz, 1H), 6.98 – 6.92 (m, 2H), 6.71 (dd, *J*= 8.4, 7.2 Hz, 1H), 3.84 (s, 3H).

The characterizations are in accordance with the previously reported data. [170]

Compound A2 *N*^{1}-(4-methoxyphenyl)-1,2-benzenediamine



A_2

Chemical Formula: $C_{13}H_{14}N_2O$
Molecular Weight: 214,27

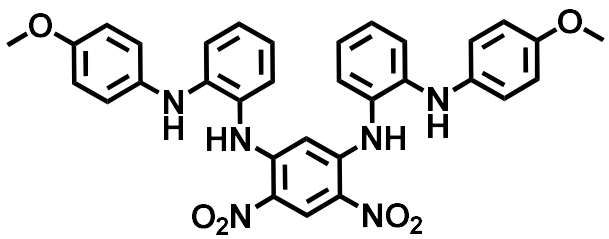
To a stirred mixture of **X2** (3.38 g, 13.86 mmol) and NH_4Cl (7.413 g, 138.6 mmol) in MeOH (32 mL) and water (16 mL) at ca 20 °C, under argon atmosphere, Zn powder was

added in one portion (4.53 g, 69.3 mmol), and the reaction mixture was heated at 45 °C for 3 hours and then allowed to cool at ca. 20 °C (TLC monitoring showed the complete consumption of the starting product **X2**). The mixture was filtered through a Celite® pad to remove Zn residues, washed with MeOH and then evaporated. The organic residue was solubilized in DCM. The resulting organic phase was washed successively by an aqueous solution of $NaHCO_3$, water and a saturated solution of NaCl before being dried over Na_2SO_4, filtered, and then evaporated to afford dark red colored oil (2.96 g, 90.5 % yield).

^{1}H NMR (400 MHz, $CDCl_3$) δ= 7.03 (dd, *J* = 7.8, 1.4 Hz, 1H), 6.95 (td, *J* = 7.6, 1.5 Hz, 1H), 6.84 – 6.81 (m, 1H), 6.81 – 6.78 (m, 3H), 6.75 (m, 2H), 5.01 (s, 1H), 3.77 (s, 3H), 3.71 (s, 2H).

The characterizations are in accordance with the previously reported data.[171]

Compound B2



B_2

Chemical Formula: $C_{32}H_{28}N_6O_6$
Molecular Weight: 592,61

Method 1:

To a mixture of **A2** (670 mg, 3.12 mmol) and DIPEA (3.12 mmol, 0.54 mL), 1,5-difluoro-2,4-dinitrobenzene (159 mg, 0.178 mmol) was added in one portion. The resulting mixture was heated in a sealed tube at 120 °C for 4 hours and then allowed to cool at ca. 20 °C. The red precipitate was filtered through a Celite® pad, washed by hot water and by cold EtOH. Silica gel chromatography via DCM: Petroleum Ether/4:1 was used to isolate the desired product as a red powder (Rf = 0.45, 119 mg, 26 % yield).

Method 2:

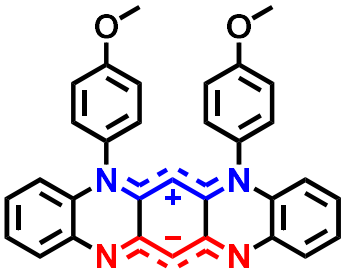
To a mixture of **A2** (2.68 g, 12.5 mmol) and DIPEA (12.5 mmol, 2.17 mL), 1,5-difluoro-2,4-dinitrobenzene (1.27 g, 6.25 mmol) was added in one portion, and the reaction mixture was heated in a sealed tube to 120 °C for 24 h and then allowed to cool at ca. 20 °C. The red precipitate was filtered through a Celite® pad, washed by hot water and by cold EtOH. The powder was then washed by petroleum ether and ethyl acetate, and then dried under vacuum to get the desired title compound as an orange powder (3.47 g, 94 % yield).

^{1}H NMR (400 MHz, DMSO-d_6) δ= 9.37 (s, 2H), 9.00 (s, 1H), 7.31 (s, 2H), 7.06 (t, *J* = 6.8 Hz, 4H), 6.90 (d, *J* = 8.3 Hz, 2H), 6.83 – 6.69 (m, 10H), 5.87 (s, 1H), 3.69 (s, 6H).

^{13}C NMR (100 MHz, DMSO-d_6) δ 154.53, 146.86, 141.27, 135.15, 127.72, 127.65, 125.10, 124.58, 122.26, 118.75, 114.92, 114.31, 95.10, 55.21.

HRMS (ESI) calculated for $C_{32}H_{28}N_6O_6^+$ ($[M+H]^+$) 593.2143, found 593.2144.

Compound ZTAP$_2$



ZTAP$_2$

Chemical Formula: $C_{32}H_{24}N_4O_2$
Molecular Weight: 496,57

METHOD 1: To a solution of **B$_2$** (200 mg, 0.33 mmol) in EtOH (20 mL) at *ca*. 20°C under argon, Pd/C (5 %, 200 mg) was added in one portion. The mixture was stirred for 20 min then transferred to an autoclave that was evacuated and flushed with hydrogen 3 times (approx. 2 bar). The reaction mixture was then left to stir under an atmosphere of dihydrogen (20 bar) for 12 hours. TLC monitoring showed the complete consumption of the starting material and the Pd/C was filtered through a Celite® pad and washed with DCM to dissolve the precipitate. All solvents were evaporated to afford a brown oil.

The resulting oil was then directly solubilized in EtOH (20 mL) and left to stir at *ca* 20 °C under an atmosphere of air. Hydrochloric acid (36 %, 2 mL) was added dropwise and the color of the reaction mixture became purple then dark blue. The mix was left to stir under reflux for 4 hours, then left to cool at *ca* 20 °C. The mixture was then made basic by the addition of ammonia (28 %, 2.48 mL) and the color of the mixture turned dark green. The resulting purple precipitate was filtered, washed by hot water (60°C) and by cold EtOH and dried under vacuum to afford the title compound as a dark green powder (100 mg, 61 % yield).

METHOD 2: To a solution of **B$_2$** (516 mg, 0.87 mmol) and EtOH (20 mL) at *ca*. 20°C under argon, Pd/C (5 %, 200 mg) was added in one portion. The mixture was stirred for 20 min then transferred to an autoclave that was evacuated and flushed with hydrogen 3 times (approx. 2 bars). The reaction mixture was then left to stir under an atmosphere of dihydrogen for 12 hours. TLC monitoring showed the complete consumption of the starting material and the Pd/C was filtered through a Celite® pad and washed with hot EtOH to dissolve the red precipitate.

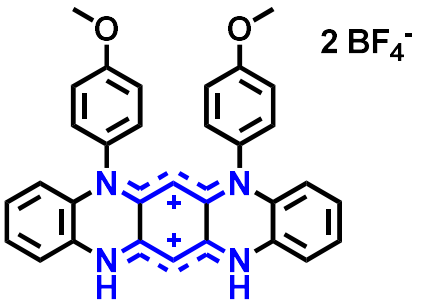
The light brown colored filtrate was then heated to reflux. When the mixture color turned to green, it was concentrated and left to cool down on the bench for 8 hours. The resultant precipitate was filtered and washed with 5 mL of cold EtOH to afford the title compound as a green powder (37 mg, 8.5 %).

^{1}H NMR (400 MHz, $CDCl_3$) δ = 7.63 (q, *J* = 8.1 Hz, 4H), 7.49 (t, *J* = 7.5 Hz, 2H), 7.33 (s, 1H), 7.29 (s, 8H), 7.00 (d, *J* = 8.5 Hz, 2H), 5.48 (s, 1H), 4.09 (s, 6H).

^{13}C NMR could not be recorded due to poor solubility.

HRMS (ESI) calculated for $[M+H]^+$: 497.1972 ($C_{32}H_{24}N_4O_2^+$), found: 497.1972.

Compound $ZTAP_2.2H^{2+}$



$ZTAP_2.2H^{2+}$

Chemical Formula: $C_{32}H_{26}N_4O_2$
Molecular Weight: 498,59

To a suspension of **$ZTAP_2$** (9.6 mg, 0.019 mmol) in acetonitrile (3 mL) at RT, was added aqueous tetrafluoroboric acid (45 %, HBF_4, 0.26 mL). The color of the mixture turned deep blue and the suspension dissolved. The mixture was filtered through a Celite® pad and then added dropwise to stirred diethyl ether (25 mL). The color of the solution becomes troubled. The stirring is stopped and the flask is placed in an ice bath. Pink/gold colored powder precipitates and is collected by filtration, and dried (3 mg, 31 %).

Compound X_3 2-Nitro-N-octylbenzenamine



X_3

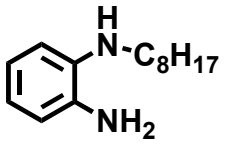
Chemical Formula: $C_{14}H_{22}N_2O_2$
Molecular Weight: 250,34

To a stirred mixture of 1-fluoro-2-nitrobenzene (1.47 mL, 14.1 mmol) and octylamine (2.32 mL, 14.1 mmol), DIPEA (7.36 mL, 42.3 mmol) was added, and the reaction mixture was heated to 140 °C for 24 hours and then allowed to cool at ca. 20 °C. The mixture was diluted with DCM and washed by diluted aqueous HCl (10 %) to remove unreacted amines. The organic layer was washed with a saturated solution of NaCl, separated, dried over anhydrous Na_2SO_4, filtered, and then evaporated to afford dark red colored oil in 99 % yield.

^{1}H NMR (400 MHz, DMSO-d_6) δ = 8.10 (t, *J* = 5.1 Hz, 1H), 8.04 (dd, *J* = 8.6, 1.5 Hz, 1H), 7.56 – 7.45 (m, 1H), 7.03 (d, *J* = 8.5 Hz, 1H), 6.65 (m, 1H), 2.49 (s, 1H), 1.67 – 1.55 (m, 2H), 1.40 – 1.16 (m, 10H), 0.95 (d, *J* = 6.4 Hz, 1H), 0.84 (m, 3H).

The characterizations are in accordance with the previously reported data. [172]

Compound A_3 *N*^{1}-octyl-1,2-benzenediamine



A_3

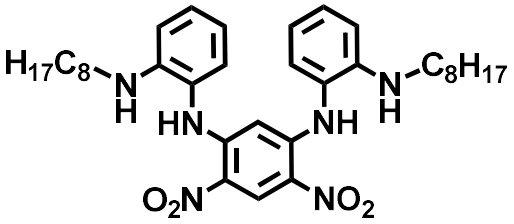
Chemical Formula: $C_{14}H_{24}N_2$
Molecular Weight: 220,36

To a solution of **X_3** (520 mg, 2.077 mmol) and NH_4Cl (1.11g, 20.77 mmol) in MeOH (20 mL) and water (10 mL) at ca 20 °C, under argon, Zn powder was added in one portion (678 mg, 10.4 mmol), and the reaction mixture was heated to 45 °C for 3 hours and then allowed to cool at ca. 20 °C. The mixture was filtered through a Celite® pad to remove Zn residues, then dissolved in DCM. The organic layer was washed with a saturated solution of NaCl, dried over anhydrous Na_2SO_4, filtered, and then evaporated and dried to afford a dark red colored oil (388 mg, 84 %).

^{1}H NMR (400 MHz, DMSO-d_6) δ= 6.53 – 6.43 (m, 2H), 6.41 – 6.33 (m, 2H), 4.46 (s, 2H), 4.29 (s, 1H), 2.98 (m, 2H), 1.57 (m, 2H), 1.27 (d, *J* = 3.7 Hz, 10H), 0.93 – 0.78 (m, 4H).

The characterizations are in accordance with the previously reported data. [173]

Compound B_3



B_3

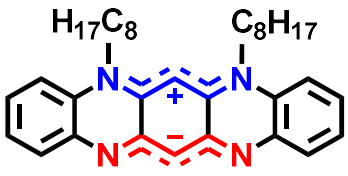
Chemical Formula: $C_{34}H_{48}N_6O_4$
Molecular Weight: 604,80

1,5-difluoro-2,4-dinitrobenzene (509 mg, 2.5 mmol) and compound **A_3** (1.1 g, 4.99 mmol) were dissolved in absolute EtOH (10 mL). N,N-diisopropylethylamine (0.87 mL, 4.99 mmol) was added to the solution. The resulting mixture was stirred at 80 °C for 24 hours. The reaction mixture was cooled to room temperature and evaporated under reduced pressure. The residue was dissolved in dichloromethane. This organic phase was washed successively by a saturated aqueous solution of NH_4Cl and by water. The organic layer was dried over anhydrous Na_2SO_4, filtered and evaporated. Purification by column chromatography over silica gel using petroleum ether/ethyl acetate (95:5 to 9:1) as eluent afforded the product as an orange oil that solidified on standing (1.444 g, 96 %). **Rf:** 0.68 (SiO_2, petroleum ether/ ethyl acetate, 9:1).

^{1}H NMR (400 MHz, $CDCl_3$): δ = 9.32 (s, 1H, CH), 9.21 (br s, 2H, NH), 7.10 (t, ^3J = 7.6 Hz, 2H, CHAr), 6.93 (d, ^3J = 7.6 Hz, 2H, CHAr), 6.59 – 6.55 (m, 4H, CHAr), 5.72 (s, 1H, CH), 3.66 (br s, 2H, NH), 2.96 (m, 4H, NCH_2), 1.49 (m, 4H, CH_2), 0.87 – 0.86 (m, 10H, CH_2 and CH_3). **^{13}C NMR (100 MHz, $CDCl_3$):** δ = 147.7 (C), 144.0 (C), 129.2 (CH), 129.0 (CH), 126.9 (CH), 125.6 (C), 122.0 (C), 116.8 (CH), 111.5 (CH), 96.62 (CH), 43.7 (NCH_2), 31.9 (CH_2), 29.6 (CH_2), 29.5 (CH_2), 29.4 (CH_2), 27.3 (CH_2), 22.8 (CH_2), 14.2 (CH_3).

HRMS (ESI) calculated for $[M+H]^+$: 605.3810 ($C_{34}H_{49}N_6O_4^+$), found: 605.3812.

Compound $ZTAP_3$



$ZTAP_3$

Chemical Formula: $C_{34}H_{42}N_4$
Molecular Weight: 508

Compound **B_3** (500 mg, 0.827 mmol) and 5 wt. % Pd over carbon (264 mg, 0.124 mmol, 15 mol %) were dissolved absolute EtOH (80 mL). Hydrazine monohydrate (2.02 mL, 41.3 mmol) was added ant the resulting mixture was stirred at 80 °C for 16 hours. The reaction mixture was cooled to room temperature, filtered on a Celite® plug, the Celite® was rinsed with MeOH and the collected fractions were evaporated under reduced

pressure. Then the residue was dissolved in absolute EtOH (150 mL) and the solution was stirred at 80 °C for 18 hours in the presence of air. After cooling down the solution to room temperature, the mixture was evaporated and the residue was taken up in dichloromethane. The organic phase was washed by a saturated aqueous solution of $NaHCO_3$, dried over anhydrous Na_2SO_4, filtered and evaporated. The obtained solid was washed with diethyl ether and filtered on a sintered glass to afford the product **ZTAP$_3$** as a green powder (320 mg, 76 %).

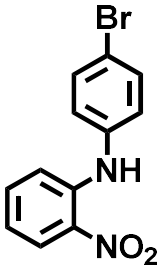
mp: 204-206 °C. **^{1}H NMR (400 MHz, $CDCl_3$)**: δ = 6.98 (d, ^3J = 7.9 Hz, 2H, CHAr), 6.84 (d, ^3J = 7.47 Hz, 2H, CHAr), 6.65 – 6.58 (m, 4H, CHAr), 6.12 (s, 1H, CH), 5.56 (s, 1H, CH), 3.84 (m, 4H, NCH_2), 1.67 (m, 4H, CH_2), 1.46 (m, 4H, CH_2), 1.29 (m, 16H, CH_2), 0.90 (m, 6H, CH_3).

^{13}C NMR (100 MHz, $CDCl_3$): δ = 150.3 (C), 144.7 (C), 142.2 (C), 128.5 (C), 126.7 (CH), 126.0 (CH), 122.9 (CH), 114.1 (CH), 103.7 (CH), 88.5 (CH), 46.2 (NCH_2), 31.9 (CH_2), 29.7 (CH_2), 29.5 (CH_2), 27.4 (CH_2), 26.3 (CH_2), 22.8 (CH_2), 14.2 (CH_3).

IR (neat, cm^{-1}): ν = 2952, 2920, 2851, 1611, 1561, 1515, 1460, 1441, 1351, 1294, 1226, 1153, 1123, 917, 837, 882, 803, 733.

HRMS (ESI) calculated for $[M+H]^+$: 509.3639 ($C_{34}H_{45}N_4^+$), found: 509.3634.

Compound X_4 *N*-(4-bromophenyl)-2-nitrobenzenamine



X_4

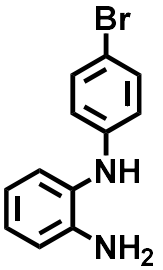
Chemical Formula: $C_{12}H_9BrN_2O_2$
Molecular Weight: 293,12

To a stirred mixture of 1-fluoro-2-nitrobenzene (0.37 mL, 3.51 mmol) and 4-bromoaniline (600 mg, 3.51 mmol), triethylamine (0.48 mL, 3.51 mmol) was added, and the reaction mixture was heated to 140 °C for 24 hours and then allowed to cool at ca. 20 °C. The mixture was then diluted with DCM. The organic phase was washed by diluted aqueous HCl (10 %) to remove unreacted amines. The organic layer was washed with brine, separated, dried over Na_2SO_4, filtered, and then evaporated to afford the final compound **A_1** as an orange powder (979 mg, 95 % yield).

^{1}H NMR (400 MHz, DMSO-d_6) δ = 9.27 (s, 1H), 8.10 (m, 1H), 7.62 – 7.45 (m, 3H), 7.33 – 7.15 (m, 3H), 7.02 – 6.83 (m, 1H).

The characterizations are in accordance with the previously reported data [174]

Compound A_4 N^1-(4-bromophenyl)-1,2-benzenediamine



A_4

Chemical Formula: $C_{12}H_{11}BrN_2$
Molecular Weight: 263,14

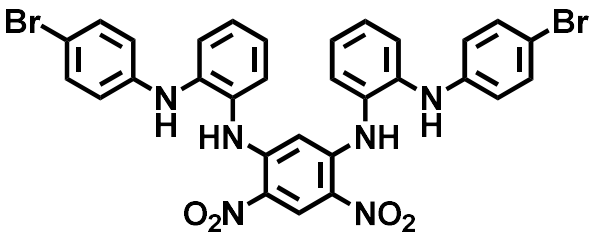
To a stirred mixture of **X_4** (500 mg, 1.7 mmol) and NH_4Cl (909 mg, 17 mmol) in MeOH (30 mL) and H_2O (15 mL) at ca 20 °C, under argon, Zn powder was added in one portion (557 mg, 8.52 mmol). The reaction mixture was heated to 45 °C for 12 hours and then allowed to cool at ca. 20 °C. The mixture was filtered through a Celite® pad to remove Zn residues that was washed with MeOH. The collected filtrates were evaporated under vacuum. The resulting residue was dissolved in DCM. The organic layer was washed successively by a saturated solution of $NaHCO_3$, water and a saturated solution of NaCl, then dried over anhydrous Na_2SO_4 and filtered. The resulting organic mixture was

evaporated and dried under vacuum to afford the title compound **A4** as a light brown powder (410 mg, 91 %).

^{1}H NMR (400 MHz, DMSO-d$_6$) δ 7.31 (s, 1H), 7.27 – 7.18 (m, 2H), 6.95 (dd, *J* = 7.8, 1.3 Hz, 1H), 6.85 (td, *J* = 7.8, 1.4 Hz, 1H), 6.72 (dd, *J* = 7.9, 1.4 Hz, 1H), 6.64 – 6.57 (m, 2H), 6.52 (m, 1H), 4.73 (s, 2H).

The characterizations are in accordance with the previously reported data [174]

Compound B4



B4

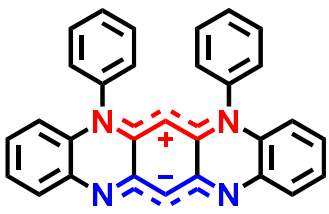
Chemical Formula: $C_{30}H_{22}Br_2N_6O_4$
Molecular Weight: 690,35

To a stirred solution of **C** (200 mg, 0.38 mmol) and 1,5-difluoro 2,4-dinitrobenzene (78 mg, 0.38 mmol) in a sealed tube, DIPEA (0.76 mmol, 0.13 mL) was added at ca 20 °C. The reaction mixture was heated to reflux for 12 hours and was allowed to cool at ca. 20 °C. The dark red precipitate was filtered through a Celite® pad, washed with hot water, cold EtOH, petroleum ether and dried to afford the compound **D** as a brown powder (259 mg, 99 %).

Mp= 263-270°C; **^{1}H NMR (400 MHz, DMSO-d6)** δ 9.38 (s, 2H), 8.93 (s, 1H), 7.72 (s, 2H), 7.26 – 7.20 (m, 4H), 7.16 – 7.06 (m, 6H), 6.93 – 6.85 (m, 2H), 6.68 – 6.60 (m, 4H), 5.87 (s, 1H).

HRMS (ESI) calculated for $[M+H]^+$: 688.9979 ($C_{30}H_{22}N_6O_4^+$), found: 688.9974.

Compound C



C

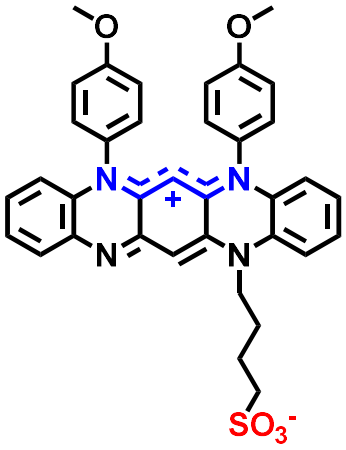
Chemical Formula: $C_{30}H_{20}N_4$
Molecular Weight: 436,52

To a stirred solution of compound **B4** (36 mg, 0.052 mmol) and absolute EtOH (25 mL) at *ca*. 20 °C under argon, Pd/C (5 %, 37 mg) was added in one portion. The mixture was

stirred for 20 minutes then transferred to an autoclave that was evacuated and flushed with dihydrogen 3 times (2 bar). The reaction mixture was then left to stir under an atmosphere of dihydrogen (20 bar) for 12 hours. TLC monitoring showed the complete consumption of the starting material and the Pd/C was filtered through a Celite® pad and washed with hot EtOH to dissolve the precipitated amine. The resulting brown ethanolic solution was heated under reflux until its color turned to green. It was then concentrated and left to cool down on the bench. The dark green precipitate was then filtered and washed with cold EtOH and dried to afford **C** as a dark green powder (31 mg, 13 %).

The characterizations are in accordance with the previously reported data. [6,142]

Compound R-ZTAP$_2$



R-ZTAP$_2$

Chemical Formula: $C_{36}H_{32}N_4O_5S$
Molecular Weight: 632,73

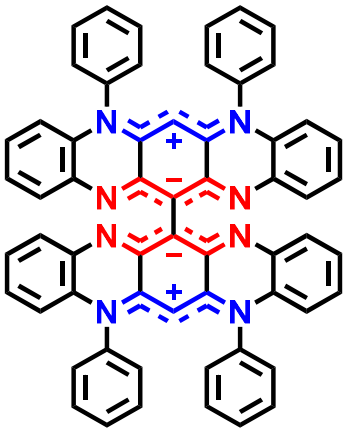
A mixture of **ZTAP$_2$** (10.9 mg, 0.021 mmol) and 1,4-butane sultone was stirred under at 120 °C overnight in a Schlenk tube under argon atmosphere. The color of the mixture turned from green to dark blue in an hour. The reaction mixture was allowed to return to 20 °C and solubilized in MeOH. The MeOH solution containing the product and the excess of butane sultone was gradually diluted with water. The mixture was then subjected to evaporation to remove the MeOH. As a result, the 1,4-Butane sultone remained dissolved in water, while **R-ZTAP$_2$** precipitated as a pink/gold powder. The powder was subsequently isolated by filtration (4 mg, 30 %).

Mp= 290 °C; **^{1}H NMR (400 MHz, CDCl$_3$)** δ = 7.90 (d, *J* = 8.4 Hz, 1H), 7.50 (t, *J* = 7.2 Hz, 1H), 7.36 (dd, *J* = 21.5, 8.4 Hz, 2H), 7.12 (d, *J* = 7.7 Hz, 5H), 7.09 – 7.01 (m, 4H), 6.89 (d, *J* = 8.4 Hz, 1H), 6.81 (s, 1H), 6.77 (t, *J* = 7.7 Hz, 1H), 6.32 (d, *J* = 7.9 Hz, 1H), 4.83 (s, 1H), 4.05 (s, 2H, CH), 3.92 (d, *J* = 9.4 Hz, 6H, OCH_3), 2.95 (t, *J* = 5.5 Hz, 1H, CH), 2.12 (s, 4H, CH).

No **^{13}C NMR** spectrum could be recorded owing to the poor solubility of this compound.

MS 871.32 calculated for $C_{60}H_{38}N_8^+$ ([M+H]$^+$), found 871.3.

Compound d-ZTAP$_1$



d-ZTAP$_1$

Chemical Formula: $C_{60}H_{38}N_8$
Molecular Weight: 871,02

To a stirred solution of **ZTAP$_1$** (9.3 mg, 0.02 mmol) in $CHCl_3$ (0.8 mL) at RT was added N-bromosuccinimide (NBS) (4.19 mg, 0.023 mmol). The color of the mixture changes from dark green to dark blue instantly; the mixture was left to stir for 4 hours. TLC monitoring showed the complete consumption of the starting material. The green mixture was dissolved in $CHCl_3$. The organic layer was washed 6 times with water, separated, dried over anhydrous Na_2SO_4, filtered, and then evaporated and dried to afford the title compound **d-ZTAP$_1$** as a dark blue powder (6.6 mg, 66 %).

^{1}H NMR (400 MHz, TFA-*d*) δ = 7.82 (s, 16H), 7.61 (s, 6H), 7.55 (d, *J* = 6.7 Hz, 10H), 6.97 (d, *J* = 8.2 Hz, 4H), 5.81 (s, 2H).

No ^{13}C NMR spectrum could be recorded owing to the poor solubility

MS 871.32 calculated for $C_{60}H_{38}N_{8+}$ ($[M+H]_+$), found 871.3.

The characterizations are in accordance with the previously reported data.[6]

D. Python code

Δf^* and V_{CPD} map code

```
import scipy as sc
import numpy as np
import matplotlib.pyplot as plt

from scipy import integrate
from scipy.optimize import curve_fit
from tkinter import Tk, filedialog
import os
import re

def CoordSpectro(nom_de_la_spectro):
    # Find the indices of X, Y, and Z in the spectrum filename
    indice_X = nom_de_la_spectro.find("X")
    indice_Y = nom_de_la_spectro.find("Y")
    indice_Z = nom_de_la_spectro.find("Z")

    # Extract the 2 characters following X, Y, and Z
    derniers_caractère_apres_X = nom_de_la_spectro[indice_X + 2:indice_X + 4]
    derniers_caractère_apres_Y = nom_de_la_spectro[indice_Y + 2:indice_Y + 4]
    derniers_caractère_apres_Z = nom_de_la_spectro[indice_Z + 2:indice_Z + 4]

    # Store the results
    X = int(derniers_caractère_apres_X)
    Y = int(derniers_caractère_apres_Y)
    Z = int(derniers_caractère_apres_Z)

    return(X, Y, Z)
```

```
# Polynomial function to fit the data (quadratic form)
def poly2(x, a, b, c):
    return (a * x ** 2 + b * x + c)

# Initial guess for the polynomial coefficients
pinit = (-6, -8, -11)

######## OPEN *.Parameter.dat FILE ######################

# Create an instance of the Tkinter main window
root = Tk()

# Hide the main window
root.withdraw()

# Display the file selection dialog
fichier_selectionne = filedialog.askopenfilename(
    parent=root,
    title="Select the parameters file in the spectroscopy directory to process",
    filetypes=[("Parameters.dat files", "*Parameters.dat"), ("All files", "*.*")])

# Display the selected file path and name
print("Selected file:", fichier_selectionne)

# Extract the file name from the full path
nom_fichier = os.path.basename(fichier_selectionne)

# Extract the folder path from the full file path
chemin = os.path.dirname(fichier_selectionne)
print("Selected directory:", chemin)

########### Extract parameters from the *.Parameter.dat file ###########

# Dictionary to store spectroscopy grid parameters
parametres = {}
```

```
# Open the file in read mode
with open(fichier_selectionne, 'r') as fichier:
    lignes = fichier.readlines()

# Scan the file lines and exclude the first 15 lines
for ligne in lignes[0:15]:
    # Check if the line contains the '=' sign
    if '=' in ligne:
        # Split the line at '=' to get the parameter name and value
        elements = ligne.split('=')

        # Extract the parameter name (before '=')
        nom_parametre = elements[0].strip()

        # Extract the parameter value (after '=')
        valeur_parametre = float(elements[1].strip())

        # Store the parameter and its value in the dictionary
        parametres[nom_parametre] = valeur_parametre

# Extract grid dimensions and scale factor
Nx = int(parametres["Points X"])
Ny = int(parametres["Points Y"])
Nz = int(parametres["Number of Z measurements"])
SizeX = parametres["Width (m)"]
SizeY = parametres["Height (m)"]
pasZ = parametres["DZ (m)"]
scale_factor = SizeX / Nx * 1e9

######## Extraction of CPD and Df* for all spectroscopies in the folder #########

# Get the list of all files containing 'Bias_Spectro' in the same folder
liste = []
if chemin:
```

```
    liste = [fichier for fichier in os.listdir(chemin)
            if os.path.isfile(os.path.join(chemin, fichier))
            and "Bias_Spectro" in fichier]

# Total number of spectroscopies in the folder
NbSpectro = len(liste)

# Initialize arrays to store CPD and Df* values
CPDfit = np.zeros((Nx, Ny, Nz))
Dfstarmap = np.zeros((Nx, Ny, Nz))

# Loop through all the spectroscopies in the folder
for i in range(NbSpectro):
    spectro = liste[i]
    chemin_complet = os.path.join(chemin, spectro)

    # Load data from the spectroscopies file, skipping the first 197 rows
    A = np.loadtxt(chemin_complet, skiprows=197)
    X, Y, Z = CoordSpectro(spectro)
    print(X, Y, Z)

    # Extract data from the file
    V = A[:, 0]
    I = A[:, 1]
    Phase = A[:, 2]
    Ampli = A[:, 3]
    FreqShift = A[:, 4]
    Excitation = A[:, 5]

    # Fit the frequency shift data with the polynomial
    (para, ki) = curve_fit(poly2, V, FreqShift, pinit)
    fit = poly2(V, para[0], para[1], para[2])

    # Calculate Df* and find the maximum of the fit
    Dfstar = np.max(fit)
```

```
        IndiceMaxfit = np.argmax(fit)

        # Store CPD and Df* values in the corresponding coordinates X, Y, Z
        CPDfit[Y-1, X-1, Z] = V[IndiceMaxfit]
        Dfstarmap[Y-1, X-1, Z] = Dfstar

    # Set up the coordinate ranges for plotting
    X1_nm = np.arange(CPDfit.shape[1])
    Y1_nm = np.arange(CPDfit.shape[0])

    X2_nm = np.arange(Dfstarmap.shape[1])
    Y2_nm = np.arange(Dfstarmap.shape[0])

    # Plot the CPD and Df* maps for each Z layer
    for i in range(Nz):
        plt.figure(figsize=(12, 12))

        # First subplot for Dfstarmap
        plt.subplot(1, 2, 1)
        img1 = plt.imshow(Dfstarmap[:, :, i], interpolation='hanning', origin='lower',
cmap='viridis', extent=[X1_nm[0], X1_nm[-1], Y1_nm[0], Y1_nm[-1]])
        cbar = plt.colorbar(label='Δf* map (Hz)', orientation='vertical', shrink=0.38)
        plt.title(f'Δf* map (Hz)', fontsize=16)
        ax = plt.gca()
        ax.set_xlabel('X (pixel)', fontsize=14)
        ax.set_ylabel('Y (pixel)', fontsize=14)

        # Second subplot for CPDfit
        plt.subplot(1, 2, 2)
        img2 = plt.imshow(CPDfit[:, :, i], interpolation='hanning', origin='lower',
cmap='gray', extent=[X2_nm[0], X2_nm[-1], Y2_nm[0], Y2_nm[-1]])
        cbar = plt.colorbar(label='V$_{{CPD}}$ map (V)', orientation='vertical', shrink=0.38,
format='%.2f')
        plt.title(f'V$_{{CPD}}$ map (V)', fontsize=16)
        ax = plt.gca()
        ax.set_xlabel('X (pixel)', fontsize=14)
```

```
    ax.set_ylabel('Y (pixel)', fontsize=14)

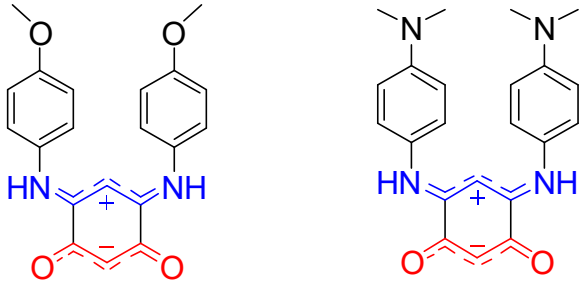
    # Show the figure
    plt.show()

# Plot Df* values for a specific pixel across all Z layers
for i in range(Nz):
    plt.plot(Nz, Dfstarmap[6, 6, Nz-1])
plt.show()
```

E. Challenges and unsuccessful attempts

In this subsection we show the attempts of creating a periodic self-assembled zwitterionic molecular network on HOPG or Gr/SiC surfaces by changing the peripheral functional groups of the DPQZ molecule.

The molecules tried are the di-methoxyphenyl functionalized QZ molecule (DMPQZ) and the bis [4-(dimethylamino)phenyl] functionalized QZ (DPDQZ) that were synthesized by Dr. Simon Pascal according to an established procedure.[175]



DMPQZ **DPDQZ**

*Figure 121: Schematic representation of the di-methoxyphenyl p-benzoquinonemonoimine zwitterion molecule (**DMPQZ**) and the bis [4-(dimethylamino)phenyl] p-benzoquinonemonoimine zwitterion (**DPDQZ**)*

DMPQZ on HOPG : assembly

All STM experiments and sample preparations were performed under UHV conditions using a commercial low-temperature STM (78 K) with pressures in the 10^{-11} mbar range. The HOPG and Gr/SiC samples were prepared as described in the Chapter III. The samples were then transferred into the analysis chamber and cooled down to LN_2 temperature. The cleanliness and structural quality of the substrates was checked by STM prior to any deposition. The STM images were obtained in constant current mode at a temperature of 78 K for both the sample and tungsten STM tip. All STM images presented are raw acquired data except for standard plane subtraction and one-dimensional Fast Fourier Transform (1D-FFT) filtering at 150Hz along the horizontal direction.

The **DMPQZ** molecules were deposited with high reproducibility by thermal sublimation from a molecular Kentax evaporator with the quartz crucible held at 135 °C. 1 ML of these molecules was deposited on a HOPG surface at room temperature after 8 min of exposure under UHV in the 10^{-10} mbar range during the deposition. These deposit conditions are similar to the ones used to obtain a ML of DPQZ on HOPG.

The constant current STM image in Figure 122(a) shows the extended molecular phase after the deposition of DMPQZ molecules on a HOPG surface.

The bent bands horizontally across the image are dislocations or stacking defaults on the HOPG surface attributed to the stacking of HOPG sheets. On the medium-scale STM image in Figure 122(b) we can see that DMPQZ form a compact self-assembly on HOPG.

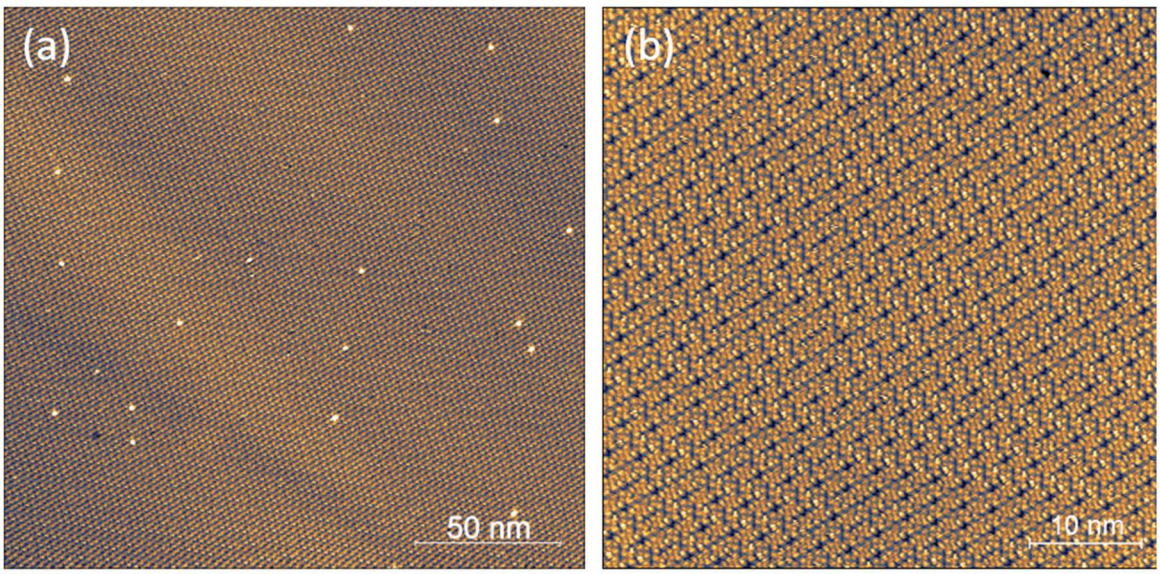


Figure 122: STM images of DMPQZ molecules adsorbed on a HOPG surface at different scales. Tunneling conditions: I_t= 5 pA, V_{bias}=1.60 V.

On the smaller scale STM image of Figure 123(b) the ML is observed to be composed of 3 different motifs that we will describe in detail. The motif 1 comprises 6nine bright features that we can assimilate to a dimer of molecules. Motif 2 could be assimilated to a molecule adsorbed on the edge, and motif 3 is a dimer of a dimer (dimer of motif 1). These motifs self-assemble in ribbons that show irregularities in their assembly. In fact; the methoxy group has 3 rotational degrees of freedom, which could contribute to the formation of the 3 distinct motifs observed.

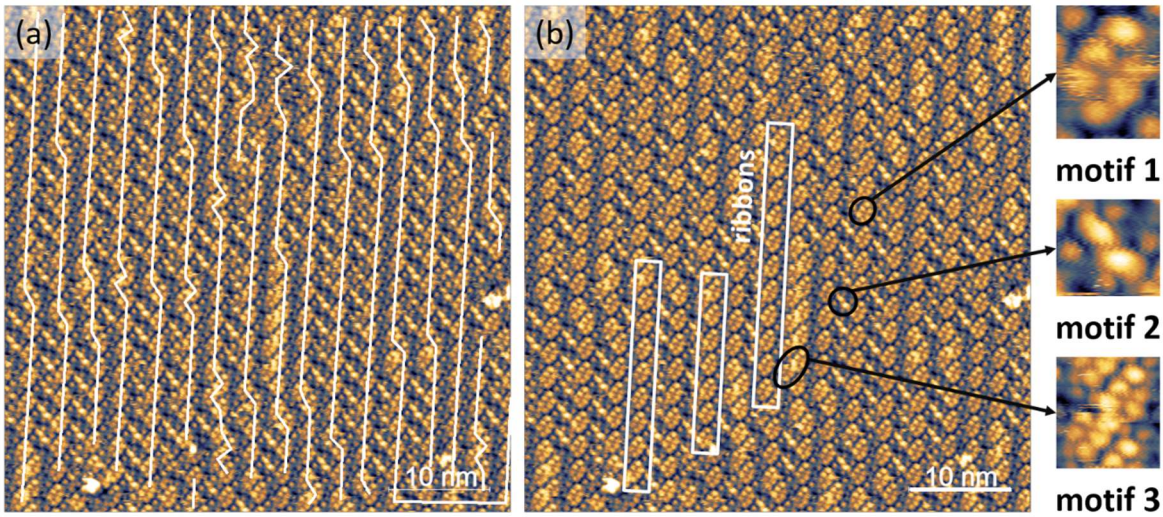


*Figure 123: STM images of the adsorbed monolayer of **DMPQZ** on the HOPG surface. I_t=5 pA, V_{bias}=1.6 V. (a) White lines delimit ribbons growth path on the surface. (b) 3 motifs features are circled in black.*

DMPQZ on HOPG : epitaxy with the substrate

Studying an image at the interface between the organic layer and HOPG by the STM cross correlation method explained in V.1.1.3.

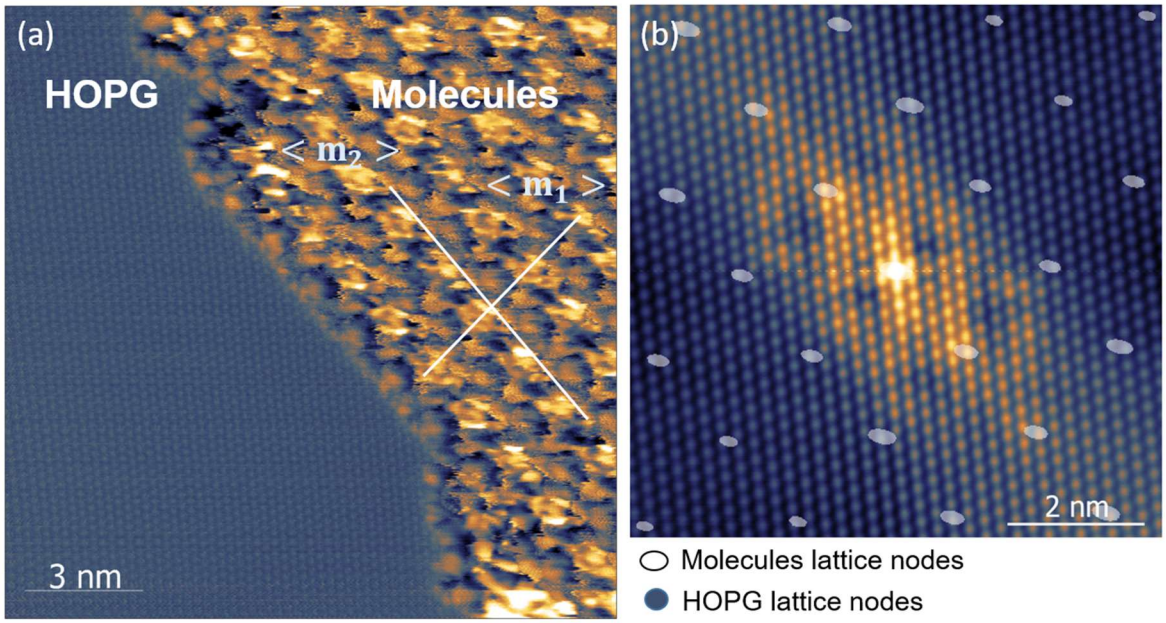


Figure 124: (a) STM image of less than a monolayer of DMPQZ molecule with atomic resolution on HOPG. Tunneling conditions: V_{bias}= 0.80 V, I_t= 6 pA. (b) Superposition image resulting from applying the autocorrelation method on the interface between the DMPQZ molecular layer on HOPG.

Figure 124(a) shows an STM image with a DMPQZ deposit of 4 minutes on HOPG. The imaging was done on the border between the HOPG (with atomic resolution) and the DMPQZ layer. This layer has a poor resolution because the tunneling parameters used to

gain atomic resolution on HOPG are very different than those used to image the molecules. From this molecular layer we can discern a motif, growing linearly along the $\mathbf{m_2}$ direction.

We superpose the autocorrelation images of each of the lattices to deduce the relative position of the molecule lattice nodes with respect to graphene lattice nodes and we obtain Figure 124(b). We could not identify molecular nodes possessing equivalent sites with respect to HOPG on the scale of this image. This doesn't exclude the fact that they might still be present at a larger scale. The white nodes are the molecule lattice nodes with lattice vectors ($\mathbf{m_1}$,$\mathbf{m_2}$) and the blue nodes represent that HOPG lattice nodes with lattice vectors ($\mathbf{g_1}$,$\mathbf{g_2}$).

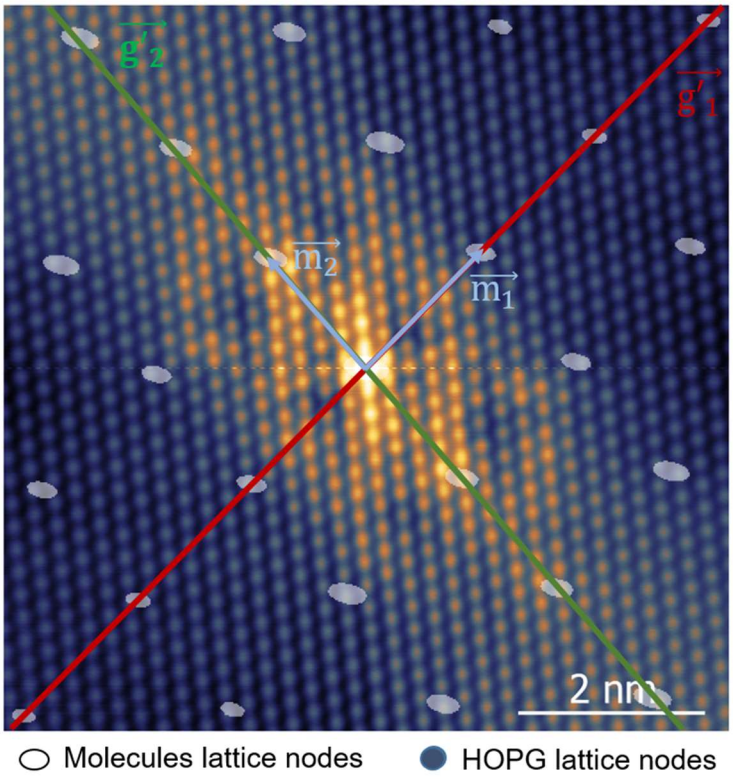


Figure 125: Superposition image that results from the autocorrelation method on the interface between the DMPQZ molecular layer on HOPG.

We observe coincidences between the nodes of the molecular network in 2 directions: the first, $\mathbf{g'_1}$, is a crystallographic direction of HOPG of the 4th order, and another coincidence with a direction $\mathbf{g'_2}$, which is a crystallographic direction of HOPG of the 7th order. We can determine the epitaxial relationships of these growth directions with respect to this basis of vectors ($\mathbf{g'_1}$, $\mathbf{g'_2}$).

We find commensurability with the substrate in the $\mathbf{m_1}$ direction after 174 nodes of $\mathbf{g'_1}$, and commensurability with the substrate in **the** $\mathbf{m_2}$ direction after 52 nodes of $\mathbf{g'_2}$.

$$\begin{pmatrix} m_1 \\ m_2 \end{pmatrix} = \begin{pmatrix} \frac{174}{89} & 0 \\ 0 & \frac{52}{53} \end{pmatrix} \begin{pmatrix} g_1' \\ g_2' \end{pmatrix} \quad \text{(A. 23)}$$

We conclude that commensurability with the substrate is found at scales larger than the molecular domain size, and therefore, the molecular phase of DMPQZ is incommensurate with HOPG.

DPDQZ on HOPG : assembly

The DPDQZ molecules were deposited on a HOPG substrate for 8 minutes under UHV with the substrate held at RT.

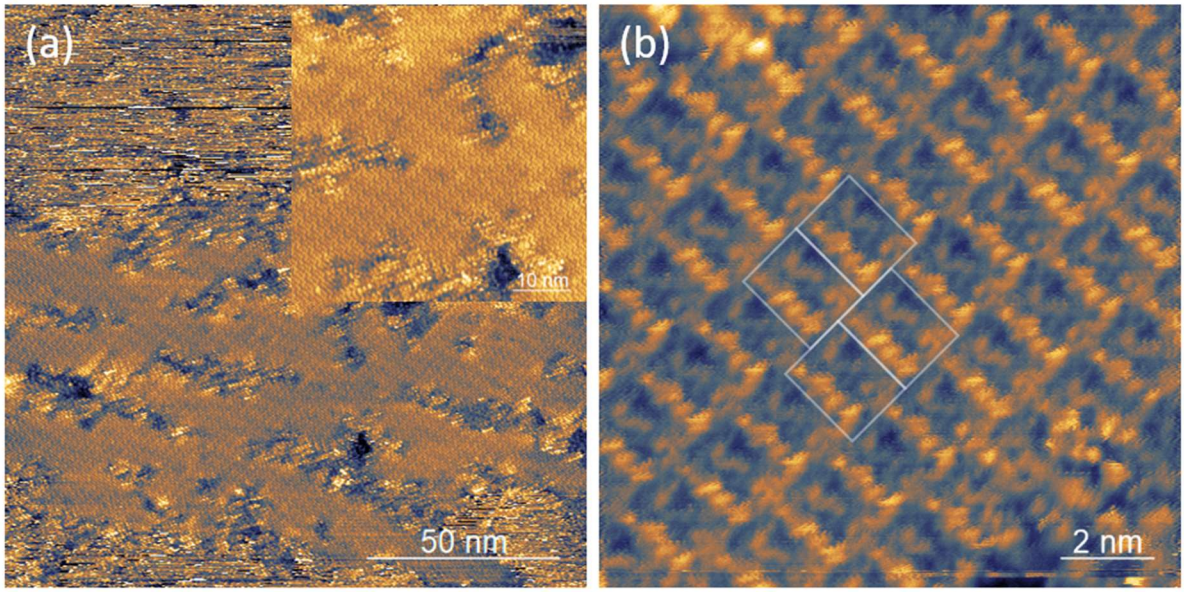


Figure 126: (a) STM image showing the deposit DPDQZ molecules on HOPG. In inset is a zoom-in on the assembled molecular phase Tunneling conditions: V_{bias}= 1.50 V, I_t= 5 pA. (b) STM image of the assembled molecular phase, showing a quincunx pattern. The motif is highlighted by white rectangles. Tunneling conditions: V_{bias}= 1.0 V, I_t= 5 pA.

In the Figure 126(a), we can see a well-defined structure (with a smaller scale image in the inset on this structure), where the molecules form a distinct molecular phase, than on the edges. Figure 126(b) shows the resultant ordered molecular phase where the molecules assemble in a quincunx pattern, where each repeating unit is indicated by a white rectangle. A possible interpretation for this behavior could be that the bulky N-methyl groups might hinder the close packing of the DPDQZ molecules, which explains the spacing between the bright features in each motif in the core phase, while still allowing dipole interactions or π-π stacking to occur. The peripheral molecules have less interaction with the substrate and could possibly adopt different conformations or orientations that lead to a more disordered dynamic boundary.

For comparison, DPDQZ were deposited on a graphene substrate held at RT during deposition. Figure 127(a, b, c) shows STM images of a deposit of DPDQZ of 4 minutes. There is no self-assembly as well and there is a lack of even surface coverage. If we multiply the deposition time by 2 (Figure 127(d)), the molecules still randomly spread out on the surface and cluster in batches that pack now more closely together.

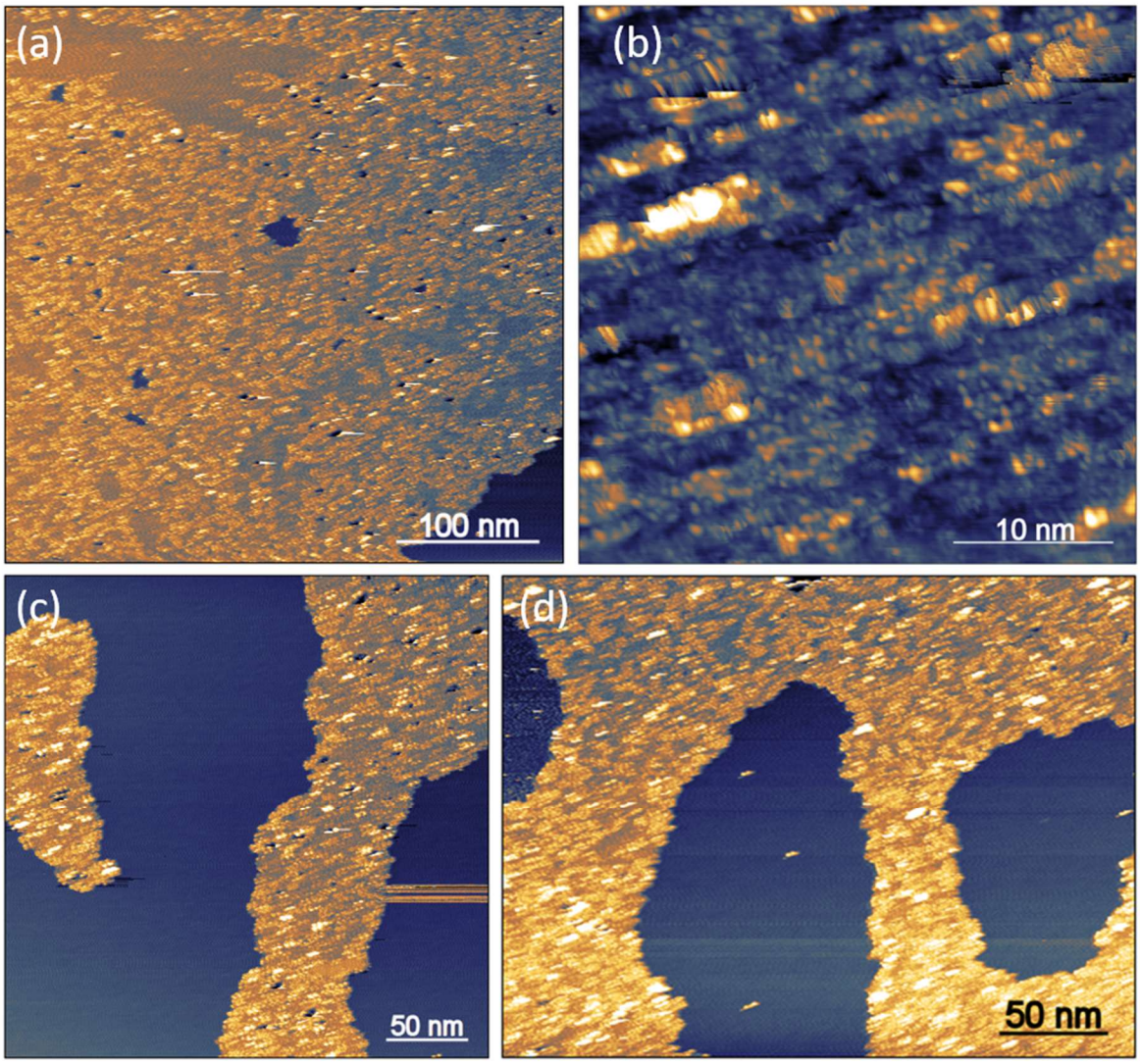


Figure 127: STM images of DPDQZ on graphene after a 4 minutes deposit (a) Large scale image showing the distribution of the molecules on the surface. Tunneling conditions: V_{bias}= 1.41 V, I_t= 5 pA. (b) Medium scale image showing the clusters of different sizes and shapes, as well as holes in the layer. Tunneling conditions: V_{bias}= 1.80 V, I_t= 5 pA. (c) Large scale image showing an example of the molecules batches on the graphene surface. Tunneling conditions: V_{bias}= 1.70 V, I_t= 5 pA. (d) 8 minutes deposit. Large scale image showing the surface after 8 min deposit. The surface coverage increases in a non-uniform way. Tunneling conditions: V_{bias}= 1.41 V, I_t= 5 pA.

We conclude that the addition of the N-methyl groups provide additional insight on how intermolecular forces change and it is seen to play an important role in defining the structure stability and the dynamics of the molecular assembly. However, it shows to

possess potential for assemblies on HOPG that could be tuned by changing the substrate temperature during molecular deposition or the flux of the molecules.

Our primary objective was to investigate how varying functional groups influence the intermolecular interactions and consequently the self-assembly patterns on surfaces resulting from this interaction. By maintaining the same QZ core of the molecule, we were able to isolate the effects of the different peripheral functional groups on the phenyls and gain a deeper insight of their roles in directing molecular organization.

The comparative study showed that even slight modification of the functional groups, such as adding a methoxy group can lead to significant differences in the self-assembly on HOPG. For instance, the methoxy groups led to a disordered network mainly due to the functional group's 3 rotational degrees of freedom that led to the observation of 3 different motifs on the surface. These motifs grow in ribbons Also, the small extension of the functional group led to a completely different epitaxy with the substrate, going from a high-order commensurate phase to an incommensurate phase.

The addition of N-methyl groups showed an intricate balance between intermolecular forces which are modulated by the presence of different functional groups. On both HOPG and graphene, the DPDQZ did not converge to a stable self-assembled system in deposition conditions similar to previous systems. However, this system shows to possess potential for assembly on HOPG, so future work will be to change these conditions in a way to control the assembly outcome.